Over the last decade Organ-on-Chip (OoC) emerged as disruptive technology combining aspects of microfluidics and tissue engineering. OoCs culture human tissues in tailored microenvironments under microfluidic perfusion, yielding an unprecedented recapitulation of human physiology. So far, most systems predominantly focus on physiological tissue generation. However, it is crucial to integrate stimulation and readout capabilities, leveraging OoCs from bare tissue generation tools to advanced integrated experimental platforms. This thesis focuses on the development and characterization of novel microphysiological systems to probe and actuate tissues on the microscale. We present two Heart-on-Chip platforms enabling the generation of aligned cardiac muscle fibers and investigate the integration of force and O_2 sensing as well as electrical stimulation capabilities. Furthermore, we introduce and characterize two OoCs enabling the precise delivery of biomechanical stretch and compression stimuli. All in all, the systems developed in the framework of this thesis provide a flexible toolkit amenable for disease modeling or personalized medicine, offering advanced experimental capabilities for manipulating and interrogating integrated tissues.

ISBN 978-3-946412-10-6

CBM-11 (2022)

O. Schneider

Sensing and stimulation in microfluidic Organ-on-Chips

Generation, probing, and biophysical stimulation of human microtissues in microfluidic Organ-on-Chip platforms

Oliver Schneider

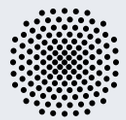

vorgelegt an der
Universität Stuttgart

Generation, probing, and biophysical stimulation of human microtissues in microfluidic Organ-on-Chip platforms

Von der Fakultät Bau- und Umweltingenieurwissenschaften der Universität Stuttgart zur Erlangung der Würde eines Doktor-Ingenieurs (Dr.-Ing.) genehmigte Abhandlung

Vorgelegt von

Oliver Schneider

aus Kempten (Allgäu), Deutschland

Hauptberichter:	Prof. Oliver Röhrle, PhD
Mitberichter:	Prof. Dr. Peter Loskill
2. Berichter:	Prof. Dr. Torsten Mayr
Tag der mündlichen Prüfung:	12. Juli 2022

Institut für Modellierung und Simulation Biomechanischer Systeme der Universität Stuttgart

2022

Report No.: CBM-11 (2022)
Institute for Modelling and Simulation of Biomechanical Systems
Chair for Continuum Biomechanics and Mechanobiology
University of Stuttgart, Germany, 2022

Editor:
Prof. O. Röhrle, PhD

Institute for Modelling and Simulation of Biomechanical Systems
Chair for Continuum Biomechanics and Mechanobiology
University of Stuttgart
Pfaffenwaldring 5a
70569 Stuttgart, Germany

ISBN 978-3-946412-10-6
(D 93 - Dissertation, Universität Stuttgart)

Abstract

Over the last decade Organ-on-Chip (OoC) emerged as disruptive technology with the potential to revolutionize pharmaceutical R&D and biomedical research. By combining aspects of microfluidics and tissue engineering, human tissues are cultured in tailored microenvironments under microfluidic perfusion, yielding an unprecedented recapitulation of human physiology. OoC technology allows to bridge the gap between 2D cell culture and animal testing with possible applications in personalized medicine or drug development. In analogy to microchips, miniaturization and parallelization promise an unrivaled increase in throughput for biopharmaceutical applications.

So far, a variety of OoCs emerged which are tailored to the respective mimicked tissue type. However, most systems rely on manual cell injection protocols, leading to uncontrolled loading pressures and non-standardized tissue generation, hampering the application of OoCs in an industrial large-scale setting. In addition, most systems mostly focus on physiological tissue generation, thus neglecting another major opportunity of OoCs which is the integration of stimulation and readout capacities. The integration thereof allows the study of tissue responses to external stimuli and leverages OoCs from bare tissue generation tools to advanced integrated experimental platforms.

This thesis focuses on the development and characterization of novel microphysiological systems to probe and actuate tissues on the microscale. In particular, we investigate biomechanical cues.

As the human heart is characterized by an intricate coupling between chemical, electrical, and mechanical hallmarks, it is an ideal testbed to study biophysical aspects in OoCs. We develop and compare two distinct Heart-on-Chip (HoC) platforms enabling the generation of aligned cardiac muscle fibers within a perfusable microfluidic environment, representing functional units of the native myocardium. The centrifugal HoC enables the upscaled parallelized culture of eight tissues within one chip and is characterized by a newly developed loading mechanism via centrifugation, allowing precise control of injection parameters and standardized tissue generation. The Spheroflow-HoC accumulates injected cardiac spheroids in dog bone-shaped tissue chambers which subsequently merge to one single unit. By combining spheroid and OoC technology, a scalable pipeline is created, enabling the medium- to high-throughput application of OoCs.

As key metric for characterizing and comparing cultured tissues, beating kinetics

are extracted from brightfield video microscopy recordings via a newly developed open source framework. Based on this non-invasive readout, we demonstrate the applicability of the centrifugal HoC for drug testing.

Furthermore, we introduce a user-friendly approach for integrating electrodes into both developed chip types. Thus, cultured tissues can be electrically stimulated, adapting their beating rate to externally forced frequency. Integrated stimulation capability can be utilized to study the influence of pacing on tissue maturation or to normalize the beating rate as baseline in drug testing studies. We present the blueprint of an Arduino-based low-cost pulse generator, allowing a scripted control of pacing experiments.

As further readout, we investigate the integration of oxygen sensors into OoC platforms to gain insights into tissue metabolism. We present a novel integration concept and demonstrate oxygen measurements coupled to simultaneous electrical tissue stimulation, revealing frequency-dependent changes in oxygen consumption.

For assessing biomechanical properties of cardiac tissues, we integrate force sensing pads to determine tissue twitch forces via traction force microscopy. We compare various integration methods and present a flow-based substrate characterization as well as proof-of-concept measurements on integrated tissues.

In addition to biomechanical sensing capabilities in HoC systems, we further investigate two OoCs enabling the delivery of defined biomechanical stimuli. We fabricate a novel strain OoC for defined stretching of cells cultured on a flexible membrane. By integrating a flexible membrane out of thermoplastic elastomer into microphysiological systems, we demonstrate a scalable fabrication approach. As the membrane can be actuated by pressures in the physiological range, it allows for an application in Lung-on-Chip models. Furthermore, we designed a compression platform for the compression of cell-laden hydrogels within a microphysiological system. By tailoring the tissue chamber shape to a hemisphere, simulations predict a more homogeneous compression, compared to conventional planar chamber geometries. We investigate fabrication approaches to realize the hemispherical geometry and develop injection protocols for bubble-free filling of the dome structure. Ultimately, both mechanical stimulation systems are characterized by tracking deposited fluorescent beads under various mechanical loading, assessing the actuation range for further cell loading experiments.

All in all, the systems developed in the framework of this thesis provide a flexible toolkit amenable for disease modeling or personalized medicine, offering advanced experimental capabilities for manipulating and interrogating integrated tissues. The tailored combination of various sensing and stimulation approaches delivers fit-for-purpose models addressing distinct scientific problems.

Deutsche Zusammenfassung

Im letzten Jahrzehnt ist *Organ-on-Chip* (OoC) als bahnbrechende Technologie in Erscheinung getreten und besitzt das Potenzial die pharmazeutische F&E sowie biomedizinische Forschung zu revolutionieren. Die Kombination von Mikrofluidik und Tissue Engineering ermöglicht die Kultivierung menschlichen Gewebes in maßgeschneiderten Mikroumgebungen unter kontinuierlicher Perfusion, was zu einer unvergleichbaren Nachahmung der menschlichen Physiologie führt. OoC-Technologie verspricht die Lücke zwischen 2D-Zellkulturen und Tierversuchen zu schließen, und könnte u.a. in der personalisierten Medizin oder der Arzneimittelentwicklung eingesetzt werden. In Analogie zu Mikrochips versprechen Miniaturisierung und Parallelisierung eine immense Steigerung des Durchsatzes für biopharmazeutische Anwendungen.

Bislang wurde eine Vielzahl von OoCs entwickelt, welche jeweils individuell auf den nachgeahmten Gewebetyp zugeschnitten sind. Die meisten Systeme basieren auf der manuellen Injektion von Zellen, was zu unkontrollierten Drücken während des Ladevorgangs und großen Variationen zwischen erzeugten Geweben führt. Dies erschwert die Anwendung von OoCs in einem industriellem Maßstab. Darüber hinaus beschränken sich die meisten Systeme auf die Erzeugung von physiologischen Gewebemodellen und vernachlässigen die Integration von Sensoren und Stimulationsmöglichkeiten. Eine Integration ermöglicht die Untersuchung der Reaktionen von kultivierten Organeinheiten auf externe Stimuli und wertet OoCs von Instrumenten zur reinen Gewebeerzeugung zu ausgereiften integrierten Versuchsplattformen auf.

Die vorliegende Doktorarbeit entwickelt und charakterisiert neue mikrophysiologische Systeme, welche die integrierte Untersuchung und gezielte Stimulation von Geweben auf der Mikroskala erlauben. Im Vordergrund stehen dabei biomechanische Stimuli.

Das menschliche Herz ist durch eine fein abgestimmte Kopplung zwischen chemischen, elektrischen und mechanischen Eigenschaften gekennzeichnet und stellt damit ein ideales Testsystem für die Untersuchung biophysikalischer Aspekte in OoCs dar. Es werden zwei verschiedene *Heart-on-Chip* (HoC)-Plattformen vorgestellt, welche die Erzeugung von ausgerichteten Herzmuskelfasern in einer mikrofluidischen Umgebung ermöglichen und somit funktionelle Grundeinheiten des Herzmuskels nachahmen. Der *centrifugal HoC* erlaubt die parallele Kultivierung von acht Geweben in einem Chip und stellt einen neuen Injektionsmechanismus vor. Dieser basiert auf Zentrifugation einer Zellsuspension und ermöglicht die präzise Kontrolle der Injek-

tionsparameter sowie eine standardisierte Gewebeerzeugung. Der *Spheroflow-HoC* hingegen injiziert Herz-Sphäroide, welche sich durch die angepasste Kanalgeometrie in ausgerichteten Gewebekammern ansammeln und in anschließender Kultivierung zu einem einzigen Gewebe verschmelzen. Die Kombination von Sphäroid- und OoC-Technologie liefert ein skalierbares System, welches die Anwendung von OoCs für den mittleren bis hohen Durchsatz zulässt.

Wir extrahieren das Schlagverhalten aus Videos von kultiviertem Herzgewebe mittels einer neu entwickelte Open-Source-Software und ziehen es als Schlüsselparameter zur Charakterisierung von Herzgewebe heran. Basierend auf diesem nichtinvasiven Messverfahren demonstrieren wir die Anwendbarkeit des zentrifugalen HoCs für Medikamententests.

Zusätzlich stellen wir einen benutzerfreundlichen Ansatz zur Elektrodenintegration in beide entwickelte Chiptypen vor. Diese ermöglicht die elektrische Stimulation von kultiviertem Gewebe, welche zur Anpassung der Schlagfrequenz an die von außen vorgegebene Frequenz führt. Die integrierte Stimulationsmöglichkeit kann dazu genutzt werden, den Einfluss elektrischer Stimulation auf die Gewebereifung zu untersuchen oder um die Schlagfrequenz in Medikamententests auf einen Referenzwert zu normalisieren. Wir stellen den Bauplan eines kostengünstigen Arduino-basierten Pulsgenerators bereit, der die programmierbare Durchführung von Stimulationsexperimenten ermöglicht.

In dieser Arbeit untersuchen wir zudem die Integration von Sauerstoffsensoren in OoC-Plattformen, die zusätzliche Erkenntnisse über die metabolische Aktivität kultivierter Gewebe liefern. Wir stellen ein neues Integrationskonzept vor und kombinieren Sauerstoffmessungen an Herzgeweben mit elektrischer Stimulation. Dadurch kann eine frequenzabhängige Änderung des Sauerstoffverbrauchs nachgewiesen werden.

Zur Untersuchung biomechanischer Eigenschaften von Herzgeweben werden flexible Substrate in untersuchte HoCs eingebracht, welche die Messung von Kontraktionskräften mittels *traction force microscopy* ermöglichen. Wir vergleichen verschiedene Integrationsmethoden und präsentieren eine flussbasierte Charakterisierung des Substrats sowie integrierte Messungen an Herzgeweben.

Zusätzlich zur Integration von Kraftsensoren in HoC-Systeme werden zwei weitere OoCs entwickelt die eine gezielte biomechanische Stimulation ermöglichen. Wir stellen eine OoC-Plattform vor, in der Zellen auf einer flexiblen Membran kultiviert und einer definierten Dehnung ausgesetzt werden können. Die Integration einer flexiblen Membran aus thermoplastischem Elastomer stellt dabei einen neuen skalierbaren Herstellungsansatz dar. Da die Membran durch Drücke in einer physiologischen Größenordnung ausgelenkt werden kann, ist sie für eine Anwendung in *Lung-on-Chip*-Modellen geeignet. Darüber hinaus wurde eine Plattform entwickelt welche die Kompression von zellbeladenen Hydrogelen in einem mikrophysiologischen System erlaubt. Simulationen der angepassten halbkugelförmigen Gewebekammerform zeigen eine homogenere Kompression im Vergleich zu konventionellen planaren Kammergeometrien. Wir untersuchen Herstellungsansätze zur Realisierung der halbkugelförmigen Geometrie und entwickeln Injektionsprotokolle für eine luftblasenfreie

Befüllung der Kuppel mit Hydrogel. Die Deformation beider mechanischen Stimulationsplattformen wird durch integrierte fluoreszente Mikropartikel für verschiedene mechanische Belastungen charakterisiert, so dass eine Kalibrierung für künftige Zellexperimente zur Verfügung steht.

Zusammengefasst stellen die im Rahmen dieser Arbeit entwickelten Systeme ein flexibles Instrumentarium aus fortschrittlichen experimentellen Werkzeugen für die Manipulation und Untersuchung von integrierten Geweben bereit, welches für Krankheitsmodelle oder die personalisierte Medizin eingesetzt werden kann. Die maßgeschneiderte Kombination verschiedener Sensor- und Stimulationsansätze liefert flexible Modelle welche auf konkrete wissenschaftliche Fragestellungen anpassbar sind.

Contents

Abbreviations

1D	one-dimensional
2D	two-dimensional
3D	three-dimensional
APC	allophycocyanin
APTES	(3-Aminopropyl)triethoxysilane
B27C	B27 complete supplement
B27-I	B27 supplement without insulin
CHIR	Wnt agonist CHIR99021
CM	cardiomyocyte
CNC	computerized numerical control
cTnT	cardiac troponin T
DAC	digital-to-analog converter
DAPI	4',6-Diamidino-2-phenylindole dihydrochloride
DI	de-ionized
EC	endothelial cell
EHT	engineered heart tissue
FCS	fetal calf serum
FEM	finite element method
gui	graphical user interface
hESC	human embryonic stem cell
hiPSC	human induced pluripotent stem cell
HoC	Heart-on-Chip

IPA	isopropyl alcohol
LSM	laser scanning microscope
mvEC	microvascular endothelial cell
OHW	OpenHeartWare
OoC	Organ-on-Chip
OpAmp	operational amplifier
PBS	phosphate-buffered saline
PDMS	polydimethylsiloxane
PET	polyethylene terephthalate
PET-G	polyethylene terephthalate glycol
phDF	primary human dermal fibroblast
PMMA	polymethylmethacrylate
PSF	point spread function
PVA	poly(vinyl alcohol)
px	pixel
RH	relative humidity
RPMI	RPMI 1640 medium
RI	ROCK inhibitor Y-27632
roi	region of interest
RT	room temperature
SD	standard deviation
SLA	stereolithography
TFM	traction force microscopy
UV	ultraviolet
µ-tissue	microtissue

Introduction

The COVID-19 pandemic drastically demonstrated that humankind crucially depends on a fast and efficient drug development process [1]. Unfortunately, current drug development evolved into an ineffective and time-consuming process [2]. The development and approval of one drug starting from 10 000 initially identified candidates takes on average 13.5 years and costs about 2.6 billion US$ [3–5]. In the time span from 1950–2010, the amount of newly approved drugs per billion US$ in R&D spending decreased exponentially [6]. While 88 new drugs were submitted to the Food and Drug Administration in 1995, the number declined to just 49 in 2004 [4].

One major bottleneck in prevailing drug development process is the frequent late stage attrition of drug candidates [3]. Once in clinical stage, the overall success rate of a new compound amounts to roughly 10 % as currently applied preclinical models fail to reliably predict drug efficacy and safety in humans [7]. An improved discovery pipeline would already filter out toxic components in the preclinical stage, following the tenet "fail early to fail cheap". Thereby, the time consuming clinical phase, responsible for a majority of the drug development costs, could be avoided [5].

Currently, preclinical studies rely on *in vitro* cell culture models and *in vivo* animal studies [8]. While animal models are considered as gold standard, they are cost intensive, ethically questionable, and exhibit physiological differences with limited translatability to humans. Vice versa, conventional cell culture models offer human genetic background but mostly grow immortalized cell lines in 2D on hard plastic surfaces without perfusion, missing a complex three-dimensional (3D) tissue architecture [9]. The revolutionary discovery of human induced pluripotent stem cells (hiPSCs) offers unprecedented opportunities for generating personalized models taking genetic predisposition, age, or ethnicity into account [10, 11]. However, due to the limitations of classical two-dimensional (2D) models, hiPSCs can not not unfold their full potential yet.

Organ-on-Chips (OoCs) aim to provide physiologically more relevant *in vitro* systems by culturing minimal functional tissue units in precisely tailored microenvironments, emulating human physiology. OoCs promise better translatability, leading to a reduction or even potentially complete replacement of animal testing. In addition to being mere cell culture platforms, OoCs enable the integrated application of biophysical stimuli and investigation of tissue-specific key parameter. Notably, due to the potential to precisely tailor tissue environment considering geometry and

mechanical properties, OoCs are a perfectly suited tool for studying biomechanics of tissues [12, 13].

Mechanical influences which are obvious in our perceivable macroscopic world, e.g., working out results in muscle growth, stubbing a toe leads to swelling, were left unconsidered on cellular level for a long time. However, there has been a resurgence of mechanics in cell biology in the last 25 years [14]. Physical forces are shown to affect gene transcription, guide stem cell differentiation fate or influence tumor metastasis and are seen equally as important as biochemical stimuli [15–17]. For instance, Dobbs *et al.* displayed the influence of periodic stretching on phenotype expression of alveolar epithelial cells [18]. So far, several OoCs integrated mechanical cues for achieving physiological responses, ranging from passive stimuli like a defined matrix stiffness to active stimuli in form of periodic stretching or compression [19–21]. Generally, introduced models manage to recapitulate mechanical cues but are prone to individual limitations and challenges considering material choice for enabling scalable fabrication, O_2 permeability, and preventing small molecule absorption, as well as a physiological distribution of applied stimuli.

In addition to the application of biophysical stimuli it is just as important to measure forces exerted by tissues. The human heart is the poster child of a mechanically active tissue which is coupled to chemical and electrical cues for its vital function. It is characterized by an arrangement of highly aligned contracting muscle fibers. Models of the human heart are of special interest in drug testing studies as cardiotoxicity is one of the main reasons for drug withdrawal in late phase clinical trials [22]. So far, a variety of Heart-on-Chip (HoC) systems emerged, enabling the generation of aligned cardiac muscle fibers within a perfused microfluidic environment [23–26]. However, as contractile force is one main characteristic of cardiac tissue function, it is crucial to integrate force sensing capabilities into current HoCs, providing a readout of this fundamental key metric.

This thesis introduces and thoroughly characterizes four OoCs enabling the application and study of biophysical key parameters and provides proof-of-concept of successful integrated cell culture. The focus lies on mechanically active tissues, i.e., the myocardium, cartilage, and lung. We introduce two HoCs which are coupled to distinct novel cell injection concepts, generating aligned cardiac muscle fibers for emulating the microstructure of the native myocardium. In addition to bare tissue culture, we extract and characterize beating kinetics from brightfield video microscopy, verifying the application of developed HoCs for drug testing. Furthermore, we study the integration of force sensing pads and oxygen sensors into multilayer OoCs, enabling probing of physiological key parameters. Ultimately, we develop novel approaches for integrating stimulation capabilities into microphsiological systems. First, we integrate electrodes into developed HoCs and demonstrate successful electrical stimulation of cardiac tissues. Second, we present two OoCs capable of mechanical stimulation for applying defined stretch to endothelial cells or compressing cell-laden hydrogels.

This thesis is structured into following major topics: In chapter 1 we review OoC technology, providing a brief background of implemented techniques and micro-

physiological systems. Detailed protocols of the conducted experiments are listed in chapter 2. In chapter 3, we investigate strategies for generating aligned cardiac fibers in microphysiological systems and present two developed HoCs with benefits over currently employed HoCs. We thoroughly characterize generated tissues and present an optical analysis concept, which was developed within the course of this thesis. Chapter 4 focuses on the integration of sensing capabilities in OoCs. We demonstrate successful integration of oxygen and force sensing into developed HoCs. Furthermore, we present and discuss challenges and adaptions in chip fabrication for a successful sensor integration. Chapter 5 investigates approaches for applying defined biophysical stimuli to tissues cultured in OoC platforms. We divide applied stimuli into electrical stimulation, integrated into the HoCs, and mechanical stimulation. We focus on the application of stretch and compression as mechanical stimulus and introduce two novel microphysiological systems: A stretching platform for perspective application in a Lung-on-Chip and a compression platform for modeling of cartilage tissue.

Research presented in this thesis has been previously published in following manuscripts:

- Schneider, O., Moruzzi, A., Fuchs, S., Grobel, A., Schulze, H. S., Mayr, T. & Loskill, P. Fusing Spheroids to Aligned µ-Tissues in a Heart-on-Chip Featuring Oxygen Sensing and Electrical Pacing Capabilities. *Mater. Today Bio* **15**, 100280 (2022) [27]

- Schneider, S., Brás, E. J. S., Schneider, O., Schlünder, K. & Loskill, P. Facile Patterning of Thermoplastic Elastomers and Robust Bonding to Glass and Thermoplastics for Microfluidic Cell Culture and Organ-on-Chip. *Micromachines* **12**, 575 (2021) [28]

- Schneider, O., Zeifang, L., Fuchs, S., Sailer, C. & Loskill, P. User-Friendly and Parallelized Generation of Human Induced Pluripotent Stem Cell-Derived Microtissues in a Centrifugal Heart-on-a-Chip. *Tissue Eng. Part A* **25**, 786–798 (2019) [29]

Chapter 1

State of the art & theoretical background

1.1 Organ-on-Chip

OoCs are microfluidic cell culture devices which culture functional tissue units in a continuously perfused microenvironment [30, 31]. OoC technology emerged over the last decade as symbiosis between tissue engineering and microfluidics technology. Harnessing advanced microfabrication techniques enables precise tailoring of a tissue-specific cellular microenvironment and provides exact control of microfluidic flows guiding nutrient supply and chemical gradients. One of the key features in OoC technology is the emulation of vascularization which is mostly neglected in traditional tissue engineering models relying on static media exchange or perfused bioreactors, exhibiting different cell-media ratios than occurring *in vivo*. Instead of recreating complete organs, OoCs aim to recapitulate physiological key units and functions of distinct organs on the microscale. OoCs combine advantages of conventional cell culture and animal models, providing *in vitro* platforms with human genetic background featuring a complex 3D tissue architecture and perfusion. In addition to a mere combination of both model systems, OoCs provide novel unprecedented opportunities emerging from system miniaturization. For instance, the reduced size enables a parallelized generation and analysis of tissues on a small footprint and lowers assay costs due to decreased reagent consumption.

One of the first OoCs was presented by Huh *et al.* in 2010, mimicking the alveolar-capillary interface of the lung [19]. The chip consisted of two super-imposed microchannels separated by a flexible porous membrane and cultured human alveolar epithelial cells and microvascular endothelial cells on opposite sides of the membrane. The membrane could be periodically stretched, emulating *in vivo* breathing motions. This next generation system accurately recapitulated a physiological lung response, revealing the tremendous potential of OoCs.

The general blueprint of a OoC device consists of a tissue-specific culture chamber which is separated by an endothelial-like barrier from a perfusable channel, emu-

lating vascularization. Cultured tissues can be optically analyzed in real-time or extracted for further off-chip analysis. Furthermore, sensors may be integrated into OoCs offering *in situ* readouts of electrical activity or oxygen content. Additionally, chips can be equipped with stimulation capabilities for mimicking electromechanical cues occurring *in vivo*.

OoCs are fit-for-purpose devices with architectures tailored to investigated tissue and function, provided with stimuli and readouts for addressing a distinct scientific question. Moreover, OoC technology offers the opportunity to connect multiple organ chips, thus recreating a body-on-chip [32]. Thereby the interplay between organs can be studied, enabling the investigation of drug metabolism impacts [33]. Generally, OoC is an area of ongoing research with open questions considering optimal device material, standardization, parallelization and cell sourcing [34, 35]. Although the field is still in its infancy, OoC is a disruptive *in vitro* technology for biopharmaceutical applications such as drug development or personalized medicine [36, 37]. In the following subsections we discuss biophysical aspects occurring *in vivo* and their integration in OoCs as well as focus on developed HoC platforms as testbed for the study of biophysical aspects in OoCs.

1.1.1 Biophysical aspects of OoCs

Generally, tissues are exposed *in vivo* to a variety of external influences contributing to individual tissue development and function. Thus, for an accurate *in vitro* recapitulation, OoCs aim to integrate these tissue-specific contributing factors.

Essentially, tissue dimensionality plays a crucial role [38]. Although monolayers exist in the human body, e.g., formed by epithelial cells, the majority of organs rely on a complex 3D arrangement, providing a different *in vivo* cellular microenvironment [39]. Compared to established 2D well plate cultures, the transition to 3D influences, i.a., diffusion dynamics, concentration gradients or force distribution and should be considered in the specific device design. Another aspect guiding OoC design is the correct scaling of individual tissues [40, 41]. Especially in systems coupling multiple organs, individual tissues interact via secreted metabolites and should be adequately proportioned with respect to each other for correctly replicating human responses.

In vivo, mechanical cues play a crucial role for biological systems and can interact actively or passively with cells [12, 13]. Mechanical properties of the microenvironment such as substrate/matrix stiffness, topography, or geometrical confinement are considered as passive stimuli. OoC technology provides a precisely controlled tissue-tailored microenvironment for adjusting passive stimuli [42]. Environmental stiffness as well as cell shape is directly influencing stem cell differentiation [16, 43]. Furthermore, it has been shown that micropatterning of substrates for engineered cardiac muscles guides tissue alignment and leads to improved calcium handling and tissue maturation [44, 45]. Franco *et al.* demonstrated alignment of endothelial cells (ECs) on microstructured substrates integrating grooves [46]. Nikolaev *et al.* provided a model of the intestine based on an organoids-on-chip platform, precisely

tailoring mechanical properties of a hydrogel environment [21]. By patterning hydrogel microcavities to recapitulate the geometry of native crypts in the mouse small intestine, tube-shaped epithelia formed, as found *in vivo*.

In addition to passive mechanical cues, cells are also actively influenced *in vivo* by the application of forces. Blood flow in vessels exerts a shear stress to cells lining the vasculature. It has been demonstrated, that exerted shear stress influences tumor metastasis, stem cell differentiation, platelet adhesion, and leads to endothelial cell alignment [47–51]. Huh *et al.* presented a microphysiological system which studied the effect of shear stress exerted onto epithelial cells by propagation of a liquid plug, as observed during mechanical lung ventilation [52, 53]. Generally, microphysiological devices enable precise adjustment of exerted shear stress for recapitulating disease-specific conditions [54]. Another active mechanical influence is stretch, i.a., occurring during pulsatile blood pumping in vessels or during breathing in the lung alveoli. Huh *et al.* presented one of the initial OoCs, enabling defined stretching in a Lung-on-Chip device [19]. Compression is another common active stimulation occurring in the human body, influencing bone and cartilage tissue. It has been shown that compressive mechanical loading strongly impacts chondrocyte behaviour. For instance, stimulation could influence metabolic activity or lead to gene changes affecting extracellular matrix accumulation [55–57]. Although most studies focus on the investigation of a single stimulus, generally an interplay between various mechanical stimuli occurs *in vivo* [58, 59].

In addition to mechanical cues, electrical stimuli compose another important biophysical aspect for recapitulating tissue function. Electrical stimuli are predominantly involved in neuron communication in the central nervous system or trigger muscle contractions. By electrically stimulating cardiac and skeletal muscle tissues, improved tissue alignment and, in the case of cardiac tissues, expression of cardiac markers has been achieved [60–62]. Microfluidic structures can be used to guide axonal growth, generating defined network structures, thus enabling the study of basic mechanisms of information processing [63].

Furthermore, many processes in the human body are regulated by chemical stimuli and guided by local concentrations of, e.g., O_2, glucose, or insulin. Chemokine gradients play a vital role in shaping the tumor microenvironment [64, 65]. Moreover, the brain is strongly influenced by the chemical environment. So far, OoCs enabled the recapitulation of a blood-brain barrier and study of integrity and involved diffusion dynamics [66]. Generally, OoC technology allows precise dosing of chemical factors and the generation of chemical gradients for studying tissue-specific influence. For instance, Shamloo *et al.* induced endothelial cell polarization and chemotaxis by applying defined growth factor gradients in a microfluidic device which protects cells from applied shear forces [67].

In addition to recreating mentioned stimuli, it is vice versa also crucial to provide tools to precisely determine those biophysical cues. The integration of sensing capabilities into OoCs does not only provide a control mechanism to verify the correct application of desired stimulation, it also allows to track tissue characteristics in general as well as in response to exerted external stimuli.

By integrating electrodes, action potentials and conduction velocities can be determined in electrically active tissues [68]. Especially electrodes in form of microelectrode arrays allow spatial recordings at cellular resolution, such that Ca conduction velocities can be determined in cardiac tissues or firing of individual neurons determined to investigate formed neural networks [69, 70]. In addition, single electrodes can be used for integrated measurements of transepithelial electrical resistance to investigate the barrier integrity in microfluidic models of the blood–brain barrier [71–73].

For sensing of analytes such as O_2, pH, or glucose, electrical or optical sensors are frequently used [74]. They allow, e.g., the determination of O_2 gradients in cardiac tissues or tracking of changes in tissue metabolism [75–77].

Ultimately, forces are not only sensed by cells but also actively exerted on their surroundings, e.g., in contracting cardiac tissues. So far, a variety of approaches has been presented for measuring forces in HoC systems [78–80].

All in all, human physiology is guided by an intricate interplay of a variety of biophysical aspects. Although no all-encompassing model has been presented so far, OoCs can precisely recapitulate individual biophysical cues and help in better understanding the influence of distinct stimuli.

1.1.2 Heart-on-Chip

The human heart is a muscular organ of vital function, composing the center of the circulatory system. Its complex architecture enables pumping of blood throughout the body by coordinated contractions, providing tissues with nutrients and oxygen. *In vivo*, the myocardium is mainly composed of cardiomyocytes (CMs) which are electrically coupled with each other and cardiac fibroblasts (FBs) via gap junctions. CMs are arranged in parallel and organized in units of highly aligned fibers [83–85]. The anisotropic fiber structure is essential for optimized contraction and electrical signal propagation [86].

Cardiac tissue engineering aims to recapitulate the aligned tissue structure of the native myocardium. One of the key challenges in modeling the human heart is the limited proliferation potential of adult CMs. *In vitro*, they lose their aligned phenotype and dedifferentiate. In principle, hiPSCs offer an unlimited supply of patient-specific CMs with unprecedented opportunities for disease modeling [87–89]. However, CMs differentiated from hiPSCs are generally in a juvenile state characterized by an electrical and structural immature phenotype, which is, i.a., expressed by spontaneous beating activity [10, 90–92].

To overcome these limitation, several strategies evolved in cardiac tissue engineering for advancing tissue maturation [93–95]. In a pioneering study, Eschenhagen *et al.* cultured CMs in a collagen matrix between two glass capillaries [96]. CMs compacted and formed aligned 3D tissues, attached between both capillaries. The model system of culturing cardiac tissues attached to two opposing pillar structures is known as engineered heart tissue (EHT) and became a widely adapted technique for generating aligned 3D cardiac tissues (Fig. 1.1 A). Radisic *et al.* demonstrated

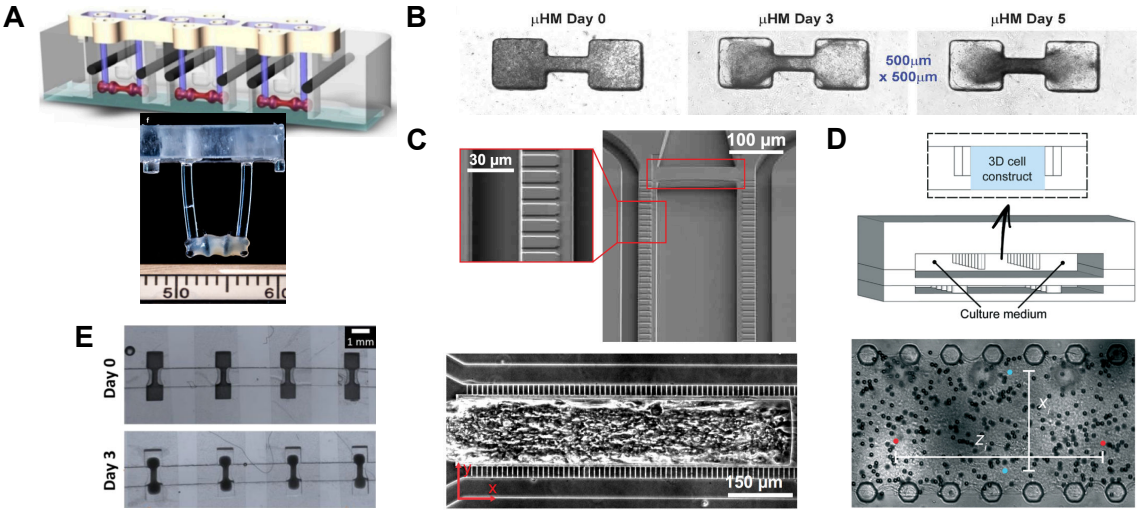

Figure 1.1 Overview of cardiac tissue engineering approaches. **(A)** Suspension of tissues between two micropillars. Contractile forces can be determined from elastic pillar deflections. **(B)** Culture in dog bone-shaped tissue stencils. Chamber geometry leads to attachment in the knobs and tissue alignment. **(C)** HoC culturing cardiac μ-tissues in the central compartment separated by a porous barrier. Nutrients are supplied via flanking media channels. **(D)** HoC concept similar to (C) with additional mechanical stimulation capabilities. Pressurizing the subjacent compartment leads to membrane deflection and tissue stretching. **(E)** HoC approach combining geometry-guided alignment with a continuous media perfusion. Tissue chambers are separated via a porous membrane from a shared subjacent media channel. (A) reprinted by permission from Springer Nature Customer Service Centre GmbH: Springer Nature, Nature, Ref. [81], © 2018. (B) and (C) reproduced from Refs. [82] and [23], respectively, available under CC BY 4.0 license. (D) reproduced from Ref. [24] with permission of the Royal Society of Chemistry. (E) reproduced from Ref. [26], available under CC BY-NC-ND 4.0 license.

in an EHT system further tissue maturation induced by electrical stimulation [97]. Since then, downsized EHTs as well as parallelized platforms in well plate format were presented [98–100]. Pillar structures are mostly composed of a soft material, enabling the additional measurement of fiber stress and contractile forces in cultured EHTs. For instance, Ronaldson-Bouchard *et al.* stimulated EHTs generated from hiPSCs in early stages with increasing intensity, yielding a positive force-frequency relationship as indicator of advanced maturation [81]. The Biowire and I-wire platforms suspend cardiac tissues between horizontally aligned elastic fibers, investigating biomechanic tissue properties and demonstrating the application for disease modeling [80, 101–103]. Feyen *et al.* studied in an EHT system further maturation via an improved media composition [104].

Deviating from predominant EHT approaches, Huebsch *et al.* presented a microfabricated system which achieved alignment of 3D cardiac microtissues (μ-tissues)

by constraining tissues to dog bone-shaped microchambers (two square knob regions connected by a narrower connecting shaft) [82]. Upon subsequent culture, the central region lifted off the substrate, yielding aligned tissues which are attached to the substrate in the knob region (Fig. 1.1 B). Morimoto *et al.* generated similar suspended tissue constructs by patterning cell-laden hydrogels with a polydimethylsiloxane (PDMS) stamp [105]. In a different approach, Grosberg *et al.* introduced a muscular thin film (MTF) platform generating anisotropic 2D cardiac muscle tissue on micropatterned elastomeric thin films [106]. While developed model enables the generation of aligned tissue structures and subsequent analysis of contraction from substrate deflections, it fails in generating thick 3D tissues.

Although several of presented *in vitro* models are termed "Heart-on-Chip", they do not culture cardiac tissues in a perfused microfluidic environment. The native myocardium is characterized by a high metabolic activity and corresponding dense vascularization, which should also be recapitulated in an ideal model [107, 108].

Mathur *et al.* presented a HoC enabling the perfused culture of an aligned 3D cardiac tissue [23]. The microphysiological system is composed of a central elongated tissue chamber which is separated by a porous side wall from two adjacent media channels (Fig. 1.1 C). The porous barrier protects cultured tissues from excessive shear forces and allows for a diffusive supply of nutrients. Contrary to previous approaches, the tissue chamber is loaded with a suspension of single cells without any hydrogel, leading to the formation of a dense tissue construct. Upon subsequent culture under media perfusion in the adjacent channels, aligned tissue beating and ultrastructural organization could be observed. The HoC was subsequently modified to integrate micropillars for force measurements and utilized for investigating a novel maturation mechanism via fatty-acid based media or for screening of COVID-19 therapeutics [109, 110]. Ellis *et al.* extended the model by co-culturing endothelial cells differentiated from the same donor in both flanking media channels [25]. Furthermore, Marsano *et al.* integrated mechanical and electrical stimulation capabilities into a HoC of similar geometry [24, 62]. Compared to the HoC by Mathur *et al.*, cells are embedded in a hydrogel which is constrained to the tissue compartment by a row of pillars (Fig. 1.1 D). Presented system was further scaled up to integrate five tissues per chip and effects of tissue composition as well as perfusion rates were investigated [108, 111]. Recently, Vivas *et al.* reported on a multilayer HoC which harnesses the shape-induced alignment approach [26]. In developed chip, multiple dog bone-shaped tissue chambers are separated via a porous membrane from a shared subjacent media channel (Fig. 1.1 E). The device recapitulates native tissue structure and enables active perfusion as well as drug dosing, mimicking drug kinetics more closely to *in vivo*.

In addition to listed HoCs culturing cardiac tissues in enclosed compartments, several other approaches have been developed for generating aligned cardiac tissues with integrated vasculature. The INVADE platform presented by Lai *et al.* couples an EHT attached to horizontal cantilevers with a perfusable porous vascular scaffold in the central region [112]. The internal lumen of the scaffold is lined with endothelial cells mimicking cardiac vasculature. Although a perfusable co-culture

system is established, cardiac tissues are not predominantly supplied with nutrients from the perfused vessel and rely on conventional static media exchanges in the cardiac compartment. Zhang *et al.* presented a bioprinting approach for generating an endothelialized HoC [113]. The authors printed anisotropic 3D scaffolds, directly integrating endothelial cells. Seeded CMs subsequently aligned on the long axis of the scaffold. However, the scaffold had to be manually transferred into a perfusion chamber and did not allow perfusison of the endothelialized fibers.

All in all, a variety of cardiac model systems emerged in the last decade, all amenable to generate aligned cardiac tissues. By adding perfusion and downscaling tissue size, HoC technology provides physiologically more relevant cardiac models with parallelization and upscaling potential. The crucial next step is to extend developed microphysiological systems to combine successful approaches and integrate maturation strategies as well as enable the readout of contractile forces.

1.2 Sensing in OoCs

The integration of sensors into microphysiological systems plays a pivotal role in OoC technology, providing additional readout capabilities which extend bare optical tissue analysis. Integration strategies can draw on experience of probing approaches introduced in tissue engineering and Lab-on-Chip technology. In the following subsections we focus on integrated force and O_2 sensing. We discuss measurement techniques for probing forces in biological systems and give a detailed description of traction force microscopy (TFM). Furthermore, we review O_2 sensing approaches via luminescent sensors and their integration into microfluidic systems.

1.2.1 Integrated force sensors

Cellular forces play a crucial role in a myriad of biological processes, ranging from individual cells up to the scale of an entire organism. Macroscopically perceivable muscle contraction as well as embryonic development or cancer extravasation are all influenced by mechanical properties [16, 17, 114]. Contraction force is a key metric for the evaluation of cardiac tissue models [79]. In the following, we present an overview of available tools for measuring forces in biological systems with focus on cardiac tissues and integration into microfluidic systems. We provide the theoretical background for integrated force sensing via TFM.

Force sensing in biological systems

Within the continuous advancements of *in vitro* models a plethora of force measurement techniques emerged, allowing the determination of forces in systems ranging in size from single cells to tissues [115, 116]. Developed tools extract forces by evaluating the influence of cultured cellular constructs onto sensor structures of defined mechanical properties.

Initial studies investigated contraction in macroscopic cell-laden collagen gels [117, 118]. Large tissue constructs, e.g., early realizations of the EHT model system, permit manual handling and can be directly attached to commercially available force transducers [119].

As further tissue miniaturization complicates the integration of external force transducers, tissues are frequently suspended between two elastic pillars of known elastic properties and geometrical arrangement. By optically tracking pillar deflections (either static deflections in compacting tissues or dynamic deflections in actively contracting tissues), strain and twitch forces can be determined [79, 99, 120–122]. Similarly, cardiac tissues can be suspended between horizontally fixed microwires, enabling a determination of twitch forces from wire displacements [103, 112]. Zhao *et al.* further attached magnetic spheres to the elastic probing pillars, enabling external tissue actuation and active probing [123].

In a different approach, Ma *et al.* utilized a filamentous matrix as scaffold for cultured cardiac tissues and determined contraction forces from individual fiber deflections [124]. Agarwal *et al.* patterned cardiac tissues as muscular thin films (MTFs) and determined exerted stresses from the optical analysis of deflected film curvature [78, 125]. Lind *et al.* subsequently demonstrated upscaling of the MTF platform to a 24-well plate format [126]. By integrating electrodes, cantilever deformations can be correlated to changes in resistance, enabling parallelized electrical readout of contraction forces. Similarly offering an electrical readout, Qian *et al.* proposed the determination of contraction forces from impedance measurements of thin film electrodes deposited on the substrate of an open top culture system [127].

For measuring space-resolved cellular forces of adherent cells, TFM and micropillar arrays have been established as standard techniques [128]. Both techniques infer applied traction stresses from substrate displacements.

In case of TFM, cells are cultured on an elastic substrate and displacements determined from tracking of fluorescent beads. Several groups studied single CMs with TFM, e.g., investigating the influence of substrate stiffness and cell shape on contractility [129, 130]. Kijlstra *et al.* coupled TFM measurements with fluorescent voltage receptors, yielding additional information on the electrical activity of CMs [131]. Ribeiro *et al.* further combined TFM on micropatterned substrates with brightfield analysis and myofibril staining, enabling the simultaneous determination of sarcomere shortening [132]. TFM experiments were further extended to measurements on two coupled CMs, or even multiple CMs embedded in hydrogels forming patterned tissue-like monolayers [133–135].

Despite being entitled as muscle-on-a-chip, the TFM platform presented by Aratyn *et al.* is not embedded into a microfluidic environment, lacking perfusion [136]. The platform investigates traction forces of two coupled CMs on micropatterned substrates. Das *et al.* integrated a silicone TFM substrate into a PDMS-based microchannel and presented proof-of-concept TFM measurements on adherent fibroblasts [137]. In a recent approach, Guo *et al.* attached dog bone-shaped PDMS stencils to soft PDMS substrates for measuring contractile forces in aligned cardiac tissues [138]. However, the integration of TFM substrates into perfused HoCs has

not been demonstrated so far.

Traction forces are measured with micropillar arrays by culturing cells on top of periodical arrangements of elastic pillars with diameters smaller than cell size [139, 140]. Analogous to systems integrating two larger pillars, space-resolved applied forces can be inferred from pillar deflections. Lam *et al.* facilitated the integration of micropillar arrays into PDMS-based microfluidic environments [141].

Novel approaches enable high-resolution imaging of tractions by integrating molecular tension sensors, exhibiting distinct shifts in emission as a function of strain in their polymeric molecular spring [142]. Furthermore, deforming oil droplets or acrylamide microspheres have been recently introduced as suitable strain gauges [114, 143].

Traction Force Microscopy

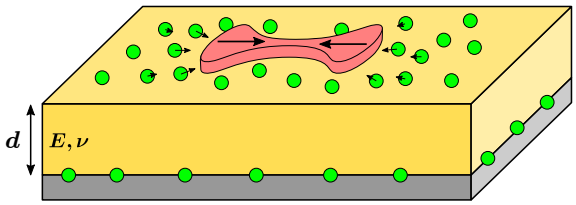

Figure 1.2 Concept of TFM. Cells/tissues are cultured on a soft substrate of defined height d, Young's modulus E and Poisson ratio ν. Forces exerted by adherent cells lead to substrate deformations which are subsequently determined from surface-attached fluorescent beads. A second layer of fluorescent beads can be used as fixed reference and for gauging substrate height.

Traction force microscopy (TFM) is an experimental technique to measure cellular forces exerted by adherent cells. By culturing cells on a soft substrate with defined mechanical properties, traction forces can be determined on a spatially resolvable subcellular level from substrate deformations (Fig. 1.2).

In their pioneering experiments, Harris, Wild, and Stopak observed wrinkling of soft silicone films caused by adherent fibroblasts [144]. Initial studies only estimated cellular forces from determined wrinkling. The technique was further extended allowing to precisely determine substrate displacements by means of substrate-attached latex beads [145]. In the following, Dembo *et al.* introduced quantitative reconstruction methods for determining traction fields from observed displacement fields and measured traction forces of keratocytes on silicone sheets [146]. Due to facilitated fabrication and reproducibility, subsequent experiments utilized polyacrylamide gels as substrate for the determination of traction fields of adherent fibroblasts [147].

Since then, TFM evolved with improvements in reconstruction algorithms as robust experimental tool [148, 149]. Applications of TFM have been extended to 3D, multiple cells (advancing epithelial sheets), or the investigation of colloidal coatings [150–152].

In the following brief derivation of the theoretical framework, we follow the comprehensive tutorial review of Style *et al.* describing the determination of traction forces by Fourier transform traction cytometry [153].

Deformations of a substrate with Poisson ratio ν and Young's modulus E, which are small compared to substrate thickness, are considered as elastic problem, such that the relation between stresses $\boldsymbol{\sigma}$ and strains $\boldsymbol{\epsilon}$ is described by the tensorial version of Hooke's law. Under mechanical equilibrium $\boldsymbol{\nabla} \cdot \boldsymbol{\sigma} = 0$, the displacement field $\mathbf{u}$ must fulfill

$$(1 - 2\nu)\boldsymbol{\nabla}^2\mathbf{u} + \boldsymbol{\nabla}(\boldsymbol{\nabla} \cdot \mathbf{u}) = 0. \tag{1.1}$$

Eq. 1.1 is a classical problem, with known solution found by Boussinesq [154]. Butler *et al.* considered the Boussinesq solution in Fourier space [155]. Thereby, Fourier transforms of the traction stresses $\hat{\boldsymbol{\sigma}}$ are linearly related to Fourier transforms of displacements $\hat{\mathbf{u}}$ via the matrix $\mathbf{Q}$ in Fourier space k_x, k_y. At the substrate surface ($z = h$) we obtain

$$\hat{\boldsymbol{\sigma}}_i(k_x, k_y) = \mathbf{Q}_{ij}(k_x, k_y)\hat{\mathbf{u}}_j(k_x, k_y). \tag{1.2}$$

Thus, in a TFM experiment, the surface displacement field $\mathbf{u}$ is determined by tracking fluorescent beads and interpolated on a regular grid. Subsequently, $\mathbf{Q}$ is calculated and applied to the Fourier transformation of the displacement field $\hat{\mathbf{u}}$, yielding the Fourier transformation of the stress field $\hat{\boldsymbol{\sigma}}$. Finally, traction stresses are extracted from the inverse Fourier transformation of $\hat{\boldsymbol{\sigma}}$.

The interpolation of $\mathbf{u}$, calculation of $\mathbf{Q}$ as well as corresponding Fourier transformations are conveniently bundled in the Matlab script provided by Style *et al.* and can be directly applied to a given displacement field as input [153].

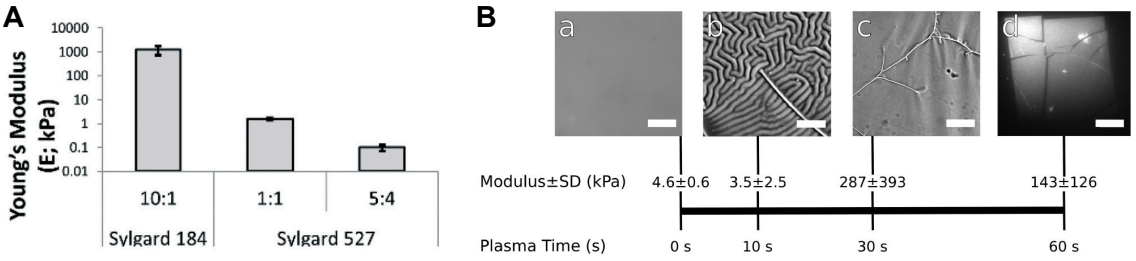

Figure 1.3 Stability of soft substrate's (Sylgard 527) Young's modulus. **(A)** Impact of mixing ratio. A variation in mixing ratio of 25 % leads to a decrease in elastic modulus of one magnitude. **(B)** Influence of plasma treatment. Prolonged treatment times lead to a brittle surface layer with increased Young's modulus. (A) reproduced from Ref. [156] with permission of the Royal Society of Chemistry. (B) reproduced from Ref. [157] with permission of the American Chemical Society (ACS). Further permission related to the material excerpted should be directed to the ACS.

All in all, the main prerequisite for embedded TFM measurements is the integration of a soft substrate into the chip. The substrate should be well defined, i.e.,

exhibit a defined and homogeneous height and Young's modulus. Silicone gels (= soft PDMS) are frequently deployed as soft substrate, preferable over polyacrylamide gels which are influenced by drying and swelling [153, 158, 159]. However, it has been shown that the elastic modulus of silicone gels strongly depends on the exact mixing ratio of prepolymer components [156] (Fig. 1.3 A). Furthermore, plasma activation of soft PDMS creates a brittle surface layer, modifying the elastic modulus [157] (Fig. 1.3 B). Due to the expected influence on force sensing, both aspects should be considered in intended fabrication approaches. Ideally, a force sensing chip would allow for gauging of substrate properties after fabrication.

Gutierrez *et al.* presented a method for measuring substrate Young's modulus within a perfused microchannel with embedded soft substrate of thickness d [158]. By perfusing a rectangular channel of width w, height h, aspect ratio $\alpha = h/w$ with a liquid of viscosity η at flow rate Q, the shear stress exerted on the substrate can be approximated for $\alpha < 1/3$ by [160]

$$\tau = \frac{2\eta Q}{wh^2}\left(\frac{m+1}{m}\right)(n+1), \tag{1.3}$$

$$m = 1.7 + 0.5\alpha^{-1.4},\ n = 2. \tag{1.4}$$

Assuming an incompressible substrate, the elastic modulus can be extracted from measured central substrate displacement Δx by [158]

$$E = \frac{3d}{\Delta x}\tau. \tag{1.5}$$

1.2.2 Luminescent oxygen sensors

As oxygen is a key factor for many cellular processes, the determination of oxygen levels within OoCs is of particular interest for all investigated tissue types [161]. The integration of luminescent sensors into Lab-on-Chip/OoC systems attracts more popularity, as these sensors offer real-time and non-invasive optical readouts without the need of wired chip connections [74, 162]. So far, the integrated measurement of a variety of analytes, e.g., O_2, pH, or glucose, has been demonstrated [163–166].

Briefly, a luminescent indicator dye is integrated within a polymer matrix into the microfluidic environment (Fig. 1.4 A). The indicator dye is sensitive to targeted analyte or influenced by it via an added enzyme (e.g., in the case of glucose measurements, glucose oxidase converts glucose to measurable oxygen levels). For sensing of O_2, the fluorescence of the implemented dye molecule is quenched by the presence of O_2 [167, 168]. Thus, the lifetime τ of the radiative transition and corresponding emission intensity is decreased. Although O_2 levels can be inferred from intensity measurements, sensor readouts in the frequency-domain via phase fluorimetry are established as most robust approach [169, 170].

In phase fluorimetry measurements the sensor dye is optically excited by a light source modulated at frequency f. Corresponding emitted light is phase-shifted by

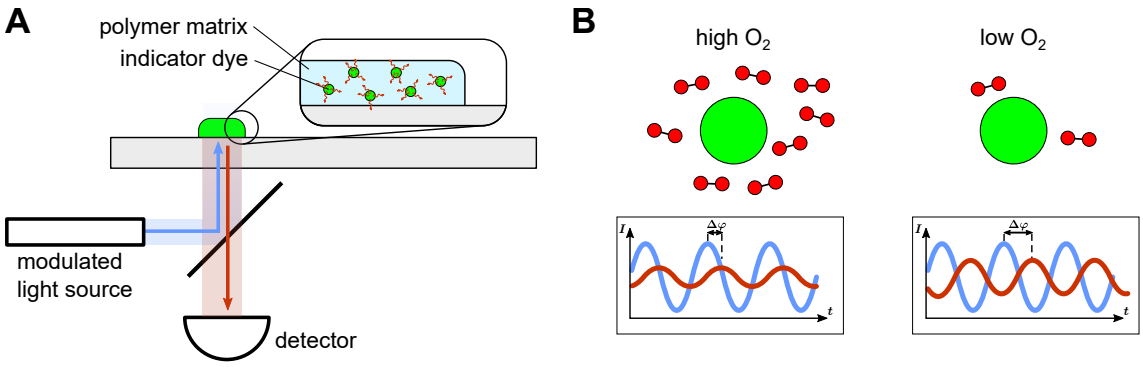

Figure 1.4 Concept of luminescent sensor spots. (**A**) Measurement setup. Sensor spots are deposited on a transparent substrate and excited by a modulated light source. Emitted light is spectrally separated and detected. Spots consist of an indicator dye dispersed in a polymer matrix. (**B**) Influence of O_2 on emitted signal of an oxygen-sensitive indicator dye (green): The emitted signal (red) is decreased in intensity and phase-shifted by $\Delta\varphi$ with respect to the excitation signal (blue). Higher O_2 levels lead to a quenching of fluorescence lifetime, resulting in a decreased phase shift and intensity.

$\Delta\varphi$ (Fig. 1.4 B). From the measured phase shift, the lifetime τ can be determined via

$$\tau = \tan(\Delta\varphi)/2\pi f. \tag{1.6}$$

The unquenched lifetime τ_0 compared to the lifetime in the quenched state τ is related to the oxygen partial pressure p_{O_2} via the Stern-Volmer quenching constant K_{SV} via [171]

$$\frac{\tau_0}{\tau} = 1 + K_{SV} \cdot p_{O_2}. \tag{1.7}$$

K_{SV} is usually determined from indicator dye calibration experiments. In microheterogeneous environments the relationship is more complicated, such that a two-site model is generally applied for relating p_{O_2} to measured lifetimes [171]. Commercially available measurement frameworks solely require the determination of $\Delta\varphi$ in a fully oxygenated and oxygen depleted state and implement appropriate conversions internally.

Thus, for determining in-chip levels of O_2, the integration of O_2 sensing indicator dye is required. Generally, indicator dyes can be deposited prior to chip sealing as sensor film covering a larger chip area or as confined sensor spots at defined positions [74, 172]. Another integration option is to add dissolved indicator dyes in a liquid phase or as suspension of individual sensor particles to the finished microchannel.

Sin *et al.* demonstrated one of the initial microfluidic integrations of luminescent O_2 sensors by immobilizing dye molecules in a resin/PDMS matrix and depositing the mixture in embedded grooves [173]. Ehgartner *et al.* integrated O_2 sensor spots

by airbrush spraying of the sensor cocktail onto patterned substrates, covering unwanted deposition regions with a stencil mask [174]. In a different approach, Zirath *et al.* manually dispensed drops of indicator dye on glass substrates, forming sensor spots after drying. The chip was subsequently attached via patterned double-sided adhesive tape [175]. Sticker *et al.* flushed indicator bead solution ($d = 5\,\mu m$) into an assembled chip, leading to a deposition of sensor particles on the channel walls after 10 min incubation [176]. Recently, Müller *et al.* deposited O_2 and pH sensor spots with a microdispenser, attached to a computerized numerical control (CNC) machine, into injection-molded thermoplastic chip layers [77]. Developed deposition technique allowed the generation of sensor spots of diameters as small as 500 µm. The chip was afterwards sealed with a cyclic olefin copolymer layer attached by double-sided adhesive tape. Subsequently, the authors demonstrated the determination of acidification and respiration rates of cultured lung carcinoma cells. All listed systems consisted of single-layer microfluidic modules, enabling the culture of introduced cells directly within a perfusable channel.

1.3 Stimulation in OoCs

Generally, tissues are exposed *in vivo* to electrical, mechanical and chemical cues. The Lung-on-Chip model by Huh *et al.* demonstrated already in an early OoC realization the importance of integrating external stimuli for recapitulating physiological tissue responses [19]. We review stretching approaches introduced into microphysiological systems and provide the theoretical framework for describing deflections of a pressurized rectangular membrane. In addition, we give an overview of developed platforms for compressing tissues on the microscale and summarize established approaches for electrically stimulating cardiac tissues.

1.3.1 Lung-on-Chip stretching platforms

Stretching platforms are predestined for the study of lung models. During physiological breathing, pressures of $p < 10\,mbar$ occur in the alveoli, leading to periodic stretching of alveolar cells [177]. In early studies, Mead and Collier observed *in vivo* changes in lung compliance as an effect of mechanical ventilation, giving rise to a variety of *in vitro* models allowing the study of stretching effects under defined conditions [178, 179].

Wirtz *et al.* developed a stretch device enabling stretching of cells cultured on a circular silicone membrane [180, 181]. Membranes could be deflected by applying hydrostatic pressures in a sealed compartment beneath clamped membranes. With developed device, Dobbs *et al.* analyzed how the alveolar epithelial phenotype is influenced by distension [18]. Similarly, Tan *et al.* actuated a microstructured flexible membrane pneumatically [182]. Stretching studies by Anderson *et al.* utilized the commercial stretching apparatus FlexerCell [183]. Cells are cultured on flexible silastic™ (Dow Corning) membranes in multiwell culture plates. The central well

area is supported by a loading post. By applying a controlled vacuum in the bottom comportment, the edge region of the membrane is deflected downwards, stretching the central part. Similarly in the device from Moraes *et al.*, a loading post is pneumatically actuated and pushed upwards for stretching a membrane [184]. Kamotoni *et al.* presented microwell arrays where an integrated porous membrane is stretched via Braille pins [185].

The Lung-on-Chip platform by Huh *et al.* integrates stretch stimulation capabilities into a microphysiological system [19]. A flexible PDMS membrane is stretched in plane by applying cyclical pressure variations in adjacent actuation channels. The same principle is subsequently applied for biaxial stretching [186, 187]. Stucki *et al.* presented a different Lung-on-Chip approach, stretching an integrated flexible PDMS membrane with adherent epithelial and endothelial cells via hydraulic pressure variations in the bottom compartment [188]. By actuating a micro-diaphragm pneumatically, the pressure is mediated by the liquid in the bottom compartment, leading to a membrane deformation. Subsequently, the platform was parallelized, and active as well as passive media pumping was introduced via valves in the bottom compartment [189]. Deinhardt-Emmer *et al.* presented an Alveolus-on-Chip model based on the multiorgan tissue flow (MOTIF) biochip, similar to the approach of Jain *et al.* [190–192]. Although both systems enable the generation of an air-liquid tissue model, they do not integrate a stretchable membrane.

In general, there is need for flexible membranes which can be integrated into microfluidic systems. Zamprogno *et al.* refined the platform by attaching a collagen-elastin membrane onto a hexagonal gold mesh, mimicking the physiological alveolar structure [193]. The hydrogel membrane could be actuated pneumatically. Pasman *et al.* reported on a novel stretchable polymer membrane for OoC applications [194]. However, to date scalable porous membrane fabrication and integration approaches are still lacking.

1.3.2 Membrane deflection

The problem of a rectangular plate deflection under uniform load has been extensively studied with an initial description by Timoshenko and Woinowsky-Krieger [195]. They provide tables of numerical solutions for large deflections of distinct plate aspect ratios. Analytical solutions are not known for the general case.

In the case of a rectangular plate with aspect ratio $length/width > 4$, the center-plane deflection along the shorter dimension can be described with the solution of an infinite plate clamped at the longitudinal edge. In that case, the deflection profile for a plate of width l under load p is given by [195]

$$w(x) = \frac{pl^4}{16u^3 D \tanh(u)} \left\{ \frac{\cosh(u(1-\frac{2x}{l}))}{\cosh(u)} - 1 \right\} + \frac{pl^2(l-x)x}{8u^2 D}, \tag{1.8}$$

with the stress parameter u and flexural rigidity $D = \frac{Eh^3}{12(1-\nu^2)}$, calculated from the membrane thickness h, Young's modulus E and Poisson ration ν. The spatial

coordinate x runs along the shorter membrane side.

The shape function is composed of a parabolic term dominating at the membrane center and a cosh term dominating at the membrane edge [196].

Focusing on the membrane center, the profile and central deflection w_0 is frequently approximated by

$$w(x) = \frac{w_0}{a^2}\left(a^2 - x^2\right), \tag{1.9}$$

$$w_0(p) = \left(\frac{3pa^4(1-\nu^2)}{4Eh}\right)^{\frac{1}{3}}, \tag{1.10}$$

with a representing half of the membrane width [197, 198]. By measuring central deflections w_0 for varying pressures p, the term $\frac{E}{1-\nu^2}$ can be determined from eq. 1.10.

The relative length change of the central profile occurring during deflection is frequently approximated by

$$\frac{\Delta l}{l_0} = \frac{1}{2a}\int_{-a}^{a}\sqrt{1+\left(\frac{dw}{dx}\right)^2}dx - 1 \approx \frac{1}{4a}\int_{-a}^{a}\left(\frac{dw}{dx}\right)^2 dx \tag{1.11}$$

assuming $\sqrt{1+x} \approx 1 + x/2$ for small x [196].

For membrane deflections which do not vary along the longitudinal side, the area strain $\epsilon_\mathrm{A} = \frac{\Delta A}{A_0}$ corresponds to the relative length change: $\epsilon_\mathrm{A} = \frac{\Delta l}{l_0}$.

Inserting the parabolic profile from eq. 1.9 into eq. 1.11 yields

$$\epsilon_\mathrm{A}(w_0) = \frac{\Delta l}{l_0} = \frac{2}{3}\frac{w_0^2}{a^2}. \tag{1.12}$$

As the arc length is obtained from integrating the shape function over the whole membrane width, ϵ_A is an average measure and does not vary along the membrane width. Utilizing the relation $w_0(p)$ from eq. 1.10, we obtain the pressure dependent average area strain as

$$\epsilon_\mathrm{A}(p) = 6^{-1/3}\left(\frac{(1-\nu^2)}{Eh}\right)^{2/3} a^{2/3}p^{2/3}. \tag{1.13}$$

We calculate position-dependent area strains from measured displacement fields $\mathbf{u}$ from basic geometrical considerations, neglecting displacements along the membrane longitudinal side u_y and assuming an initially unstretched plane membrane state by

$$\epsilon_\mathrm{A} = \frac{\Delta A}{A_0} \approx \frac{\Delta l}{l_0} = \sqrt{\left(1+\frac{\partial u_x}{\partial x}\right)^2 + \left(\frac{\partial u_z}{\partial x}\right)^2} - 1. \tag{1.14}$$

For fits to recorded membrane profiles, we modify the shape function from eq. 1.8 to account for sample displacements x_0, z_0 and tilts α (Fig. 1.5). Furthermore, we

reparametrize the function, substituting applied load p by the central deflection w_0 and the stress parameter u by the in-plane stress S_0 [197], yielding

$$w(x) = z_0 + \hat{w}\left(\frac{x - x_0}{a}\right) + \tan(\alpha)x, \tag{1.15}$$

$$\hat{w}(x) = \kappa\left((1 - x^2) - 4\frac{\cosh(\sqrt{S}/2) - \cosh(x\sqrt{S}/2)}{\sqrt{S}\sinh(\sqrt{S}/2)}\right), \tag{1.16}$$

$$\kappa = w_0\left(1 - 4\frac{\cosh(\sqrt{S}/2) - 1}{\sqrt{S}\sinh(\sqrt{S}/2)}\right)^{-1}, \; S = \frac{S_0 a^2}{D}. \tag{1.17}$$

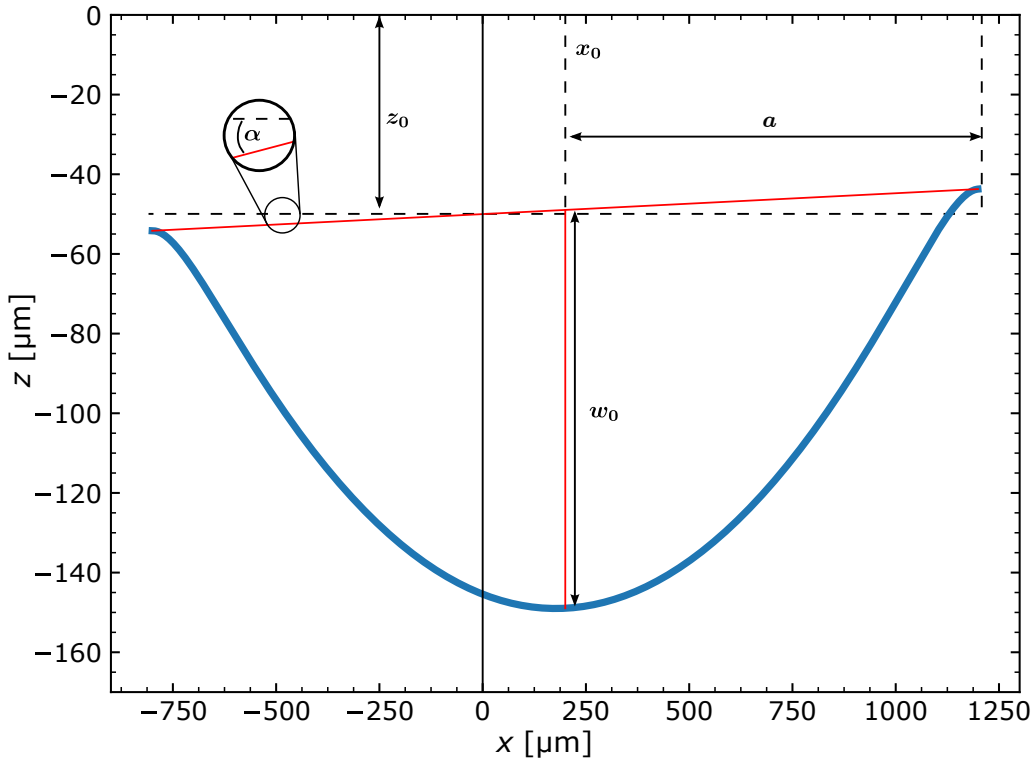

Figure 1.5 Employed profile for fits to deflected membrane shapes highlighting geometrical key parameters. Width a, center position x_0, baseline height z_0, central deflection w_0 and tilt α. Parameters for shown representative profile: $x_0 = 200\,\mu\text{m}$, $z_0 = -50\,\mu\text{m}$, $w_0 = 100\,\mu\text{m}$, $\alpha = 0.3°$, $S = 1000$, $a = 1000\,\mu\text{m}$.

1.3.3 Compression platforms

Compression platforms enable the application of defined mechanical compressive loads to *in vitro* models for studying (patho)-physiological effects of biomechanical stimuli. Lee *et al.* provides an extensive overview over systems developed in the last decades for studying the influence of mechanical loading on chondrocytes [199].

Initial approaches focused on the compression of macroscopic tissue constructs, i.e., compressing tissues in form of cell-laden hydrogel cylinders or growth plate explants between motorized loading plates or plungers [200–202]. In a further adaption to well plate format, Bougault *et al.* compressed agarose gels utilizing the commercial Flexercell Compression FX-4000C device [203]. In this system the well plate bottom is composed of a flexible membrane which is enforced in the central region. By applying positive pressures from the membrane backside, the membrane is pushed upwards, compressing the embedded sample in the enclosed well. As predominantly the unenforced membrane part is stretched, compression takes place between two parallel plates. Similarly utilizing a supported membrane, Moraes *et al.* presented a PDMS-based microfabricated platform enabling the parallelized compression of 25 cell-laden biomaterial microconstructs within one device [204]. Cylindrical loading posts ($d = 500\,\mu m$) are attached to a flexible membrane and deflected upwards upon pressure application. Hydrogels which are spatially confined via photopolymerization to the post regions are thus compressed in the culture chamber ($h = 200\,\mu m$). The device was adjusted by Lee *et al.*, compressing hydrogels by pneumatic actuation of an unsupported membrane from below [205]. Instead of patterning by ultraviolet (UV) light, the presented approach fabricates hydrogel arrays via replica molding and attached them in a reversible sealing process to the compression device. Hsieh *et al.* developed a multilayer microfabricated PDMS device enabling static compression of introduced gels [206]. By injecting defined volumes of hydrogel into a planar chamber, the flexible top membrane bulges upwards. The hydrogel is polymerized via UV lithography in circular stripes leading to height gradients as a function of radius. Subsequent release of hydrostatic pressure returns the membrane into a plane state yielding varying compressions in the gel stripes.

Occhetta *et al.* reported on a microphysiological system enabling the compression of perfused gel constructs within a microfluidic device [20]. Cell-laden hydrogels are cultured in a central compartment, separated by pillar structures from two adjacent media channels. The bottom of the culture chamber is composed of a flexible membrane which can be pneumatically actuated from below. As integrated pillars do not span the full height of the culture chamber, the flexible membrane can be pushed upwards until contact with the pillars is established. Integrated gels are thus compressed to the remaining volume defined by the pillar height. Paggi *et al.* presented a monolithic microphysiological system, compressing injected hydrogels horizontally [207]. Cell-laden hydrogels are cultured in a central compartment, separated by pillar structures from only one adjacent media channel. Gels can be compressed from the opposite side by applying pressures to three actuation compartments which are separated by a thin vertical membrane from the culture compartment and subsequently deform.

1.3.4 Electrical stimulation of cardiac tissues

The native myocardium is orchestrated by an intricate network of interconnected CMs providing the electrical conductive system for stimulating its vital mechani-

cal functioning [208, 209]. *In vitro* culture of primary CMs is an unsolved challenge as adult CMs undergo phenotypic changes and dedifferentiation [210, 211]. By introducing electrical stimulation to cultured monolayers of rat CMs, Berger *et al.* observed that the contractile function is maintained under stimulation [212]. Pacing experiments were carried out in modified culture flasks incorporating two parallel carbon rods as electrodes. The authors applied field strengths of 0.5 V/cm in 5 ms square pulses for frequencies ranging from (0.1–5.0) Hz. To select physiological stimulation parameters, many studies refer to the work of Nuccitelli [213]. Nuccitelli determined the range of endogenous direct current fields in multicellular tissues of a variety of species to (0.01–2.00) V/cm and hypothesized negligible alternating current effects backed up by applied alternating fields of 12 V/cm in neural crests. In a pioneering study, Radisic *et al.* paced cardiac tissue constructs, formed from neonatal rat CMs on collagen scaffolds, via well-embedded carbon electrodes [97]. Improvements of conductive and contractile properties were observed in cardiac constructs stimulated over five days at 5 V/cm, 2 ms rectangular pulses and 1 Hz, thus inducing maturation in the neonatal cell type.

Since then, electrical stimulation evolved into a standard technique in cardiac tissue engineering with well-established experimental protocols adapting electrical field strengths of 5 V/cm magnitude and pulse widths in the range of 4 ms as common pacing parameter [214]. LaBarge *et al.* electrically stimulated cardiac spheroids, leading to improved tissue maturation [215]. Barash *et al.* stimulated macroscopic tissues ($d = 5$ mm, $h = 2$ mm, formed on alginate scaffolds from neonatal rat CMs) in a perfusion bioreactor, leading to increased expression of the gap junction protein Connexin 43 [216]. Similarly, Chan *et al.* observed increased expression of cardiac markers and improved calcium handling in embryoid bodies formed from human embryonic stem cell (hESC)-derived CMs, stimulated in a well plate [217]. Aligned 3D tissue constructs formed from hESC- and hiPSC-derived CMs were paced in the Biowire platform by Nunes *et al.*, resulting in improved ultrastructural organization and conduction velocity [101]. Hirt *et al.* as well as Ronaldson-Bouchard *et al.* reported on pacing experiments in aligned pillar-suspended cardiac tissues formed from neonatal rat CMs as well as hiPSC-derived CMs, yielding improved structural organization [61, 81, 218]. In the experiments of Ronaldson-Bouchard *et al.*, stimulation at fixed 2 Hz was compared with stimulation using increasing frequencies, ramped up from (2–6) Hz by 0.33 Hz/day. Tissues undergoing ramped pacing exhibited improved electrophysioloigcal properties. All described pacing experiments were carried out in well-like setups either culturing tissues in wells with embedded parallel graphite rods or transferring cultured tissues to equally prepared stimulation chambers.

For an integration of pacing capabilities into microfluidic modules, Pavesi *et al.* demonstrated the injection of a PDMS/carbon nanotube mixture into dead-end PDMS microchannels. Subsequent chemical etching excavated the electrode surface, yielding chip-integrated 3D electrodes [219]. Zhang *et al.* directly integrated electrodes into flexible pillars by molding the pillars with a mixture of platinum powder and PDMS prepolymer, demonstrating successful subsequent tissue stimu-

lation [220]. Zhao *et al.* combined device structuring and electrode integration in one single hot embossing step. In the further developed process, carbon rods are directly integrated into hot embossed tissue wells in a 96-well plate format [221]. Further integrated stimulation approaches utilized patterned indium tin oxide thin film electrodes on glass substrates as sensing and pacing electrodes [222]. Visone *et al.* demonstrated a facile electrode integration concept by inserting stainless steel wires into PDMS modules, forming two parallel electrodes for subsequent cardiac tissue stimulation [62].

Generally, exogenous electrical fields can induce Faradaic reactions at the electrode interface. While some reactions can be reversed by applying biphasic pulses, thus redistributing the accumulated charge, non-reversible Faradaic reactions can generate persisting toxic byproducts or reactive oxygen species [223, 224]. Applied pacing voltage should be kept as low as possible to prevent water electrolysis ($U > 1.23\,\mathrm{V}$) or potential redox reactions ($U > 4\,\mathrm{V}$) in glucose-rich media leading to pH shifts [91]. Tandon *et al.* investigated the charge transfer of various electrode materials with electrochemical impedance spectroscopy, determining carbon as most suitable electrode material [225, 226]. The authors observed different beating rates upon stimulation with stainless steel electrodes in static culture (media not exchanged for five days) but do not rule out the usage of stainless steel electrodes for pacing experiments in cultures involving more frequent media changes. Ultimately, tissue conductivity itself is a contributing factor in pacing experiments. For improving electrical conductivity in the tissue environment, nanowires were integrated into cardiac patches or cells cultured on biohybrid collagen/graphene substrates [227, 228].

Chapter 2

Materials & methods

In consecutive sections we list employed protocols for chip fabrication and cell culture. Furthermore, we provide information on utilized stimulation, analysis and modeling approaches.

Methods involving the centrifugal HoC (fabrication, cell culture (hiPSC differentiation, Cor.4U® CMs), centrifugal injection, live/dead & immunofluorescence staining, nutrient supply simulation) have been previously published in "Schneider, O. *et al.* User-Friendly and Parallelized Generation of Human Induced Pluripotent Stem Cell-Derived Microtissues in a Centrifugal Heart-on-a-Chip. *Tissue Eng. Part A* **25,** 786–798 (2019) [29]". Methods involving the Spheroflow-HoC (resin-based fabrication of chips integrating O_2 sensors, cell culture (hiPSC differentiation, primary human dermal fibroblasts (phDFs), spheroid formation), spheroid injection, immunofluorescence staining, Ca-analysis, electrical field simulation, electrical stimulation, EASYPACE development, and sensor spot readout) are included in the manuscript "Schneider, O. *et al.* Fusing Spheroids to Aligned µ-Tissues in a Heart-on-Chip Featuring Oxygen Sensing and Electrical Pacing Capabilities. *Mater. Today Bio* **15,** 100280 (2022) [27]". The characterization of small molecule absorption was part of a study investigating thermoplastic elastomer (TPE) as novel chip material and has been previously published in "Schneider, S. *et al.* Facile Patterning of Thermoplastic Elastomers and Robust Bonding to Glass and Thermoplastics for Microfluidic Cell Culture and Organ-on-Chip. *Micromachines* **12,** 575 (2021) [28]".

2.1 Chip fabrication

The following subsections describe common fabrication procedures employed in multiple projects and provide fabrication protocols for individual microphysiological systems. If not explicitly specified, procedures were carried out following protocols listed in common fabrication steps.

Common fabrication steps & materials

Substrate cleaning Microscope slides and cover slips were thoroughly rinsed with acetone, isopropyl alcohol (IPA), and subsequently blow dried. Thermoplastic substrates were rinsed with IPA and blow dried. PDMS modules were cleaned with IPA, blow dried, and residual particles removed with scotch tape. The same procedure was applied for PDMS modules with bonded membrane, omitting the application of scotch tape on bonded membrane. Lasercut polyethylene terephthalate (PET) membranes were rinsed in ethanol for > 1 min and left to dry on a polymethylmethacrylate (PMMA) transfer layer for subsequent plasma activation.

Plasma activation All referred plasma activation steps were carried out using radio frequency O_2 plasma (13.56 MHz, 50 W; Zepto, Diener) at chamber pressures ≤ 2 mbar.

Lasercutting Structuring via lasercutting was performed with a CO_2 laser cutter (10 W; VLS2.30, Universal Laser Systems) at 1000 pulses per inch. Material-specific structuring parameter are listed in Table 2.1.

Table 2.1 Employed lasercutting parameter for microstructuring microfluidic modules. (×2) indicates cutting the structures twice with specified parameter.

material	P_{cut} [%]	v_{cut}[%]
PMMA (engraving)	50	90
PMMA (2 mm)	85	3
PET-G (500 µm)	50	5
PET membranes	30	50
TPE (750 µm)	(×2) 55	5
TPE (40 µm)	5	5
Arcare 90106	(×2) 35	15
Solder Tape 5414	5	5

PET membranes Track-etched PET membrane with a pore size of 3 µm (03044, SABEU) were plasma coated following previously published procedure by an external service provider, enabling bonding to PDMS layers [229].

Soft lithography

We manufactured PDMS (Sylgard 184, Dow Corning) modules to be used as as channels, stamps, and injection cavities following broadly established soft lithography workflows [230].

Wafer molds Masters for subsequent molding with PDMS were fabricated by UV lithography on silicon wafer out of the negative photoresist SU-8. For achieving distinct layer heights between (30–150) µm, two formulations of SU-8 were employed (SU-8 50 & SU-8 100, MicroChem) and fabrication protocols adjusted on the basis of manufacturer's protocols. Briefly, a silicon wafer (∅ = 100 mm, Siegert Wafer) was dehydrated at 150 °C for 15 min. The wafer was transferred and centered on a spin coater and 4 ml photoresist deposited into the central region. Accelerating the wafer at $\alpha_{\mathrm{coat}} = 100\,\mathrm{rpm/s}$ to $\omega_{\mathrm{coat}} = 500\,\mathrm{rpm}$ and spinning for $t_{\mathrm{coat}} = 10\,\mathrm{s}$ evenly distributed the resist on the whole wafer surface. Subsequent spinning with acceleration ramp $\alpha_{\mathrm{spin}} = 300\,\mathrm{rpm/s}$, spinning time t_{spin} and spinning rate ω_{spin} lead to the generation of a defined layer height. Afterwards, the wafer was transferred to a first soft bake at $T_{\mathrm{sb1}} = 65\,°\mathrm{C}$ for t_{sb1} and a second soft bake at $T_{\mathrm{sb2}} = 95\,°\mathrm{C}$ for t_{sb2}. After cooling to room temperature (RT), the wafer was transferred and fixed via vacuum in a UV exposure unit (ABM Series 60 Exposure Systems, ABM Inc.). Photomasks were designed (CorelCAD 2019, Corel Corporation) and purchased from an external manufacturer (KOPP-desktopmedia), yielding transparent structures on opaque masks. The desired photomask was aligned onto the wafer and covered as well as fixed by a glass plate using soft contact vacuum. After exposure at H_{exp}, the wafer was transferred to a post exposure bake at $T_{\mathrm{peb1}} = 65\,°\mathrm{C}$ for t_{peb1} followed by $T_{\mathrm{peb2}} = 95\,°\mathrm{C}$ for t_{peb2}. In the following, the resist was developed for t_{dev} in SU-8 developer (SU-8 developer, Kayaku Advanced Materials), washed with IPA for 4 min and blow dried. The wafer was hard baked at 150 °C for 30 min and treated with 100 µl trichloro(1H,1H,2H,2H-perfluorooctyl)silane (448931, Sigma-Aldrich) in a desiccator overnight at reduced pressure, yielding a functionalization for simplified PDMS release. For the fabrication of wafer masters for the centrifugal HoC, chlorotrimethylsilane (386529, Sigma-Aldrich) was deposited instead in a desiccator for 2 h. Employed parameters for individual layer heights are listed in Table 2.2. In case of a multilayer wafer fabrication, the resist was not developed after post exposure bake and the next layer directly spin coated on the first one. Alignment marker on both masks allowed manual alignment of both layers.

Table 2.2 Process parameter for SU-8 based fabrication of master wafer.

layer	SU-8	t_{spin} [s]	ω_{spin} [rpm]	t_{sb1} [min]	t_{sb2} [min]	H_{exp} [mJ/cm^2]	t_{peb1} [min]	t_{peb2} [min]	t_{dev} [min]
30 µm	50	30	3100	5	15	175	1	3	8
80 µm	50	30	1600	8	25	200	1	8	10
100 µm	50	30	1000	10	30	250	1	10	10
150 µm	100	30	1750	20	50	350	1	12	20

For the conventional molding of PDMS slabs of defined heights (3 mm), wafers were fixed in 3D-printed holders and molded with PDMS prepolymer. After overnight curing at 60 °C, cured molds were peeled off the master and cut to chip size.

In order to fabricate exclusion molded layer, 0.6 g of PDMS prepolymer was deposited on the central wafer region and left to cover the whole wafer surface within ≈ 15 min, tilting the wafer for better coverage. Subsequently, a polymer film (Scotchpak 1022, 3M) was added on the covered layer, avoiding introduction of air bubbles between film and wafer. Afterwards, a glass plate was added on top of the foil and the whole assembly sandwiched between two PMMA layers (5 mm) and tightly fixed with a screw clamp following previously established protocols [231]. After curing at 60 °C for 4 h, the assembly was opened and the film carefully released from the wafer. The exclusion molded layer was fixed on the film and investigated with an upright microscope. Enclosed channel structures were manually opened with help of a dentist probe.

3D printed molds A stereolithography (SLA) printer (Form 3, Formlabs) was employed for rapid prototyping of PDMS molds out of UV curable resin (clear resin, Formlabs). The general mold blueprint consisted of four chip structures arranged in a 2x2 grid, confined by an outer frame in desired chip height. The mold was aligned on the print platform such that molded surface containing channel features pointed upwards and was thus aligned in parallel to the print surface. Molds were printed at highest layer height resolution (25 µm). Following printing, the mold was post-processed according to manufacturer's protocol: Briefly, molds were thoroughly rinsed in IPA for 9 min, left to dry, and cured by UV exposure (Form Cure, Formlabs) for 15 min. To ensure detachment of cured PDMS, cured molds were submerged in de-ionized (DI) water for 1 h and subsequently placed at 60 °C over night. For molding with PDMS, a PMMA layer (2 mm; Oroglas cast acrylic glass, Trinseo) was clamped to the mold, sealing all sides except an upper injection port, enabling the molding of layers of defined height. Next, PDMS prepolymer was poured into the open port, ensuring complete removal of air bubbles. PDMS was hardened at 60 °C over night. After curing, the PMMA plate was released and molded slabs were removed.

Hot embossing

We embossed microstructures into thermoplastic substrates with stamps fabricated out of PDMS similar to previous approaches [232]. Stamps were either molded from structured silicon wafer or 3D-printed molds, exhibiting stamp negatives. Molded PDMS stamp was hardened overnight at 150 °C. Thermoplastic substrates were trimmed to sizes slightly exceeding stamp size, and cleaned. Subsequently, the PDMS stamp was aligned onto the substrate and the assembly tightly clamped. In the case of single-unit embossing, stamp and substrate were clamped between two microscope slides via four foldback clips. For stamps incorporating multiple chip units, a customized clamping device provided uniform clamping pressure between a bottom aluminum plate and a mirror polished stainless steel plate (0.8 mm, TGA GmbH). The clamped assembly was placed for t_{emboss} into a convection oven at T_{emboss}. Parameter for individual substrate materials are listed in Table 2.3. After

cooldown to RT, structured substrates were removed and cropped to individual chip size, removing the melted edge at the stamp boundary. Structured layers were cleaned with IPA, blow dried, and stored until further usage.

Table 2.3 Employed hot embossing parameter for microstructuring microfluidic modules.

substrate	T_{emboss} [°C]	t_{emboss} [min]
PET-G	115	30
PMMA	145	10
PS	150	90

Bonding of PDMS to thermoplastic layers

Structured thermoplastic layers were cleaned, activated with O_2 plasma (60 s) and submerged in an (3-Aminopropyl)triethoxysilane (APTES) solution (4 % vol/vol in DI; A3648, Sigma-Aldrich) heated to 75 °C, adapting the protocol of Sonney *et al.* [233]. After 20 min the substrates were removed, rinsed in DI water and blow dried. PDMS was cleaned, treated with O_2 plasma (30 s) and aligned on the thermoplastic layer. The assembly was kept at 60 °C for > 1 h to stabilize the bonding.

Centrifugal HoC fabrication

The centrifugal HoC is composed of two microfluidic modules sandwiching a PET membrane. Individual modules were molded with PDMS from silicon wafer masters, featuring microchannels and chambers with heights of 100 µm.

Inlets for the medium channels and, in the case of an external electrode integration, access ports, were punched perpendicularly into the medium layer with a biopsy puncher (504529, World Precision Instruments). The inlet for tissue channels was generated by punching a slanted channel at an angle of 15° (relative to the surface of the upper chip). Briefly, the biopsy puncher is disassembled and tilted inlets are punched with the core unit either manually or guided by a 3D-printed holder.

Cleaned PDMS modules were then treated with O_2 plasma (15 s) and bonded to the PET membrane (structured side of the medium module) and a microscope glass slide (unstructured side of the tissue module), followed by a 2 h bake at 60 °C. Media and tissue modules were then bonded together using another O_2 plasma treatment (15 s), thereby sandwiching the membrane. Before use, the chips were sterilized and hyrophilized by a 4 min exposure to O_2 plasma.

Centrifugal HoC integrating force sensors

Groove modules were replicated with PDMS and injection ports for the soft substrate punched with biopsy punchers of distinct sizes for inlet and outlet (injection inlet: 2.0 mm, injection outlet: 0.75 mm; 504529 & 504531, World Precision Instruments). A sucrose solution (50 % wt/vol in DI; S9378-500G, Sigma-Aldrich) was spin coated (1000 rpm, 60 s) onto a plasma-treated (60 s) silicon wafer (100 mm). Groove modules were cleaned and arranged on the sucrose layer, ensuring conformal contact without channel collapse. Both prepolymer components of the soft substrate (Sylgard 527, Dow Corning) were mixed, degassed and filled into a 10 ml syringe with attached dispensing tip (21 GA; KDS212P, Kahnetics). The assembled wafer was heated to 60 °C, and soft substrate prepolymer injected into the groove filling port, completely filling the inlet. After ≈ 90 min, groove channels were filled with the prepolymer and the assembly was placed for 4 h into an convection oven at 60 °C fully solidifying the polymer. The wafer was submerged in DI water, dissolving the sacrificial layer. Generally, after ≈ 2 h all modules completely detached from the wafer and floated in the water. Groove surfaces were covered for 10 min with a solution of APTES (1 % vol/vol in DI; A3648, Sigma-Aldrich) followed by a full coverage for 10 min with fluorescent bead solution. Subsequently, modules were rinsed in DI water and carefully blow dried. Media-membrane assemblies were prepared following centrifugal HoC protocol and bonded to exclusion-molded tissue layers attached to the transfer film via plasma-treatment (15 s). The bonding was hardened at 60 °C for > 1 h and the transfer film removed. Tissue and groove layer were plasma treated (30 s), aligned, and bonded at 60 °C overnight.

Spheroflow-HoC fabrication

Resin-based HoC The HoC is composed of a tissue stencil molded from UV curable resin NOA 81 (NOA 81, Norland adhesive), a media module out of PDMS and a PET membrane. The media module and tissue layer patterning stamp were manufactured by soft lithography and replica molding with PDMS (media module: positive structures, 150 µm channels; tissue stamp: negative structures, 150 µm channel & 30 µm constriction). Inlets for media and tissue channels were punched with a biopsy puncher (504529, World Precision Instruments) into the media module. Access ports for resin injection were punched with a biopsy puncher (504531, World Precision Instruments) in all four corners of the injection cavity region of the tissue patterning stamp. The PET membrane was bonded to the media module similar to the centrifugal HoC fabrication procedure.

#1.5 cover slips were utilized for chip fabrication on glass substrates and thoroughly cleaned. For the fabrication of Spheroflow-HoCs integrating O_2 sensor spots, a sensor substrate was utilized, provided by a cooperation partner (Stefanie Fuchs, TU Graz). Briefly, O_2 sensor spots were deposited onto adhesive coated PET foil at positions matching the chip geometry. The sensor substrate was rinsed with IPA, blow dried, treated with O_2 plasma (60 s) and covered with a solution of APTES

(1 % vol/vol in DI; A3648, Sigma-Aldrich). After 10 min the sensor substrate was rinsed with DI water and blow dried.

The tissue stamp was cleaned and placed onto the substrate, ensuring full contact of stamp structures with the substrate while avoiding collapsing of the glue injection cavity. In case of the sensor substrate, tissue knobs were precisely aligned on deposited sensors. NOA 81 was inserted into a 10 ml syringe (BD Plastipak, BD) with attached dispensing tip (21 GA; KDS212P, Kahnetics) and both resin injection ports were filled to the top. Resin started to fill the micro cavity immediately. For complete molding, injection ports were filled again after a stopping of filling was observed. After 20 min the molding cavity was completely filled and the assembly exposed to UV light at 188 mJ/cm^2. All resin UV exposures were carried out in an UV oven (λ = 365 nm, LED UV mini-Oven, Novachem). The stamp was carefully removed, cleaned with adhesive tape and stored for repeated use. Prepared media-membrane assembly was cleaned and plasma treated (60 s). Activated surface was covered with APTES (1 % vol/vol in DI; A3648, Sigma-Aldrich) for 10 min. The module was rinsed in DI water, blow dried and aligned onto the tissue stencil molded from resin. Slight pressure was applied to remove trapped air bubbles and the assembly was cured with UV light at 21 J/cm^2. Finalized chip was baked for 12 h at 60 °C to improve adhesion. Channels were rinsed with ethanol to remove any remaining, potentially cytotoxic, glue components and left to dry.

PDMS-based HoC Tissue-modules integrating multilayer structures (150 µm channel, 25 µm constriction) were molded with PDMS from SLA-printed masters. For initial flow-based loading tests, access ports were punched into the tissue module and the chip was plasma-bonded (30 s) to a microscope slide, sealing molded channels. The complete culture chip was assembled following the PDMS-based centrifugal HoC fabrication protocol, sandwiching the same PET membrane between tissue and media layer.

Spheroflow-HoC integrating force sensors

Groove injection layers were hot embossed into polyethylene terephthalate glycol (PET-G) substrates (500 µm; 3011211-ST, Modulor GmbH) and injection ports manually drilled ($\varnothing$ = 2.0 mm, Dremel 3000, Dremel). Following channel cleaning, water-soluble tape (Water-Soluble Wave Solder Tape 5414, 3M) was lasercut and attached to the substrate, sealing the groove channel. Soft PDMS (Sylgard 527, Dow Corning) prepolymer was mixed, degassed, and added to the inlet via a syringe with attached glue dispensing tip (21 GA; KDS212P, Kahnetics). Pad-channels reliably filled within 15 min without air bubbles. Following polymer curing at 60 °C over night, substrates were submerged in DI water leading to tape crumbling and partial lift off. After removal of tape residues with tweezers, beads were deposited similar to the centrifugal HoC force sensor fabrication and substrates were cleaned with IPA and left to dry.

The top layers were fabricated and attached following resin-based chip fabrication protocol, utilizing a structured PDMS layer as sealing for the initial resin molding step. Briefly, the resin stamp of the tissue layer was sealed with a structured PDMS layer providing an edge channel, overlapping at the tissue layer edge. After UV resin injection and polymerization (146 mJ/cm^2), the tissue stamp was removed and the layer transferred and aligned on the substrate with integrated soft pads. The assembly was exposed to UV light (63 mJ/cm^2), the structured PDMS layer removed and the media-membrane module attached via a final UV curing step (21 J/cm^2).

Dispensing of soft substrate prepolymer

Multilayer channel geometries encompassing grooves for soft substrates were embossed into PET-G substrates (500 µm; 3011211-ST, Modulor GmbH) and cleaned. A CNC machine (D.300, Stepcraft) was modified by attaching a 3D-printed holder to the translation stage, enabling the fixation of a USB microscope (TO-5139591, Toolcraft) and 10 ml syringe. The holder was tailored to allow the microscope to focus on a dispensing tip attached to the inserted syringe. The machine was controlled by a microcontroller (Arduino UNO, Arduino) with grbl[1] firmware connected to a computer running the Python-based bCNC[2] CNC controlling software. Soft PDMS (Sylgard 527, Dow Corning) prepolymer was mixed, degassed, and 3 ml filled into a 10 ml syringe with attached dispensing needle (30 GA, Kahnetics). The syringe was fixed in the 3D-printed holder and the microscope focused on the tip. Subsequently, a pressure-controlled glue dispenser (0.1 bar; YDL-983A, Bmgiant) was attached to the syringe. Embossed substrates were fixed with adhesive tape on the CNC table and cavities were filled by manually aligning the dispensing tip with the CNC controller and ejecting multiple 1 s pulses of prepolymer until satisfactory filling was achieved.

Stretch chip fabrication

For the characterization chip, TPE membranes (40 µm, provided by Fraunhofer Institute for Process Engineering and Packaging IVV) were cut to chip size by lasercutting. Membranes were sandwiched between 2 PMMA layers (2 mm; Oroglas cast acrylic glass, Trinseo), which are structured by lasercutting, integrating a rectangular cutout. Membranes were always transferred on the protective liner, for the cutting process only the top liner was removed.

Following top PMMA layer cleaning and plasma activation (1 min), the membrane was attached to the top, covering the whole chip surface. The assembly was clamped between two microscope slides and the bonding stabilized for 2 h at 60 °C. Next, the membrane back liner was carefully removed and the bottom PMMA layer attached undergoing identical bonding.

[1] https://github.com/grbl/grbl
[2] https://github.com/vlachoudis/bCNC

Subsequently, the top part of the chip was sealed with a PDMS slab. Briefly, PDMS was molded on a PMMA layer with engraved markers indicating subsequent inlet positions. After molding, inlets were punched and the module was cleaned. Following plasma activation (1 min), double-sided adhesive tape (Arcare 90106, Adhesives research), lasercut to chip size providing a bonding frame, was attached to the PDMS surface. Next, the assembly was attached via the bottom side of the adhesive tape to the PMMA channel. For tracking membrane deformations, 100 µl of fluorescent bead solution were deposited on the accessible bottom side of the membrane. After 10 min, the surface was rinsed with DI water and the chip placed at 60 °C over night ensuring complete drying.

For the sealed stretch chip enabling the culture of cells in the perfused bottom channel, mentioned protocol was adjusted as following: The bottom PMMA layer was exchanged for a TPE channel layer (750 µm, provided by Fraunhofer Institute for Process Engineering and Packaging IVV) with lasercut channel structures. After TPE membrane attachment to the top PMMA layer, the protective layer was removed from the membrane and the TPE channel layer attached. In the following, a PMMA layer (250 µm, PLEXIGLAS Resist Clear 99524 GT, Röhm) was attached to the TPE layer for sealing the chip and the assembly clamped and bonding stabilized at 60 °C overnight. Compared to the test chip design, layer geometries were adjusted to integrate access ports for the bottom channel module.

Compression chip fabrication

Two-part dome molds were either fabricated by SLA 3D-printing or purchased from an external supplier as CNC-milled aluminum mold (InstaWerk). Top and bottom mold were aligned to each other and clamped with two foldback clips, yielding a dead-end injection cavity. PDMS prepolymer was mixed, degassed and added with a plastic pipette to the polymer injection funnel of the mold. After 15 min, the funnel was filled up with prepolymer again and the assembly placed at 60 °C overnight, fully curing the polymer. The next day, the mold was opened from the injection side with help of a screw driver. Molded dome layers were carefully removed with tweezers. During dome removal, IPA was repeatedly sprayed between detached parts and mold to prevent rupture of the fragile PDMS layer. Access ports were punched and the mold cropped to chip size.

The compression module was replicated with PDMS from a lasercut PMMA master, providing a chamber covering all domes for the application of defined pressures as well as connecting ports to the dome injection channels.

To assemble the characterization chip, the dome layer was attached to a #1.5 cover slip by plasma bonding (30 s). A PMMA piece (2 mm; Oroglas cast acrylic glass, Trinseo) with cutouts matching dome positions, ensuring the application of pressures on the whole bonding surface, was directly aligned on the dome layer. The assembly was clamped between microscope slides and placed at 60 °C over night. Afterwards, the compression module was plasma-bonded (60 s) and the chip clamped between microscope slides and bonding hardened at 60 °C over night.

For the cell culture chip, the media layer was molded from a silicon wafer as PDMS slab (500 µm) and attached to a #1.5 cover slip by plasma bonding (30 s). The compression module was attached to the dome layer via plasma bonding (60 s). Subsequently the assembly was plasma-bonded (15 s) to a lasercut PET membrane. Finally, the assembled compression-dome-membrane module was attached to the media channel via plasma bonding (60 s).

2.2 Cell culture

hiPSC-derived CMs

In-house differentiated hiPSC-CMs used in this thesis were differentiated from the hiPSC line Coriell GM25256 (RRID: CVCL_Y803, Gladstone Institute for Cardiovascular Disease, San Francisco), originally derived from a healthy volunteer with a normal electrocardiogram and no known family history of cardiac disease. Differentiation was achieved using an optimized protocol for the small-molecule manipulation of Wnt signaling adapted from the study by Lian *et al.* [234]. Cells utilized in experiments involving the centrifugal HoC were differentiated by Silvia Kolbus-Hernandez or Lisa Zeifang. Cells utilized for spheroid formation and subsequent culture in the Spheroflow-HoC were differentiated by Alessia Moruzzi, following a modified protocol.

hiPSC differentiation for centrifugal HoC After thawing, hiPSCs were passaged on growth factor-reduced Matrigel-coated (354277, Corning) T25 flasks at a density of 8000 cells/cm^2. Subsequently, cells were cultured in Essential 8 (05990, STEMCELL Technologies) medium (supplemented with 10 µM ROCK inhibitor Y-27632 [RI; Y0503, Sigma-Aldrich]) for the first 24 h after passaging. hiPSCs were passaged at least three times before initiation of differentiation. On day −3, hiPSCs were dissociated with Accutase (A6964, Sigma-Aldrich) and seeded onto Matrigel-coated six-well plates at a density of 25 000 cells/cm^2 in Essential 8 medium (supplemented with 10 µM RI for the first 24 h). On day 0, the medium was replaced by RPMI 1640 medium (RPMI; 1185063, Gibco) containing B27 supplement without insulin (B27-I; A1895601, Gibco) and 12 µM of the Wnt agonist CHIR99021 (CHIR; 4423, Tocris Bioscience). Exactly 24 h after adding CHIR, the medium was changed to RPMI + B27-I without CHIR. On day 3, the medium was changed to RPMI + B27-I supplemented with 5 µM Wnt inhibitor IWP-2 (3533, Tocris Bioscience). On day 5, the medium was changed to RPMI + B27-I and two days later (on day 7) to RPMI containing B27 complete supplement (B27C; 17504044, Gibco), which was thereafter used for CM culture, and exchanged every second day.

hiPSC-CM sheets were first washed in Dulbecco's phosphate-buffered saline (PBS+; 1 ml/well; D8662, Sigma-Aldrich) and then incubated in a dissociation buffer (1 mg/ml collagenase II [LS004174, Worthington] with 40 U/ml DNase I [M0303S, BioLabs Inc.] in Hank's balanced salt solution [H9394, Sigma-Aldrich]) for

1.5 h. The dissociation buffer was aspirated and cells were washed in PBS without calcium and magnesium (PBS-; D8537, Sigma-Aldrich). After discarding the PBS-, hiPSCs were incubated in 0.25 % trypsin/EDTA (15400054, Gibco) for a maximum of 5 min until they detached from the surface. The wells were flushed with RPMI + B27C after which the floating cells were transferred to a 50 ml centrifuge tube (Greiner Bio-One) and centrifuged for 3 min at 138 × g. The pellet was then resuspended to the final loading concentration in RPMI + B27C media, enriched with 10 mM RI.

hiPSC differentiation for Spheroflow-HoC After thawing, hiPSCs were plated on growth factor-reduced Matrigel-coated (354277, Corning) six-well plates at a density of 25 000 cm^2. Cells were cultured in TeSR-E8 (05990, STEMCELL Technologies) medium, supplemented with 10 µM RI (05990, STEMCELL Technologies) for the first 24 h after thawing or passaging. hiPSCs were passaged with Accumax (SCR006, Sigma-Aldrich) at least once before initiation of differentiation. Upon reaching ≥ 90 % confluence (day 0), media was exchanged to RPMI (1185063, Gibco) supplemented with B27-I (A1895601, Gibco) and 10 µM CHIR (S2924, Selleckchem). Exactly after 24 h, medium was changed to RPMI + B27-I. After 2 days (day 3), the medium was changed to RPMI + B27-I with 5 µM Wnt inhibitor IWP-4 (SML1114, Sigma-Aldrich) and incubated for 48 h. On day 5, medium was changed to RPMI + B27-I and on day 7 to RPMI supplemented with B27C (17504044, Gibco), which was thereafter used for CM culture, and exchanged every second day. At around day 9-12, cells showed spontaneous beating and were dissociated on day 15 by incubation with 280 U/ml collagenase (LS004174, Worthington) and 40 U/ml DNase (LS006331, Worthington) in RPMI + B27C for 1.5 h. Detached monolayers were collected in a 50 ml conical centrifuge tube containing 20 ml of PBS-, centrifuged at 200 × g for 3 min and resuspended in Accumax solution followed by 25 min of incubation at 37 °C. After singularization, cells were washed and resuspended in RPMI + B27C with 10 µM of RI. At this point, CM purity was checked by flow cytometry (Guava easyCyte 8HT, Luminex) for the cardiac marker cardiac troponin T conjugated to Allophycocyanin (cTnT, APC; 1:50; 130-119-674, Miltenyi Biotec), and cells were frozen in RPMI + B27C with 10 µM of RI + 10 % fetal calf serum (FCS) + 10 % dimethyl sulfoxide. Only hiPSC-derived CMs with purity ≥ 80 % were used for further experiments.

Before loading, CMs were thawed in RPMI + B27C with 10 µM of RI and plated at a cell density of 2 × 10^6 cells/well in a six-well plate coated with Matrigel. After 24 h, media was exchanged to RPMI + B27C and after three days of culture cells were used for experiments.

Cor.4U® CMs Precultured hiPSC-derived CMs were purchased from Ncardia (Cor.4U®, RRID:CVCL_Y550, Ncardia). They consist of 60 % ventricular, 30 % atrial, and 10 % nodal cells according to the cell provider. Cells were cultured using Cor.4U® complete culture medium (Ax-MHC250, Ncardia) and detached following

supplier's protocol.

iCell® CMs Frozen hiPSC-derived CMs were purchased from Fujifilm Cellular Dynamics International (Lot 103321; iCell® Cardiomyocytes 11713, Fujifilm Cellular Dynamics International). They represent a reliable source of spontaneously electrically active human myocytes [235]. Cells were thawed and seeded following supplier's protocol. For centrifugal chip injection, cells were detached according to supplier's protocol with trypsin and subsequently cultured using provided Maintenance Medium.

phDFs

phDFs were isolated from juvenile foreskin and expanded in culture. 1×10^6 cells were plated in a T175 flask in Dulbecco's Modified Eagle Medium (DMEM; P04-04515, Pan-Biotech) supplemented with 10 % FCS and 1 % Penicillin-Streptomycin. Media was changed every three days. After seven days, the cells were confluent and were either passaged or cryopreserved in DMEM + 10 % FCS + 10 % dimethyl sulfoxide. Cells were passaged at least once before any experiment and only used for experiments up to passage 9.

Spheroid formation

Spheroids were formed following a previously established approach [236]. Briefly, wells of a six-well microwell culture plate (AggreWell™400, STEMCELL Technologies) were replicated out of Hydrosil (101301, SILADENT) [237]. Both silicone components were mixed (1:1 wt), 2.5 g was added into each well and the well plate was centrifuged at $55 \times g$ for 60 s. After curing the silicone for 1 h at 60 °C, well replicas were carefully removed, and circular segments punched out ($d = 20$ mm). Circular segments were glued with an epoxy adhesive (UHU PLUS sofortfest, UHU) to a PMMA holder such that the structured side represented the bottom surface of a well ($d = 15.5$ mm, $h = 2$ mm) which could be remolded with agarose, fitting into a well of a 24-well plate.

This reusable master mold was sterilized with 70 % ethanol before every experiment. 650 µl of 3 % agarose solution in DMEM, liquified by preheating in a microwave, was deposited onto the master mold and solidified within 10 min. Once solid, agarose molds were inserted into wells of a 24-well plate with the structured side pointing upwards. 1 ml/well of PBS- was then added to each well and the plate centrifuged at $1300 \times g$ for 3 min to remove any air bubbles trapped at the bottom of the inverted pyramid microstructure.

CMs and phDFs were dissociated by incubation with 0.05 % trypsin/versene for 10 min at RT. Wells were flushed with respective media and cells transferred into a 15 ml conical centrifuge tube and centrifuged for 3 min at $200 \times g$. CMs were resuspended in RPMI + B27C containing 10 µM of RI, phDF in DMEM complete. Cells were mixed at a ratio of 3:1 (CMs : phDF). A total of 0.5×10^6 cells was

added to each well and centrifuged at 300 × g for 3 min with a deceleration ramp setting of 3. Cells were incubated (37 °C, 5 % CO_2) for 24 h. The next day, around 1200 spheroids/well were formed and could be used for chip loading.

2.3 Chip injection & culture

Centrifugal HoC

To ensure adequate cell attachment, the surfaces of the tissue module were first coated with fibronectin (20 µg/ml in PBS-, 33010018 Gibco; both hiPSC-CM types). A 200 µl pipette tip (Eppendorf), filled with 10 µl of the coating solution, was inserted into the slanted tissue inlet on the edge of the chip, the medium in- and outlets were sealed with stainless steel plugs, and the entire chip was placed in a 50 ml conical centrifuge tube (Eppendorf). Devices with integrated force sensors, not bonded to a microscope slide, were inserted into 3D-printed holders and similarly transferred to centrifuge tubes. The system was then centrifuged at 200 × g for 3 min, followed by incubation for 2 h. For venting, the pipette tip was filled with 100 ml of the appropriate cell culture medium for each cell type, after which the system was centrifuged at 200 × g for 3 min. Cell suspensions with a concentration of 1×10^6 CMs/ml were prepared according to the singularization protocols described above. For membrane bonding tests, 100 µl cell suspension (corresponding to 12 500 cells cells per individual tissue chamber) was pipetted into the inserted pipette tip, followed by centrifugation of the chip at 400 × g for 10 min.

For long-term culture, systems were placed in a CO_2-controlled incubator (5 % CO_2, 37 °C, 95 % relative humidity (RH); Binder). The medium channel was continuously perfused with RPMI/B27C (supplemented with RI for 24 h; GM25256) or Cor.4U® complete culture medium (Cor.4U®) at a constant flow rate of 50 µl/h by an external syringe pump (LA-190 Landgraf HLL), while the medium outflow was collected in a waste receptacle. Tissues were imaged regularly using an inverted light microscope (DMi8, Leica) with an integrated incubator.

Spheroflow-HoC

Chips were treated with O_2 plasma (60 s) for sterilization and hydrophilization and subsequently either filled for coating with a fibronectin solution (20 µg/ml in PBS-, F1141 Sigma-Aldrich) or with pre-warmed media. Coated chips were incubated for 2 h (37 °C). Pipet tips with 100 µl media were inserted into all tissue and media access ports and remaining air bubbles removed by manual flushing. Spheroids were removed from the well, collected in a 50 ml conical centrifuge tube and sedimented by gravity. Supernatant was aspirated and the spheroids were resuspended in 250 µl/well of RPMI + B27C. 100 µl media were added to the tissue inlet tip followed by 30 µl of spheroid suspension. The difference in liquid column height led to a hydrostatic flow dragging spheroids within several minutes into the cultivation

chamber, where they accumulated due to the constricting channel height. The loading process was monitored with a microscope, such that additional spheroids could be added to the inlet tip if the injected amount of spheroids was not sufficient. The same loading protocol was applied for Spheroflow-HoCs integrating O_2 or force sensors.

Following satisfactory loading, media inlet and outlet tips were topped with additional 150 µl of media and the chips were placed in a CO_2-controlled incubator (5 % CO_2, 37 °C, 95 % RH; Binder) overnight. The next day, pipet tips were removed from the tissue channel and corresponding ports sealed with stainless steel plugs. The media channel was subsequently perfused with media at a constant flow rate of 50 µl/h using an external syringe pump (LA-190, Landgraf HLL). For pacing and O_2 monitoring experiments, chips were removed with corresponding syringes from the incubator, placed into a cell culture hood with incubation conditions (5 % CO_2, 37 °C, 72 % RH; Incubator FlowBox™, ALS) and reattached to the syringe pump.

Stretch chip

Chips were sterilized by submerging in 70 % EtOH for 1 h, verifying complete filling of the culture channel. Channels were flushed with DI water, coated with 0.1 % gelatine for 30 min at 37 °C and equilibrated with media. 50 µl of cell suspension ($6 \times 10^6\,\mathrm{ml}^{-1}$) were flushed into the channel. Immediately, the chip was flipped, leading to sedimentation of ECs onto the membrane. After 1 h, the chip was turned to an upright position and pipet tips filled with 200 µl media attached for subsequent culture. Pipet tips were exchanged for tips with fresh media every day.

Compression chip

Collagen gel was prepared by mixing 20 µl collagen (FibriCol, 5133, Advanced BioMatrix) with 60 µl PBS- and 20 µl of fluorescent bead solution. Subsequently, the pH was adjusted to 7.5 by adding 0.1M NaOH.

250 µl of HyStem®-C hydrogel (GS312, Advanced BioMatrix) were prepared by mixing gel components according to manufacturer's instructions (volume ratio Extralink : Glycosil : Gelin-S = 1 : 2 : 2), additionally adding 15 µl of fluorescent bead solution.

Following plasma treatment (5 min) for sterilization and hydrophilization, an empty pipet tip was attached to the channel outlet. A pipet tip filled with 20 µl of hydrogel was added to the dome injection port and the pipet removed. Hydrostatically-driven flow started filling the channel. If ceasing of filling flow was observed, slight pressure was applied to the injection pipet by briefly re-attaching the pipet. Following bubble-free chamber filling, gel was equilibrated in both pipet tips by applying pressure to the inlet tip. The chip was transferred into an incubator for > 1 h ensuring complete gelification, after which chips were used for compression experiments. For compression of domes filled with HyStem®-C, pipet tips were removed and channels sealed with stainless steel plugs.

For seeding of cells, FBs (final concentration $1 \times 10^6\,\mathrm{ml}^{-1}$) were embedded in HyStem®-C and injected following similar procedure. Pipet tips filled with 100 µl media were connected to the media channel and cells cultured under static conditions.

2.4 Staining & optical analysis

centrifugal HoC

Live/dead staining Live/dead staining solution was prepared by mixing PBS-, propidium iodide (PI; 1 mg/ml in PBS-; P4170 Sigma-Aldrich), and fluorescein diacetate (FDA; 1 mg/ml in acetone; F7378 Sigma-Aldrich) at a ratio of 30:6:1. Tissues were washed in PBS- by flushing the medium channels and subsequently incubated with the staining solution for up to 15 min depending on cell number. Subsequently, the tissues were washed again with PBS- and then imaged using fluorescence microscopy (DMi8, Leica).

Immunofluorescence staining For whole-mount immunofluorescence staining, a previously established protocol was adopted [23]. Tissues were fixed at RT for 15 min, using a 4 % solution of Roti®-Histofix (P087, Carl Roth), and then permeabilized for 15 min with 0.1 % Triton X-100 (28314, Thermo Fisher Scientific). After blocking for 1 h with 3 % bovine serum albumin (A9418, Sigma-Aldrich), systems were incubated overnight at 4 °C with primary antibodies for sarcomeric α-actinin (1:1000, ACTN2, clone EA-53; HPA008315, Sigma-Aldrich) and then incubated overnight at 4 °C with secondary antibodies (1:500, Alexa Fluor 488; A32723 Thermo Fisher Scientific). Additionally, nuclei were stained using 4',6-Diamidino-2-phenylindole dihydrochloride (DAPI, 1 mg/ml; D9542 Sigma-Aldrich) diluted 1:500 in PBS- with an incubation time of 30 min. In between steps, tissues were flushed thoroughly with PBS-. To obtain optimal imaging conditions, cardiac chips were taken apart by removing the medium layer. As the membrane still remained on the tissue layer and kept the tissues in place, the chip could be flipped over onto a 170 µm thick cover glass and imaged with a magnification of up to 63× using a laser scanning microscope (LSM; LSM 710, Zeiss).

Spheroflow-HoC

Immunofluorescence staining Tissues were fixed inside the chips at RT for 15 min by inserting a 4 % solution of Roti®Histofix (P087, Carl Roth), and then permeabilized for 15 min with 0.1 % Triton X-100 (28314, Thermo Fisher Scientific). The medium layer was removed, facilitated by a weaker bonding of the membrane-covered region between tissue and media module. After blocking for 1 h by adding a drop of 3 % bovine serum albumin (A9418, Sigma-Aldrich) onto exposed tissue, the tissue was incubated with added staining buffer overnight at 4 °C. The staining

buffer was composed of APC conjugated cTnT antibody (1:50; 130-119-674, Miltenyi Biotec), DAPI (1 mg/ml, final dilution 1:250; D9542, Sigma-Aldrich), 0.1 % Saponin (84510-100G, Sigma-Aldrich), and 0.1 % bovine serum albumin (A9418, Sigma-Aldrich), diluted in PBS-. Between steps, tissues were flushed with PBS-. For imaging, the chip was flipped onto a #1.5 coverslip and imaged with a magnification of up to 63× using a LSM (LSM 710, Zeiss).

For visualizing the cytoskeleton in Spheroflow-HoCs loaded with phDFs, the cTnT antibody was exchanged for a Phalloidin stain (final concentration: 0.165 µM, Alexa Fluor® 546; A22283, Invitrogen).

Calcium imaging Ca signaling was analyzed in the Spheroflow-HoC by introducing a Ca sensitive dye into the media compartment following established protocols [238]. Media supply tubing was disconnected and the media channel flushed with dye solution (10 µM Fluo-4 AM [F14201, Invitrogen] in Tyrode's solution [T2397, Sigma-Aldrich]) via pipet tips by inserting an empty tip into the outlet, adding a tip filled with 200 µl dye solution into the inlet, and starting the flow by manually applying slight pressure. The chip was subsequently incubated in the dark for 15 min and transferred to the microscope with integrated incubator. Already inserted stainless steel plugs sealing the tissue compartment were utilized as pacing electrodes and connected with alligator clips to the EASYPACE pulse generator. Tissues were paced with biphasic pulses at 1 Hz with positive as well as negative polarity of the first pulse phase and the fluorescence signal of the Ca dye recorded at 188 fps.

Stretch chip

Cultured hiPSC-derived ECs were fixed by flushing the channel with paraformaldehyde (4 %) and subsequent incubation at 37 °C for 10 min. Cells were permeabilized and blocked by incubation with normal donkey serum (3 %; 017-000-121, Dianova) for 1 h at RT. The channel was flushed with VE-cadherin primary antibody (1:100; AF938, R&D Systems) and incubated over night at 4 °C. Afterwards, the secondary antibody (1:200; 705-545-003, Jackson ImmunoResearch) and DAPI (1:200; D1306, Invitrogen) were added and incubated for 1 h at RT in the dark. The channel was rinsed with PBS- and chips were imaged with a fluorescence microscope (DMi8, Leica).

Compression chip

On day 3 of static culture, the media channel was flushed with PBS- and a live/dead staining solution (135 µg/ml PI, 27 µg/ml FDA in PBS-) was injected. Following chip incubation at 37 °C for 5 min, the chip was imaged with a fluorescence microscope (Axio Observer 3, Zeiss).

Fluorescent beads

For tracking deformations of TFM substrates, deflected membranes and compressed hydrogels, we deposited fluorescent beads into corresponding systems. Following previously established protocols, carboxylate-modified fluorescent microspheres ($d = 0.2\,\mu m$, $\lambda_{ex} = 505\,nm$, $\lambda_{em} = 515\,nm$, F8811, Thermo Fisher Scientific) were diluted in a solution of sodium tetraborate (3.8 mg/ml; 221732-100G, Sigma-Aldrich), boric acid (5 mg/ml; B0394-500G, Sigma-Aldrich) and N-(3-Dimethylaminopropyl)-N′-ethylcarbodiimid-hydrochlorid (EDC, 0.1 mg/ml; E7750-1G, Sigma-Aldrich) [153]. The bead stock solution was diluted by a factor of $c/c_0 = 0.5 \times 10^{-4}$, yielding a bead concentration of $c \approx 2 \times 10^8\,ml^{-1}$.

Recording of point spread functions

For the acquisition of point spread functions, 50 µl of fluorescent bead solution were deposited on investigated foils (coated PET, 125 µm: Melinex® 506, DuPont Teijin Films; coated PET, 50 µm: Lumirror® 40.01, Toray Films; PMMA, 50 µm: PLEXIGLAS Film 0F072 Röhm; uncoated PET, 100 µm: TF, Transparent Paper Ltd.) and left to dry at 60 °C. z-stacks of single beads were acquired through the substrate backside with a fluorescence microscope (DMi8, Leica) at 20× magnification and $\Delta z = 0.5\,\mu m$ plane spacing.

2.5 FEM simulations

Fluid flow, electric field distribution and deformation by mechanical loading were simulated in corresponding developed microphysiological devices by finite element method (FEM; COMSOL Multiphysics® v5.6, COMSOL AB).

Flow and nutrient supply

Medium flow and nutrient supply was simulated for the centrifugal HoC design with tilted main channel. The membrane was treated as a porous region with a hydraulic permeability of $k = 1.45 \times 10^{-14}\,m^2$ and a porosity of $p = 0.056$, similar to previous work [239]. The flow was described by the Navier–Stokes equation in the free region and the Brinkman equation in the porous region, assuming a water-like medium and a total medium flow rate of $Q = 13.9 \times 10^{-12}\,m^3/s$ (= 50 µl/h). To include the diffusive transport of diluted species through the membrane, a time-dependent study using the "Transport of Diluted Species in Porous Media" module was performed, assuming a constant inflow of medium with a concentration of $c = 1\,mol/m^3$ and a diffusion coefficient of $D = 1 \times 10^{-9}\,m^2/s$ for biological molecules in water.

Electrical field distribution

Electrical field strength within paced chips was simulated in a stationary study with the electric currents physics interface. Inserted pacing electrodes were modeled as cylinders with an applied potential difference U between the surfaces of both cylinders. PDMS was treated as insulator and a conductivity of $\sigma = 1.5\,\mathrm{S/m}$ and relative permittivity of $\epsilon_\mathrm{r} = 80.1$ was assigned to the media domain, adapting previously published material parameters [62].

For the centrifugal HoC, electrodes were inserted into the media module at the branching of the media supply channel. Initially, the electric field distribution was analyzed in the isolated media module for an applied voltage of $U = +5\,\mathrm{V}$. Subsequently, for reducing computation time, the model was adjusted to include only one tissue chamber with overlying media supply, applying previously computed potential difference between media inlet and outlet. Following preliminary simulations explicitly modeling membrane pores, the membrane was neglected and treated as fully conducting fluidic phase.

The model of the Spheroflow-HoC considered cylindrical electrodes in media inlet and outlet with a potential difference of $U = +10\,\mathrm{V}$ between the surfaces of both electrodes. Similar to the centrifugal HoC, the membrane was neglected in the simulation.

Mechanical actuation

Deformations in the actuated dome and stretch chip were simulated in a stationary study with the solid mechanics interface. All studies considered geometric nonlinearities. Variations in device geometry or material properties were evaluated via parametric sweeps. For obtaining converging solutions at elevated pressures, auxiliary sweeps were employed, subsequently ramping up applied pressure (continuation method).

Membrane deflection The membrane was modeled as rectangular plate ($l = 10\,\mathrm{mm}$, $w = 2\,\mathrm{mm}$, $h = 40\,\mu\mathrm{m}$) clamped on all edges, under a homogeneous load p_0 acting on the top surface. For comparison with experimentally determined deflections, $E = 1.3\,\mathrm{MPa}$ was set, corresponding to measured Young's modulus. A Poisson ratio of $\nu = 0.49$ was used, as frequently estimated in literature for SEBS [240, 241]. Applied pressures were sweeped and evaluated for $p_0 = (2,\ 4,\ 6,\ 8,\ 10,\ 15,\ 20,\ 30 \text{ and } 40)\,\mathrm{mbar}$.

Dome compression The plane compression compartment was modeled in radial symmetry as cylindrical chamber ($d = 1.5\,\mathrm{mm}$, $h = 350\,\mu\mathrm{m}$) filled with a compressible material ($\nu = 0.3$, $E = 1\,\mathrm{kPa}$) mimicking injected hydrogel. Pressure was applied homogeneously on a PDMS membrane ($\nu = 0.49$, $E = 2\,\mathrm{MPa}$, $t = 0.2\,\mathrm{mm}$) sealing the compartment.

For modeling the dome compression compartment, a hemisphere ($d = 1.5\,\mathrm{mm}$) was added on top of the cylindrical chamber. The chamber was filled with a compressible material of identical properties and sealed with a PDMS membrane of the same thickness. Pressure was applied homogeneously on the outer dome surface.

For comparison of both compression geometries, applied pressures were sweeped and the compression distribution was compared for pressures yielding a maximum compression of $\epsilon_\mathrm{V} = \frac{\Delta V}{V_0} \approx 10\,\%$ in each system (plane geometry: $p = 70\,\mathrm{mbar}$, dome geometry: $p = 480\,\mathrm{mbar}$).

For evaluating the compression of various introduced hydrogels, p_0 was sweeped from (0–600) mbar for $E = (0.2,\ 1.0$ and $10.0)\,\mathrm{kPa}$ and the mean compression throughout the dome compartment calculated.

2.6 Image analysis

Optical analysis of beating rate

Brightfield videos of beating cardiac tissues were analyzed with the newly developed Python-based software OpenHeartWare[3] (OHW). The software allowed for a scripted analysis of videos via the command line but also exposed all analysis options in a user-friendly graphical user interface (gui) based on the Qt gui framework.

Videos are read in as 3D numpy arrays and motion is determined by block matching. Briefly, each frame is divided into square blocks of pixel (px) size w_b (default: 16 px). For each block in frame i, the best matching position in frame $i + d$ (default: 2 frames) is determined. All blocks in frame i are iterated and corresponding position is determined in frame $i + d$ considering a search area of enlarged block size $w_\mathrm{b} + s$ (default: 7 px), centered to the original block position. Best matching of the iterated block within the search area is found by the OpenCV function `matchTemplate()`. The function calculates the sum of squared pixel intensity differences for all possible shifted positions. The position which minimizes calculated metric is considered as best match. Thus, a motion vector is obtained from shifted position for each block and frame, yielding a space- and time-resolved displacement field. Depending on used magnification and frame rate during recording, analysis parameter were adjusted. Motion vectors obtained in px were further converted to beating velocities with physical units µm/s by considering the spatial image calibration, frame rate and frame delay d.

For a one-dimensional (1D) representation of beating kinetics, the beating velocity was spatially averaged, excluding non-moving regions. Peaks were detected via the scipy method `signal.find_peaks()` with input parameters *prominence* (default: 2) and *number of neighbours* (default: 4). Wrongly detected peaks of decreased magnitude were filtered out by setting a minimum peak height with respect to the highest detected peak. (default: 0.3) Identified peaks were optically checked, if no satisfactory matching was achieved, peaks could be manually added or removed.

[3] https://github.com/loslab/ohw

Contraction intervals were extracted from differences between detected peak times. Beating frequency and estimated error were subsequently determined from mean and standard deviation of the inverse contraction intervals.

Determination of Ca propagation velocity

Recorded fluorescence videos were analyzed with a custom Python script. The recorded fluorescence signal was averaged for each frame along the y-axis (perpendicular to the tissue alignment direction) and binned in 10 px bins along the x-axis. For each binned position on the x-axis, the frame of signal onset was determined by the video frame in which the maximum of signal derivative on the rising edge of a peak is detected. The onset frame was converted to pulse onset time relative to the first pulse t_{pulse} and fitted as a linear function of position x, yielding the signal propagation velocity v_{sig} from the slope.

Analysis of rhodamine absorption

For comparing absorption in microfluidic devices fabricated from PDMS and TPE, chips featuring a straight channel ($l = 1.2\,\mathrm{mm}$, $w = 400\,\mu\mathrm{m}$, $h = 100\,\mu\mathrm{m}$) were fabricated by S. Schneider and E. Brás on microscope slides. Briefly, TPE devices were embossed with an epoxy stamp and bonded to glass following a silane treatment. PDMS devices were molded from wafer masters and bonded to glass following plasma treatment.

Three different rhodamine dyes (Rhodamine B, 83689; Rhodamine 6G, 83697; Rhodamine 101, 83694; all Sigma-Aldrich) were utilized to investigate the partitioning of small molecules into the chip material. All dyes were reconstituted in PBS- to a final concentration of 100 µM. Each solution was filtered through a 0.22 µm pore size filter (P666.1, Carl Roth). For each chip material and rhodamine, three different chips were analyzed.

Prior to introducing dye solutions into the channels, chips were treated with O_2 plasma (5 min). An empty pipet tip (300 µl, Sapphire Pipette Tip, Greiner Bio-One) was added to the outlet port; then, a pipet tip containing 50 µl of respective rhodamine solution was added to the inlet. The channel was flushed by applying pressure to the inlet tip via the hand held pipet until both liquid columns of the inlet and outlet tips were equilibrated. After filling, all samples were spatially fixed in 3D-printed holders designed to fit into the microscope stage. Samples were imaged utilizing a fluorescence microscope (DMi8, Leica) with a magnification of 10× and a rhodamine filter set ($\lambda_{\mathrm{ex}} = 546/10\,\mathrm{nm}$, $\lambda_{\mathrm{DM}} = 560\,\mathrm{nm}$, $\lambda_{\mathrm{em}} = 585/40\,\mathrm{nm}$). Images were taken in the center of the channel and focused in the z direction to the TPE/PDMS–glass interface. Imaging conditions were kept the same for each rhodamine between materials and imaging time points. Starting immediately after rhodamine injection, samples were imaged every 24 h for three days. All samples were imaged before and after washout of the rhodamine solutions after 72 h of incubation. In between each recording, samples were stored in an enclosed light-protected

box containing a water-filled crystallization dish to prevent excessive evaporation of the different rhodamine solutions from the pipet tips. After 72 h, the dye solution was washed out of the chip by manually flushing the channel three times with approximately 80 µl of PBS via pipet tips.

Fluorescence images were processed by correcting small sample tilts, centering the channel, and cropping a defined region around the channel center via a custom Python script[4]. Briefly, fluorescence intensity profiles perpendicular to the channels were extracted by taking the mean of the fluorescence values along the full, visible channel length in each tilted and cropped image.

For each rhodamine and material combination, profiles were further averaged among all replicates (as leakage occurred after 48 h in the PDMS–rhodamine 6G sample 2, this sample was excluded from the mean value of time points 72 h and 72 h washout). Fluorescence intensity was normalized to the mean value in the channel center of all samples filled with the same rhodamine solution after initial injection. Displayed fluorescence images are cropped, showing 50 % of the full, analyzed raw image.

Tracking of fluorescent beads

Bead positions were extracted from 2D fluorescence images or 3D stacks with Trackpy which provides a Python interface for tracking beads via the Crocker Gier algorithm [242, 243]. An estimated spot size (generally used: $d_x = d_y = 7\,\mathrm{px}$, $d_z = 11\,\mathrm{planes}$) and minimum particle intensity (varies between datasets but can be extracted from a distinct peak in the intensity histogram) was provided as input. Found particles were overlain on the raw dataset, enabling visual control of found particles and further refinement of intensity cutoff. Trackpy includes a linking algorithm, linking found features to trajectories, thus enabling the determination of displacement fields. Displacement fields were visualized using the Python package vedo [244].

Traction Force Microscopy

Images and videos of substrate-adhered fluorescent beads were recorded at 20× magnification with a fluorescence microscope (FITC filterset; DMi8, Leica)

Soft substrate characterization For the flow-based characterization of integrated soft substrates, a 10 ml syringe was filled with DI water and attached to a single channel syringe pump (LA-30, Landgraf HLL). The chip was fixed on the microscope stage and connected with tubing to the pump, ensuring a bubble-free tubing and testing channel. The flow rate was ramped up in 100 µl/min steps up to 1000 µl/min and one image was acquired for each flow rate in the channel center. Bead positions were extracted for each image and linked between images recorded of successively increased flow rates with Trackpy. Only beads tracked in all frames

[4] https://github.com/loslab/rhodabs

were considered for analysis. Average sample tilt was calculated from maximum displacements of beads in the central region ($w = 400\,\mu m$) and displacements accordingly corrected, yielding flow-related displacements along the x-axis. For each applied flow rate Q, corresponding theoretical shear stress τ was calculated following eq. 1.3. For each characterization chip, distinct substrate height d was determined by focusing on embedded beads below and on top of the substrate. x-displacements were averaged in the central region, normalized to d and fitted as a function of corresponding shear stress τ. The Young's modulus was extracted from the fit according to eq. 1.5.

Determination of traction forces In order to calculate traction forces exerted by cardiac tissues cultured in devices with implemented soft substrates, fluorescent bead locations were determined via Trackpy from recorded videos. Subsequently, bead positions were linked between consecutive frames with Trackpy, keeping only beads tracked in every recorded frame. Acquired time-dependent displacement field was exported as MATLAB `.mat` file. The MATLAB-based TFM calculation script from Styles *et al.*, intended for the calculation of traction stresses between a displaced and a reference image, was extended to calculate traction stresses for all time points in exported time-dependent displacement field in relation to a specified reference frame [153]. Traction stress magnitude was calculated from x- and y-components of extracted traction stress and integrated over the tissue-chamber area, yielding a temporal description of the sum of traction forces. In the case of force-measurements on electrically stimulated systems, videos were recorded for distinct pacing frequencies and traction forces determined analogously.

Determination of 3D displacement fields

For the determination of 3D displacement fields of the stretched membrane and the compressed hydrogel, z-stacks ($\Delta z = 5\,\mu m$ plane spacing) were recorded of deposited beads at $10\times$ magnification with a fluorescence microscope (FITC filterset; DMi8, Leica). Several planes above and below observable beads were included in the stack, preventing occurrence of beads at edge positions in z direction.

Stretch chip A possible tilt deviating from a parallel membrane orientation to the field of view was calculated by extracting a subset of beads on a contour line in deflected membrane state (e.g. $-200\,\mu m < z < -195\,\mu m$) and fitting a linear tilt ($z \propto \tan(\varphi)x$). The dataset was subsequently rotated by detected tilt and the 1D profile $z(y)$ investigated. Outlier were detected by deviating more than *z-score* standard deviations (generally *z-score* = 2) from the mean value of 50 nearest neighbours (queried by a k-d-tree) and subsequently removed, resulting in a preprocessed dataset (Fig. 2.1).

Eq. 1.15 was fitted to $z(y)$, extracting the central deflection w_0 and width a. From the fit of $p(w_0)$ according to eq. 1.10, E is determined, assuming $\nu = 0.49$.

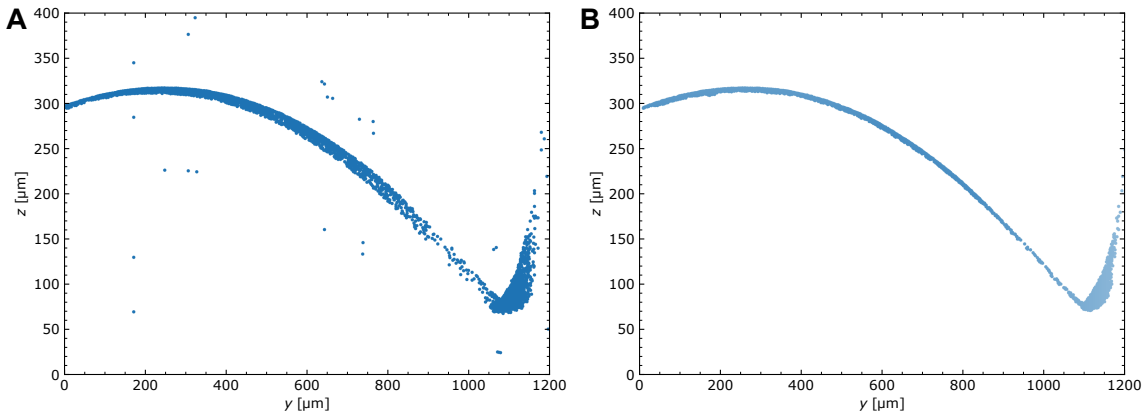

Figure 2.1 Pre-processing of point clouds from detected bead positions. **(A)** Raw bead positions of beads pre-selected by a minimum intensity. **(B)** Processed dataset used for profile fits. Bead positions are corrected by subtraction of a sample tilt around the z-axis and removal of local outliers.

Particles were linked in the pre-processed $z(x, y)$ dataset by subtracting the individual local mean height $\bar{z}(x, y)$ of displaced particles, linking positions in a planar configuration, and adding previously subtracted mean height again. Displacements were interpolated in y direction, yielding $u_{\mathrm{y}}(y)$ and $u_{\mathrm{z}}(y)$, from which the area strain was calculated according to eq. 1.14.

Compression chip Extracted particle positions were linked between z-stacks recorded at increasing pressures with Trackpy. Outliers were removed analogously to the stretch chip post-processing workflow, separately considering variations in u_{x}, u_{y}, and u_{z} (z-*score* $= 1$). Filtered displacement field was interpolated on a regular grid approximating the amount of tracked beads with the amount of grid positions. Spatial compression ϵ_{V} was calculated from the divergence of interpolated displacement field: $\epsilon_{\mathrm{V}} = \frac{\Delta V}{V_0} \approx \boldsymbol{\nabla} \cdot \mathbf{u}$. For the determination of mean compression, compression was averaged over all volume elements containing detected beads.

2.7 Stimulation

Electrical stimulation

Tissues were field-paced using the custom-built Arduino-based electrical stimulator EASYPACE. Briefly, individual electronic components were hand-soldered on a custom pcb ordered from an external provider (Beautiful Boards, AISLER). Detailed build instructions including a bill of materials are listed in the Github repository[5]. The stimulator was connected via a flat ribbon cable to an intermediate connector pcb attached to a chip holder. The connector pcb enabled the connection of four

[5]https://github.com/loslab/easypace/

chips via alligator clips. For pacing, alligator clips were attached to inserted carbon electrodes (C-00-RD-000108, Goodfellow) or fluidic media connectors (21 GA, KDS212P, Kahnetics).

Developed stimulator is able to deliver biphasic pulses ($U = -U_0$ for $t = t_w$, followed by $U = +U_0$ for $t = t_w$, repeated after $t = 1/f$) in adjustable 0.1 Hz frequency steps, 1 ms pulse width steps at an amplitude of up to $U_0 = 12.5$ V and allows a scripted control of pacing parameters.

If not stated otherwise, a pulse width of $t_w = 50$ ms and amplitude of $U_0 = 10$ V were used for pacing tissues in the Spheroflow-HoC. These parameters were determined as most robust for inducing pacing in investigated cultured tissues. For pacing tissues cultured in the centrifugal HoC, an initial prototype of EASYPACE was employed, limiting the output amplitude to $U_0 = 5$ V in pacing experiments.

Mechanical stimulation

Stretch chip The compression compartment was connected to an external pressure pump (OB1 MK3+, Elveflow) which allowed the application of static and sinusoidally varying periodic pressures. Distinct pressures were applied up to 40 mbar and surface profiles extracted from recorded z-stacks. For long-term stretching experiments, periodical pressures oscillating between (0–30) mbar were applied at 0.3 Hz.

Compression chip Distinct pressures were applied with an external pressure pump (MFCS™-EZ EZ-00345001, Fluigent) which allowed the application of up to 345 mbar.

2.8 Readout of O_2 sensor spots

Chips were fixed with magnets on a custom-built sensor platform out of PMMA containing cutouts with geometrically matching sensor positions of four adjoining Spheroflow-HoC chips (4 possible sensor spots per chip × 4 chips → 16 measurement cutouts). Optical fibers could be press fitted into provided cutouts, enabling a flexible configuration of the measurement setup. The arrangement of measurement positions also allowed a versatile positioning and investigation of sensors on other substrates and geometrical arrangements.

Sensor spots were read out using a 4-channel phase fluorimeter (FireSting pro, Pyroscience) with connected optical fibers ($d = 1$ mm, $l = 1$ m). The phase fluorimeter was set to an illumination intensity of 100 % and detection amplification of 400×.

Shperoflow-HoCs were manually aligned for an optimal positioning of the sensor spot above the fiber, yielding signal intensities above $U = 100$ mV for every measurement. All measurements were carried out with the same phase shift calibration, previously obtained from a phase shift measurement of the bare sensor substrate at

37 °C, covered with well-aerated water ($p_{O_2} = 100\,\%$, $\Delta\varphi = 20.4°$) or a 10 % Na_2SO_3 solution in DI (quenching solution; $p_{O_2} = 0\,\%$, $\Delta\varphi = 53.8°$). In order to characterize sensor spots on PET substrates before and after addition of the resin-based tissue layer, bare substrates were fixed on the sensor platform in a similar manner. The phase shift was constantly monitored and individual sensors were covered with a drop of well-aerated water (well shaken DI water before deposition), followed by a drop of quenching solution. After tissue layer attachment, the calibration procedure was repeated.

Signal intensities of integrated sensor particles were evaluated with a single channel phase fluorimeter (Piccolo2, Pyroscience), equipped with a gradient index lens, set to an illumination intensity of 100 % and detection amplification of 400×. The chip was fixed with magnets on the sensor platform and probed with the phase fluorimeter from below.

2.9 Centrifugal HoC sealing tests

Centrifugal HoCs composed of a hot embossed tissue layer sealed with unstructured PDMS were tested for tightness by centrifugation. A 200 µl pipet tip filled with 200 µl water color was inserted into the injection inlet. Following centrifugation for 3 min, the chip was investigated by eye for leakage of water color. Occurring pressures during centrifugation at angular velocity ω were estimated following

$$p = \frac{1}{2}\rho\omega^2({r_2}^2 - {r_1}^2), \tag{2.1}$$

assuming the density ρ of water and radial liquid column positions of $r_1 = 20\,\text{cm}$ and $r_2 = 24\,\text{cm}$ [245].

For the investigation of membrane tightness in hot embossed centrifugal HoCs sandwiching a PET membrane between tissue layer and PDMS-based media layer, chips were sealed and vented as described previously. 20 µl of a suspension of fluorescent beads ($d = (10\text{–}15)\,\mu\text{m}$; F8844, Thermo Fisher Scientific) were added to the pipet tip and injected following cell-based centrifugal HoC loading protocols.

Chapter 3

Heart-on-Chip

Native cardiac tissue is characterized by an abundance of cell-cell contacts and an intricate anisotropic structure of layers of aligned CMs. Therefore, high cell densities and tissue alignment are two essential prerequisites for an accurate recapitulation of functional cardiac units inside microphysiological systems.

In the following sections we discuss two developed HoC platforms introducing novel cell injection and tissue generation concepts, yielding dense 3D and aligned cardiac tissues. We present tailored microfabrication approaches, two distinct chip concepts, and a thorough characterization of formed µ-tissues.

The presented fabrication approach of resin micromolding and the Spheroflow-HoC concept with corresponding tissue characterization has been previously published in "Schneider, O. *et al.* Fusing Spheroids to Aligned µ-Tissues in a Heart-on-Chip Featuring Oxygen Sensing and Electrical Pacing Capabilities. *Mater. Today Bio* **15,** 100280 (2022) [27]". The concept of the centrifugal HoC as well as corresponding tissue characterization is published in "Schneider, O. *et al.* User-Friendly and Parallelized Generation of Human Induced Pluripotent Stem Cell-Derived Microtissues in a Centrifugal Heart-on-a-Chip. *Tissue Eng. Part A* **25,** 786–798 (2019) [29]".

3.1 Tailored microfabrication approaches

In the scope of this thesis, we established several fit-for-purpose microfabrication techniques for the realization of introduced chip concepts. We mainly focus on novel chip materials, enabling the accurate fabrication of PDMS-free tissue modules. In addition, we discuss port generation concepts, enabling the injection of cells by centrifugation via lateral inlets.

3.1.1 Hot embossing of thermoplastic substrates

Due to excellent rapid prototyping properties, mutilayerd OoCs are frequently fabricated out of PDMS modules, sandwiching a porous membrane. However, absorption

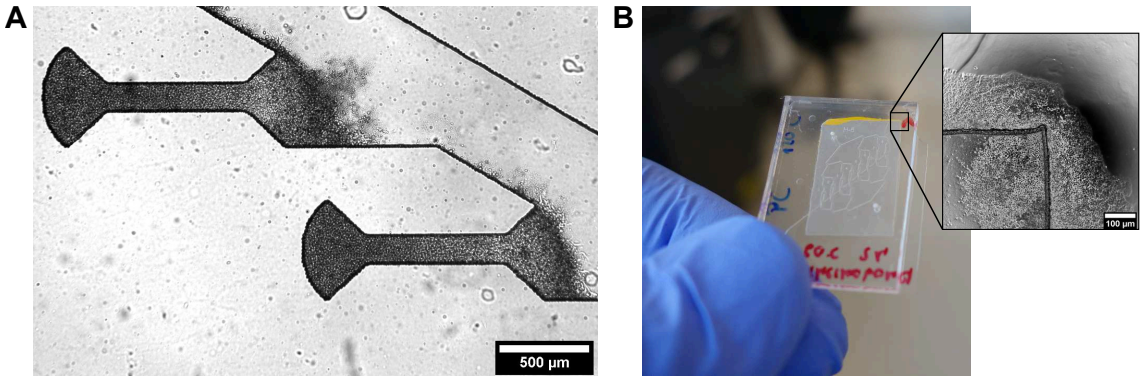

Figure 3.1 Thermoplastic-based chip fabrication. **(A)** Hot embossed tissue module (centrifugal HoC design) sealed with an unstructured PDMS module. During centrifugal loading, cells reliably fill chambers without spilling. **(B)** Loading of a complete microphysiological system with media supply consisting of a tissue layer structured by hot embossing and a PDMS-based media module with bonded membrane. Spilling of cells/microspheres below tissue layer and membrane is observed, indicating weak membrane-thermoplastic bonding.

of small molecules as well as a comparably weak PDMS-PDMS bonding are two major disadvantages of the described chip blueprint. We investigated a novel fabrication concept based on thermoplastic tissue layers, structured by hot embossing. Compared to a similar embossing approach for structuring cardiac tissue chambers, we focus on the sealing of the embossed layer to create a multilayered system integrating a porous membrane [80].

Embossing of channel structures into thermoplastic substrates out of PMMA, PS, or PET-G yielded an accurate reproduction of dog bone-shaped chamber geometries (Fig. 3.1 A; channel geometry corresponds to the tissue layer of the centrifugal HoC discussed in subsection 3.2.1). We adapted a previously published chemical bonding protocol for subsequently sealing the embossed channel with an unstructured PDMS top layer [233]. Bonding strength was evaluated by attaching a pipet tip filled with 200 µl water color to the dead-end channel and subsequent centrifugation of the chip. We centrifuged three replicates for $t = 3\,\text{min}$ at each spinning rate at increasing centrifugal accelerations of $a_\text{c} = (200,\ 400,\ 600,\ 800 \text{ and } 1000) \times g$ (corresponding to a maximum pressure of 3 bar for a liquid column height of 4 cm). All tested chips were tight and did not display depletion of liquid from the pipet tip up to the highest tested acceleration. Cells were injected into embossed dead-end channels via centrifugation at $a_\text{c} = 400 \times g$ for $t = 10\,\text{min}$, yielding satisfactory filling of individual dog bone-shaped tissue chambers with introduced cells (Fig. 3.1 A). We did not observe leakage of developed single-layer chip.

Subsequently, we attached a structured PDMS layer comprising media channels and a bonded PET membrane to the embossed tissue layer, following similar chemical bonding protocol. Centrifugation of cells as well as fluorescent microbeads revealed tight chips. However, centrifuged particles escaped the tissue channel and

accumulated at the edge of the sandwiched bonded membrane, detrimental for a controlled tissue generation (Fig. 3.1 B).

3.1.2 Micromolding of UV curable resin

Interfacing sensors integrated into the substrate of OoCs requires robust fabrication of open-sided tissue layers (stencils). Therefore, we established a novel chip fabrication protocol based on micromolding the tissue layer out of the thiol-ene based resin NOA 81 following previous approaches [246]. Several groups already demonstrated biocompatibility of employed UV curable resin NOA 81, making it a suitable candidate for OoC applications [247–250].

The concept allows the fabrication of resin-based microphysiological systems on a variety of substrates. Dependent on the intended use, O_2 sensor spots can be integrated into the substrate, however the fabrication concept is universal, allowing also the fabrication on unstructured substrates, e.g., cover slips. In case of an integration of O_2 sensor spots, sensors are deposited at defined positions via a CNC microdispenser onto adhesive treated PET-foil (Fig. 3.2 A i) . To ensure robust bonding between UV curable resin and a thermoplastic-based bottom layer, the substrate is functionalized with APTES (Fig. 3.2 A ii). A stamp made out of PDMS, replicating the desired microstructure of the tissue module, is placed onto the substrate. As reproduced from established soft lithography techniques, the stamp comprises micron-sized lateral resolution and can feature regions of varying channel heights.

For an integration of sensor spots, the stamp is precisely aligned to cover the spot with the stamp area corresponding to the future tissue chamber (Fig. 3.2 A iii). As the spot can be considered as fairly flat ($h < 5\,\mu m$), the stamp covers the spot completely, circumventing coverage with resin in following steps. Resin is injected into the stamp injection port and completely fills the void, corresponding to prospective channel walls, within 30 min (Fig. 3.2 A iv + v, B). The whole assembly is exposed to UV light, solidifying the bulk part of injected resin (Fig. 3.2 A vi). However, resin in contact with PDMS remains uncured, as the O_2 permeability of PDMS leads to localized availability of O_2, preventing full curing in the contact region. After removal of the stamp, tissue channel geometries are thus replicated with a sticky surface of uncured resin, integrating the sensor spot into the channel without any coverage (Fig. 3.2 A vii). The media module consisting of media channels replicated in PDMS and a joined PET membrane is treated with APTES and aligned to the tissue channel (Fig. 3.2 A viii). APTES treatment enables a thorough curing without cure inhibition and thus subsequent bonding of resin to the PDMS layer [251]. Finally, the assembly is cured with UV light. One major benefit of the fabrication procedure is the reusability of PDMS stamps (tested for > 10 molding cycles).

We verified successful resin injection and generation of stencil structures on cover slips as well as PET substrates incorporating luminescent sensor spots (Fig. 3.2 B). Finalized microphysiological systems comprise a thin bottom layer, potentially in-

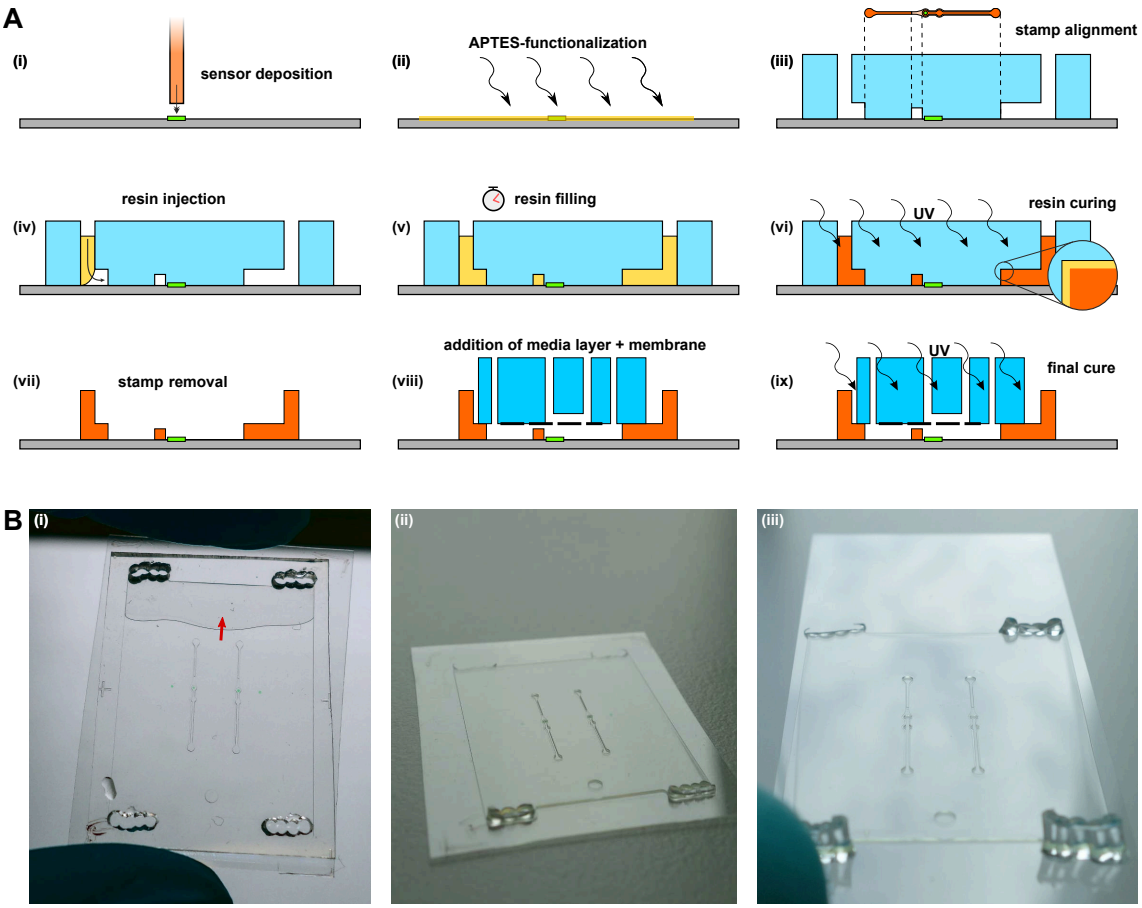

Figure 3.2 UV resin-based fabrication of microphysiological systems. **(A)** Microfabrication steps. (i) Deposition of O_2 sensor onto substrate and (ii) further surface functionalization (both optional). (iii) Addition of PDMS-stamp on substrate with precise alignment of dog bone-knob onto sensor spot. (iv) Injection, (v) capillary filling and (vi) curing of resin. Resin in contact with PDMS does not solidify due to locally available O_2 and remains sticky (inset). (vii) Removal of PDMS-stamp exposes open tissue channels with uncured resin layer. (viii) Addition of APTES-treated media module with bonded membrane and (ix) another UV curing step finalizes the chip. **(B)** Pictures of fabrication process. (i) PDMS stamp on thermoplastic substrate with injected resin. Resin is filling the molding cavity (red arrow). Molded tissue layer after UV curing and stamp removal on (ii) a thermoplastic substrate and (iii) a #1.5 cover slip. (A) adapted from Ref. [27] under CC BY-NC 4.0 license.

tegrate sensors, and allow fluidic connections via the PDMS top layer (Fig. 3.3 A).

Bonding strength of devices assembled with developed fabrication technique was evaluated via burst tests. We tested devices fabricated on glass, PET, and PMMA as substrate material. Spheroflow-HoCs (concept and device geometry discussed in subsection 3.2.2) were fabricated and only one out of eight inlets punched, ensuring a

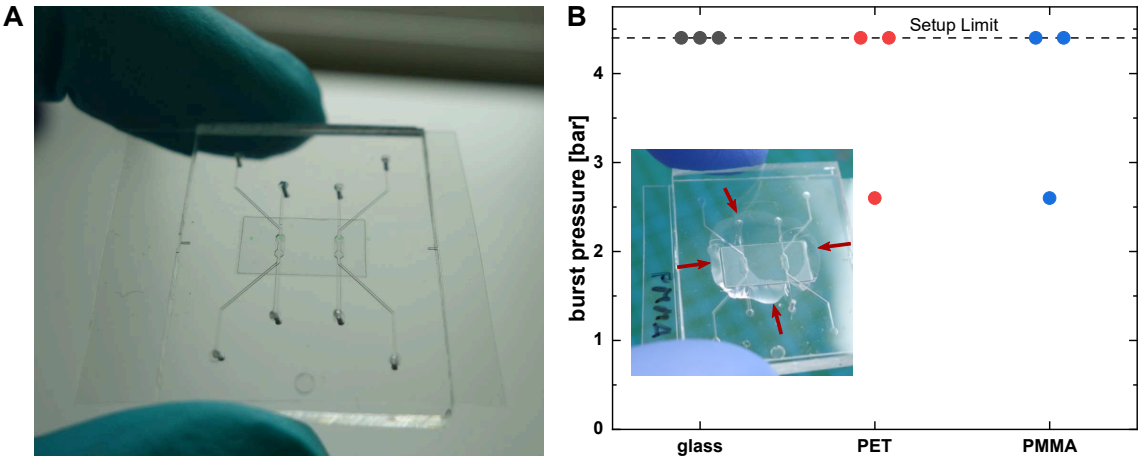

Figure 3.3 Finalized resin-based chip. **(A)** Picture of finalized resin-based Spheroflow-HoC. The tissue layer is closed with a PDMS media module, yielding simple fluidic connections combined with a thin bottom layer. **(B)** Burst tests on resin-based chips fabricated on a variety of substrates. All tested samples are stable up to at least 2.6 bar. Failed samples did not delaminate at the edge but exhibited a cone-shaped rupture of PDMS in the central region (inset, rupture highlighted with red arrows). (A) adapted from Ref. [27] under CC BY-NC 4.0 license.

dead-end access port for the application of testing pressures. To account for potential cross talk between both systems via an edge crevice along bonded membrane, only one out of two individual systems was accessed. Pressurized air was connected to the chip and subsequently ramped up. By submerging tested devices in water, device failure was asserted upon visible detection of leaking air bubbles (Fig. 3.3 B). Generally, devices on all substrate materials were leak-tight up to at least 2.6 bar.

For glass-based devices, we did not observe any device failure at the maximum applied pressure of 4.4 bar. For devices using a PET or PMMA foil as substrate, we observed one out of three tested samples failing at 2.6 bar, while the others did not leak at maximum applied pressure. Investigating failed devices, we did not observe any delamination of the substrate/NOA or NOA/PDMS connection. Rather, the PDMS top layer is ruptured in a cone shape (Fig. 3.3 B, inset).

3.1.3 Defined port generation

Contrary to inlets for interfacing microfluidic systems which are generally punched perpendicular to the channels into the top surface, developed centrifugal HoC concept requires an inlet connecting the tissue channel predominantly coinciding with the channel plane. A minimization of tilt angle is desired for optimal loading conditions. Therefore, we investigated novel fabrication techniques to generate inlets lying on the side of PDMS modules. For reliable device functionality, a standardized inlet angle and position is crucial. As PDMS modules are usually molded in heights of $h \leq 3\,\mathrm{mm}$, precise vertical alignment is necessary to center the inlet allowing a

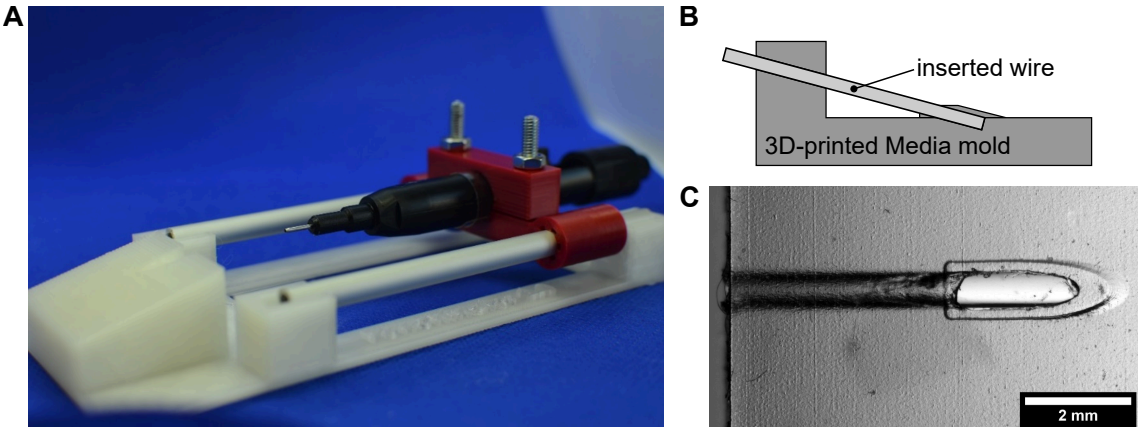

Figure 3.4 Generation of slanted inlets into PDMS modules for centrifugal cell injection. **(A)** Custom-built punching device. Media modules are placed onto a punching block, tilted by 15° with respect to the puncher axis. A biopsy puncher can be manually driven along a fixed axis to punch a defined inlet into the media module. **(B)** Schematic of implemented wire molding technique. Stainless steel wires are inserted in predefined mounting holes of a 3D-printed master mold. After PDMS molding wires are removed, creating inlets at defined positions with a defined angle. **(C)** Inlet in PDMS media module fabricated by wire molding as described in (B).

tight pipet tip connection, preventing an undesired channel opening to the top.

Initial approaches incorporated a marker for the inlet position in the PDMS replica and the inlet was manually punched with a biopsy puncher. As the housing of utilized punching device did not permit punching in small angles, the puncher core unit is removed from the housing. Manually punched inlets resulted in a high failure rates ($\approx 50\,\%$ of usable devices) as the punched inlet frequently ripped the channel open towards the PDMS top. Furthermore, angle and position exhibited high variations between devices.

We designed and constructed a punching device, fixing the core puncher on a movable rail, restricting its displacement to one axis (Fig. 3.4 A). A punching platform, precisely tilted by 15° with respect to the punching axis, is attached to the punching rail. For punching of inlets, the PDMS module is aligned on the block, fixed by hand, and the puncher slided into the PDMS slab. The developed device decreased failure rates by $80\,\%$ ($\approx 90\,\%$ of usable devices) and provided inlets of a defined angle of 15°. However, inter-chip variations were still present due to the manual alignment on the punching block and variations in molded layer height and lateral dimensions, originating from hand-operated cropping of the mold.

Furthermore, we explored 3D-printed PDMS molds for the generation of defined horizontal loading ports. Contrary to wafer-based molds, restricting feasible geometrical arrangements to mostly several layers of defined height, 3D-printed molds allow patterning of arbitrary 3D arrangements, with the only caveat of slightly reduced lateral resolution. Molds are designed to include access ports for the integration

of wires during the molding process (Fig. 3.4 B). Wires are inserted via the side of the mold and guided into a cavity on the mold surface. The cavity is elevated with respect to the mold bottom, providing an additional transition zone between tissue channel and wire-molded inlet, acting as funnel. After molding the master with PDMS, wires are removed from the solidified mold, exposing precisely aligned inlets at defined angle (Fig. 3.4 C). Developed 3D-mold based inlet generation provided superior success rates (100 % of usable devices) with excellent reproducibility compared to both other investigated port generation concepts.

3.1.4 Discussion

A large part of OoCs introduced in recent years is based on PDMS fabrication concepts, which allow for rapid prototyping but pose challenges for a scalable fabrication and suffer from small molecule absorption. Generally, there is need for flexible microfabrication concepts which allow to tailor chip composition to its intended use, providing leak-tight chips on thin substrates for optimal imaging conditions. For the integration of sensors into the substrate, open bottom tissue layers are essential. We investigated two fabrication concepts integrating non-PDMS tissue layers into OoCs, enabling the embedding of sensing capabilities. Furthermore, we explored techniques for generating lateral access ports in PDMS media modules. Contrary to conventional interfacing from top, the centrifugal HoC requires lateral inlets for introducing cells via centrifugation.

Chip fabrication We established chip concepts based on hot embossing of thermoplastic substrates and resin micromolding. Both concepts yield hybrid multilayer OoCs which combine a gas permeable PDMS media module with a gas impermeable thermoplastic/glass tissue layer and substrate. The combination merges the benefits of PDMS, enabling media oxygenation and providing a facile fluidic connection, with reduced small molecule absorption in the tissue compartment, characteristic of a non-PDMS layer. Both approaches are flexible in their substrate choice and can provide optimal imaging conditions due to a decreased distance between tissue and outer chip surface. Fabrication concepts are based on PDMS stamps manufactured with established soft lithography protocols, yielding the same structural accuracy, excelling other structuring techniques, e.g., CO_2 laser cutting, in lateral resolution. Both approaches involve silane-based chemical bonding and deliver devices which are stable at pressures exceeding pressures conventionally applied in microphysiological systems ($p \leq 2\,\mathrm{bar}$) [248].

Hot embossing offers a scalable approach amenable for large-scale chip production. Furthermore, substrate and channel layers are directly combined, eliminating an additional bonding step. However, the integration of a PET-membrane led to inadequate sealing of the tissue channel, resulting in spillage of cells between structured tissue layer and membrane upon centrifugation. As the chip is tight in general, spillage occurs due to insufficient bonding between membrane and tissue layer. The membrane is only sandwiched between bonded media layer and substrate. Thus,

decreasing the membrane size could help in sealing the tissue channel by inhibiting possible membrane lift off due to a tighter membrane fixation. It is conceivable that a flow-based loading could be still implemented, excerting reduced pressures onto the sandwiched membrane. A thermofusion bonding step prior to media module attachment could help in tightly sealing the membrane to the tissue layer. Regardless of a direct tissue module integration, embossed layers can be still utilized for structuring the substrate, thus enabling the integration of sensors right below the tissue module.

Resin-based micromolding allows a flexible combination with a variety of materials, enabling the chip fabrication on top of different substrates. Thus, chips can be tailored to their respective application. For instance, the chip can be assembled on a pre-fabricated PET substrate, offering optimized adhesion for luminescent sensor spots. Contrary, chip assembly on cover slips yields optimal imaging conditions, enabling the analysis of cultured cardiac µ-tissues via Fluorescence Lifetime Imaging or Raman Imaging. Occurring rupture potentially occurs due to insufficient bonding at the NOA/membrane interface as well as penetration of air into a small edge crevice around the embedded membrane. As pressure is excerted only in a confined region, this pointwise loading might lead to observed localized bursting of the PDMS module.

Due to observed good contact between PDMS stamp and substrate, micromolding reliably creates stencil structures, advantageous over error-prone exclusion molding of PDMS. However, if, e.g., for a different substrate material a conformal contact cannot be established, resin might spill below substrate and stamp, preventing the generation of completely open structures. Similarly, sensors of increased height compared to employed luminescent spots, could lead to a spilling of resin. In that case, it is thus conceivable to mold the stencil structure on an unstructured PDMS layer first, providing good sealing and preventing full curing of the bottom surface due to O_2 permeability. Especially substrates incorporating mechanically fragile structures benefit from a pre-assembly of the stencil layer, omitting a direct placement of the stamp onto the substrate. Envisioned fabrication concept however requires an additional curing step, increasing complexity and probably impacting bonding strength.

Comparing both approaches, micromolding is based on manual resin injection but offers superior membrane attachment as well as the ability to fabricate chips directly on top of structured substrates. Thus, we mainly focused on resin-based microfluidic systems for investigated chip prototypes. However, we also combined both concepts and fabricated resin-based OoCs on substrates structured by hot embossing.

Defined port generation We investigated three distinct methods for generating tilted access ports. The wire-based inlet generation technique is superior among investigated methods considering inlet reproducibility. However, major drawbacks, originating from the 3D-printing process, are a decreased lateral resolution of integrated channels as well as a rough surface of the PDMS mold, hampering the bonding

of the mold to other surfaces. Thus, media modules with wire-molded inlets require more advanced chemical bonding protocols for sufficient bonding strength, especially crucial in a centrifugation-based system. Punching of inlets with developed punching device provided a good compromise between reproducibility and bonding strength.

3.2 Cell injection & tissue generation concepts

Many HoCs currently rely on the injection of cell-laden hydrogels, yielding low cell densities. On the other hand, flow-based injection of cell suspensions usually deploys micron-sized retaining features for accumulating cells in defined geometries, which, however, are prone to clogging during the loading process, yielding uncontrolled loading pressures, ceasing of flow and low densities. Here, we investigate two novel cell injection & tissue generation concepts for the formation of dense aligned cardiac µ-tissues within microphysiological systems, demonstrating possible solutions to aforementioned challenges.

3.2.1 Centrifugal HoC

The centrifugal HoC hosts the capability to generate eight individual cardiac tissues. All tissue chambers branch off a main channel (500 µm wide, 100 µm high) that is tilted by 45° with respect to the central axis, that is, the axis parallel to the longer side of the rectangular chip outline, and are arranged parallel to the referred axis (Fig. 3.5 A). The tissue chambers are designed in a characteristic dog bone-shaped geometry with a 150 µm wide and 1 mm long shaft, favoring the formation of an elongated cardiac muscle strand as reported previously [82]: being offered a large adhesion area at both ends, cells can attach at the endpoints and form a connecting fiber in the middle shaft region, thereby acting as a physiologically relevant model system of a myocardial subunit that consists of multiple aligned fibers [84].

Medium channels are located directly above the tissue chambers and are arranged in such a way that all chambers are perfused with the same amount of medium (Fig. 3.5 A, B). An isoporous membrane acting as an endothelial-like barrier separates the two layers and enables a fluidic connection between medium channels and tissue chambers. Numerical simulations of the velocity profile in described geometry confirmed the confinement of the convective flow to the medium compartment, thus protecting cultured tissues from additional external forces (Fig. 3.5 C). Due to porosity of the membrane, cultured tissues are supplied with nutrients by diffusive transport, as verified by the simulated concentration profile (Fig. 3.5 D). The concentration in tissue chambers trailed that of the medium channel with a sub-minute delay, indicating effective transportation of soluble compounds, such as nutrients or administered drugs.

The centrifugal HoC was mounted on a microscope slide for convenient handling (Fig. 3.6 A). The whole system is designed such that during the loading process

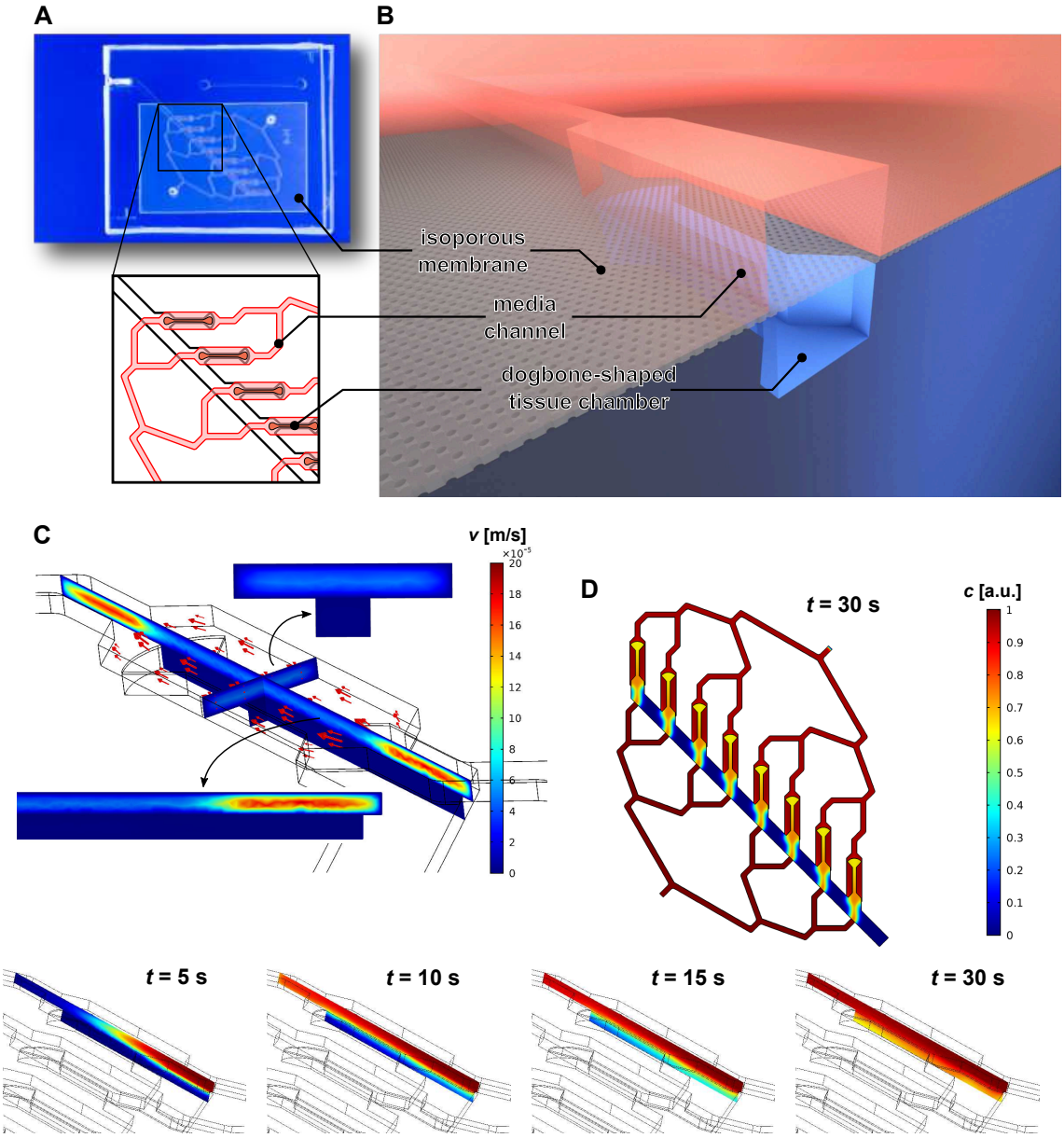

Figure 3.5 Concept of the centrifugal HoC. **(A)** Photo of the HoC platform featuring a main channel tilted by 45° with respect to the central axis and multiple parallel, dog bone-shaped tissue chambers. The zoomed-in top view highlights the parallelized medium supply of individual chambers. **(B)** Detailed side view illustrating the employed multilayer approach. hiPSC tissues are cultured in the lower tissue module, separated by an isoporous membrane from the upper medium channels. **(C)** Simulated velocity profile of the medium supply. No additional shear forces act on tissues in the tissue chambers because of the confinement of convective transport to the separate medium module. **(D)** Simulated concentration profile at $t = 30\,\mathrm{s}$ after starting the medium flow. Diffusion of nutrients is equal for all tissues and occurs in the desired sub-minute temporal range, enabling culture of viable tissues. The exact temporal evolution is shown for one tissue chamber at (5, 10, 15 and 30) s. Figure adapted from Ref. [29] under CC BY 4.0 license.

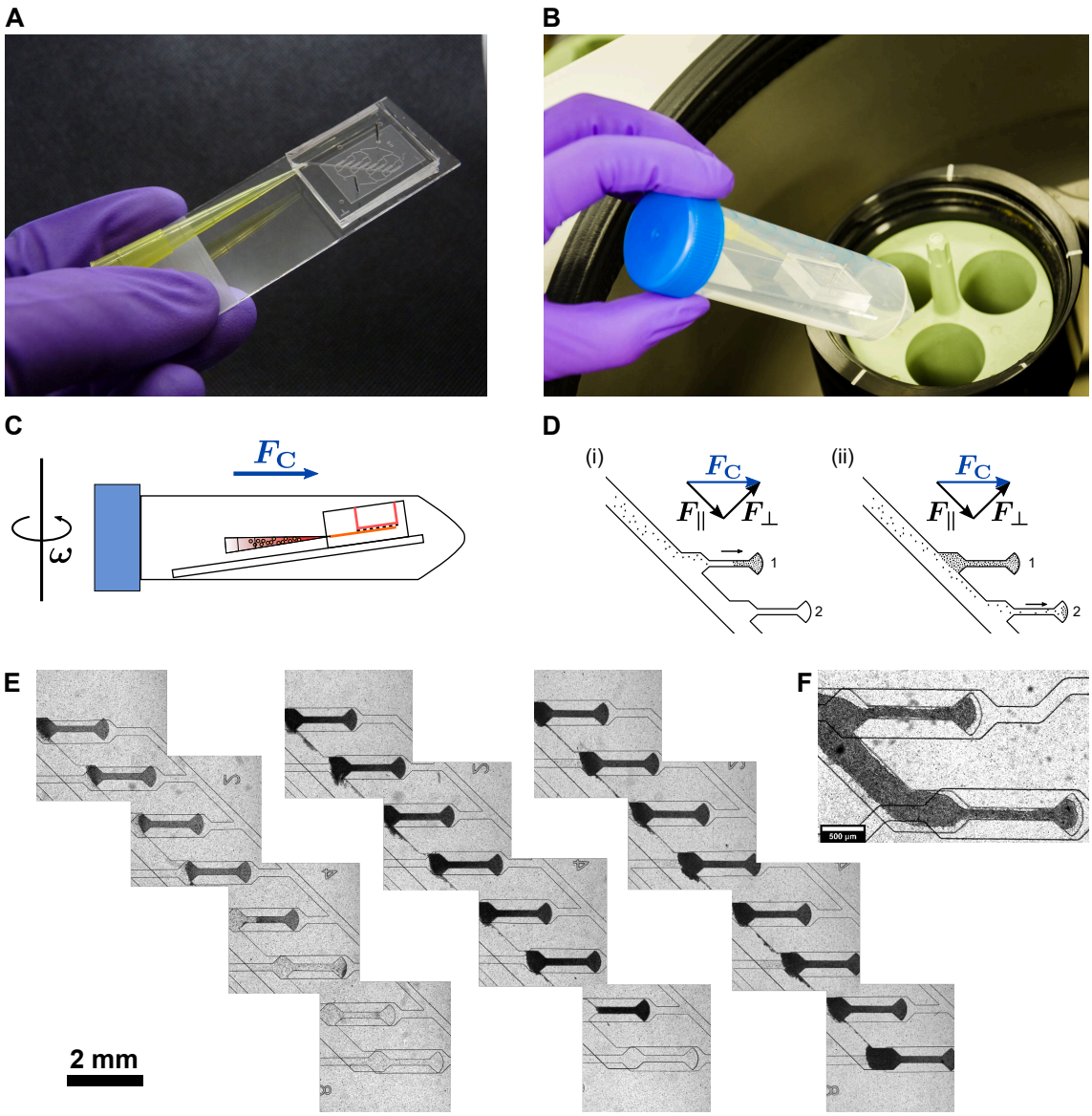

Figure 3.6 Loading procedure of the centrifugal HoC. **(A)** Photo of an assembled centrifugal HoC. Medium in- and outlets are reversibly sealed by stainless steel plugs, while a pipette tip is utilized to introduce the cell suspension into the chip. **(B)** Photo of chip insertion into a common laboratory centrifuge. A centrifuge tube conveniently acts as sterile interface for accessing the centrifuge. **(C)** Schematic of the system during centrifugal cell injection. During centrifugation with rotational speed ω, the tube is tilted into a horizontal position and the centrifugal force transports cells into the chip. **(D)** Detailed illustration of the filling mechanism. As the main channel is tilted by 45°, individual tissue chambers are filled subsequently in a self-organized metering manner. **(E)** Stitched images of centrifugal HoCs loaded with varying amounts of cells (GM25256, different geometry of the medium module used here). Introducing a sufficient amount of cells leads to eight filled chambers (right image), whereas loading with fewer cells leads to fewer generated tissues (left and middle images); however, all individual tissue chambers are filled entirely, there is no waste of cells. **(F)** Image of loaded chip with too many cells resulting in connected tissues. Figure adapted from Ref. [29] under CC BY 4.0 license.

the chip can be placed into a conventional centrifuge, transporting the cells into individual tissue chambers by centrifugation instead of conventional external pumps. A pipette tip, which is inserted into the chip at an angle of 15° with respect to the microscope slide plane, allows an easy interface for inserting a cell suspension into the main channel and remains inserted in the chip during the centrifugation step. During centrifugation, medium in- and outlets are reversibly sealed to prevent any convective flow and the entire chip is conveniently placed into a 50 ml conical centrifuge tube that ensures a tight-fitting and, additionally, sterile process environment (Fig. 3.6 B).

One major advantage of cell injection through centrifugal forces is the removal of air bubbles, thereby providing a well-defined system. Before introducing cells, a venting step is carried out during which the pipette tip is only filled with media and subsequent rotation ejects remaining air bubbles from the chip. While the pipette tip is still mostly filled with media, subsequent injection of the cell suspension does not introduce new air bubbles, ensuring a robust cell loading process during centrifugation (Fig. 3.6 C).

The basic property of centrifugal force, that is, its directionality in contrast to isotropic forces during conventional pressurized loading, allows for its exploitation for novel loading concepts. As cells are introduced into the tissue module, the tilted channel design ensures that cells (which are transported radially outward in the completely air-free channel) accumulate at the distal channel wall during centrifugation, due to their higher density. The centrifugal force acting on cells may be decomposed into one component parallel to the channel wall and one component perpendicular to it (Fig. 3.6 D). As long as the wall compensates the perpendicular force component, cells are driven radially outward along the radially outer-lying channel edge.

As cells reach the first tissue chamber, they are trapped and start filling the 3D chamber completely, from the radially distal-lying parts upward, that is, toward the chamber entrance. Only after the first chamber has been filled entirely, consecutive cells will travel further downstream and start filling the next chamber. This ensures that during the loading procedure, cells fill consecutive chambers in a self-organized metered behavior, providing uniformly filled, densely packed tissue chambers. Centrifugation parameters were optimized to the lowest centrifugal force still able to reliably and repeatedly fill the tissue chambers.

If the proper amount of cells is loaded, all filled tissue chambers contain the same amount of cells, whereas the intermediate channel is free of cells, leading to generation of independent, unconnected, cardiac muscle strands during further culture. On reducing the number of introduced cells (Fig. 3.6 E), one of the key advantages of the used geometry becomes evident: even if the volume of the introduced cell suspension is insufficient to fill all chambers, the chip and especially the deployed cells are not wasted because the described approach leads to consecutive loading of individual chambers, still creating multiple identical—although fewer—tissues.

Other approaches in which the total amount of cells is evenly distributed between all chambers would lead to chambers only partially filled with cells, precluding its use

for further comparable and standardized tissue analysis. Nevertheless, if excessive cell numbers are injected and the volume of introduced cells exceeds the added up volume of all tissue chambers, the main channel fills up, leading to a short circuit by connecting neighboring tissues (Fig. 3.6 F).

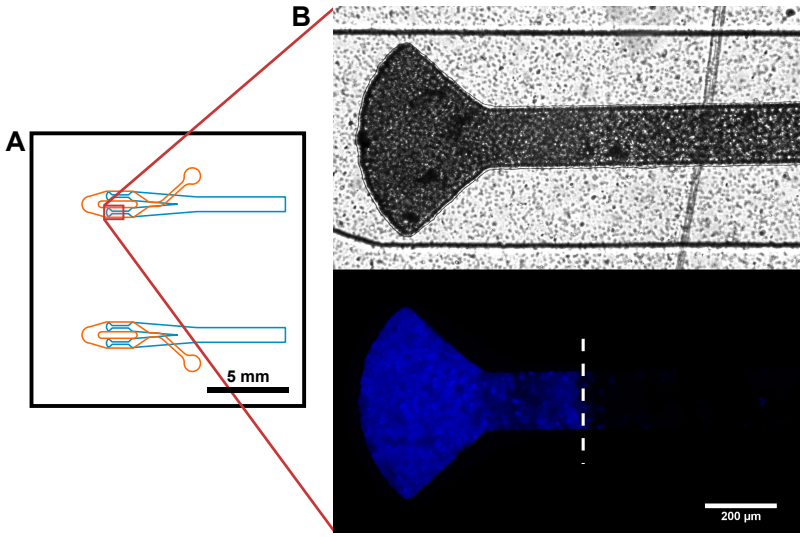

Figure 3.7 Centrifugal co-loading. **(A)** Modified centrifugal HoC geometry featuring an even branching of the main channel (blue), optimized for successive loading passes. One chip holds two separate systems, which are perfused by overlying medium channels (orange). **(B)** Brightfield image of a cardiac tissue chamber filled with CMs (Cor.4U®, d0, upper panel). The loading process was decomposed to first introduce a cell population labeled with a cell tracker dye, followed by the pristine population. Fluorescence microscopy reveals a defined cell distribution (lower panel, border of cell populations highlighted with dashed white line), illustrating the opportunity of the centrifugal HoC to generate precisely controlled cocultivations. Figure adapted from Ref. [29] under CC BY 4.0 license.

Utilizing a slightly different chip design with modified loading channel geometry, the centrifugation-based loading concept also opens up the possibility of generating defined co-cultures by consecutive loading steps (Fig. 3.7 A). The loading channel is arranged in parallel to the direction of the centrifugal force and evenly branches into two separate dog bone-shaped tissue culture chambers. Each chip comprises two individual systems which are separated by an isoporous membrane from overlying media channels, enabling perfusion of both tissue chambers in parallel. Upon cell injection via centrifugation, introduced cells fill up the chambers in a parallelized manner due to the even branching, contrary to the tilted channel design where chambers get filled consecutively. This approach enables the centrifugal generation of patterned tissues. In an initial loading step we injected CMs labeled with cell tracker via centrifugation, leading to a partial filling of the tissue chamber (Fig. 3.7 B). Afterwards, we injected unlabeled CMs, filling the tissue chamber completely. Fluorescence microscopy indicates a clear separation between labeled and unlabeled

cells, demonstrating a precisely controllable tissue patterning mechanism along the tissue shaft direction.

3.2.2 Spheroflow-HoC

In addition to the centrifugation-based injection of single cells, we developed an alternative microphysiological system based on loading of cardiac spheroids via hydrostatic flow (Spheroflow-HoC). As the injection of singularized cell suspensions is prone to inherent polydispersity, the Spheroflow-HoC aims at increasing loading robustness by injecting precisely controllable spheroids of homogeneous size. Spheroids evolved in recent years as established model system, allowing the controlled generation of dense 3D tissues, which can even fuse to arbitrary tissue shape [252, 253].

The underlying tissue generation concept relies on an initial formation of multicellular 3D cardiac µ-tissues (Fig. 3.8 A). Spheroid formation is a widely established technique yielding 3D tissues without the use of hydrogel. While achieving physiological densities and cell-cell contacts, they cannot recapitulate structural organization and cell alignment, recapitulating human physiology only partially. The Spheroflow-HoC concept is based on the injection of pre-formed spheroids in a dog bone-shaped geometry leading to a subsequent fusion of the individual spheroids to an uniaxially aligned cardiac muscle fiber. Generation of spheroids enables a precisely controlled cellular tissue composition by mixing defined ratios of different cell types, such as CMs and FBs.

The design of the tissue module enables the injection of the spheroids simply by hydrostatic pressure-driven flow. The module is composed of structures featuring two heights h, namely a channel of $h = 180\,\mu m$ ending in a dog bone-shaped tissue chamber and a channel of $h = 30\,\mu m$. Spheroids are loaded into the tissue chamber by adding the spheroid suspension into a pipet tip in the inlet. The difference in liquid column height, with respect to the tissue outlet, induces a hydrostatic flow, dragging spheroids into the channel (Fig. 3.8 B i). As the channel constricts at the end of the tissue chamber to the narrow channel height, spheroids are not flushed to the outlet but rather accumulate inside the tissue chamber (Fig. 3.8 B ii). Clogging of the channel is avoided by a narrow side channel into which spheroids cannot penetrate, such that a constant flow is maintained during filling. By exploiting a defined spheroid size ($d = 150\,\mu m$), the chamber is thus completely filled. Introduced spheroids subsequently merge, forming an aligned tissue, tailored by the channel geometry (Fig. 3.8 B iii).

The implemented chip design comprises two independent tissue chambers with corresponding loading channels, separated by a porous membrane from individual overlying media supplies (Fig. 3.8 C). In case of O_2 sensor integration, one luminescent spot is deposited into the rear knob of each tissue chamber (cf. Fig. 3.3 A for a picture of an assembled Spheroflow-Hoc with integrated O_2 sensors). We successfully assembled the Spheroflow-HoC either completely out of PDMS, or as hybrid system featuring only a media module out of PDMS. In the hybrid version, utilizing a hot

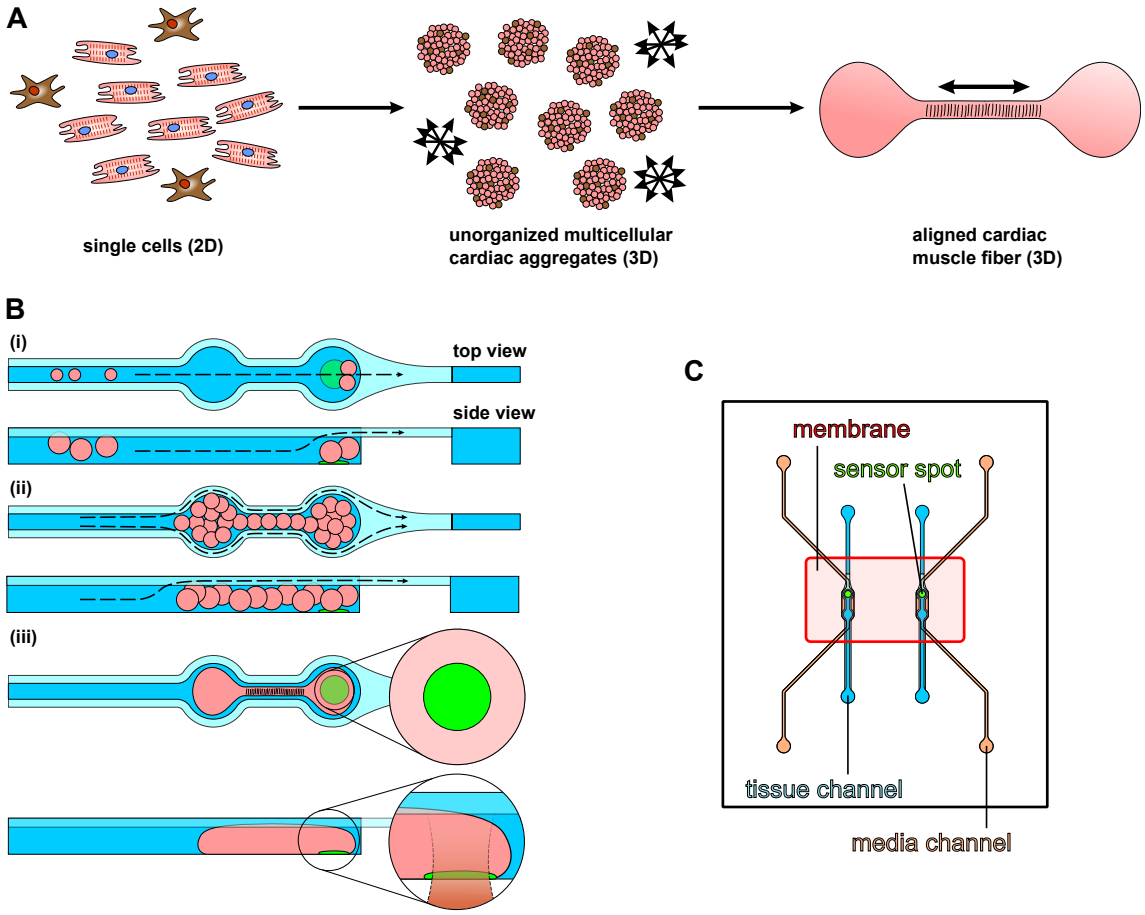

Figure 3.8 Concept of the Spheroflow-HoC. **(A)** Schematic of the bottom-up approach for generating aligned cardiac fibers. Initial compaction of a precisely defined mixture of single cells to spherical 3D spheroids. Spheroids further merge to an aligned tissue fiber, guided by provided chamber shape. **(B)** Chip loading mechanism. (i) Spheroids are introduced by hydrostatically-driven flow into the dog bone-shaped tissue compartment and fixed by the channel constriction. (ii) With gradual filling, the loading flow is maintained by the adjacent constriction channel. (iii) Individual spheroids merge to a single aligned cardiac tissue. Potentially embedded optical sensor spots in the knob region enable *in situ* readout of physiological key parameter. **(C)** Design of Spheroflow-HoC: Each chip comprises two individual systems consisting of a loading and a media channel, separated by a porous membrane. If applicable, sensor spots are integrated into the knob region of the tissue chamber. Figure adapted from Ref. [27] under CC BY-NC 4.0 license.

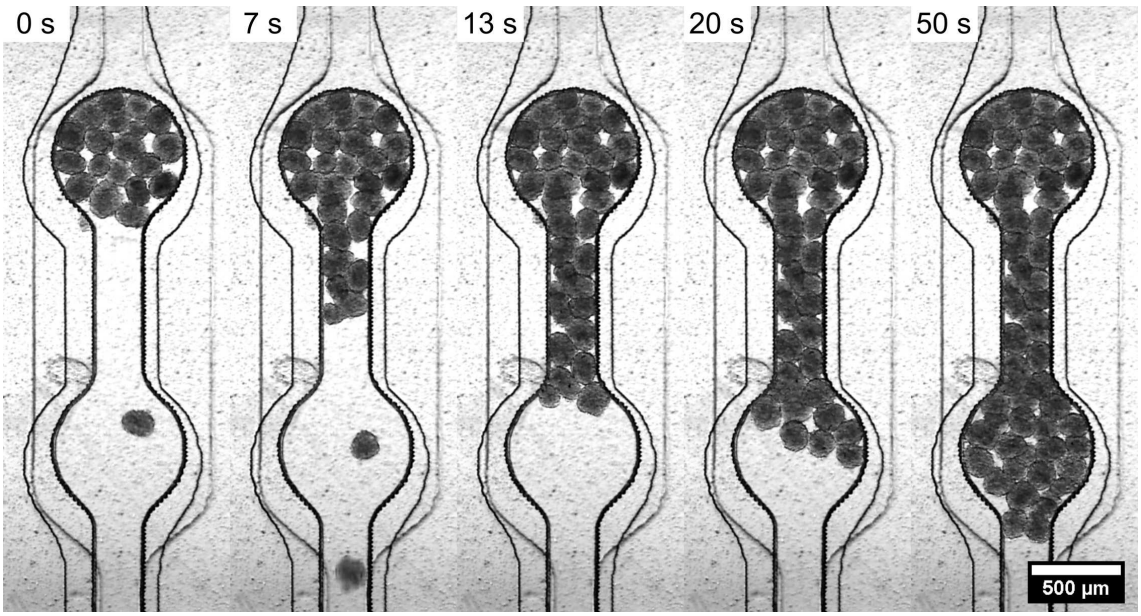

Figure 3.9 Frames recorded during hydrostatic spheroid injection into Spheroflow-HoC assembled as hybrid resin-based system. Within one minute, spheroids accumulate in the dog bone-shaped tissue chamber.

embossed thermoplastic tissue layer or a resin-based tissue layer yielded satisfactory chip quality considering structural integrity and tightness. As the resin-based fabrication technique offers advantages in further sensor integration, we focused on this chip implementation as test system for investigating spheroid loading and tissue formation inside the Spheroflow-HoC.

Following equilibration of the system with media, we inserted spheroids into the pipet tip connected to the injection port and monitored the loading process via brightfield microscopy (Fig. 3.9). Due to the difference in liquid column height between inlet and outlet tip, spheroids were reliably flushed into the loading channel and filled within one minute the entire tissue chamber. We noted crucial influence of the exact spheroid size. Too large spheroids could get stuck in the loading channel, whereas too small spheroids could squeeze into the constriction. Both deviations from the ideal diameter lead to a ceasing of the loading flow, yielding unusable devices. If ceasing of the loading flow was observed, topping up media in the inlet tip as well as slight tapping of the chip helped to achieve satisfactory filling of the tissue chamber.

3.2.3 Discussion

For an accurate recapitulation of the human heart, HoCs seek to generate dense and aligned 3D tissues. We introduced the centrifugal HoC and the Spheroflow-HoC, both achieving high cellular densities by centrifugation and the injection of preformed spheroids, respectively. Contrary to widespread approaches, both concepts

enable the hydrogel-free generation of cardiac µ-tissues, increasing tissue density compared to the injection of a cell-laden hydrogel. Introduced loading mechanisms can be universally applied for injecting cells into OoCs and are not constrained to generating cardiac dog bone-shaped tissues. The injection mechanisms are distinguished by providing a precisely defined loading process, amenable for the automatized generation of 3D cardiac tissues. Introduced HoCs feature high loading efficiencies, ensuring the delivery of all introduced cells/spheroids into culture chambers, which is crucial when working with cost-intensive patient-specific hiPSC-CMs in future industrial applications. The HoCs are designed in a multilayer architecture permitting further facile integration of additional readouts or stimuli for investigating generated tissues.

The centrifugal loading procedure solely relies on a conventional centrifuge commonly available in cell culture laboratories and allows to load multiple units in one centrifuge simultaneously. The application of centrifugal forces during cell loading exploits their unidirectionality, which aids the crucial removal of trapped air bubbles due to their low density, as well as leads to consecutive loading of chambers in a self-organized manner [254–257]. Furthermore, centrifugal loading provides the opportunity to tune cellular density with rotation speed. As proof-of-concept, a system containing eight tissue chambers was presented; however, the chip design could be further extended to include an increased number of tissues. Should the amount of introduced cells be too low to fill all chambers, the pipette tip offers an easily accessible interface for successive loading steps.

We presented an alternative chip design for loading via centrifugation, featuring a single branching of the loading channel which offers the opportunity to consecutively inject multiple cell populations in a parallelized manner. It seems straightforward to further extend chosen approach and bifurcate each dowstream channel again, resulting in a higher degree of parallelization and more generated tissues. However, a multiply branched main channel could result in reduced loading robustness. Even slightly uneven splitting of cells at one bifurcation could accumulate over multiple branches and lead to unevenly filled tissue chambers, impeding inter-tissue comparison of formed tissues. Therefore, the arrangement of a tilted main channel with branching chambers is the preferable approach for standardized tissue generation.

In contrast to the injection of single cells, the Spheroflow-HoC injects preformed cardiac spheroids into the tissue chamber. Compared to single cells, which can hardly be compacted in a tissue chamber without applying uncontrolled pressures, the utilization of spheroids as building blocks facilitates injection as they can easily be guided by a clogging-free adjacent constricted channel to desired positions. No uncontrolled manual pressure is excerted for cell injection as defined hydrostatic pressures prevail. The adjacent constrained channels prevent excessive pressure buildup, enhancing the similar trapping system presented by Bruzewicz *et al.* [258]. Presented chip concept does not depend on a distinct fabrication method. We assembled and loaded HoCs of the same design with a resin-based tissue layer on coverslips for high-resolution imaging or on top of O_2 sensor substrates.

Contrary to previous approaches which trap single spheroids in microfluidic en-

vironments, a rather large amount of spheroids ($N \approx 50$ spheroids) is constrained to a chamber of precisely tailored shape, guiding tissue architecture [259]. The microfluidic environment is thereby leveraged to a shaping tool instead of a mere capturing mechanism. Multiple devices can be easily loaded in parallel, as only simple pipetting steps are necessary which could be carried out by liquid handling robots. By merging OoC and spheroid technology, the potential of pre-culturing spheroids in suspension culture on a large scale can thus be harnessed for upscaling OoC technology [236]. So far, current implementation requires a manual monitoring and potential individual device adjustments during the loading process. To unfold its full automatization potential, an even more standardized loading behaviour is desired. Generally, proof-of-concept is demonstrated in devices fabricated with rapid prototyping methods. A further scaled up and more standardized fabrication process could help in reducing device variability. Especially coating or smoothing roughness of side walls could improve loading stability.

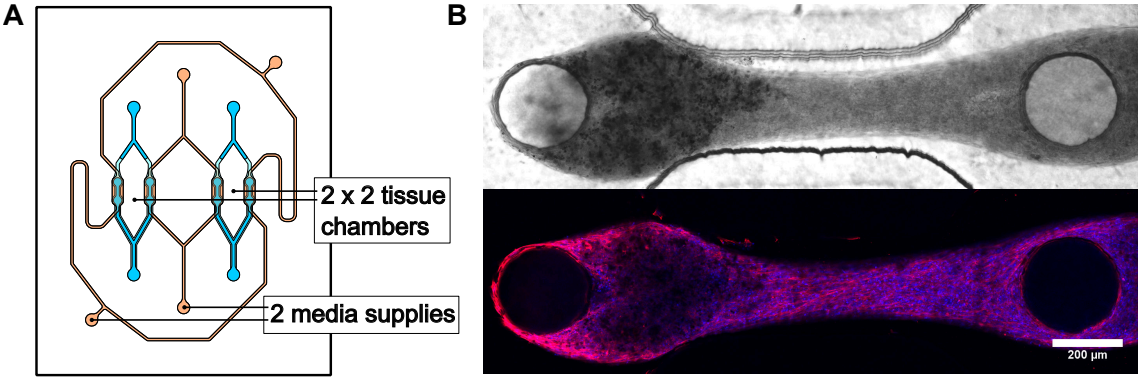

Figure 3.10 Extensibility of Spheroflow-HoC. **(A)** Modified design with branched loading channels and two shared media supplies enabling the direct comparison of tissues under different perfusion conditions. **(B)** Brightfield image and immunofluorescence staining of a FB tissue cultured in a Spheroflow-HoC with integrated pillars (red: Phalloidin, blue: DAPI). The tissue adheres to both pillars and aligns.

Compared to the centrifugal HoC, the Spheroflow-HoC is limited to one tissue chamber per injection port. We also developed a multiplexed version with branched loading channel, enabling the filling of two tissue chambers from one shared inlet (Fig. 3.10 A). By perfusing each tissue created from the same loading with two distinct media supplies which also branch and perfuse the other tissues, four distinct culture conditions (loading with two distinct cell populations $\times$ two individual media supplies) can be created in one chip and directly compared.

As further extension, we adjusted the tissue chamber PDMS mold, integrating pillars into the tissue chamber knob region (Fig. 3.10 B). Integrated pillars act as anchor for tissue suspension and alignment but do not deflect upon tissue contraction. For directly sensing forces with integrated pillars, further miniaturization and stiffness adjustments are necessary.

Generally, the centrifugal HoC offers higher parallelization compared to the

Spheroflow-HoC, generating eight tissues within one chip. However, it strongly depends on the injection of a well-singularized cell suspension, potentially impeding proper device function by clogging. In contrast, the Spheroflow-HoC provides more defined injection conditions by introducing spheroids of defined shape. Flow-based injection is less harsh compared to centrifugation due to reduced forced collisions with the side wall, however, we did not observe adverse effects in further tissue culture caused by centrifugation. Tissues generated in the Spheroflow-HoC are larger than in the centrifugal HoC ($\approx 20\,000$ cells vs. $\approx 10\,000$ cells), caused by tailoring the chamber size to introduced spheroid diameter. The flexibility in spheroid generation allows for a downscaling of the Spheroflow-HoC in further iterations. Ultimately, both concepts might be combined, increasing centrifugal loading robustness by introducing a suspension of well-defined spheroids.

The single branching version of the centrifugal HoC allowed for tissue patterning by multiple cell injections; an approach which is directly transferable to the Spheroflow-HoC. Thereby, heterogeneous tissues can be generated, such as cardiac tissues coupling healthy with fibrotic tissue or cardiac tissues which combine a ventricular and atrial end, as described previously [80]. Contrary to the concept of Zhao *et al.* which relies on manual seeding of cell populations into two ends of a shared cavity, introduced approaches enable an automated and parallelized patterning of tissues. However, a branching channel geometry shares the same challenge for both loading concepts, strongly relying on an even branching for a comparable tissue generation.

3.3 Tissue characterization

The following subsections characterize cardiac µ-tissues formed in the centrifugal HoC and Spheroflow-HoC, assessing their microscopic tissue morphology with respect to the formation of an aligned fiber.

3.3.1 Tissues formed from single cells

After centrifugal cell injection in the centrifugal HoC, medium plugs as well as the pipette tip used for cell insertion were removed, and the tissue inlet was blocked. A syringe pump was connected to the medium inlet, a waste container to the outlet, and the tissues were supplied with media at a flow rate of 50 µl/h. Generally, the cultured cardiac tissues began beating spontaneously on day 2 after seeding. During on-chip tissue formation, single CMs connect to an aligned tissue fiber and synchronize their beating pattern (Fig. 3.11 A). Cardiac µ-tissues from hiPSC-CMs could be cultured over multiple weeks and were still showing a pronounced beating motion four weeks after initial seeding. To assess tissue viability, live/dead staining was performed, confirming that even after four weeks of culture, the bigger part of the tissue was viable and dead cells occurred only sporadically, indicating an intact tissue (Fig. 3.11 A). For further physiological validation, we performed

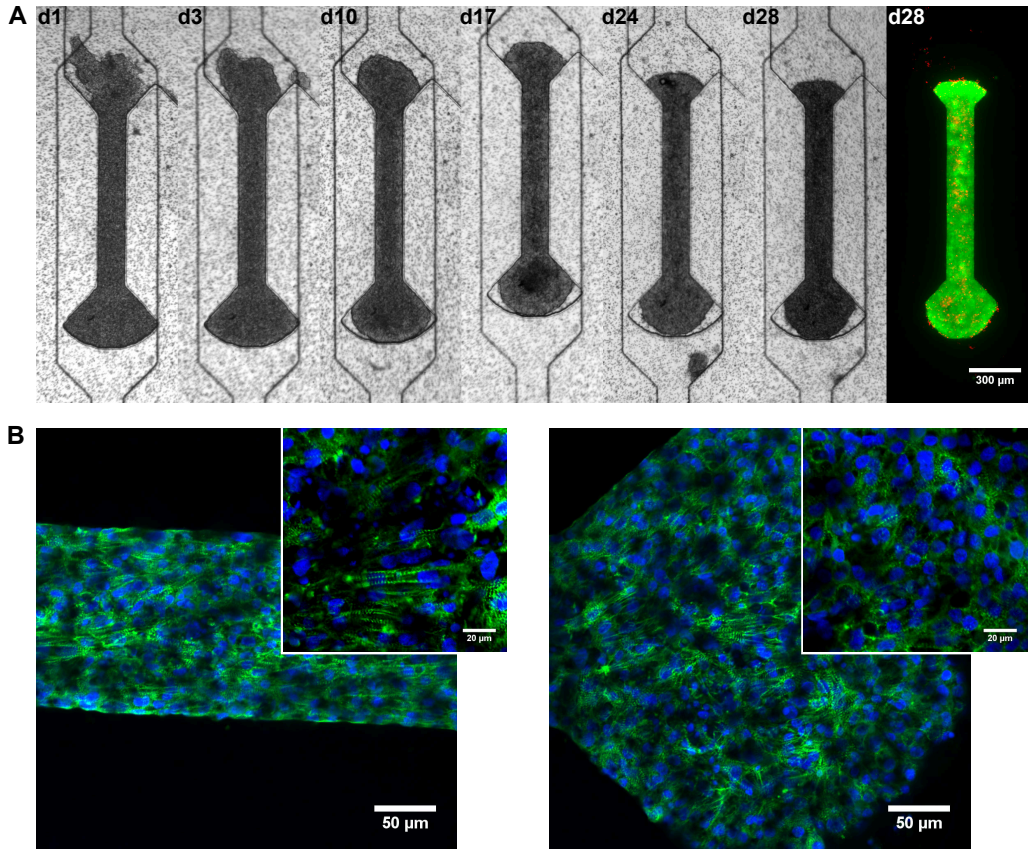

Figure 3.11 Formation of cardiac µ-tissues from single cells. **(A)** Development of hiPSC-derived cardiac µ-tissue over the time span of multiple weeks (GM25256). After cell seeding, the tissue compacts and starts beating uniaxially, still viable after four weeks, as indicated by live/dead staining (green: FDA, red: PI). **(B)** Physiological validation of cultured hiPSC-derived cardiac µ-tissues by immunostaining of α-actinin (green) and DAPI (blue), fixed on day 28 after seeding (GM25256, 25× magnification). The insets show a zoomed in view of the central region (63× magnification). Horizontally aligned sarcomeres prevail in the shaft region (left), whereas sarcomeres are randomly oriented in the knob region (right). Figure adapted from Ref. [29] under CC BY 4.0 license.

immunofluorescence staining of sarcomeric α-actinin which was analyzed by confocal microscopy (Fig. 3.11 B). The microscopy images reveal characteristically striped cytoskeletal structures (α-actinin) as well as a parallel alignment of sarcomeres, particularly in the shaft region of the tissue chambers. The sarcomeres within the shaft region show a preferred alignment parallel to the main axis of the tissue, in contrast to the knob region where sarcomeres of the substrate-adhered tissue were rather unorganized and did not show a distinct orientation.

Presented chip concept allows the generation of perfused cardiac tissues of physiological shape. For further increasing the physiological significance, the endothelial barrier is refined from a porous membrane to integrate a true tissue barrier. Follow-

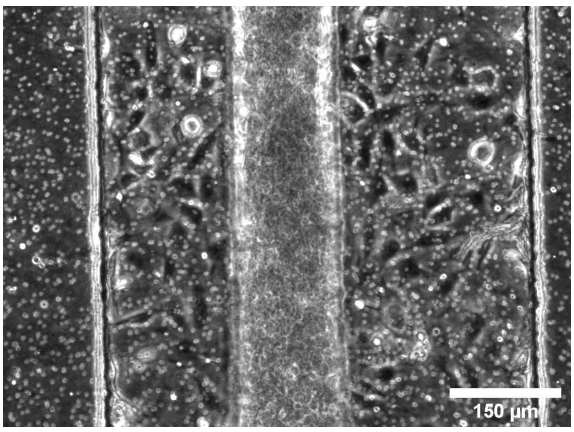

Figure 3.12 Endothelialization of cardiac µ-tissues. Phase-contrast image of a centrifugal HoC hosting mvECs in the medium channel. The 3D tissue strand (Cor.4U®, d14, center region) is co-cultured with an overlying mvEC monolayer (seeded on d6, broad outer channel). Figure adapted from Ref. [29] under CC BY 4.0 license.

ing cardiac tissue culture in the centrifugal HoC for six days, microvascular endothelial cells (mvECs) were seeded into the media channel. Upon subsequent combined culture, mvECs attached to the membrane, forming an additional biological barrier on the membrane surface opposite of the cardiac tissue (Fig. 3.12).

3.3.2 Tissues formed from spheroids

Following spheroid injection, introduced spheroids generally fused within one day, forming one coherent tissue inside the microphysiological system. During the first day, media was only supplied via the tissue injection channel. We investigated the spheroid fusion process during the first 24 h via time lapse microscopy and compared the tissue formation from CM spheroids with FB spheroids in uncoated chips (Fig. 3.13 A, B). For both spheroid types, cells solely attach to each other, forming an aligned tissue. After 24 h, individual spheroids are no longer distinguishable. Tissues formed from FBs are characterized by a more homogeneous tissue boundary. Furthermore, we compared tissue formation from CM spheroids in an uncoated device and a system coated with fibronectin (Fig. 3.13 A, C). The uncoated chip is characterized by pure spheroid fusion, whereas coated chips display spreading of individual spheroids with a preferred attachment to the coated side walls. Compared to $t = 1\,\mathrm{h}$, where individual spheroids can be distinguished by a sharp boarder, individual spheroids can not be located anymore after one day in the coated chip. Regions of varying tissue density can be observed, most likely originating from individual spheroids. However, no clear boarder exists anymore. Thus, individual spheroids fused also in the coated sample, displaying less pronounced tissue alignment.

Generally, the microphysiological system lead to a change in tissue morphology

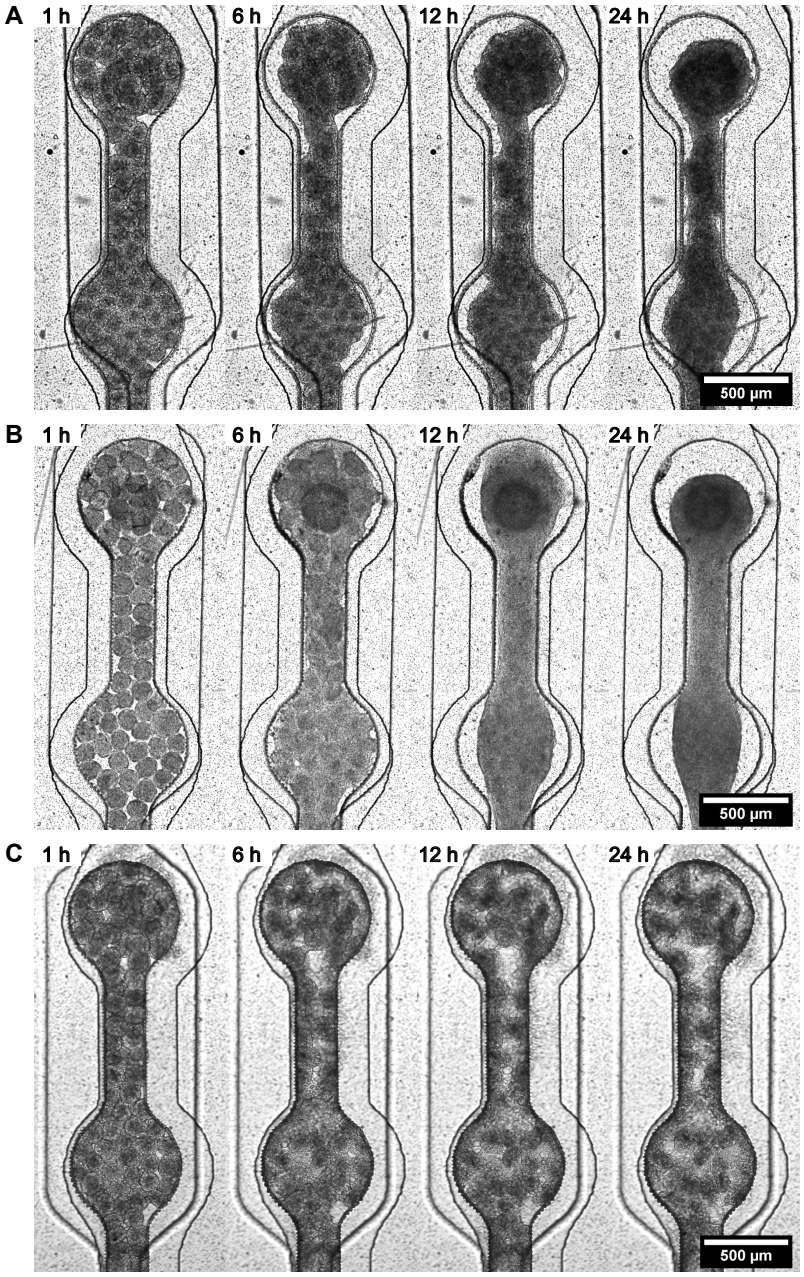

Figure 3.13 Time-lapse video microscopy of tissue formation inside Spheroflow-HoC. **(A)** Tissue formation from CM spheroids in an uncoated chip. Spheroids favor compaction rather than spreading out and adhering to the chamber. **(B)** Tissue formation from FB spheroids in an uncoated chip. Tissues compact similar to A, featuring a more homogeneous tissue boundary. **(C)** Tissue formation from CM spheroids in a chip coated with fibronectin. Spheroids spread out and attach over the surface of the whole tissue chamber. (A) adapted from Ref. [27] under CC BY-NC 4.0 license.

of initially round spheroids. As starting point, mixtures of hiPSC-derived CMs and phDFs (3:1 cell number ratio) were centrifuged into inverted microwells and reliably aggregated within 24 h, yielding spheroids of homogeneous size ($d \approx 150\,\mu m$) (Fig. 3.14 A). Investigating the morphology of fused tissues in the Spheroflow-HoC via immunofluorescence staining, an alignment of cTnT fibers along the main axis of the dog bone shape is observed (Fig. 3.14 B). Stacked layers of nuclei can be identified along the z direction, verifying the generation of a 3D tissue. Hence, cells of individual spheroids reorganize, forming a single aligned cardiac fiber out of initially individual µ-tissues.

To demonstrate the broad applicability of our developed platform to merge individual spheroids into an aligned tissue of defined shape, we also injected spheroids formed from phDFs into the Spheroflow-HoC. Phalloidin staining reveals an alignment of the cytoskeleton parallel to the shaft orientation (Fig. 3.14 C). Analogous to formed cardiac µ-tissues, individual phDF spheroids are no longer distinguishable, one coherent fibroblast tissue with dog bone shape is generated.

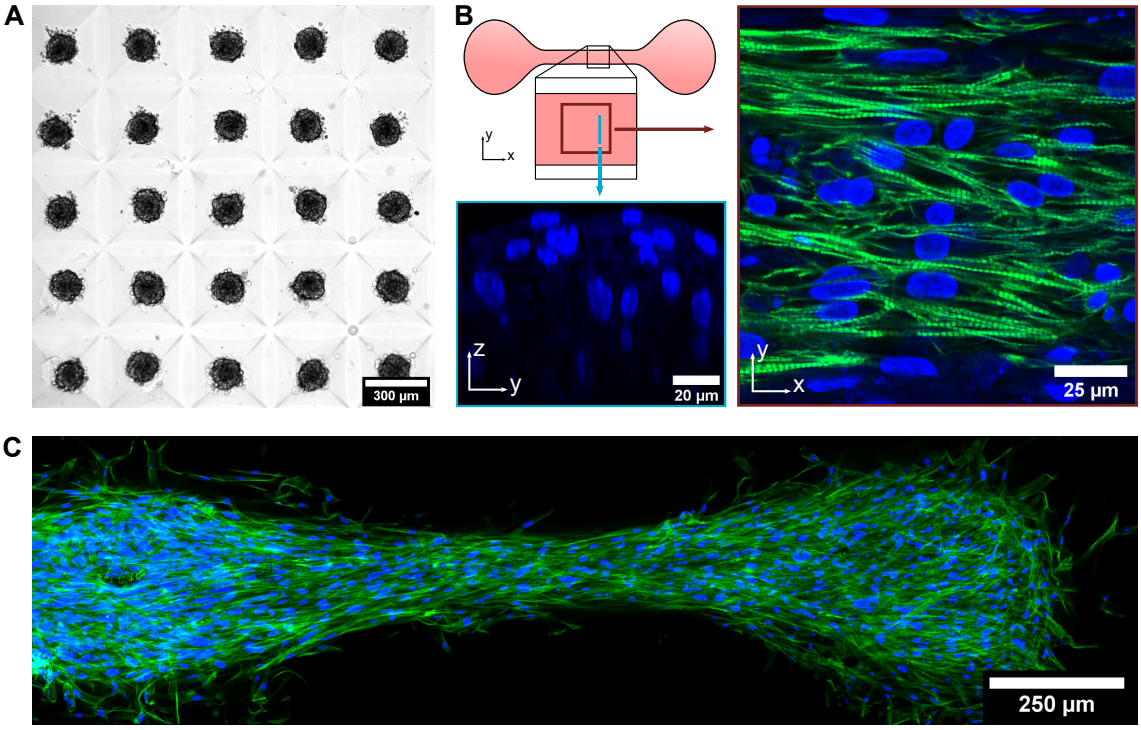

Figure 3.14 Characterization of µ-tissues formed in Spheroflow-HoC. **(A)** Defined generation of uniformly sized cardiac spheroids in microwells. **(B)** Physiological validation of generated cardiac muscle fiber by immunostaining of cTnT (green) and DAPI (blue). The shaft region is characterized by aligned fibers (xy slice). The perpendicular z-stack view reveals stacked nuclei, indicating the generation of a multilayered 3D tissue (yz slice). **(C)** Immunostaining of Phalloidin (green) and DAPI (blue) of an aligned tissue merged from spheroids of phDFs. Figure adapted from Ref. [27] under CC BY-NC 4.0 license.

3.3.3 Discussion

One majoar goal in cardiac tissue engineering is the recapitulation of a physiological muscle fiber alignment. By constraining introduced single cells and spheroids in both platforms to dog bone-shaped tissue chambers, generated tissues feature pronounced alignment, as indicated by aligned sarcomeres in the shaft region of the tissue chambers. Thus, the HoCs accurately mimick the micro structure abundant in native cardiac tissue. Media perfusion provided a sufficient diffusive supply of nutrients in both HoCs, maintaining tissue functionality. Compared to static culture with distinct media exchanges, human physiology is mimicked more closely in both systems. The presented opportunity to include an endothelial layer leads to an improved emulation of human physiology and can be directly integrated into developed HoCs.

Cell loading through centrifugation with an acceleration of $a_c = 400 \times g$ for 10 min did not induce evident adverse effects on loaded cells and led to viable tissues. Introduced singularized cells merged to one beating tissue unit, confirming the applicability of deployed injection and culture concept. Tissues could be cultured in the HoC for a time span of more than one month, indicated by a viable beating motion and verified by live/dead staining. The potential of long-term cultures opens up the possibility for future studies aiming at creating advanced, matured, hiPSC-derived cardiac µ-tissues on chip, constituting a physiologically more relevant model system.

One drawback of the implemented chip fabrication approach is the relatively thick bottom layer ($d > 1$ mm), requiring a disassembly of the media module for high resolution imaging, potentially disrupting cultured tissues. However, as the cell injection and tissue generation concept is universal and not bound to our realized PDMS-based fabrication, the chip design could be easily transferred to other fabrication processes. By, e.g., utilizing a resin-based tissue layer stencil on a cover slip, optimal imaging conditions can be provided, enabling a detailed structural investigation of intact tissues.

We provided proof-of-concept on how to further increase the physiological relevance of developed HoC by lining the medium channel-facing surface of the PET membrane with endothelial cells. By integrating an endothelial barrier, biological transport processes are recapitulated more closer to *in vivo* conditions. The developed platform thus enables the study of co-cultured cardiac tissues and influence of an endothelial layer. To assess the integrity of formed barrier and influence on signaling properties in future studies, the media layer can be perfused with a fluorescent dye and the fluorescence intensity assessed in the tissue chamber. So far, the co-culture was carried out with CM media. To achieve satisfactory long-term culture, the media composition should be adjusted for both cell types. ECs were so far introduced following complete cardiac tissue formation, yielding varying conditions of the endothelial barrier during culture. It is also conceivable to initially form and culture the barrier tissue and introduce CMs in following steps. However, required chip centrifugation during loading might impede formed endothelial layer.

Time lapse recordings of Spheroid-HoCs confirm the merging of individual

spheroids into a tissue of dog bone shape. Thus, the newly developed approach of harnessing individual µ-tissues for the generation of a fused tissue of defined shape is validated.

One benefit of developed tissue generation approach is the defined loading process, based on the precisely controllable generation of homogeneous spheroids. By introducing a scalable intermediate spheroid formation step outside the chip, a huge number of spheroids can be produced with minimal effort in a parallelized process. With employed approach of forming spheroids in microwells, a reliable generation of spheroids with uniform size could be verified. $N = 1200$ spheroids can be simultaneously generated in one well, allowing the formation of $N = 24$ aligned cardiac tissues ($N \approx 50$ spheroids per tissue in the Spheroflow-HoC) after injection into the chip. By introducing these spheroids instead of singularized cells, the building blocks for aligned tissues are also 3D, such that only a re-organization between individual spheroids instead of a complete merging of densely packed single cells has to occur.

One drawback of implemented approach is a reduced filling of the tissue compartment, contrary to a loading with single cells. Due to the spherical shape of introduced spheroids, a full packing is not feasible, leading to dead space between individual spheroids even considering slight spheroid deformation during loading. As spheroids subsequently merge and further compact, the compartment is not entirely filled. Compared to a fully filled chamber, the fluid dynamical properties of the system are modified, potentially allowing an increased media flow through the membrane into the tissue compartment. Nevertheless, the additional flow might be beneficial for a better supply with nutrients, adding a convective nutrient delivery component to the diffusive supply. However, flow in the tissue compartment might also influence tissue functionality in undefined ways. In order to protect the tissue after compaction from shear forces, it is conceivable to inject and subsequently polymerize a hydrogel in the tissue chamber, filling the void. As the hydrogel allows a diffusive transport of nutrients, the original system configuration can be restored.

Although the envisioned application and future development of the platforms most likely be focused on hiPSCs because of their immense potential for disease modeling and personalized medicine, we confirmed the compatibility of presented systems with other cell types. We successfully generated cardiac µ-tissues based on primary rat CMs by centrifugal loading and cultured them in the centrifugal HoC [29]. We also injected spheroids assembled from FBs into the Spheroflow-HoC, yielding aligned tissues and thus confirming the universal applicability of developed approach. We are therefore confident, that both chip concepts can be further adapted to even other cell and tissue types.

Tissues formed in both HoCs were not shaped as free-standing fiber attached to the substrate in the knob region. Although substrate attachment is essential for sensing of forces via TFM, generated tissues still compose a satisfactory model system for other applications such as drug testing. However, it is unclear how long-term culture of non-adherent tissues influences tissue viability in the HoCs. Although centrifugal HoCs were coated with fibronectin prior to loading, distinct substrate attachment indicated by spreading of cells at the tissue edge could not be asserted. It

is more likely that the tissue predominantly compacts towards the chamber center and is fixed by the narrowing region in the knob areas. Coupled with the elongated chamber shape, this fixation can lead to observed structural alignment. The comparison between coated and uncoated Spheroflow-HoCs revealed a spreading of spheroids in coated samples. As tissues formed in coated centrifugal HoCs displayed tissue compaction without predominant adhesion similar to uncoated Spheroflow-HoCs, we conclude that the coating is insufficient in the centrifugal HoC. Insufficient coating might be caused by different protein adhesion on thermoplastic and PDMS substrates and could be improved by an additional substrate functionalization [260]. As fibronectin is highly susceptible to shear stress, coating via centrifugation and subsequent centrifugal loading might also lead to observed deteriorated adhesion.

For the generation of a free-standing fiber solely adhering at both knob regions, improved coating procedures are inevitable. Coating only the knob region could help in anchoring the tissues while avoiding complete spreading, leading to the formation of a free-standing fiber. As the chip comprises an enclosed system after fabrication, targeted coating of individual regions is not straightforward, requiring the investigation of novel fabrication concepts.

3.4 Optical analysis of beating kinetics

Functional µ-tissues could be optically distinguished by their noticeable beating motion. Thus, as initial non-invasive tissue analysis, brightfield video microscopy was used to quantify beating kinetics. We developed the open source software OpenHeartWare[1] (OHW) for an analysis of beating kinetics from recorded videos and characterized kinetics of cardiac µ-tissues cultured in the centrifugal HoC and Spheroflow-HoC platform.

3.4.1 Optical flow analysis framework

Videos of beating tissues were analyzed via an optical flow motion tracking algorithm similar to previous approaches [261–265]. Implemented optical flow analysis is based on block matching. Thereby, each recorded frame is divided into a grid of square blocks of fixed size w_b (Fig. 3.15 A, i, ii). To determine the space-resolved motion between video frame i and a successive frame $i+d$, the position of each block in frame i is determined in frame $i+d$. The best matching position is obtained by comparing pixel values of the block in frame i with values in frame $i+d$ in close vicinity of the original block location. The original block is compared with blocks shifted by a maximum shift s in each direction (Fig. 3.15 A, iii). By comparing all frames with corresponding frames shifted by d, the space- and time-resolved displacement field $\mathbf{u}(x, y, t)$ is obtained.

The algorithm is implemented in the Python-based program OHW[1] which offers a user-friendly gui, enabling simple processing of recorded videos (Fig. 3.15 B). After

[1] https://github.com/loslab/ohw

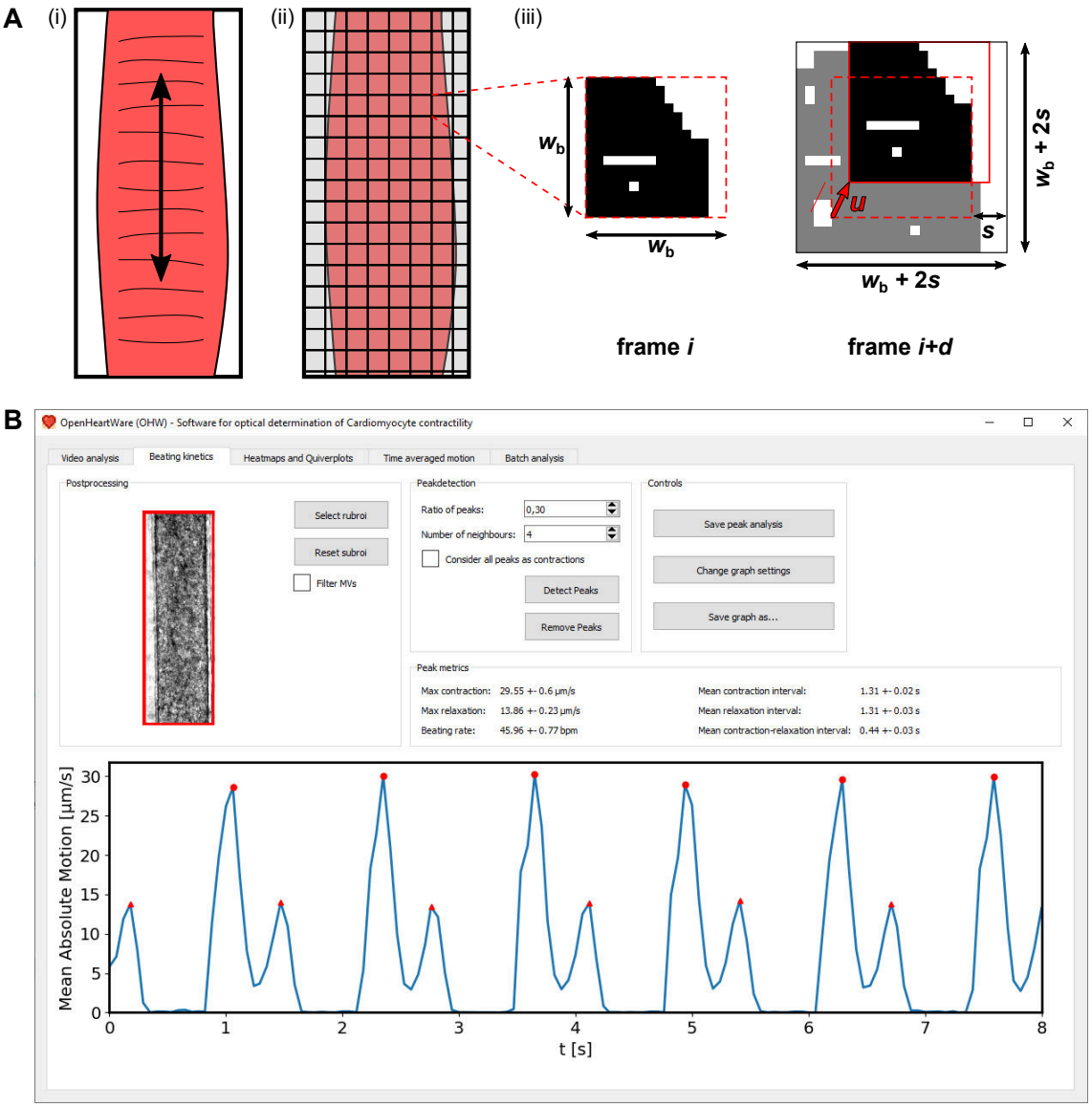

Figure 3.15 Extraction of beating kinetics from video microscopy via block matching. **(A)** Concept of employed block matching algorithm. (i) Frames of recorded videos of beating tissues are (ii) divided into blocks of fixed size w_b. (iii) For each block in video frame i, the best matching block in consecutive frame $i + d$ is determined, investigating a search window of size $w_\mathrm{b}+2s$. From obtained matching block, the displacement field $\mathbf{u}(x, y, t)$ is extracted. **(B)** Gui screenshot of developed analysis software OHW. Following analysis with adjustable parameters w_b, s and d in a chosen roi, the evaluation of motion vectors yields detailed tissue beating kinetics. The beating frequency can be determined following automated peak detection.

video import, individual block matching parameters block width w_b, frame delay d, and search range s can be set. Additionally, the software allows a region of interest (roi) selection and a downscaling of the input video for faster processing. The soft-

ware uses the OpenCV[2] package, providing access to fast image analysis operations, relying on optimized C code. Furthermore, OHW offers a batch mode, enabling an unattended analysis of multiple experiments. OHW saves obtained raw vector fields, allowing a later post-processing or the selection of sub rois without a necessary recalculation of motion vectors. Obtained vector field is used as starting point for further motion analysis. By spatially averaging the motion, 1D beating kinetics are obtained which can be utilized to precisely determine the beating frequency (Fig. 3.15 B, bottom part of gui screenshot).

3.4.2 Beating characterization

We recorded videos of beating cardiac µ-tissues cultured in the centrifugal HoC and analyzed them with OHW. Obtained time-dependent displacement vector field $\mathbf{u}$ serves to characterize and compare beating patterns of individual tissues and can be overlain to the raw video recording to visualize the beating behavior more clearly (Fig. 3.16 A; Vid. 1, 2).

During all phases of periodic contraction and relaxation, the coordinated movements in tissue regions could be monitored accurately against the non-moving background. For further analysis of the spatial distribution of beating in tissues, the displacement velocity was averaged temporally over the complete recorded time frame and decomposed into its x and y movement components (Fig. 3.16 B, C). A spatial distribution of average displacement velocities ranging from $\bar{v} = (1\text{–}4)\,\mu\text{m/s}$ could be determined in the tissue. Comparisons of x and y movements revealed a clearly dominating y movement in the shaft region, confirming creation of a physiologically relevant, uniaxially beating tissue strand.

The beating velocity was further spatially averaged and evaluated as a function of time, resulting in a periodic beating pattern in which contraction peaks and beating frequency could be detected with ease (Fig. 3.16 D). An exemplary analysis of the beating behavior of the hiPSC-based µ-tissues (GM25256) at day 2 ($f = (0.40 \pm 0.01)\,\text{Hz}$) and day 28 ($f = (0.79 \pm 0.01)\,\text{Hz}$) shows an increase of the beating frequency to a physiological range (Fig. 3.16 C; Vid. 1, 2).

To verify the independence of individual µ-tissues within one chip, pairwise videos were recorded of neighboring tissues on a chip hosting seven µ-tissues (Cor.4U®) on day 5 (Fig. 3.17). Thereby, individual beating kinetics could be related to each other. All tissues beat within the same physiological range of $f = (0.75 \pm 0.03)\,\text{Hz}$. Neighboring tissues are, however, not synchronized in their beating behavior as contractile peaks occur at different time points (Fig. 3.17; Vid. 3).

Functional characterization of the system was performed by treatment with the selective β-adrenergic agonist, isoproterenol. The perfusion medium was supplemented with isoproterenol (1 µM) and delivered through the medium channel. Beating kinetics extracted by means of optical flow of a representative µ-tissue (GM25256) after six days of culture, before, during, and one day after isoproterenol treat-

[2]https://opencv.org/

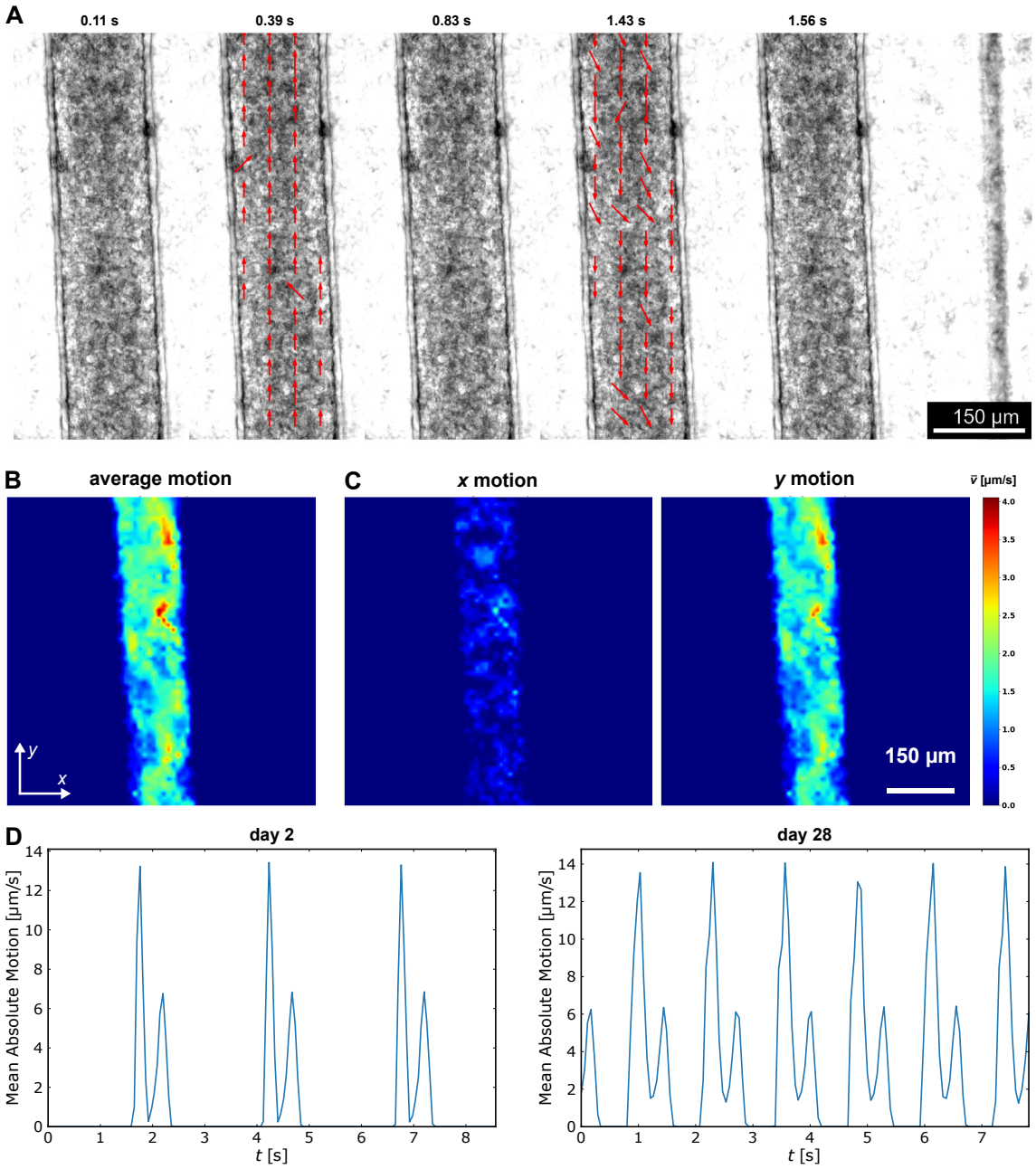

Figure 3.16 Analysis of beating pattern based on video microscopy (GM25256, d6). **(A)** Quiver plots at various time points illustrating the space-resolved tissue movement indicated by red arrows. At $t = 0.39\,\mathrm{s}$, a predominantly parallel downward motion is observable, whereas at $t = 1.43\,\mathrm{s}$, the tissue contracts again in the opposing direction. **(B)** Heat map expressing the time-averaged absolute tissue movement, revealing tissue movement in the complete shaft. **(C)** Heat maps of the decomposed absolute tissue movement for x and y movements indicating a predominant direction of contraction along the channel axis (y-axis). **(D)** Beating kinetics of the investigated tissue on days 2 and 28, revealing an increase in beating frequency. Figure adapted from Ref. [29] under CC BY 4.0 license.

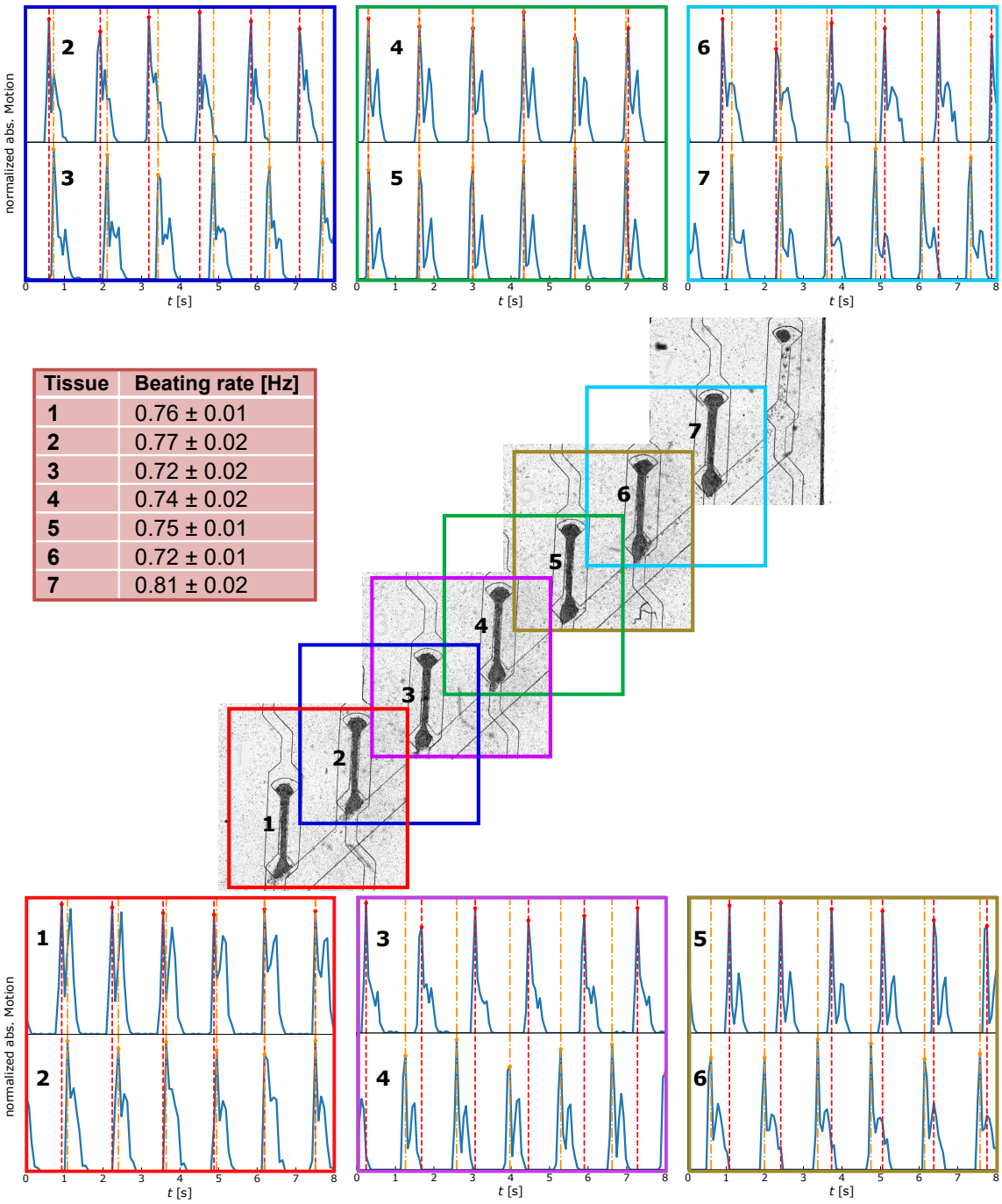

Figure 3.17 Correlation between generated µ-tissues. Stitched image of a centrifugal HoC on day 5, hosting seven hiPSC-derived cardiac µ-tissues (Cor.4U®). In each colored region, the beating behavior of two neighboring tissues is analyzed simultaneously using video microscopy and depicted pairwise for comparison (top and bottom). In each panel, peak positions are marked for comparison (upper peaks: red, lower peaks: orange). All tissues display an independent beating behavior decoupled from their neighbor as their contraction peaks do not overlap. Individual beating rates lie in a close physiological range of $f = (0.75 \pm 0.03)$ Hz (left center). Figure adapted from Ref. [29] under CC BY 4.0 license.

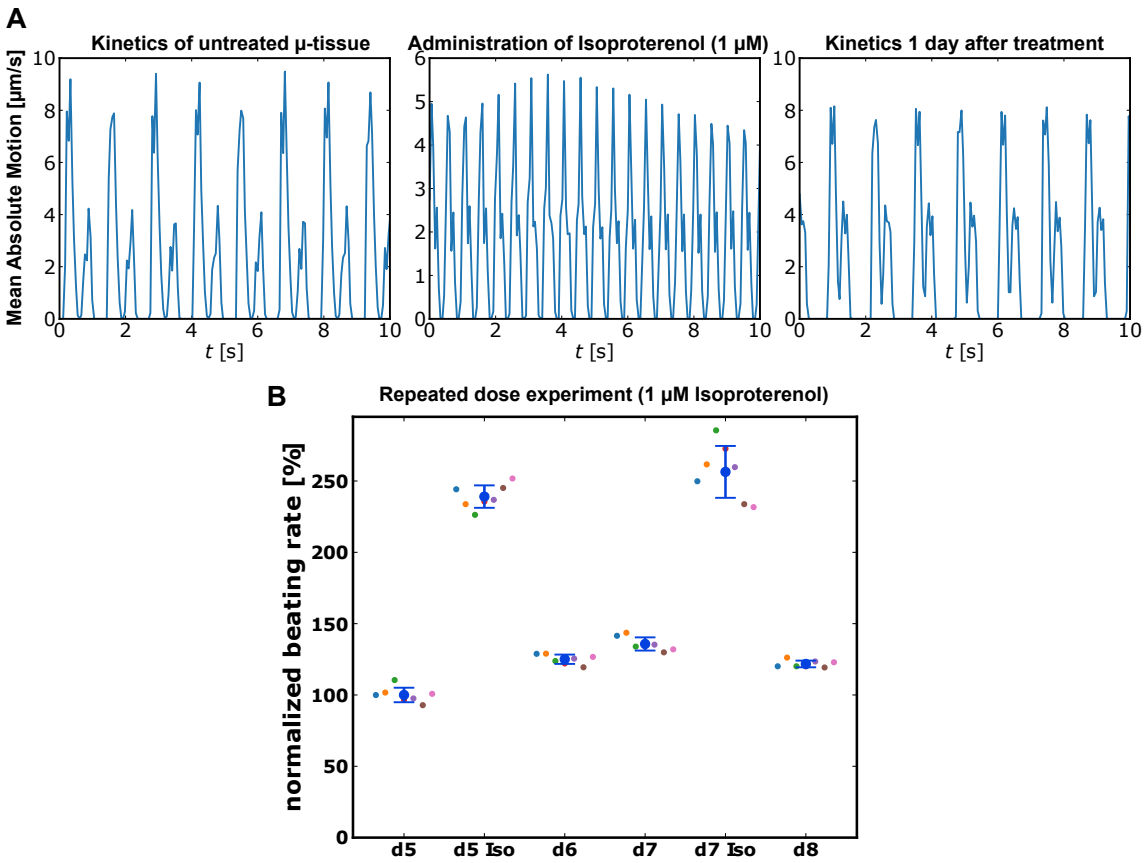

Figure 3.18 Drug testing in hiPSC-derived cardiac µ-tissues. **(A)** Beating kinetics extracted by optical means of a µ-tissue (GM25256) before and during administration of 1 mM isoproterenol (recorded 5 min after inclusion of isoproterenol into the medium, both day 6), as well as one day after drug administration. An increased beating rate can be clearly recognized after drug administration, indicating the suitability of the system for compound testing. **(B)** Optically extracted beating rate from seven tissues (Cor.4U®) within one chip, normalized to the mean beating rate on day 5. Individual tissues as well as the mean values are depicted. Isoproterenol (1 µM) was administered on days 5 and 7 through the culture media. Isoproterenol treatment results each time in a pronounced beating rate increase with a decline to physiological beating rates on the following day. Figure adapted from Ref. [29] under CC BY 4.0 license.

ment, revealed an initial increase in the beating frequency and subsequent recovery of baseline beating after washout: the beating frequency increased within 5 min from $f = (0.77 \pm 0.02)$ Hz to $f = (2.00 \pm 0.05)$ Hz, representing an increase by $f/f_0 = (160 \pm 12)$ %, and relaxed on the following day to the initial beating frequency again (Fig. 3.18 A; Vid. 4, 5, 6).

In a repeated dose experiment, isoproterenol (1 µM) was administered on days 5 and 7 after loading to a chip hosting seven functional µ-tissues (Cor.4U®). The

beating frequency was measured for each individual tissue before and 5 min after drug administration, as well as after washout of the drug in the unperturbed state on days 6 and 8 (Fig. 3.18 B). Isoproterenol administration on day 5 led to an increase in relative beating frequency to $f/f_0 = (239 \pm 8)\,\%$, which relaxed to $f/f_0 = (125 \pm 3)\,\%$ (day 6) and $f/f_0 = (136 \pm 5)\,\%$ (day 7). Subsequent drug administration led to an increase to $f/f_0 = (256 \pm 18)\,\%$, which relaxed to $f/f_0 = (122 \pm 2)\,\%$ (day 8).

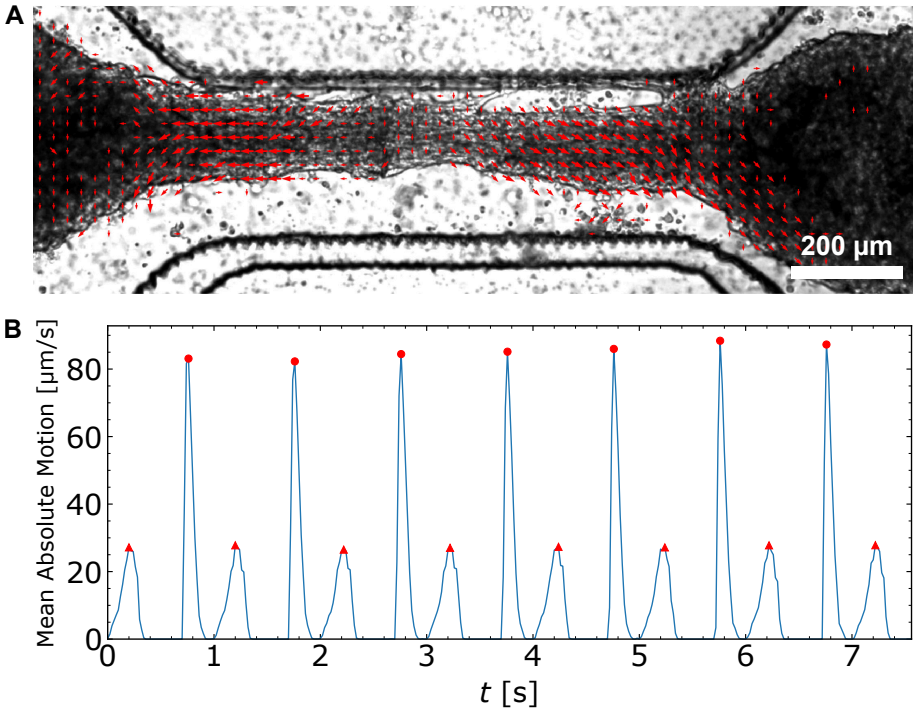

Figure 3.19 Optical analysis of beating kinetics of a µ-tissue merged from individual spheroids inside the Spheroflow-HoC. **(A)** Characterization of beating motion in cultured fiber. Motion vectors at time point of tissue contraction reveal a collective displacement. **(B)** Optically determined beating kinetics, amenable for further beating frequency extraction (circle: contraction, triangle: relaxation). Figure adapted from Ref. [27] under CC BY-NC 4.0 license.

We analyzed videos of beating µ-tissues formed from injected spheroids in the Spheroflow-HoC with OHW. Extracted time-dependent vector field revealed a collective synchronized motion without distinguishable individual spheroid beating (Fig. 3.19 A). Antiparallel motion can be observed at both ends of generated fiber. Spatially averaging the beating motion, a 1D representation of beating kinetics with distinguishable peaks of tissue contraction and relaxation is obtained, amenable for further beating frequency determination (Fig. 3.19 B).

3.4.3 Discussion

In addition to tissue generation, it is crucial to provide tools for investigating cultured tissues. The optical analysis of beating kinetics offers a non-invasive readout for the characterization of cardiac µ-tissues. We introduced an optical flow-based analysis framework, evaluated beating kinetics in both HoCs and demonstrated its application in drug testing studies.

Implemented algorithm accurately determines motion in videos of beating cardiac µ-tissues and can be used as initial non-invasive analysis for inter-chip comparison. The algorithm is sufficiently fast, i.e., the processing of 100 frames of size 1024×1024 px takes about 15 s. Processing times can be further reduced by downscaling the video or selecting an appropriate roi. Generally, implemented block matching approach is a brute force method with pixelwise block comparison, which scales with employed search range s by $\mathcal{O}[(2s+1)^2]$. For an even faster analysis, it is possible to constrain the search range to a defined subregion or to evaluate only a fraction of blocks at points of interest.

Alternatively, it is straightforward to implement other optical flow algorithms provided by OpenCV, such as Gunnar Farnebäck and Lucas Kanade, potentially speeding up the analysis due to an optimized algorithm implementation in C. If a spatially resolved motion analysis is not needed, e.g., for a bare determination of average beating frequency, it is conceivable to average intensity changes on pixel-level between subsequent frames, an approach which is applied in the frequently used ImageJ script MUSCLEMOTION [266]. An implementation of the analysis algorithm in Python is straightforward. Especially the utilization of vectorized operations on numpy arrays would yield speed improvements over the Java-based ImageJ application.

All in all, the developed software OHW offers a powerful framework for the analysis of videos of beating cardiac tissues. The gui enables simple access for users inexperienced in bioinformatics methods, empowering the focus on essential data analysis. Especially the batch functionality and storage of raw results, enables a productive workflow as the time-consuming analysis can be conducted over night, while maintaining the flexibility of a possible preceding manual post-processing. The modularized composition of OHW offers a seamless integration of other motion detection algorithms, such that a shared pipeline of video import, pre-processing, motion analysis, post-processing and export of results can be utilized, leveraging OHW to a valuable tool in cardiac tissue engineering.

We verified successful application of OHW for the analysis of videos recorded from cardiac µ-tissues cultured in the centrifugal HoC and Spheroflow-HoC. The beating motion, distinguishable by naked eye, could be accurately quantified, yielding a time-and space-resolved characterization. Tissue movement in the shaft region is aligned in parallel to the main axis of the chamber, validating the desired mimicry of a myocardial fiber with uniaxial contractile motion. The observed collective tissue motion in the Spheroflow-HoC indicates fusing of individual spheroids to a single µ-tissue. Thus, the optical analysis confirms the bottom-up tissue generation

approach, harnessing individual spheroids as building blocks for aligned cardiac tissues.

Measured beating velocities are of the order of magnitude of 10 µm/s comparable with other similar systems [23, 24, 256]. Although coinciding, absolute mean beating velocities determined by motion tracking should be interpreted with care, as they strongly depend on chosen analysis region. Non-moving areas next to the fiber or reduced displacements in the knob region obviously lower the average velocity. One possible solution would be to constrain the averaged region to only moving areas. However, this spatial filtering requires the determination of a cutoff velocity, already heavily influencing the mean beating velocity on its own, overestimating beating velocities. Nevertheless, spatial beating patterns, as well as beating frequencies can accurately be determined from a qualitative analysis of extracted motion vectors.

In the centrifugal HoC an increase in beating frequency to physiological values could be asserted over the timespan of four weeks, indicating viable tissue culture, coinciding with carried out live/dead staining. Although all tissues are fluidically connected in the centrifugal HoC via the tilted main channel, the pairwise analysis of neighbouring tissues confirms independence of cultured µ-tissues. Considering their beating motion as only endpoint, individual tissues are thus technical replicates.

Nevertheless, due to the close distance between cultured tissues, a potential cross-talk via signaling molecules can not be ruled out. The same cross-talk would also occur in a multiplexed Spheroflow-HoC with branched loading channel. One approach to further decouple neighbouring tissues could be the injection and polymerization of hydrogel in the loading channel, following cell loading and tissue formation. Although hydrogel would still allow a diffusive transport of signaling factors, the diffusivity is lowered compared to a direct connection via a liquid media phase. Still, individual tissues are linked via the shared media supply. However, as the media channel is continuously perfused, factors secreted through the membrane into the media channel are actively transported downstream at a faster rate than passive diffusion, such that a cross-talk via the media channel can be ruled out.

As proof-of-concept for application in drug testing, an increase in beating rate as a response to administration of isoproterenol was observed, similar to previous studies [105]. Despite the media module being fabricated out of PDMS, the administered drug was washed out and the chip could be further investigated on following days, demonstrating its use as long-term testing platform. Drug testing in a resin/thermoplastic-based Spheroflow-HoC would further benefit from reduced drug absorption in the tissue compartment. Compared to other microphysiological systems solely integrating one tissue unit per chip, the centrifugal HoC directly provides the statistical evaluation of eight tissues in one integrated module. Generating the same amount of datapoints in single-unit devices would require considerably elevated efforts, especially considering the necessity for individual media supplies.

Due to the comparatively low number of $N \approx 12\,500$ required cells per individual µ-tissue unit, the system could be easily scaled up to perform drug testing even on a much larger scale, with more doses and/or drugs, exploiting the benefit of multiple replicates within one chip. As neighbouring tissues can be simultaneously

monitored in the field of view at 4× microscope magnification, two tissues can be directly compared without the need of rearranging the microscope position. By modifying the media supply in future chip iterations, providing an individual supply for each tissue, adjoining tissues could thus be cultured under varying conditions with a direct and synchronized readout.

The optical analysis framework requires no additional laboratory hardware other than a microscope, providing a user-friendly initial tissue characterization capability. By placing multiple chips in a motorized microscope stage, videos of tissues could be successively recorded in an automated manner, yielding, e.g., 10 s long videos at 1 h intervals for each tissue of up to $N = 360$ tissues ($10\,\mathrm{s} \times 360 = 1\,\mathrm{h}$). OHW enables the automated determination of beating frequencies from recorded videos or even on-the-fly, facilitating the screening of multiple tissues in a medium throughput setting.

So far, our developed system provides only optical readouts of cultured tissues. The following chapters focus on the integration of additional on-chip sensing and stimulation capabilities. However, more advanced tissue analyses are frequently conducted by specialized instruments which require direct access to the biological sample. Modifying the geometry of the centrifugal HoC by adding an inlet channel to the dead-end tissue chamber would allow a defined on-demand tissue extraction. Individual tissues could be flushed out into the main channel and collected at the loading port. Thus, advanced off-chip biological analysis can be performed, e.g., single cell sequencing.

Chapter 4

Integration of sensing

The following sections discuss functional integration of sensing capabilities into OoCs. We focus on the investigation of key parameters in cardiac tissues, namely contractile forces and O_2 consumption. The integration of luminescent O_2 sensor spots into resin-based OoCs has been previously published in "Schneider, O. *et al.* Fusing Spheroids to Aligned µ-Tissues in a Heart-on-Chip Featuring Oxygen Sensing and Electrical Pacing Capabilities. *Mater. Today Bio* **15,** 100280 (2022) [27]".

4.1 Integrated force measurements

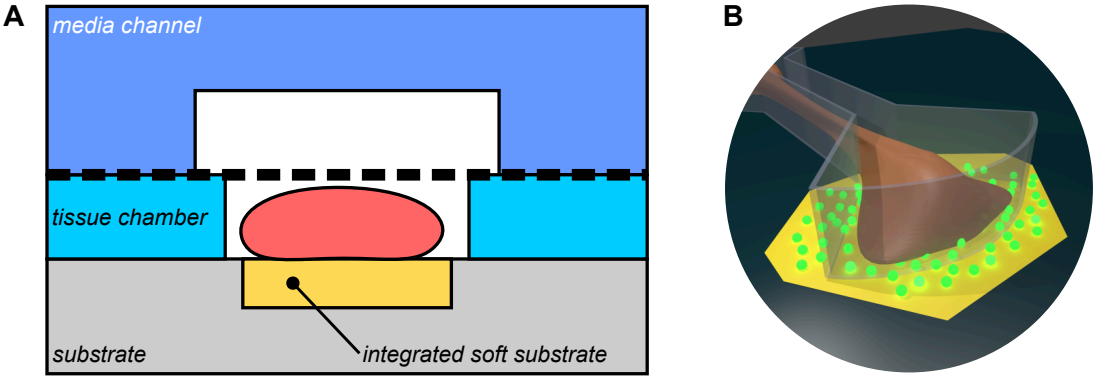

Figure 4.1 Blueprint of modified chip composition enabling integrated TFM measurements. **(A)** Side view of individual layers. An elastic pad of defined mechanical properties (yellow) is integrated into the chip substrate and the tissue (red) cultured on top. **(B)** Schematic of finalized system. The µ-tissue is anchored on the soft pad and pad deformations, caused by the tissue beating motion, are tracked with help of fluorescent beads deposited on the surface.

We investigated capabilities to integrate TFM-based force sensors into established HoC systems. Generally, it is necessary to integrate a soft substrate into the chip

which is in direct contact with cultured tissue (Fig. 4.1 A). Hence, compared to fabrication concepts employed for bare tissue generation, the tissue chamber should encompass a stencil topology with an open top and bottom, allowing both media supply from the top and contact with the soft substrate on the bottom. To integrate force sensors with established bonding protocols, the soft substrate should be constrained to the tissue chamber region, allowing unchanged bonding properties of layers next to the soft substrate. Considering the lateral channel arrangement, the concept of TFM pads requires no changes in channel features of established chip design. Generally for TFM, it is necessary to integrate force sensing pads predominantly in the knob region as utilized dog bone shape aims to create an anchored fiber adhering in the knobs (Fig. 4.1 B). Fluorescent beads attached to the soft substrate allow tracking of pad deformations induced by tissue contractions, which can be subsequently used to determine contraction forces.

4.1.1 Pad fabrication concepts

For accurate determination of contraction forces, a reliable integration of a soft pad into the substrate is crucial. The pad should especially be constrained to the tissue chamber, featuring a defined height and flat surface. We developed and investigated three different methods for the fabrication of integrated force pads.

Integration into PDMS substrates

For the integration of soft pads into PDMS substrates, pads are designed as microfluidic channels featuring a filling inlet and outlet. Substrates were molded from wafer masters and filling ports punched (Fig. 4.2 A). To provide a removable sealing of pad channels which does not disrupt the soft polymer after curing, a sacrificial layer was spin coated onto a silicon wafer. By placing the substrate with the channel side facing down onto the sacrificial layer, the injection channel is closed. We additionally heated the sacrificial layer, which enhanced the channel sealing [267]. Prepolymer of the soft substrate was deposited into the inlet port with a pipet tip. The absence of pressure during prepolymer injection prevents any shifting or lifting of the PDMS stamp. Capillary and hydrostatic forces fully filled the channel. Following polymer curing, the whole assembly was immersed in DI water, leading to a dissolution of the sacrificial layer, excavating the substrate with integrated soft pads. Substrates could be reliably fabricated and were used for subsequent chip fabrication in section 4.1.2.

Integration into thermoplastic substrates

We further investigated the integration of soft pads into rigid thermoplastic substrates (Fig. 4.2 B). Similar to PDMS substrates, pads are designed as connected channels with polymer injection ports. We embossed channels into the substrate and drilled access ports. The open pad channel was sealed with a water-soluble

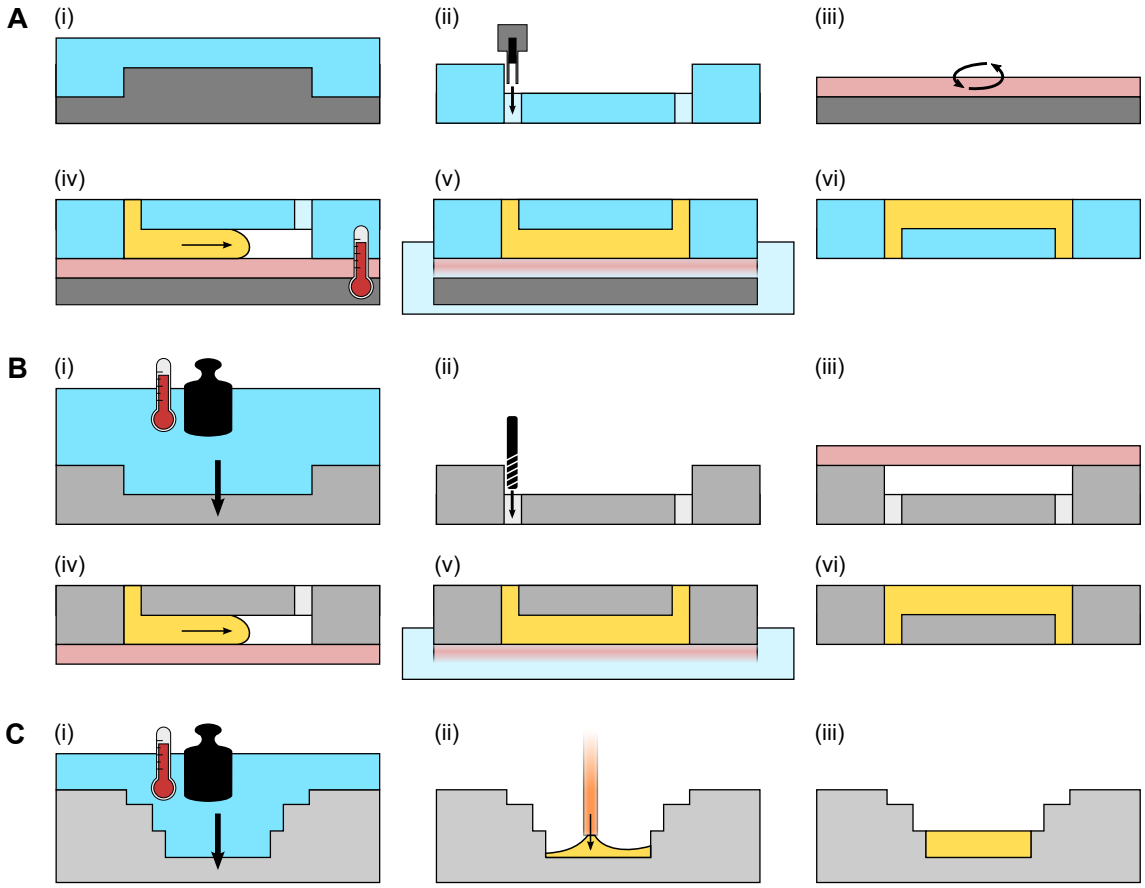

Figure 4.2 Investigated fabrication approaches for the integration of soft pads into microfluidic modules. **(A)** Capillary filling of PDMS channels. (i) Pad channels are molded with PDMS. (ii) Inlets are punched and (iii) a sacrificial layer is prepared by spin coating. (iv) The chip is placed onto the heated sacrificial layer, prepolymer is injected and fills the channel. (v) After the sacrificial layer is released in water, (vi) a structured PDMS substrate with integrated pads is obtained. **(B)** Capillary filling of hot embossed thermoplastic channels. (i) Pad channels are fabricated by hot embossing and (ii) access holes are drilled. (iii) Channels are sealed with a water-soluble tape as sacrificial layer and (iv) prepolymer is injected, filling the channel. (v) Following sacrificial layer release in water, (vi) a structured thermoplastic substrate with integrated pads is obtained. **(C)** Soft substrate injection into embossed cavities. (i) Pad grooves and tissue channels are embossed into the thermoplastic substrate in a combined step. (ii) Prepolymer is injected into the groove with a CNC glue dispenser, yielding a (iii) structured tissue channel with integrated soft pads.

poly(vinyl alcohol) (PVA) tape, acting as sacrificial layer [268, 269]. Optical investigation of utilized water soluble tape revealed an inhomogeneous, speckled surface, which, however, emerged from the non-adhesive backside, as verified by focusing on both surfaces in widefield microscopy. Subsequently, soft PDMS prepolymer was

added into the inlet and wicked into the pad channel. After polymerization of the soft pad, the water soluble tape was released by submerging the assembly in DI water, yielding an exposed soft pad. Substrates could be reliably fabricated and were used for subsequent chip fabrication in section 4.1.2.

Injection of soft pads

For both presented approaches, the pad fabrication relies on a sacrificial layer and polymer injection step. As further simplified alternative, we investigated a direct deposition of polymer into pad cavities (Fig. 4.2 C). By simultaneous hot embossing of multiple layers, spatially confined grooves for soft pads as well as channel features can be integrated into a thermoplastic substrate. Precisely injecting soft PDMS prepolymer into the pad cavity, only the pad is filled, yielding soft pads inside desired channel geometry. This approach requires a precise control of deposited volume, as insufficient or excessive filling could result into a non-planar surface.

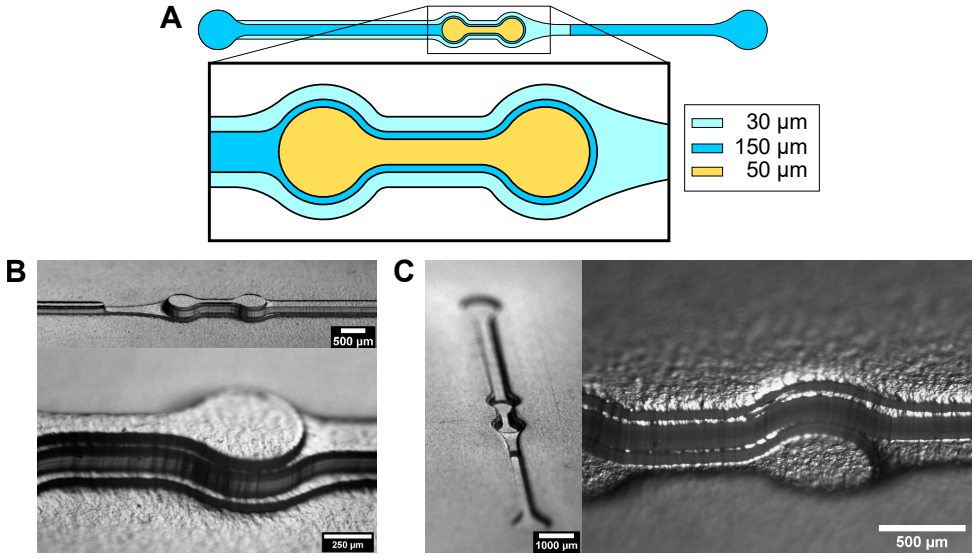

Figure 4.3 Hot embossed substrates for polymer injection. **(A)** Chip design of Spheroflow-HoC with integrated force sensing pads. Top view indicating embossed features of various heights (yellow: pad, dark blue: tissue chamber, light blue: constriction). **(B)** Multilayer PDMS stamp, replicated from 3D-printed master. **(C)** Structures embossed with PDMS stamp into PET-G substrates. The multilayer geometry is reproduced.

We investigated the integration of soft pads by direct polymer injection in the Spheroflow-HoC tissue layer. The chip substrate is designed to include a force sensing pad region, the loading channel, and the constricted side channel (Fig. 4.3 A). All layers could be fabricated simultaneously by hot embossing with a PDMS stamp molded from an SLA-printed master (Fig. 4.3 B, C). The rough surface of the SLA master is reproduced in the embossed substrate and a smooth transition between individual layers can be observed.

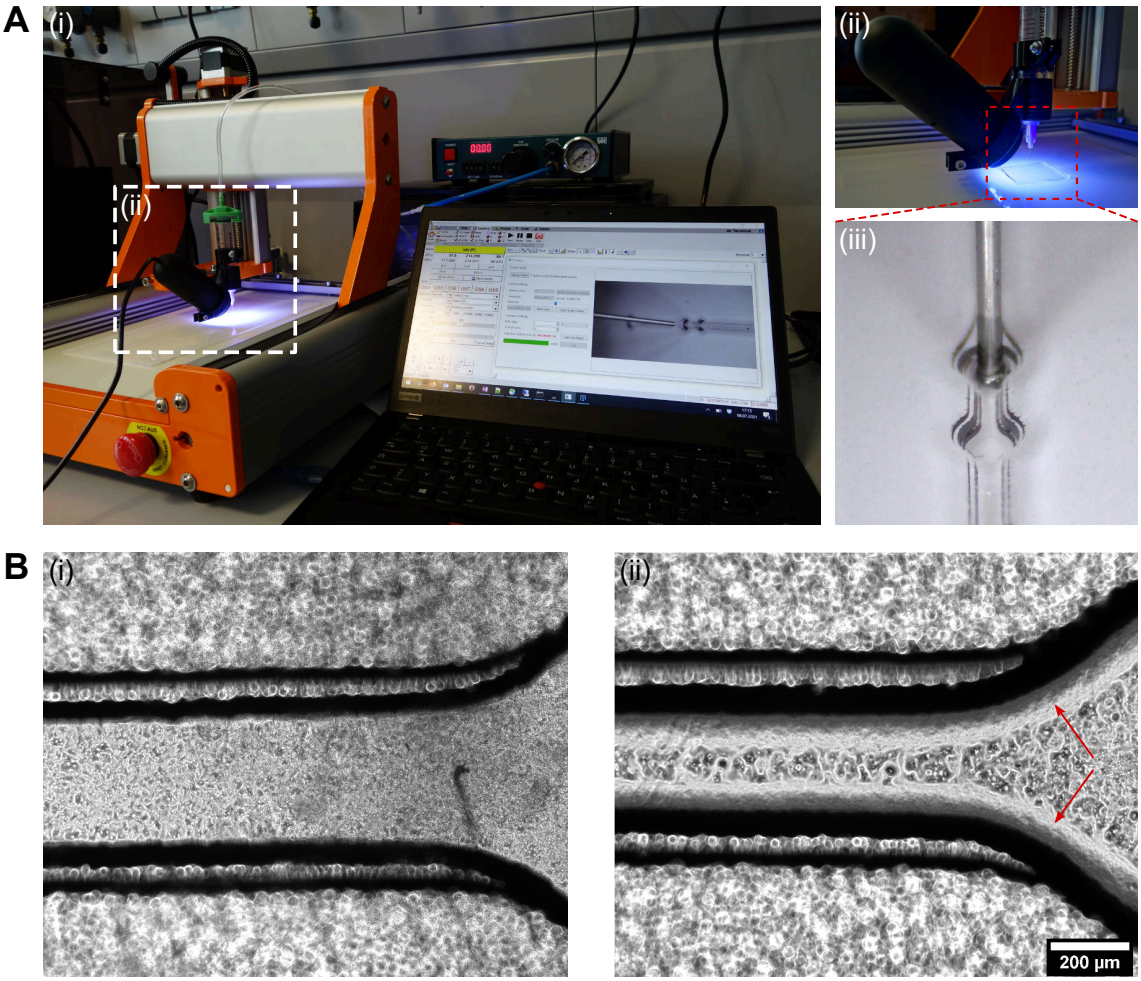

Figure 4.4 Fabrication of soft pads via polymer injection. **(A)** (i) Experimental set-up for defined polymer deposition. (ii) A customized 3D-printed camera & syringe holder is added to a CNC table. (iii) The assembly allows precise deposition of prepolymer into thermoplastic substrates utilizing a pneumatic glue dispenser. **(B)** Comparison of inlet regions. (i) Filled substrate. (ii) Unfilled substrate. Although only the pad in the tissue region was filled, prepolymer is wicked into the main channel (indicated by red arrows).

To allow precise deposition of soft PDMS prepolymer into the pad groove, we modified a commercial CNC machine and attached a 3D-printed holder to the translation stage. The customized holder allowed the mounting of a 10 ml syringe and a USB microscope (Fig. 4.4 A). After attaching a glue dispensing tip to the syringe and topping up the syringe with prepolymer, the syringe was inserted into the holder. The syringe can be precisely positioned with the CNC machine on top of the soft pad while the actual position is simultaneously verified by integrated camera. A glue dispensing controller allows the application of defined pressure pulses, ejecting prepolymer into the cavity.

After filling of the cavity, monitored with the integrated camera, the polymer was cured at elevated temperatures. Considering the tissue channel inlet region where no PDMS should be deposited, we identified soft PDMS along the channel edge from comparison between filled and unfilled substrate (Fig. 4.4 B).

4.1.2 Chip integration

PDMS-based force chips

We investigated the integration of PDMS-based force sensing substrates into the centrifugal HoC. To enable contact between cells in the tissue compartment and the soft pad, PDMS stencils were fabricated (Fig. 4.5 A). Briefly, PDMS prepolymer was poured onto the same wafer masters utilized for established centrifugal HoC fabrication and covered with a foil. The assembly was clamped to exclude any polymer between structures and foil and PDMS cured at elevated temperatures. Fabricated PDMS layer adheres to the foil and can be transferred and bonded to PDMS media modules. After foil removal, the assembly was plasma-bonded to a PDMS substrate with integrated pads covered with beads. Fabricated device fulfills the blueprint of a multilayer microphysiological system with soft pads integrated into the tissue chamber.

We integrated pads into the centrifugal HoC hosting a single branched main channel as well as a tilted main channel with multiple branching tissue chambers (Fig. 4.5 B + C). To account for potential changes in mechanical properties of the soft substrate influenced by employed fabrication protocol, each chip additionally integrates a gauging channel which can be used to determine the individual elastic modulus of each device. As the soft substrate undergoes the same treatment in the gauging channel and tissue chamber during fabrication, we consider it as sufficiently accurate approximation of elastic properties in force sensing pads. We studies approaches integrating soft pads only in both knob regions of the tissue chamber, as well as a full coverage of each tissue chamber. For all designs, pads could be reliably filled with soft PDMS and chips fabricated. We further successfully injected cells by centrifugation into fabricated chips, leading to dense compaction in dog bone-shaped tissue chambers on top of a soft substrate with linked fluorescent beads, amenable for the determination of contraction forces (Fig. 4.5 B, inset).

We identify the fabrication of tissue layer stencils out of PDMS as bottleneck in developed chip design. In most cases ($\geq 90\,\%$), PDMS is not completely excluded from the wafer structures, leading to the formation of a thin membrane covering the channel. A covered channel prevents proper attachment of cells to the substrate and following force measurements. Vice versa, bonding the tissue stencil to the substrate first would result in porous membrane coverage, preventing necessary nutrient supply. Devices were thus freed of the membrane by manual scratching with a dentist probe, rarely leading to perfectly free channels and a high variability in chip fabrication (Fig. 4.5 D).

We frequently observed penetration of cells into the soft pad filling channel during centrifugal cell injection, leading to uncontrolled loading (Fig. 4.5 E).

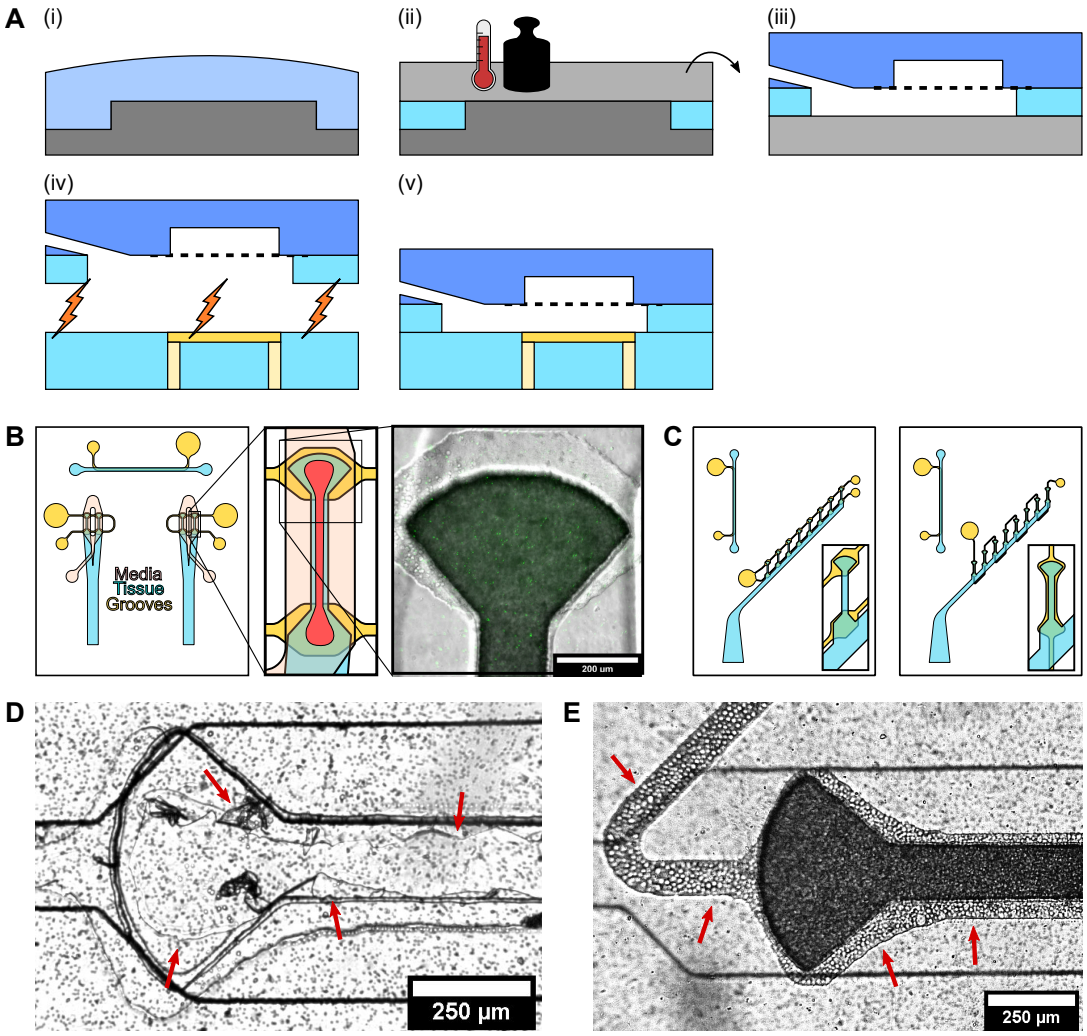

Figure 4.5 PDMS-based force sensing HoC. **(A)** Schematic of fabrication steps: (i) PDMS prepolymer is cast on the patterned wafer. The mold is covered with a foil and tightly clamped to exclude any PDMS covering the structures. (ii) The polymer solidifies at elevated temperatures and adheres to the clamped foil. (iii) The media module with bonded membrane is attached to the tissue module. (iv) After removal of the molding foil, the assembly is plasma treated and bonded to the PDMS substrate with integrated soft pads, (v) yielding a PDMS-based system enabling the perfused culture on a soft substrate. **(B)** Chip design of centrifugal HoC with integrated force sensors featuring two straight, branched loading channels. An additional straight gauging channel is implemented into the system. Pads are integrated into the knob region (zoom 1), functionalized with fluorescent beads (zoom 2), and cells are injected by centrifugation. **(C)** Chip design of centrifugal HoC with integrated force sensors featuring eight tissue chambers branching from a tilted main channel. Pad injection channels are designed to cover both knob regions (left chip) or the whole tissue region (right chip). Each chip additionally comprises a straight gauging channel (top left). **(D)** Failed exclusion molding leading to partial coverage of the soft pad with PDMS (red arrows). **(E)** Spilling of cells into the pad injection channel (red arrows) during centrifugation-based cell injection.

Resin-based force chips

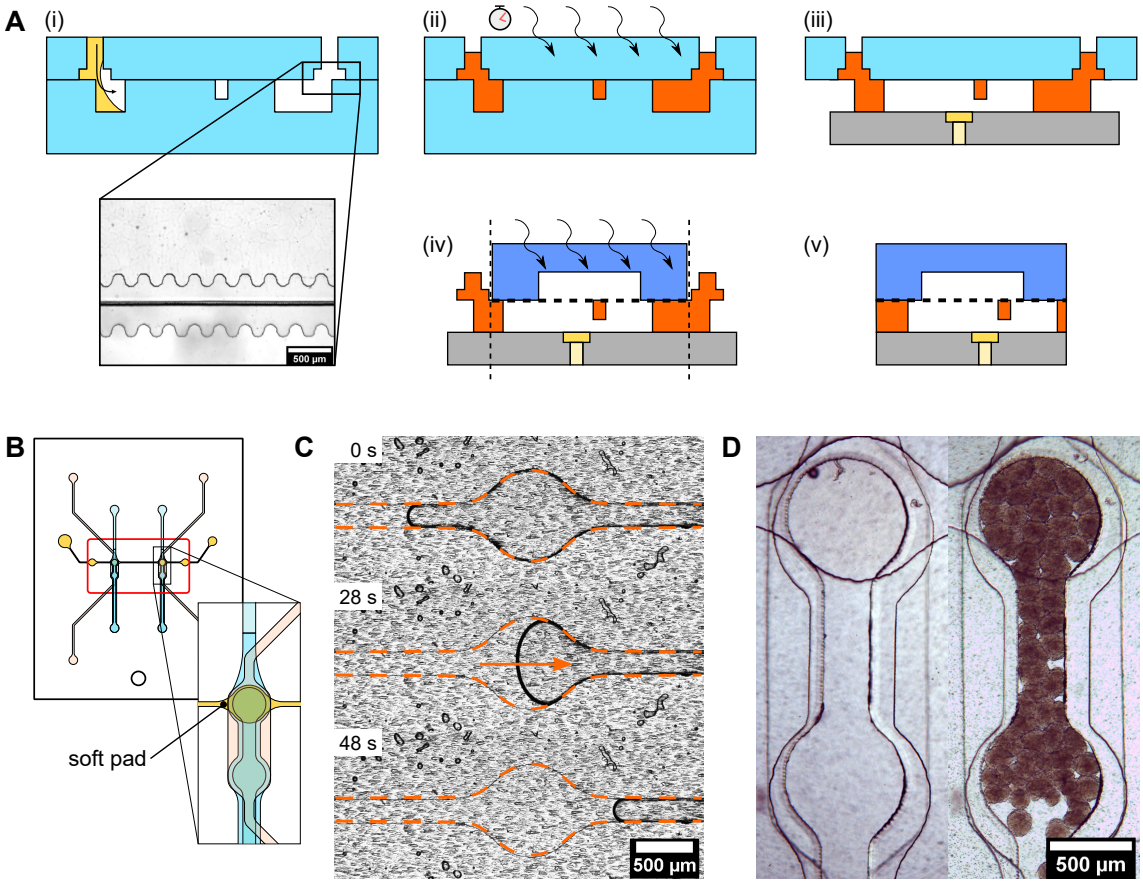

Figure 4.6 Hybrid thermoplastic/resin force sensing Spheroflow-HoC. **(A)** Schematic of individual fabrication steps. (i) The resin stamp is aligned onto a patterned bottom PDMS layer, ensuring subsequent release from stamp. (ii) Injected resin fills void completely after several minutes and is cured by UV exposure. (iii) The stamp is removed and patterned resin is placed onto bottom layer integrating force pads. UV exposure bonds resin layer to substrate. (iv) The media layer with bonded membrane is added onto patterned resin and bonded by UV exposure. (v) Finalized chip after cropping overlapping layers and final curing. **(B)** Top view of Spheroflow-HoC with integrated force pads. Pads are integrated into the second knob in flow direction. **(C)** Capillary filling of embossed force pads. Within several minutes, pad channels are filled with the prepolymer by capillary-driven flow. **(D)** Finalized chip featuring a tissue layer with constricting side channel, force pad in the knob region, and an overlying media channel enabling perfusion. Empty chip (left) and chip after spheroid injection (right).

We studied the fabrication of force sensing HoCs composed of thermoplastic substrates with integrated pads and resin-based tissue layers. Contrary to tissue layers fabricated from PDMS, the investigated approach does not involve a plasma treat-

ment step of the soft substrate. Initial resin molding protocol directly added the stamp and molded the resin on top of the substrate. In order to prevent any disruption of the soft substrate due to contact with the stamp, we implemented a fabrication protocol which seals the resin mold with a PDMS layer (Fig. 4.6 A). Initial molding trials on an unstructured PDMS substrate lead to detachment of the polymerized resin layer from the PDMS substrate with predominant adhesion to the stamp, caused by embedded stamp structures. Therefore, we added a microstructure to the PDMS substrate consisting of a shallow frame overlapping the chip edge of the molding stamp (Fig. 4.6 A, inset). By patterning the edge in a wave-like pattern, the contact area is increased, leading to satisfactory detachment of the stamp layer, allowing a transfer of molded resin stencil on the PDMS substrate to prepared force sensing layer. As the microstructured bottom layer is also composed of PDMS, a sticky layer is retained after initial exposure, allowing subsequent bonding to the force substrate. Subsequently, the transfer module could be removed, the media layer out of PDMS with bonded membrane attached and the bonding stabilized by a third UV exposure. Thus, functional devices fulfilling the prerequisite of embedded force pads were fabricated.

We implemented the fabrication protocol for the Spheroflow-HoC, allowing cell injection without centrifugation. The pad layer is designed as channel encompassing four pad regions, overlapping the rear knob of the tissue chamber (Fig. 4.6 B). Thus, pad substrates can be used in unbranched (two tissue chambers) and branched (four tissue chambers) designs. Following established protocols, pad channels could be embossed, sealed with PVA foil and reliably filled with soft PDMS prepolymer (Fig. 4.6 C). Succeeding tissue and media layer attachment, we verified successful loading with cardiac spheroids following established chip injection protocols (Fig. 4.6 D).

4.1.3 Sensor characterization

We fabricated gauging channels to characterize integrated soft pads via flow tests [158, 270]. The soft substrate is embedded as straight channel ($d = 50\,\mu m$, $w = 600\,\mu m$) into hot embossed thermoplastic substrates and a straight channel ($h = 50\,\mu m$, $w = 800\,\mu m$) molded out of UV curable resin is aligned on top (Fig. 4.7 A). An unstructured PDMS layer seals the chip, providing channel inlets. Fluorescent beads are deposited on the soft pad and the channel bottom. By perfusing the chip at defined flow rate Q, a precisely controlled shear stress τ is applied to the soft substrate. We determined corresponding substrate deformations by tracking beads for various flow rates (Fig. 4.7 B). As variations in a laminar flow profile are minimized in the central region, we considered only displacements of a $w = 300\,\mu m$ wide center region. From utilized channel geometry, applied theoretical shear stress $\tau(Q)$ is calculated from the flow rate according to eq. 1.3. By focusing on bottom and top bead layer, the exact pad height h is determined. In the following, the normalized mean displacement of all particles $\Delta x/d$ as a function of τ can be investigated (Fig. 4.7 C). We observe a linear relation between displacement and shear stress, displaying good agreement with a linear fit. From the fit slope we determine the

substrate elastic modulus, assuming a Poisson ratio of $\nu = 0.5$ [158]. From three investigated samples the elastic modulus is determined to $E = (4.0 \pm 0.2)\,\mathrm{kPa}$, considering the exact pad thickness for each sample (Fig. 4.7 D). Following drying of the channel, samples were exposed to O_2 plasma (60 s), mimicking utilized plasma sterilization protocol. Flow experiments were repeated for each sample, yielding $E = (4.3 \pm 1.1)\,\mathrm{kPa}$.

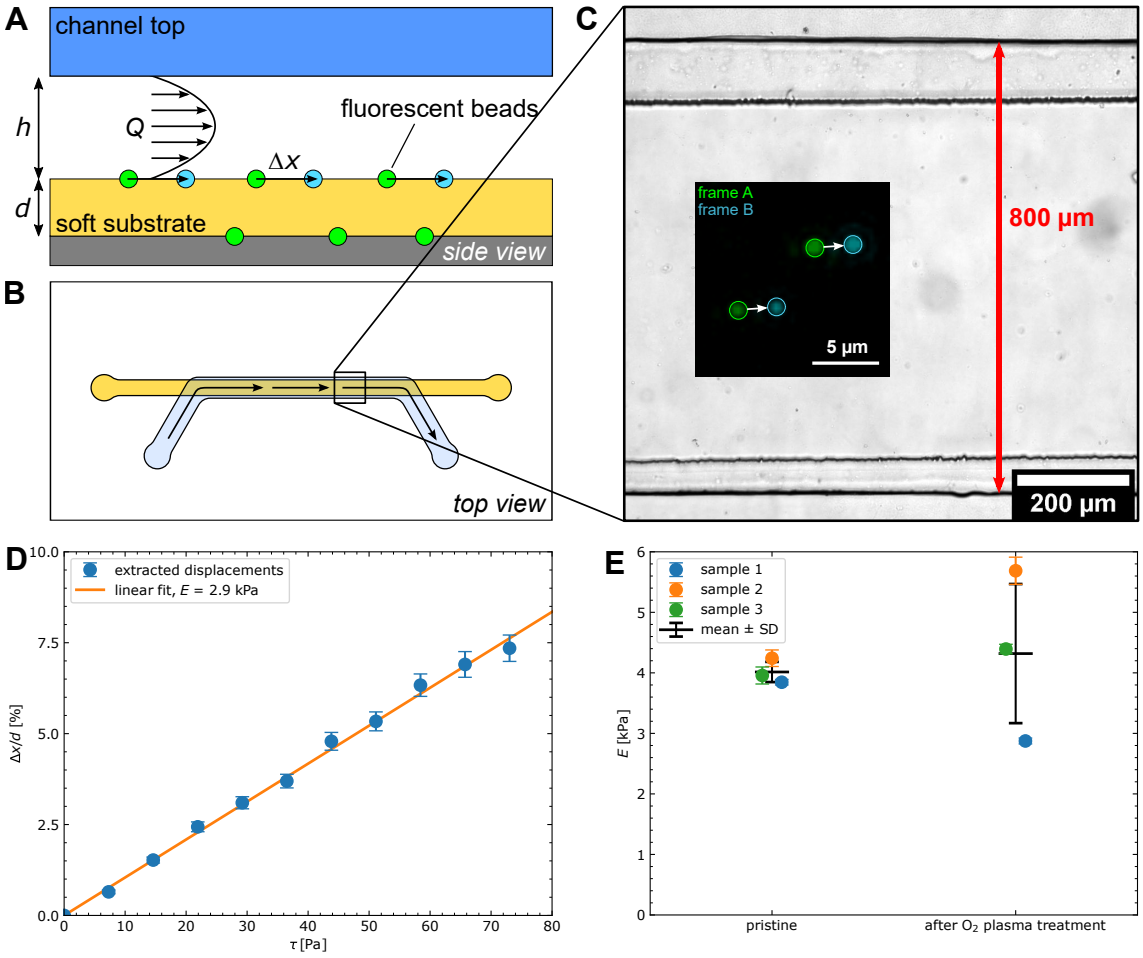

Figure 4.7 Flow tests for gauging of Young's modulus of integrated polymer. **(A)** Side view of channel geometry. The defined flow Q deflects beads on the polymer surface by Δx. With known channel height h and substrate height d, the elastic modulus can be determined. **(B)** Top view of channel geometry for flow tests. A straight gauging channel was added on top of the soft substrate. **(C)** Microscope image of fabricated testing chip. Deflected beads are shown for two frames obtained at different flow rates (inset, particle positions are highlighted with circles in corresponding color). **(D)** Linear fit to extracted mean displacements for particles tracked in the channel center as a function of applied shear stress. **(E)** Extracted elastic modulus from fits to displacements for untreated channels and channels after O_2 plasma treatment ($N = 3$, colors match the same sample).

4.1.4 Biological proof-of-concept

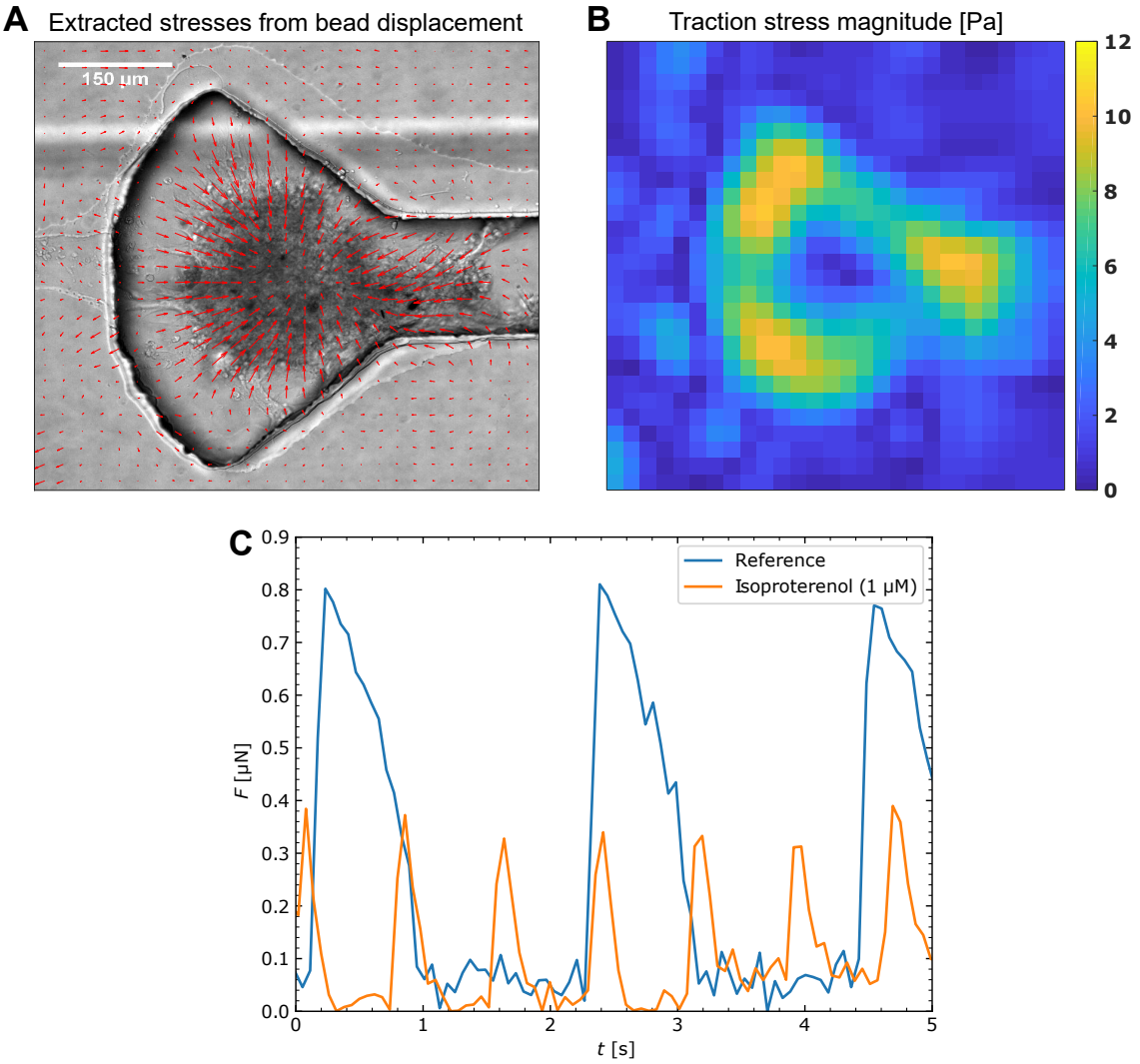

Figure 4.8 Biological proof-of-concept verifying integrated force sensing on cardiac tissues cultured in the PDMS-based centrifugal HoC. **(A)** Surface stresses extracted from bead displacements in the contracting phase, overlain on brightfield microscopy image. **(B)** Magnitude of traction stress from (A). **(C)** Time-resolved contraction forces, obtained from the integration of traction stress at each time point. Forces are compared for a tissue under media perfusion and subsequent isoproterenol treatment, indicating an increase in beating frequency, coupled to a decrease in force amplitude.

Succeeding cell injection into the centrifugal HoC comprising a branched geometry, tissues were cultured via media perfusion and adhered to integrated pads. Cultured tissues exhibit a pronounced beating motion, displacing substrate-adhered fluorescent beads. For a proof-of-concept analysis of contractile forces, we focus on a tissue chamber which was not fully filled during centrifugal loading, comprising a tissue in the knob region with visible beating towards the tissue center.

We recorded corresponding movement of integrated beads via fluorescence video microscopy and determine the time-dependent displacement field $\boldsymbol{u}(x, y, t)$ by linking particle positions between individual frames. Afterwards, the traction stress field $\boldsymbol{\sigma}(x, y, t)$ is calculated from extracted displacements and overlain on a brightfield frame at tissue contraction (Fig. 4.8 A).

The extracted displacement field indicates a tissue-related substrate deformation with displacements pointing towards the tissue center. Observed displacements decay in magnitude towards the edge of the tissue chamber. Considerably smaller displacements can be distinguished outside of the tissue chamber.

The traction stress magnitude reveals a similar pattern with maxima inside the tissue chamber, surrounding the tissue (Fig. 4.8 B). Traction stresses of magnitude comparable to the background are distinguished in the tissue center. We determine maximum traction stress magnitudes of $|\boldsymbol{\sigma}| \approx 10\,\mathrm{Pa}$.

Spatial integration of traction stress inside the tissue chamber enables the time-dependent investigation of summed up absolute contraction forces (Fig. 4.8 C, reference). We determine periodic contractions at $f = 0.5\,\mathrm{Hz}$ with maximum contraction forces of $F = 0.80\,\mu\mathrm{N}$.

Subsequently, the media channel was perfused with with the selective β-adrenergic agonist, isoproterenol. Following identical determination of traction stresses from recorded displacement fields, decreased contraction forces peaking at $F = 0.34\,\mu\mathrm{N}$ at a frequency of $f = 1.3\,\mathrm{Hz}$ are distinguishable (Fig. 4.8 C, isoproterenol). Hence, the tissue is beating faster at reduced peak force.

4.1.5 Discussion

The integration of soft pads into microfluidic environments is the prerequisite for TFM-based force measurements in HoCs. Chip architectures which enable direct contact of tissue and force sensing pad are needed, combined with fabrication concepts circumventing plasma activation of pads, potentially influencing mechanical properties. We investigated three pad fabrication approaches and combined two with the centrifugal HoC and Spheroflow-HoC. For an accurate determination of integrated pad Young's moduli, we characterized substrates by the application of defined shear forces and subsequently determined contraction forces within HoCs. All in all, introduced HoCs provide integrated force sensing capabilities, extending the informative value of current HoC models, frequently solely relying on beating frequency determination.

Pad fabrication We integrated force sensing pads by capillary filling into structured thermoplastic and PDMS substrates. By designing the pad as channel, multiple connected pads could be filled in one single step. Pads fulfilled the prerequisite of geometric confinement and, due to channel/stamp replication from a lithographically patterned wafer, defined height.

Both concepts rely on a sacrificial layer. The integration into PDMS modules requires spin coating of the sacrificial layer, resulting in a time-consuming fabrication,

aggravating a scaled up production. Furthermore, PDMS substrates are prone to small molecule absorption and careful handling protocols have to be implemented, preventing bending of the substrate which might impact integrated soft pads [271, 272]. Contrary, the integration into thermoplastic layers offers the benefit of a simplified fabrication. A clean-room fabrication step is not necessary for the formation of a sacrificial layer, as the water soluble tape can be directly purchased in sufficiently large quantities. Combined with the scalable process of hot embossing, a production in larger quantities is feasible. As most tedious step in current fabrication protocol we identify the manual drilling of access ports. All in all, the prevention of small molecule absorption, substrate rigidity as well as substrate thickness, highly favour pad integration into thermoplastic substrates. As remaining challenge for device reproducibility we identify the formation of air bubbles sporadically occurring during soft PDMS curing. Substrate curing in a vacuum oven could fully reduce air bubble formation in future implementations.

We further investigated direct polymer deposition into pad grooves, avoiding a sacrificial layer. Our approach directly integrates pad and channel structures via hot embossing into the substrate. Additionally, we presented the blueprint of a cost efficient apparatus for precise polymer injection with positioning step sizes of $\Delta r \approx 10\,\mu m$. Presented technique can be easily scaled up due to the hot embossing and automatable CNC deposition process. However, the pad fabrication is characterized by remaining challenges.

Injected prepolymer is not constrained to the pad region and could be detected in the tissue channel. This hints to creeping of injected prepolymer caused by surface phenomena. Enabled by smooth channel walls, the polymer can wet neighbouring layers and fill the channel edge, driven by capillary forces. Complete covering of the tissue channel is undesired for an application in microphysiological systems, as precise patterning is crucial for an accurate determination of forces.

As the diffuse layer edge originates from SLA printed masters, molding the embossing stamp from wafer masters with sharp edges could help in confining the polymer to the cavity. To further improve injection precision, glue dispensing tips of smaller outer diameter could be utilized (currently used: Gauge 30, $\varnothing = 300\,\mu m$, feasible: Gauge 34, $\varnothing = 190\,\mu m$), allowing the injection into features of reduced lateral dimensions. Furthermore, the opaque work surface of the CNC dispenser could be exchanged for a transparent PMMA layer, enabling the integration of an additional camera directly below the pad. Compared to current positioning approach which relies on a tilted camera view from which the exact needle position can only be estimated, a bottom camera would improve lateral positioning.

Chip integration We provided proof-of-concept for incorporating substrate-integrated force sensors into HoCs. PDMS substrates were integrated into the centrifugal HoC, thermoplastic substrates were integrated into the Spheroflow-HoC. Generally, the substrate integration is not coupled to a specific chip design.

PDMS-based integration yielded high variations in chip fabrication due to insuf-

ficient exclusion molding. As exclusion molding requires manual post-processing, it is not amenable for a production on a large scale. Generally, the integration of force sensing pads into a system designed for centrifugal loading is not recommended, as the soft substrate elasticity allows a filling of pad injection channels with cells. An adjustment of pad geometry to pads without injection channels or tailoring chip design to a flow-based injection could solve this issue. One drawback of employed fabrication protocol is a necessary plasma activation step of the substrate, potentially influencing mechanical properties of the soft substrate by creating a brittle surface.

The resin-based fabrication on a thermoplastic substrate prevents an additional plasma activation. However, implemented fabrication approach is considered rather tedious, as 3 exposure steps are required, potentially curing the resin before final exposure and degrading bonding strength. Furthermore, the stamp has to be removed with utmost care to prevent release and wrinkling of molded resin layer from the PDMS transfer substrate, impeding a scaled up production. As a plasma-free pad integration is combined with a reliable fabrication of tissue stencils, developed concept is preferred for prototype applications over a PDMS-based integration.

The defined injection of PDMS prepolymer represents the most scalable approach of investigated concepts but was not integrated in a HoC due to remaining challenges of reliable pad confinement. For sealing the chip following satisfactory pad injection, a media-membrane module has to be attached on top, which could be bonded via plasma-free chemical bonding.

Sensor characterization We were able to precisely determine mechanical properties of integrated soft substrate by means of flow tests. The elastic modulus, determined from linear fits to $E = 4\,\mathrm{kPa}$, corresponds in magnitude to the range of $E \leq 10\,\mathrm{kPa}$ frequently estimated in literature [273].

Measured value agrees well with the elastic modulus determined with AFM indentation by MacNearney *et al.* to $E = (4.6 \pm 0.6)\,\mathrm{kPa}$ as well as $E = (5 \pm 1)\,\mathrm{kPa}$, determined by Guo *et al.* via tensile testing [138, 157]. However, determined value is elevated compared to $E = (1.5 \pm 0.1)\,\mathrm{kPa}$, as measured by Moraes *et al.* via shear rheometry [156]. Generally, as the exact modulus is strongly influenced by each individual fabrication process, observed deviations are plausible. Direct integration of a gauging channel into the microphysiological system enables a precise determination of mechanical properties of each individual device or a batch control in future applications. As initial estimation we assume $E = 4\,\mathrm{kPa}$ for the determination of traction forces. The increase in elastic modulus variation after plasma treatment, determined to $\Delta E = 1.1\,\mathrm{kPa}$, agrees qualitatively with an increase in variability after 10 s plasma activation to $\Delta E = 2.5\,\mathrm{kPa}$, observed by MacNearney *et al.* [157]. Employed plasma activation time was elevated compared to MacNearney *et al.*, who observed an increase in elastic modulus of two orders of magnitude with increased treatment times. We attribute the observed reduced influence to a decreased penetration of O_2 plasma into the microfluidic channel and conclude that

short ($t \leq 60\,\mathrm{s}$) plasma treatments can be applied to increase channel hydrophilicity without drastically altering surface properties.

Biological proof-of-concept We provided proof-of-concept for the spatial and temporal determination of contraction forces in a HoC. Thus, the combination of OoC technology with the established technique of TFM is a feasible approach for integrated force measurements on physiological µ-tissues. Observed bead movements can be clearly attributed to tissue contractions, as they are localized in the tissue chamber. Upon isoproterenol injection, a decrease in contractile force coupled to an increase in beating rate could be determined, demonstrating the capability of developed force sensing HoC for drug testing studies.

For a rough comparison with contraction forces measured in other cultured cardiac tissues, we estimate the amount of introduced cells to $N = 5 \times 10^3$ cells, yielding a cell-averaged tissue force of $\bar{F} = 160\,\mathrm{pN/cell}$. Hirt *et al.* measured forces of $F \approx 40\,\mu\mathrm{N/tissue}$ on day 6 of culture for hiPSC-derived pillar-suspended tissues composed of $N = 0.5 \times 10^6$ cells, corresponding to $\bar{F} \approx 80\,\mathrm{pN/cell}$ [61]. Mannhardt *et al.* measured forces of $F \approx 150\,\mu\mathrm{N/tissue}$ on day 20–25 of culture for hiPSC-derived pillar-suspended cardiac tissues composed of $N = 1 \times 10^6$ cells, i.e., $\bar{F} \approx 150\,\mathrm{pN/cell}$ [79]. Zhao *et al.* obtained contractile forces of $F \approx 2.5\,\mu\mathrm{N/tissue}$ in tissues from hiPSC-derived ventricular CMs suspended between flexible horizontal wires composed out of $N = 1.1 \times 10^5$ cells, corresponding to an average force of $\bar{F} \approx 23\,\mathrm{pN/cell}$ [80].

Thus, comparing our findings with similar studies, a good agreement regarding magnitude of forces determined by TFM is observed. All in all, we verified a successful interaction of developed sensor system with biological systems. Presented measurement can be considered as biological proof-of-concept of developed sensor integration and loading framework.

However, fabrication complexity and low tissue generation rates, challenged a thorough study comparing multiple tissues. For a reliable scaled up study, an increase in device robustness is essential. Implemented fabrication protocol with challenges in PDMS stencil generation and the requirement of plasma activation (leading to changes in elastic modulus, discussed in subsection 1.2.1 and quantified in Fig. 1.3 B) should be improved for an increased device reliability. Force sensing in Spheroflow-HoCs fabricated on thermoplastic substrates via resin micromolding is evaluated coupled to electrical pacing in subsection 5.1.4.

4.2 Integration of O_2 sensors

As oxygen is one of the most important physiological key parameters in cell culture, we assess the suitability of directly integrating O_2 sensors into microphysiological systems, enabling *in situ* readouts.

4.2.1 Integration strategies

We focus in our studies on the integration of luminescent O_2 sensors, enabling contactless on-demand readouts once integrated into the chip. Analogous to integrated force sensing pads, close contact between sensor and tissue is desired for satisfactory measurement accuracy. However, as no mechanical transduction is involved, no direct contact has to be established; the major goal is sensing of key parameters in the tissue environment.

Resin-based integration

UV resin-based fabrication enables a reliable fabrication of open-sided stencil structures. We investigated direct molding of the Spheroflow-HoC tissue layer on top of a substrate integrating O_2 sensor spots on the surface. Contrary to force sensing pads, O_2 sensor spots are mechanically stable, such that the PDMS stamp can directly be placed on top of the sensor substrate, following developed fabrication approach described in subsection 3.1.2.

Satisfactory adhesion between substrate and deposited sensor spot is crucial for stable measurements over multiple days in microfluidic environments. We compared the integration of spots deposited on adhesion-coated PET foils with spots on glass substrates into established resin-based HoCs.

Integration in chips featuring PET substrates Sensor spots matching knob positions of the Spheroflow-HoC were deposited onto adhesion-coated PET foils. To promote subsequent attachment of resin, the substrate was O_2 plasma treated and functionalized with APTES. We added the structuring PDMS stamp on top, precisely aligning the channel structure to completely cover integrated sensor spots (Fig. 4.9 A). Sensor spots are visible as green dots by naked eye. Upon larger magnification, the sensor displays radial symmetry with imperfections in the center, hinting at slight variations in height. The deposited sensor spot is slightly reduced in size compared to the knob region, enabling complete sealing of the sensing area with the stamp. Hence, in following resin injection step, no resin should cover the sensor spot. Visual inspection revealed good adhesion of PDMS stamp to the foil, indicated by darker regions in the contact area, displaying a sharp contrast between covering channel and lifted constriction region (Fig. 4.9 A).

We fabricated Spheroflow-HoCs based on the previously established protocol from section 3.1.2, integrating the sensor spot into the tissue layer, sealing the chip with a porous membrane and the media module. Devices could be reliably fabricated without observable covering of the sensor surface with resin (Fig. 4.9 B).

Due to the thickness of employed PET foil (125 µm), chips fabricated on top should be amenable for high-resolution imaging. We imaged tissues cultured in chips assembled on PET sensor substrates using a LSM (Fig. 4.10 A). We observe aberrations, impeding proper investigation of tissue morphology.

For a characterization of utilized substrate, we recorded point spread functions

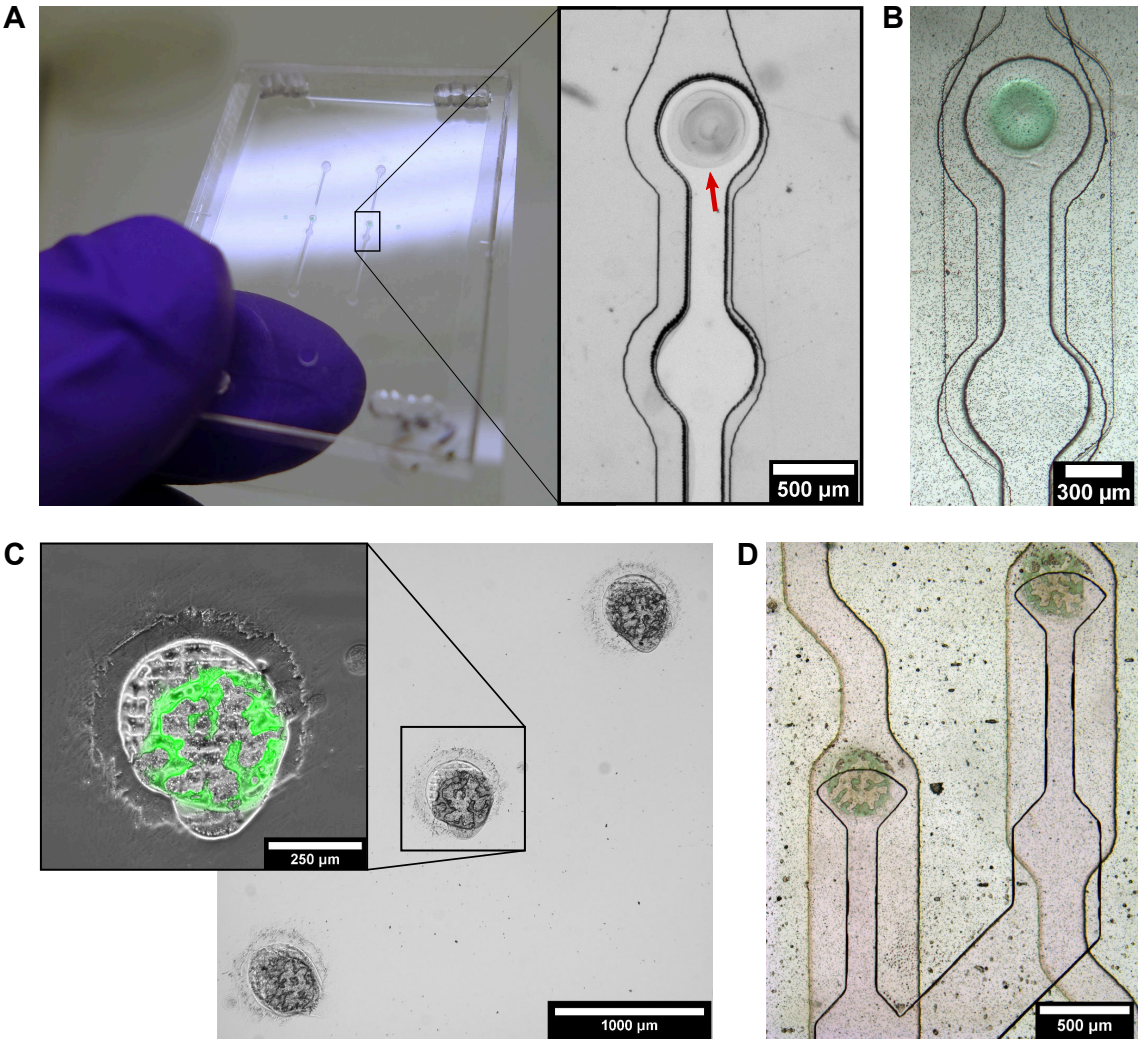

Figure 4.9 Integration of O_2 sensor spots into microphysiological systems by resin-based molding. **(A)** Integration of sensor spots on a PET foil. The PDMS stamp is placed on top of the sensor substrate, fully covering the sensor spot (zoom in, red arrow). **(B)** Finalized Spheroflow-HoC integrating the sensor spot in the knob region. Following resin micromolding, the PDMS-based media module with porous membrane is added on top. **(C)** Integration of sensor spots into glass substrates. The substrate is roughened at defined positions to ensure sensor adhesion. **(D)** Finalized centrifugal HoC integrating sensor spots in the knob region of each tissue chamber. (B) adapted from Ref. [27] under CC BY-NC 4.0 license.

(PSFs) of fluorescent beads deposited on top of various polymer foils (Fig. 4.10 B). PSFs were obtained from z-stacks of single beads, acquired through the substrate backside. We observe an asymmetry in the PSF of the sensor substrate employed for chip fabrication (coated PET, 125 µm) with two predominant radiation directions, deviating from an optimal PSF comprising radial symmetry. The asymmetry is also observed for a thinner adhesion-coated PET foil (50 µm). In comparison,

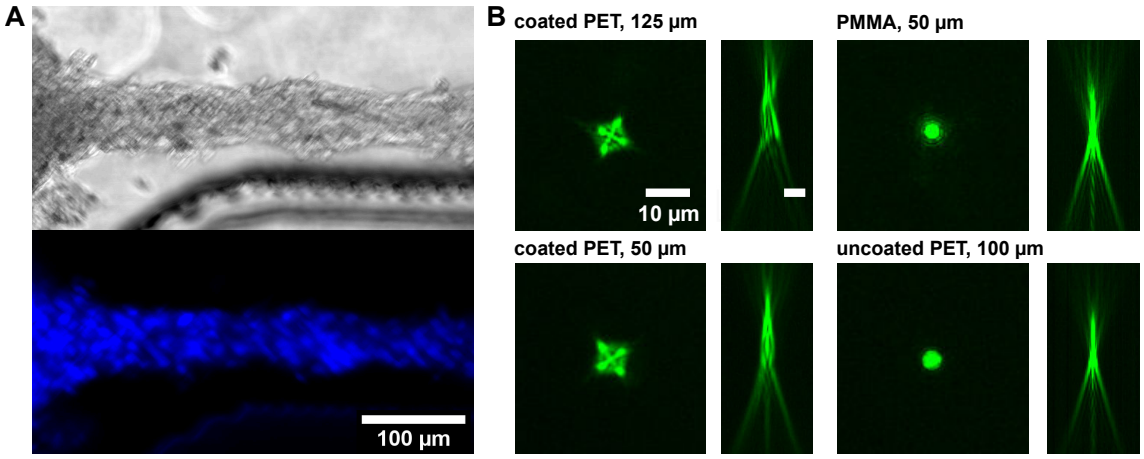

Figure 4.10 Imaging challenges with utilized PET sensor substrate. **(A)** Imaging of cardiac µ-tissue cultured in Spheroflow-HoC assembled on a PET substrate with integrated O_2 sensor spots. Image aberrations are observed in brightfield (upper panel) and in fluorescence imaging (lower panel, DAPI). **(B)** Comparison of point spread functions of different sensor substrates obtained from z-stacks recorded from deposited fluorescent beads ($d = 0.2\,\mu m$).

an uncoated PMMA foil (50 µm) as well as an uncoated PET foil (100 µm) yield symmetric PSFs, implying optimized imaging conditions.

Integration in chips featuring glass substrates For improving sensor adhesion on glass, microscope slides were roughened at defined sensor positions with a laser cutter by a cooperation partner (Tarek Gensheimer, University of Twente). Sensor positions are geometrically arranged matching knob positions of tissue chambers in the centrifugal HoC. Subsequently, sensor spots were deposited on top of roughened areas (Fig. 4.9 C). Visualizing the exact sensor shape by fluorescence microscopy, an inhomogeneous covering of engraved spot can be observed (Fig. 4.9 C, inset). Deposited sensor cocktail comprises a circular outer shape, however, exhibits blank spots in the central region. Generally, a contraction of the sensor cocktail, potentially occurring after deposition due to minimization of surface energy, is observed. In addition to sensor spots, the underlying roughened surface can be clearly distinguished.

We added PDMS stamps for resin-based micromolding of the tissue layer. Compared to the Spheroflow-HoC, the knob region does not cover the complete sensor spot such that a penetration of resin between stamp and sensor cannot be precluded *a priori*. Although the exact tissue layer shape complicates resin-based filling due to dead-end regions between tissue chambers, tissue layers were successfully replicated following stamp degassing. We successfully assembled the centrifugal HoC on top of roughened microscope slides with integrated sensor spots (Fig. 4.9 D). In finalized device, roughened spots are no longer distinguishable. The tissue chamber covers $\approx 60\,\%$ of the sensor spot.

Integration of sensor beads into spheroids

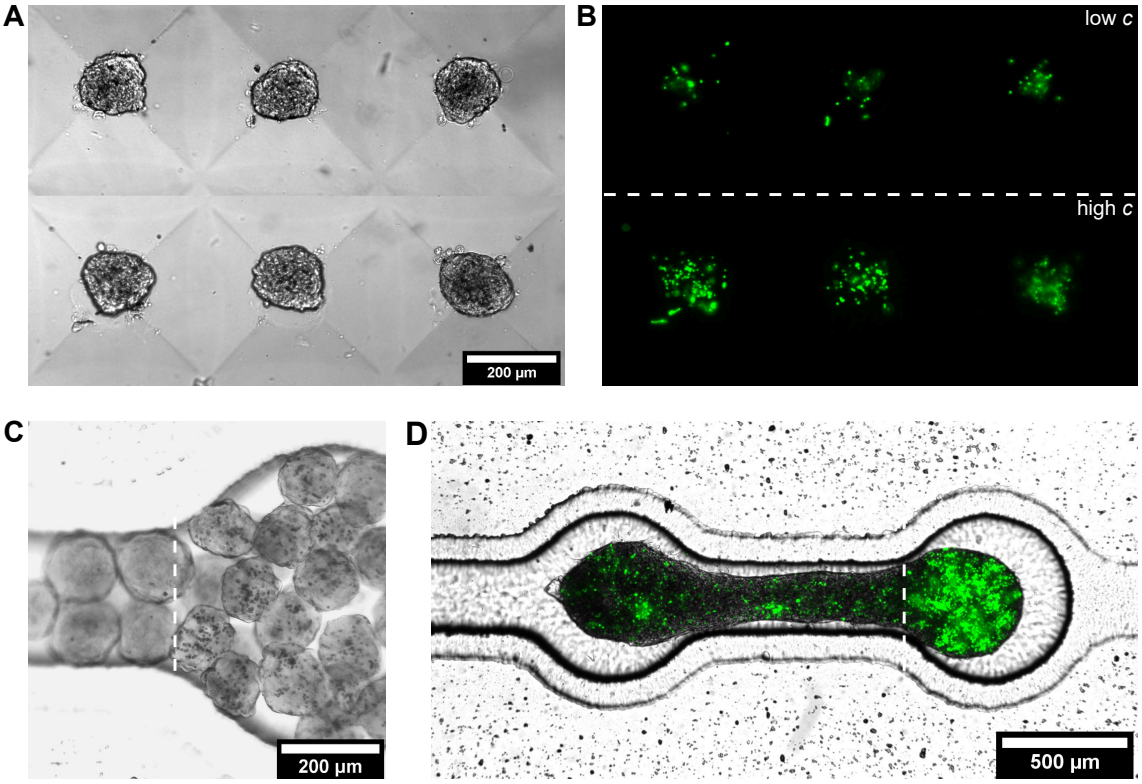

Figure 4.11 Integration of O_2 sensor beads into tissues. **(A)** Cardiac spheroids in microwells on day 1 with functionalized beads added in low concentration (upper row) and high concentration (lower row) during centrifugation. **(B)** Fluorescence image of (A) highlighting integrated O_2 sensor beads (green, Cy5 filter set). **(C)** Successive injection of spheroids, featuring two distinct concentrations of integrated beads, into the Spheroflow-HoC. **(D)** Aligned tissue on day 1, formed from fused spheroids. The tissue is patterned, exhibiting spatially defined concentrations of integrated O_2 sensor beads (green).

In addition to a chip-based integration of sensing capabilities, we investigated a direct integration of O_2 sensor particles into cultured tissues. Preceding FB spheroid formation, we added microbeads functionalized with O_2 sensing dye ($\varnothing = 5\,\mu m$, provided by Stefanie Fuchs, TU Graz), to the cell suspension. Following centrifugation, beads are distributed between microwells and intermixed with cells. Beads do not impede spheroid formation, on day 1 after centrifugation tissue compaction is visible (Fig. 4.11 A). Embedded sensor beads can be distinguished as dark spots within the tissue. We tested spheroid formation utilizing two distinct bead concentrations (high c/low c). Fluorescence microscopy reveals a corresponding occurrence of integrated beads within formed spheroids (Fig. 4.11 B).

We injected spheroids with varying bead concentration into a minimal version of the Spheroflow-HoC composed of a PDMS tissue layer bonded to glass. First, high

c spheroids are flushed in, filling the rearward knob. Subsequently, low c spheroids are injected, filling the remaining chamber (Fig. 4.11 C). Both spheroid populations can be visually distinguished from each other by the amount of integrated beads. Following static culture, tissue compaction is observed on day 1, constraining all O_2 sensing beads to the tissue region (Fig. 4.11 D). We probed the sensor signal with a phase fluorimeter with focusing lens. In the low c region we detected a signal of $U_{\text{low}} \approx 15\,\text{mV}$, whereas a signal of $U_{\text{high}} \approx 60\,\text{mV}$ was detectable in the high c region.

4.2.2 Sensor spot calibration

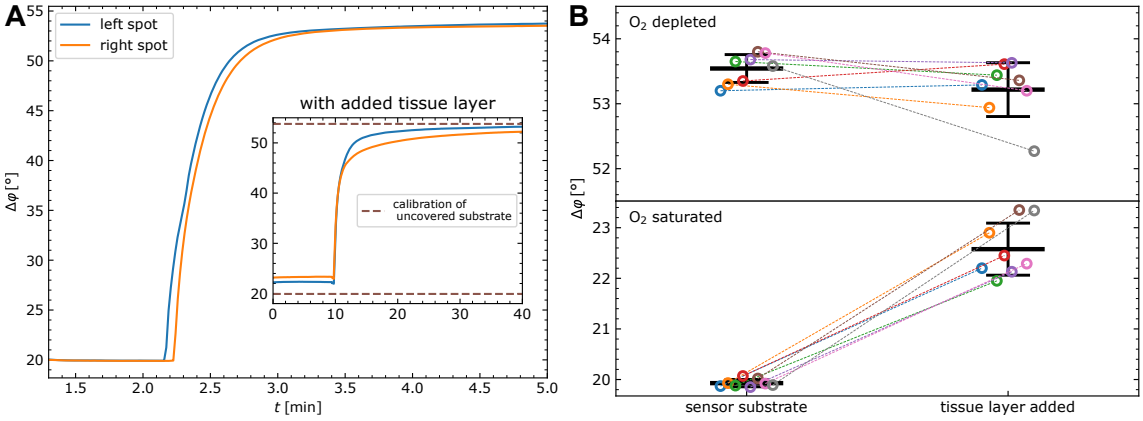

Figure 4.12 Calibration of O_2 sensor spots before and after addition of the resin layer. **(A)** Measurement of phase shift $\Delta\varphi$ before and after resin layer attachment. The bare sensor substrate is initially covered by well-aerated DI water which is exchanged to a 10 % Na_2SO_3 solution yielding an increase in phase shift. After addition of the tissue layer out of UV resin, the phase shift at O_2 saturation is elevated and the sensor response is prolonged (inset). **(B)** Comparison of phase shift measured from sensor spots on the bare sensor substrate and after addition of the tissue layer ($N = 8$ sensors).

For reliable conversions from measured phase shifts to O_2 levels, sensor spots are calibrated by determining the phase shift in the oxygenated and deoxygenated state. We compared calibrations between different sensor spots fabricated under identical conditions. As individual sensor calibrations are time-consuming, a base calibration with an estimation of fluctuations between individual systems is advantageous, enabling a quick assessment of measured O_2 partial pressures. In particular, it is not *a priori* clear, whether applied resin molding step influences the sensor response. Therefore, we calibrated sensor spots deposited on PET substrates in pristine state and after the addition of the resin-based tissue layer, including all potential influence of plasma treatment, APTES deposition and UV exposure.

We calibrated sensor spots on bare substrates by covering the spot with a drop of well-aerated water (well shaken DI water before deposition), followed by a drop of a

10 % Na_2SO_3 solution in DI. The phase shift $\Delta\varphi$ is continuously monitored during deposition of both solutions. Sensor spots display a distinct increase from phase shifts in oxygenated state $\Delta\varphi_{100\,\%} \approx 20°$ to $\Delta\varphi_{0\,\%} \approx 53°$ in deoxygenated state (Fig. 4.12 A). The signal increases in a timespan of $\Delta t \approx 1\,\text{min}$ to the elevated value, displaying further slight increase. We measured eight sensors (four substrates with two spots per substrate) in total.

Subsequently, the resin-based tissue layer was added, following established Spheroflow-HoC fabrication protocol. However, the media layer was not attached, yielding comparable experimental conditions (sensor freely accessible from top), while including all essential impacts from the complete fabrication protocol.

Following tissue layer attachment, we determined phase shifts again (Fig. 4.12 A, inset). Observed phase shift in the oxygenated state $\Delta\varphi_{100\,\%} \approx 23°$ is elevated compared to the uncovered substrate. An increased deoxygenation time is observed. Even at $\Delta t \approx 30\,\text{min}$ after Na_2SO_3 addition, measured phase shift $\Delta\varphi_{0\,\%}$ does not fully reach previously determined phase shift. However, an asymptotic approach is observable with $\Delta\varphi_{0\,\%} \approx 52°$ at $\Delta t \approx 30\,\text{min}$. Sensor spots on the same substrate slightly deviate in rise time and $\Delta\varphi_{100\,\%}$.

We compare all measured phase shifts in O_2 saturated and depleted state between the uncovered sensor substrate and the substrate with added resin layer (Fig. 4.12 B). Phase shifts are measured at $t = 3\,\text{min}$ and $t = 30\,\text{min}$ after addition of quenching solution for the bare and covered substrate respectively. The bare substrate in O_2 saturated state yields $\Delta\varphi_{100\,\%} = (19.9 \pm 0.1)°$, increasing in magnitude and standard deviation to $\Delta\varphi_{100\,\%} = (22.6 \pm 0.5)°$ after tissue layer addition. Contrary, measured mean phase shift in the depleted state decreases from $\Delta\varphi_{0\%} = (53.5 \pm 0.2)°$ to $\Delta\varphi_{0\%} = (53.2 \pm 0.4)°$ after resin layer attachment. While all phase shifts increase in the O_2 saturated state, six out of eight measured phase shifts decrease in the depleted state.

4.2.3 Characterization of integrated sensors in chip culture

We investigated O_2 levels in the Spheroflow-HoC during culture of cardiac µ-tissues. The chip was fabricated on top of a PET substrate. Pronounced oscillations of amplitude $\Delta p_{O_2} \approx 10\,\text{hPa}$ were visible upon perfusion with a syringe pump utilizing a 10 ml syringe (Fig. 4.13 A). Exchanging the syringe to a 1 ml syringe, oscillations were reduced by one order of magnitude to $\Delta p_{O_2} \approx 1\,\text{hPa}$. Observed oscillations occur at a frequency of $f_{\text{osci}} \approx 0.4\,\text{min}^{-1}$ for both syringes.

In order to elucidate the effect of perfusion onto O_2 levels, media supply was alternately set to the flow rate of 50 µl/h and stopped in 30 min intervals (Fig. 4.13 B). For all four investigated chambers a decrease in O_2 levels upon stopping of the flow is observed, followed by a reoxygenation upon reuptake of perfusion. O_2 levels instantaneously change upon flow rate variation with a faster oxygenation compared to deoxygenation time. Compared to the other chambers, chamber B displays a delayed response to variations in pumping rate (cf. pumping initiation at $t \approx 3\,\text{h}$ and $t \approx 4\,\text{h}$).

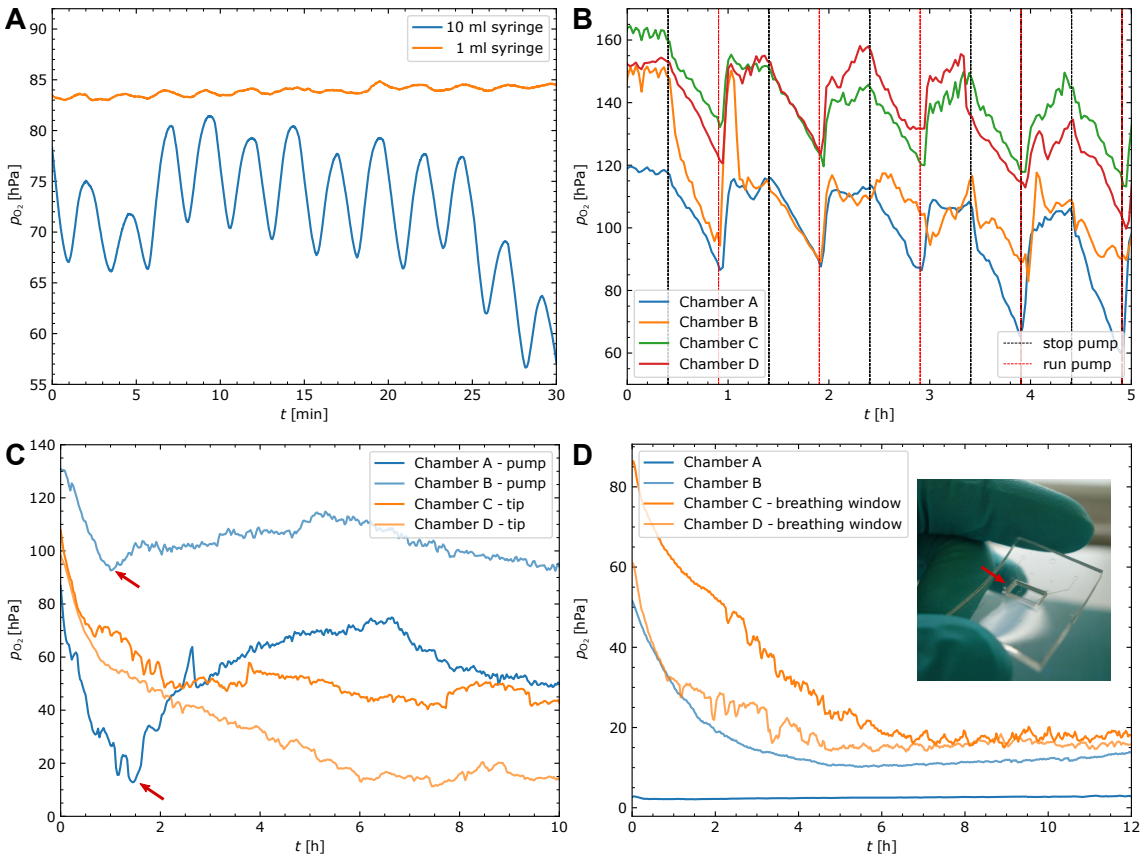

Figure 4.13 Characterization of integrated O_2 sensors. **(A)** Investigation of oscillations in O_2 levels. Syringes with a higher volume lead to pronounced oscillations in O_2 levels (different samples shown). **(B)** O_2 levels recorded under repeated starting and stopping of flow (dashed lines, time points extracted from timestamp of issued serial command). **(C)** Comparison between chips connected to pipet tips filled with media and chips perfused with a syringe pump after spheroid loading. After an initial decrease, chips connected to the pump display a reoxygenation upon onset of pumping (red arrows). **(D)** Comparison between chips built with normal media layer and media layer with reduced thickness ("breathing window"). Pipet tips were filled with media after loading and chips immediately transferred to the measuring platform.

We compared O_2 evolution between chips actively perfused by means of a syringe pump and chips with media-filled pipet tips attached to the media channel. Media levels in inlet and outlet tip differ, providing an initial hydrostatic flow, ceasing to a static media supply after liquid column equilibration. Following spheroid injection, pump or pipet tips were connected to the chip and the O_2 content of two chambers per condition was constantly monitored (Fig. 4.13 C). For all chambers, an initial ($t < 1\,\mathrm{h}$) drop in O_2 partial pressure is detectable. Compared to chambers connected to pipet tips, one actively perfused chamber displays higher O_2 levels, whereas lower

levels are measured in the other chamber. For pump-perfused chambers, a reversal point slightly differing in time between both chambers at $t \approx 1.3\,\mathrm{h}$ is detectable. In the following, O_2 levels rise again above values measured in chambers connected to pipet tips. Partial pressures in tip-connected chambers further decrease, asymptotically approaching a constant trend with remaining smaller oscillations.

In a further study, we investigated whether the oxygenation can be improved in statically cultured chips with attached pipet tips by a decreased layer height of the media module ("breathing window"), granting improved O_2 diffusion through the top layer. Therefore, we fabricated Spheroflow-HoCs comprising media layers with a decreased layer height of $\approx 150\,\mu\mathrm{m}$ in the central region above the tissue chambers (Fig. 4.13 D, inset). After spheroid loading, pipet tips with media were attached and O_2 levels continuously monitored comparing two breathing window and two reference chambers. Measured O_2 levels display an initial drop in all chambers. In one reference chamber, complete deoxygenation is distinguishable with a static partial pressure close to $p_{O_2} = 0\,\mathrm{hPa}$. Generally, measured O_2 partial pressures are increased for breathing window chambers. Breathing window chambers display a slower decrease in O_2 levels, asymptotically approaching a static state at $t \approx 7\,\mathrm{h}$.

4.2.4 Discussion

The integration of luminescent O_2 sensors in OoCs provides a non-invasive and real-time readout for assessing tissue metabolism. Compared to the embedding of sensors in the media channel, the integration in direct contact to cultured tissues offers faster response times and less influence from other microfluidic environmental factors [77, 175]. In general, a flexible integration approach is desired, offering an upgrade to existing OoCs which provides additional insights into tissue culture. We investigated the integration of sensor spots into microfluidic environments based on resin micromolding as well as the integration of sensor particles into cultured tissues. Both approaches offer a user-friendly sensor integration and can be applied for the integrated measurement of tissue metabolism in future studies. We characterized the influence of the resin-based fabrication approach on sensor readouts and discussed sensor measurements under OoC culture conditions.

Integration strategies We verified successful integration of luminescent O_2 sensor spots into multilayer HoCs. With established resin-based fabrication the sensor is integrated into the tissue chamber, yielding direct contact to the tissue. Implemented integration concept allows a flexible substrate choice such that chips can be tailored to individual applications. We compared adhesion-coated PET foils and cover slips as sensor substrates. Sensor spots adhered to PET foils without the need for further processing steps. As the foil is cut to chip size only after sensor deposition, PET substrates offer fast processing times as a large area can be equipped with sensors in a single process without the need of individual chip alignment. We identify deteriorated imaging conditions as major deficiency of employed PET substrate. By comparing PSFs recorded on other substrates, we conclude that impaired

imaging is related to the adhesion coating of the substrate, already applied by the distributor. Switching to a different polymer foil might improve optical properties but could also lead to worse sensor adhesion.

Glass substrates offer superior imaging conditions. Unfavourably, necessary substrate roughening degrades imaging conditions directly at the sensor position but should not impede the optical investigation of tissues in areas next to the sensor spot. Compared to sensor spots on PET foil, the sensor is shaped inhomogeneously, potentially affecting readout quality by overwheighting local O_2 variations. As major bottleneck of glass substrates we identify the necessity of preliminary spot engraving. Usually, glass slides have to be engraved at a different facility such that substrates are shipped back and forth, slowing down turnaround times. Furthermore, predefined sensor positions require precise alignment, leading to a necessary individual adjustment for each substrate.

Generally, PET foils offer improved sensor adhesion and a facilitated fabrication. Devices enable the determination of O_2 levels and analysis of tissue-level beating kinetics but do not allow detailed optical analysis at higher magnifications. Contrary, glass substrates are characterized by a more complicated fabrication but offer superior imaging in all regions except for the sensor spot itself. Due to higher availability from the manufacturer, we conducted experiments on PET substrates. We see huge potential for demonstrated integration approach, enabling further analysis of O_2 levels and consumption rates similarly to the Seahorse assay within a defined microphysiological environment.

In addition to a fixed chip integration, we presented proof-of-concept of a direct integration of O_2 sensing particles into spheroids, further merging to a single aligned tissue. Compared to a substrate integration, sensor particles do not require any adjustments in fabrication and can be directly integrated into tissues. It is, however, not resolved if integrated particles influence cultured tissues in some way. We did not observe any detrimental effect of added particles. Spheroid formation, injection, and tissue compaction was comparable to similar experiments without added sensing beads. For a thorough assessment, it is essential to culture tissues inside developed platform for longer times.

We demonstrated the feasibility of patterning aligned µ-tissues by injecting distinct spheroid populations. Due to the sequential loading process, the chamber is filled starting from the backward knob, such that sensors can be deposited into different regions along the fiber axis.

The ratio of signal intensities in high c and low c regions ($60\,\mathrm{mV} : 15\,\mathrm{mV} = 4 : 1$) coincides with the ratio of introduced sensor particles between both populations (high c : low $c = 4 : 1$), quantitatively confirming the patterning of both regions. Compared to measurements on O_2 sensor spots [$\mathcal{O}(10^2\,\mathrm{mV})$], the signal intensity is decreased. Generally, even the maximum detected signal intensity lies on the lower intensity limit for meaningful phase fluorimetry measurements ($U_{\mathrm{sig}} \geq 50\,\mathrm{mV}$ for detectable O_2 levels, $U_{\mathrm{sig}} \geq 100\,\mathrm{mV}$ for reliable measurements; information provided by sensor manufacturers).

Increasing the bead density per spheroid as well as constraining sensor-loaded

spheroids to a distinct detection region within the chip should help increasing the signal intensity. Demonstrated co-loading approach served as proof-of-concept, in further implementations only the knob region could be filled with spheroids featuring a high density of sensing particles, yielding one defined sensor position. Furthermore, a decrease of sensor particle diameter would allow denser compaction of sensor material within each spheroid, taking up a reduced volume within the tissue. Potential tissue irritation, caused by the integration of foreign objects, could thus be reduced.

Compared to approximately 2D-shaped sensor spots, applied sensing approach distributes individual beads within the tissue in 3D. Thus, measured signal is averaged over the whole volume. Oxygen gradients within the tissue lead to different phase shifts, potentially disturbing proper sensor readout. Contrary, individual beads also offer the opportunity for space-resolved measurements if they can be read out on an individual level. Lesher-Pérez *et al.* demonstrated the determination of radial O_2 concentration profiles via phase fluorimetry from embedded sensor particles, however, the signal is averaged over multiple beads [274].

Sensor spot calibration We obtained a reference calibration for future integrated measurements. Our findings indicate a change in sensor response after resin-based tissue layer addition, distinguishable by longer response times and an increased phase shift in the oxygenated state. In the O_2 depleted state, $\Delta\varphi$ is decreased after layer attachment. However, $\Delta\varphi$ of the bare sensor substrate lies within the standard deviation of $\Delta\varphi$ measured after tissue layer attachment.

We attribute observed difference in the O_2 depleted state to the change in response time. Due to the increased response time, determined values are acquired from a still rising signal instead of the plateau value, yielding a mainly reduced phase shift.

Increased $\Delta\varphi$ in the saturated state can be explained by partial coverage of sensor surface with resin. Covered areas might exhibit a lower O_2 content, attributing to measured increase of $\Delta\varphi$. As no direct contact between the oxygen quencher Na_2SO_3 and sensor is established in covered regions, O_2 diffuses out of covered regions with increased diffusion times compared to direct quencher contact. This would lead to observed increased response times with approaching the same deoxygenated levels. The deposited sensor consists of multiply deposited individual spots which do not perfectly overlap. Thus, perfect coverage of the whole surface can not be granted with employed channel geometry.

A covering of the sensor can explain observed change in sensor response, however changes in chemical composition triggered by impacts from the fabrication procedure are also conceivable. Adding a tissue layer comprised of extended channel dimension, thus excluding any coverage, could help to fully disentangle both effects.

Sensor characterization We investigated various factors influencing integrated O_2 sensors during chip culture. Conducted measurements were carried out with a global sensor calibration from an uncovered sensor substrate. As discussed in

previous paragraph, the addition of the resin-based layer influences the calibration. Measured values are thus discussed qualitatively.

A decrease in O_2 oscillations could be observed upon switching to a smaller syringe. Employed syringe pump advances the syringe plunger via a stepper motor, yielding $f_{\mathrm{mot}} \approx 38\,\mathrm{steps\,min^{-1}}$ for a perfusion rate of $Q = 50\,\mu\mathrm{l/h}$. Comparing observed oscillation frequency $f_{\mathrm{osc}} \approx 0.4\,\mathrm{min^{-1}}$ and the stepping frequency, we preclude direct influence of the syringe pump onto observed oscillations. However, as switching to a different syringe diameter reduced the oscillations, we believe that friction in the syringe between plunger and side wall could account for observed oscillations. The plunger is most likely not moving forward in the idealized linear way, rather a stick-slip motion is taking place where the plunger advances once the pushing load exceeds the side-wall friction, taking multiple stepper motor steps. Thus, media is perfused in a pulsatile manner at a reduced frequency compared to the stepper motor. It is thus conceivable that due to reduced friction and cross section, the 1 ml syringe displays a different stick-slip motion with reduced oscillations. Although syringes comprising higher volumes are favourable for pump-based chip culture reducing media-change efforts, we recommend the use of 1 ml syringes for sensitive O_2 measurements. In addition, low friction syringes out of glass could help for a more homogeneous perfusion, reducing O_2 oscillations. In general, an influence of cultured tissues onto observed oscillations is also conceivable. Optically determining flow rates via particle image velocimetry would allow direct comparison with observed oscillation and should yield further insights into presumed relationship in further experiments.

Observed O_2 depletion after ceasing of flow demonstrates the need for active perfusion in developed OoC, granting a sufficient O_2 supply. During perfusion, stable O_2 levels evoked by a balance between O_2 influx and O_2 consumption are distinguishable. Detected sharp increase in O_2 levels upon initiation of pumping can be explained by an exchange of media to fresh, oxygenated media, constituting a diffusion source of elevated p_{O_2}. Another explanation is an additional convective O_2 transport into the tissue chamber, as the tissue chamber is not completely filled out by the tissue.

We confirmed fast sensor response by pumping rate variations in implemented chip design integrating the sensor directly below the tissue. Hence, O_2 monitoring combined with pumping rate variations can subsequently be used to precisely determine O_2 consumption rates of cardiac tissues, comparable to previous experiments integrating sensor spots into the channel top [77]. Detected delayed response of chamber B can be explained by an air bubble in the system, introducing an additional elastic component, thus retarding the system response due to compression of the gaseous volume.

The comparison between pump-perfused chips and chips with attached pipet tips affirms the observation of improved oxygenation for perfused chips. We attribute the observed reversal point with following p_{O_2} increase to the onset of perfusion. After syringe insertion into the pump, the pump lever is not directly pushing onto the syringe plunger as implemented insertion protocol tries to avoid the application

of uncontrolled pressures onto syringes by keeping a safety margin between plunger and pump lever. Only after passing of the safety margin, the syringe is mechanically fixed and an optimal transduction between pump stepper and plunger takes place, initiating the flow. Due to the utilization of different syringe slots, both reversal points occur at slightly different time points.

The introduction of a breathing window lead to increased O_2 levels compared to reference chips. However, even chips with reduced media layer thickness displayed low O_2 levels of $p_{O_2} \approx 20\,\mathrm{hPa}$, indicating a deoxygenated environment. We conclude that the O_2 supply is mainly limited by diffusion through the porous membrane, rather than a sufficient supply of O_2 in the media compartment. Future chip designs could integrate a membrane of increased porosity for improved O_2 supply. The injection of spheroids ($\varnothing \approx 150\,\mu\mathrm{m}$) especially enables the utilization of larger pore sizes ($\varnothing = 3\,\mu\mathrm{m}$ currently). Generally, O_2 levels varied between individual tissues, such that observed improved oxygenation must not necessarily arise from the embedded oxygen window. Future studies are crucial to fully understand the influence of individual chip components onto O_2 dynamics in developed system. As with current setup only four chambers can be monitored simultaneously, a scaled up measurement platform is desirable.

Chapter 5

Biophysical stimulation of OoCs

The following sections evaluate the integration of various stimulation capabilities into microphysiological systems. In particular, we focus on electrical and mechanical stimulation concepts. We investigate the integration of electrical pacing into developed HoC systems. Furthermore, we evaluate the application of defined stretching and compression for applications in Lung-on-Chip and Cartilage-on-Chip systems.

5.1 Electrical stimulation of cardiac tissues

Muscle tissue, i.a., the myocardium, is distinguished by a coupling between electrical signaling and mechanical contraction. Hence, for an accurate modeling of cardiac tissue on the microscale, it is important to integrate the capability to deliver electrical stimuli to cultured tissues. We investigated opportunities for integrating electrical stimulation systems into HoC platforms. We demonstrate successful electrical stimulation coupled to measurements of O_2 partial pressure and Ca signal transduction. Electrical stimulation of tissues inside the Spheroflow-HoC and corresponding investigation of Ca signaling and O_2 partial pressure has been previously published in "Schneider, O. *et al.* Fusing Spheroids to Aligned µ-Tissues in a Heart-on-Chip Featuring Oxygen Sensing and Electrical Pacing Capabilities. *Mater. Today Bio* **15,** 100280 (2022) [27]".

5.1.1 Integration of pacing into HoC platforms

While graphene rods, or more generally electrode wires, are frequently integrated into open-top cardiac model systems on scales ranging from well plates to microstructured compartments, an established concept for electrode integration into HoC systems is still lacking. In general, a simple integration strategy is desired, allowing a scaled up fabrication. Depending on the intended application, electrodes need to be integrated in varying quality and geometrical accuracy, e.g., if a combination with sensing of electrical field potentials is desired, electrodes must exhibit reduced contact resistance [275]. Similarly, a spatial determination of electrical fields requires

defined geometrical arrangement of electrodes. Here, we focus on the integration of pacing capabilities on a minimal level, i.e., we aim for any feasible integration of electrodes which can deliver pulsed electrical fields to the tissue chamber.

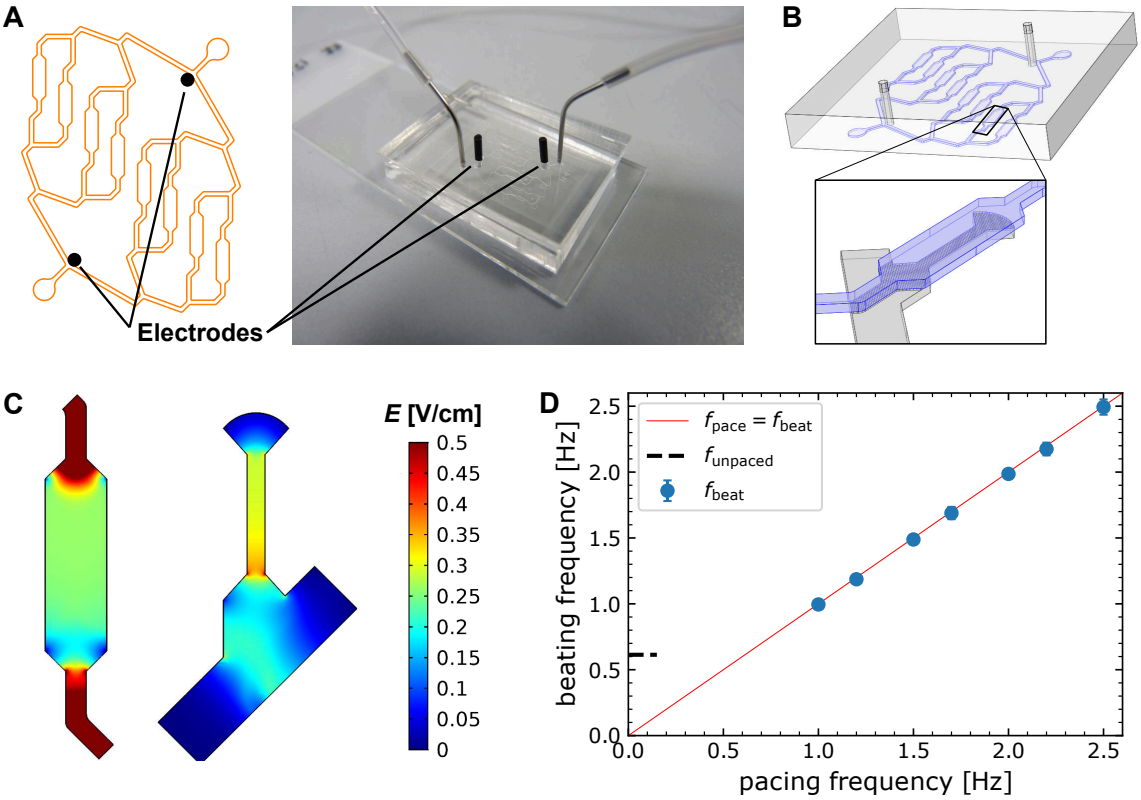

Figure 5.1 Electrical stimulation in centrifugal HoC utilizing inserted electrodes. **(A)** Schematic indicating the position of electrodes inserted into the media module and picture of centrifugal HoC with added carbon electrodes. **(B)** Model geometry used for FEM analysis of electrical field distribution. Electrodes are modeled as cylindrical rods inserted into the media module. Membrane pores are explicitly modeled in a submodel comprising one tissue chamber. **(C)** FEM analysis of electrical field distribution inside centrifugal HoC. $U = +5\,\mathrm{V}$ is applied between both electrodes and the field distribution is evaluated for one of eight parallel tissue chambers. **(D)** Extracted beating frequencies as a function of applied pacing frequency. The beating frequency is adapted to externally forced pacing frequency (red line).

Stimulation via integrated wire electrodes Following existing approaches in open-top systems, we investigated the capability to integrate electrodes in the form of conducting wires into the HoC platform for subsequent pacing. Initial trials integrating electrodes directly into the PDMS tissue compartment involved intricate molding protocols and were error-prone to coverage of electrode surface with PDMS. Thus, we investigated the approach of inserting electrode rods into the media com-

partment via punched inlets.

We punched two access ports into the media module, located at the first branching of the media channel close to media inlet and outlet. Access ports are in direct contact with the media channel but do not comprise the complete channel. Subsequently, we added two carbon rods as electrodes into fabricated ports (Fig. 5.1 A). Electrodes seal the chip during the centrifugation step for cell injection and subsequent media perfusion. An approximately 5 mm long section protrudes from the chip surface and enables the electrical connection between electrodes and a pulse generator by alligator clips. Our developed pacing concept does not provide direct contact of electrodes with the tissue compartment. Instead, implemented design aims at generating an electrical field inside the media compartment, mediated by perfused liquid. Due to chosen position, an identical electrical field distribution for all eight tissue chambers is expected. As the media channel is guided along the principal tissue chamber axis, the generation of an electrical field along the aligned tissue axis is foreseen.

We simulated the electrical field distribution via FEM modeling in designed device (Fig. 5.1 B). Electrodes are modeled as cylinders, inserted into the media module at previously described positions. A constant potential difference is applied between the surfaces of both rods. Generally, the tissue module is separated via a porous membrane from the media layer (Fig. 5.1 B, inset). An initial simulation comparing the explicit modeling of individual membrane pores with a complete neglection of a separating membrane yielded negligible differences in simulated electric fields. Hence, the membrane is considered as media in the following simulations.

The application of $U = +5\,\mathrm{V}$ predicts a homogeneous electrical field in the media compartment above the tissue chamber of magnitude $E \approx 0.25\,\mathrm{V/cm}$ (Fig. 5.1 C). In the horizontal midplane of the tissue chamber, electrical fields of magnitude $E \leq 0.2\,\mathrm{V/cm}$ are distinguished in the knob region. The electrical field decays in the shaft region along the alignment direction yielding magnitudes of $E \approx (0.25\text{–}0.35)\,\mathrm{V/cm}$, corresponding to variations of $\Delta E/E \approx 17\,\%$.

We electrically stimulated tissues (formed from iCell® CMs) cultured in the centrifugal HoC by applying monophasic pulses of $U = +5\,\mathrm{V}$ to inserted carbon electrodes at increasing pacing frequencies f_{pace}. By simultaneously monitoring tissue contraction kinetics via video microscopy, we determined the beating frequency f_{beat} with OHW (Fig. 5.1 D). The initial beating frequency of $f_{\mathrm{beat}} = (0.61 \pm 0.01)\,\mathrm{Hz}$ is increased to $f_{\mathrm{beat}} = (1.00 \pm 0.02)\,\mathrm{Hz}$ upon pacing at $f_{\mathrm{pace}} = 1.0\,\mathrm{Hz}$, matching the pacing frequency. Subsequent increases of f_{pace} lead to similar adaption of f_{beat} up to $f_{\mathrm{beat}} = (2.49 \pm 0.06)\,\mathrm{Hz}$. Exceeding this frequency, the beating frequency did not adopt to the pacing rate anymore.

Stimulation via fluidic media connectors We investigated whether tissues can be paced in the Spheroflow-HoC by harnessing utilized media connectors as electrodes, further simplifying the integration of electrodes. Compared to pacing experiments on the centrifugal HoC based on the delivery of unipolar pulses, tissues

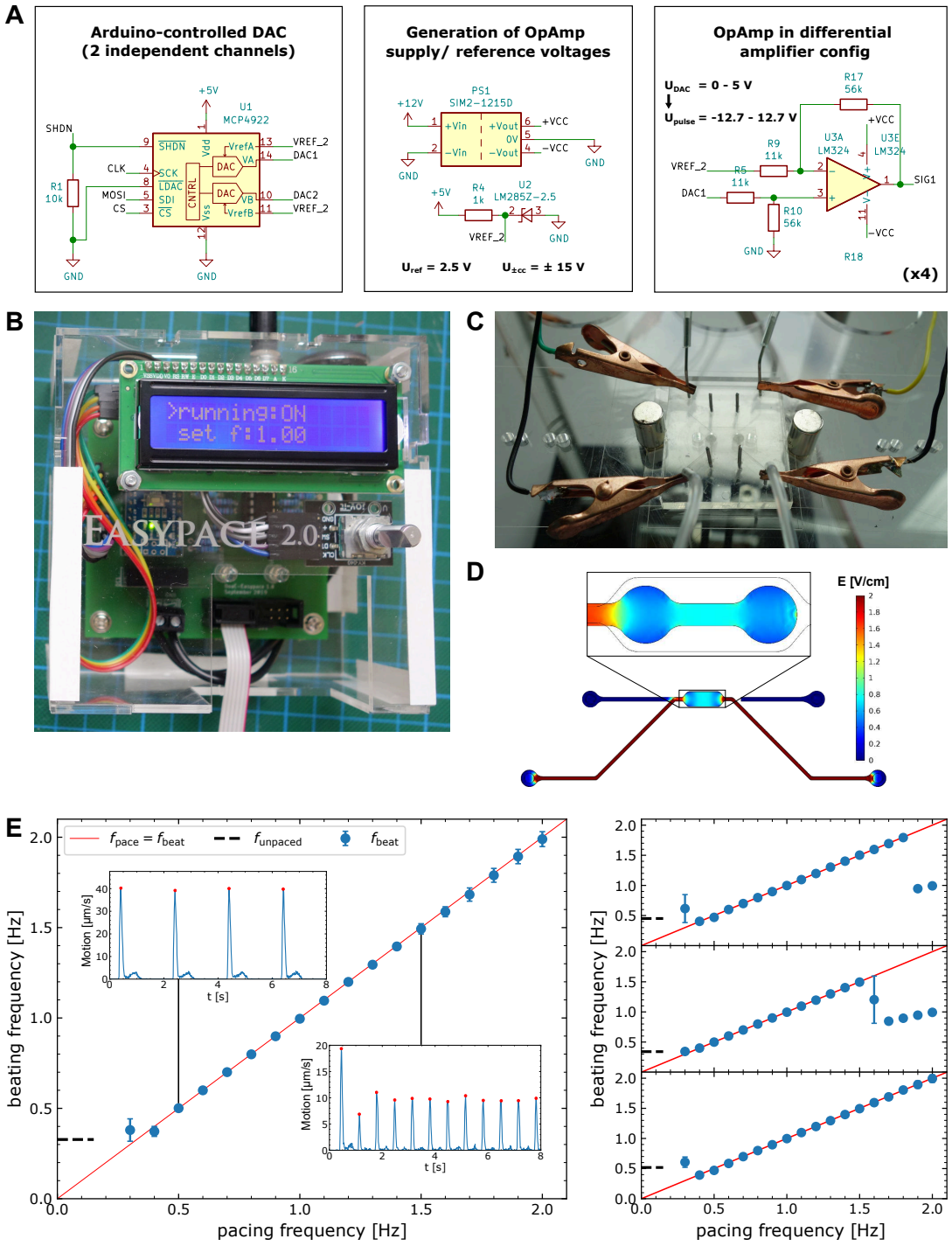

Figure 5.2 Electrical stimulation of cardiac tissues via media connectors. **(A)** Circuit schematic of key components of developed pulse generator EASYPACE. An Arduino-controlled DAC creates two independent signals that are subsequently converted to biphasic pulses via an OpAmp. **(B)** Picture of developed pulse generator. **(C)** Image of pacing setup. The pulse generator is connected via alligator clips to stainless steel fluidic connectors of the media supply. **(D)** Simulated electrical field distribution inside media- & tissue- compartments upon application of $U = +10\,\mathrm{V}$ between media in- & outlet. **(E)** Beating frequency analysis of tissues stimulated electrically at increasing frequencies. Beating frequency extracted from beating kinetics (insets) shown as function of ramped up pacing frequency for four tissues. Ideal matching of beating and pacing frequency indicated by red line. Figure adapted from Ref. [27] under CC BY-NC 4.0 license.

cultured in the Spheroflow-HoC were paced with biphasic pulses.

Therefore, EASYPACE[1], an Arduino-based pulse generator was developed to provide a cost-efficient do it yourself (DIY) platform for electrically stimulating cultured cardiac tissues. It consists of an Arduino-controlled digital-to-analog converter (DAC) which can create two individual output waveforms, which are subsequently transformed to four independent biphasic pulses by a downstream operational amplifier (OpAmp; Fig. 5.2 A). The pulse generator can be either controlled manually or remotely via serial commands, precisely adjusting parameters of the pulse shape (Fig. 5.2 B). Fluidic media connectors out of stainless steel were harnessed as pacing electrodes and connected via alligator clips to the pulse generator (Fig. 5.2 C). The theoretical electrical field distribution inside developed chip geometry was analyzed using FEM simulations for a voltage of $U = +10\,\mathrm{V}$, applied between media inlet and outlet connector. Similarly to simulations of the field distribution inside the centrifugal HoC, we neglected the porous membrane between media and tissue module. A uniform field of $|E| = 0.8\,\mathrm{V/cm}$ is predicted in the horizontal midplane of the tissue chamber shaft region (Fig. 5.2 D).

Tissues cultured in Spheroflow-HoCs were field stimulated on day 5 after injection. Distinct pacing frequencies ranging from (0.3–2.0) Hz were applied for 10 s per individual frequency and stepwise increased by $\Delta f = 0.1\,\mathrm{Hz}$. Videos of beating tissues were recorded simultaneously. By matching timestamps of each pacing frequency interval with recorded video, beating kinetics were investigated for each pacing frequency (Fig. 5.2 E, inset). Comparing determined beating frequency with applied pacing frequency, a linear relation up to a maximum pacing frequency is observed (Fig 5.2 E). Exceeding this frequency, tissues could not follow the external pacing rate anymore and therefore skipped every second pulse, adapting a beating frequency half of applied frequency. All investigated tissues could be paced up to $f_{\mathrm{pace}} = 1.5\,\mathrm{Hz}$, individual tissues up to the applied maximum pacing rate of $f_{\mathrm{pace}} = 2.0\,\mathrm{Hz}$. Thus, we could electrically stimulate integrated tissues and precisely adjust the beating frequency within a tissue-specific range.

5.1.2 Analysis of Ca signaling

We analyzed the propagation of Ca signals within paced tissues cultured in the Spheroflow-HoC via high-speed fluorescence video microscopy of a Ca sensitive dye. Cultured cardiac fiber is aligned parallel to the image x-axis during recordings. The recorded signal is averaged for each frame along the y-axis and binned along the x-axis yielding a 1D intensity trace for distinct x-positions along the fiber (Fig. 5.3 A). Comparing signal traces at opposing ends of the cardiac fiber, a difference in signal onset time is observable (Fig. 5.3 A, inset).

A linear relation is observable between pulse onset time and position (5.3 B). Contiguous regions of similar pulse onset can be located, attributed to a finite temporal acquisition resolution. From a linear fit of pulse time t_{pulse} vs. position x, the

[1] https://github.com/loslab/easypace/

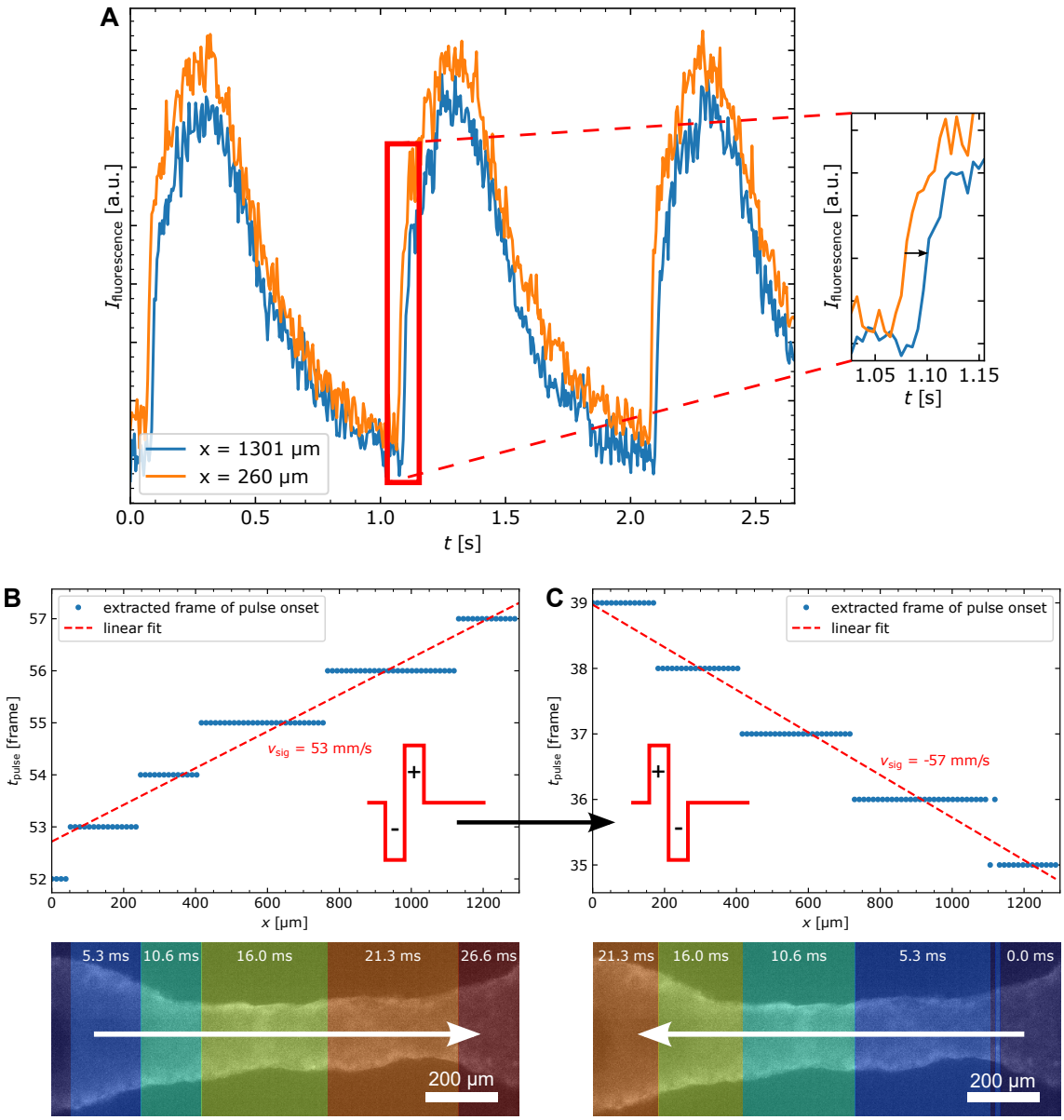

Figure 5.3 Analysis of Ca kinetics within an aligned cardiac tissue cultured in the Spheroflow-HoC platform. **(A)** Time-dependent fluorescence intensities at two distinct x-positions along the cardiac fiber, recorded by high-speed video microscopy of Fluo-4 AM Ca dye. A temporal shift in signal rise times between both positions is observed and can be used to calculate the signal propagation velocity. **(B)** Evaluation of pulse onset of paced tissue as a function of fiber position. Ca propagation velocity v_{sig} is determined from linear fit. Color-coded Ca activation map is shown as overlay to the investigated tissue. **(C)** Analysis of pulse onset for inverted pacing polarity. Propagation velocity is determined and propagation shown as overlay similar to (B). (B) and (C) adapted from Ref. [27] under CC BY-NC 4.0 license.

signal propagation velocity is determined to $v_{sig} = 53\,\mathrm{mm/s}$ and $v_{sig} = -57\,\mathrm{mm/s}$ for positive and negative pulse polarities. An inversion of signal propagation direction is monitored upon pacing polarity inversion.

5.1.3 Simultaneous stimulation and O_2 monitoring

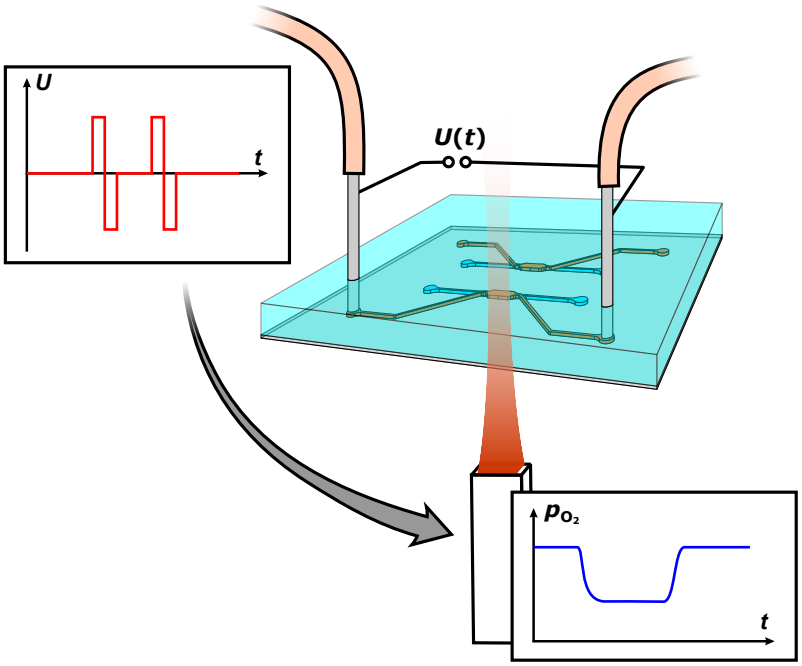

Figure 5.4 Schematic of combined stimulation and sensing inside the Spheroflow-HoC. Tissues are electrically stimulated via fluidic media connectors while O_2 levels are optically monitored with a phase fluorimeter from below. Developed setup enables monitoring of changes in metabolic activity linked to electrical stimulation. Figure adapted from Ref. [27] under CC BY-NC 4.0 license.

We combined O_2 measurements of cardiac tissues cultured inside the Spheroflow-HoC with the electrical stimulation approach utilizing fluidic media connectors as electrodes. Luminescent sensor spots on PET substrates were integrated into the chip as previously explained; no further changes in chip design are required for the application of electrical stimuli via media connectors. The combination of both concepts allows *in situ* monitoring of changes in tissue metabolism. While O_2 partial pressure is monitored via luminescent sensor spots from below, tissues are paced by stainless steel connectors (Fig. 5.4). As the beating frequency is adjusted to the externally forced frequency, the influence on O_2 consumption can be investigated.

Sensor spots in Spheroflow-HoCs with cultured beating cardiac tissues were monitored overnight. Cultured tissues were electrically stimulated by applying a cyclical variation of consecutive biphasic pulses of frequencies $f = (0.7,\ 1.0,\ 1.2 \text{ and } 1.5)\,\mathrm{Hz}$. Stimulation was carried out for each frequency for 10 min with a resting phase of

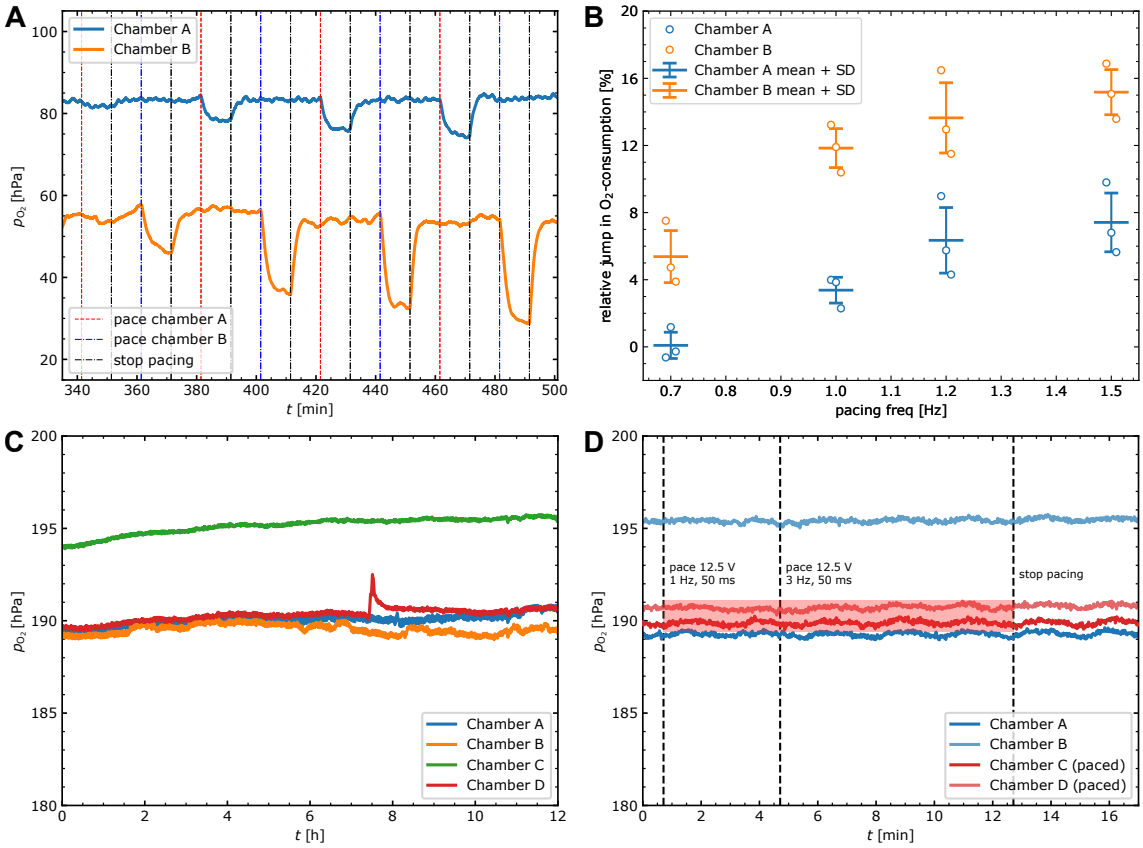

Figure 5.5 Integrated measurements of O_2 levels. **(A)** Recording of O_2 partial pressures of two tissues alternatingly paced (dashed lines) at increasing frequencies of $f = (0.7,\ 1.0,\ 1.2$ and $1.5)$ Hz. **(B)** Evaluation of frequency-dependence of relative jump heights in O_2-consumption for tissues repeatedly probed following timings in A. **(C)** Stability analysis of O_2 levels in empty systems perfused with media over 12 h. **(D)** Comparison of O_2 partial pressures between paced and unpaced chambers, measured in empty, media-perfused systems. The same behavior for both conditions excludes O_2-changes induced by electrolysis. Figure adapted from Ref. [27] under CC BY-NC 4.0 license.

30 min between the application of successive frequency (Fig. 5.5 A). Each frequency cycle was repeated for three times. In order to exclude any effects of external influences on O_2 levels, pacing cycles were temporally shifted for both paced systems by 20 min with respect to each other. Upon initiation of pacing, a drop in measured O_2 levels can be distinguished, with drop onset clearly coinciding with pacing start (cf. reference line). As in the unpaced reference tissue constant O_2 levels are detected, this drop can be attributed to a higher tissue O_2 consumption that might be caused by increased metabolic activity, triggered by electrical stimulation. Upon termination of pacing, an increase in O_2 levels towards initial partial pressures, monitored in the unpaced state, is observed. Stimulating the other tissue, the identical behavior is detected. Increasing pacing frequencies display increased jumps in O_2 levels.

Jump height is determined by the difference between O_2 partial pressure at pacing onset and pacing termination, and evaluated for both tissues as a function of applied pacing frequency. Jump heights are furthermore normalized to the difference of O_2 partial pressure between the unpaced state and the fully oxygenated state, yielding relative jumps in O_2 concentration (Fig. 5.5 B). Relative jumps expose for both investigated systems an increase with applied pacing frequency, observable in each pacing cycle.

The signal stability of developed sensor chip is investigated by perfusing four empty systems with media in culture conditions ($T = 37\,°C$, $c_{CO_2} = 5\,\%$, $Q_{\text{media}} = 50\,\mu l/h$; Fig. 5.5 C). Over the timespan of 12 h, all measured O_2 partial pressures display minimal ($\leq 1\,hPa/h$) shifts, precluding O_2 scavenging of employed resin NOA 81. Chamber 4 exhibits a spike in O_2 partial pressure, which we attribute to a passing air bubble.

In order to attribute the observed variation in O_2 levels to an increase in tissue O_2 consumption, excluding potential changes in O_2 concentration triggered by electrolysis, O_2 levels were recorded in an empty chip perfused with media, undergoing electrical stimulation. Two out of four investigated systems were stimulated at the maximum pulse generator output voltage of $U = \pm 12.5\,V$ with initial frequency of 1 Hz, further ramped up to 3 Hz for up to 8 min (Fig. 5.5 D). No drop in O_2 concentration is detected. Comparing the O_2 partial pressure trend with unpaced chambers, all exhibit a similarly constant trend.

5.1.4 Simultaneous stimulation and force sensing

We investigated the influence of electrical stimulation on contraction forces in the Spheroflow-HoC. The chip is equipped with a soft pad in the knob region and coated with fibronectin, promoting tissue attachment to the soft pad, thus ensuring force transduction during beating motion. Following spheroid injection, spreading of spheroids and beating was observed on day 3 (Fig. 5.6 A). We observed partial rupture of the soft pad in investigated device, potentially caused by touching of the pad during sacrificial layer removal. Due to a global low density of attached beads, we focused on a roi with elevated bead density for the evaluation of contractile forces (Fig. 5.6 B, inset). We observed a periodical deflection of substrate-attached beads via fluorescence video microscopy. By tracking individual beads and linking particle positions, the time-dependent displacement field $\boldsymbol{u}(x, y, t)$ is determined. We electrically stimulated the tissue via fluidic media connectors for increasing frequencies of $f = (0.5,\ 0.7,\ 1.0,\ 1.2 \text{ and } 1.5)\,Hz$ and determined the displacement field for each frequency. Subsequently, we calculated the traction stress field and obtained time-dependent contractile forces by integration (Fig. 5.6 C). Extracted contraction forces reveal periodical force variations coinciding with the externally applied pacing frequency. A decrease in peak force $F_{\max}$ with increasing pacing frequency is observed. We determine all peak positions and get the mean peak force as well as beating frequency for each applied pacing frequency (Fig. 5.6 D). An approximately linear decay of peak force with increasing frequencies is observable.

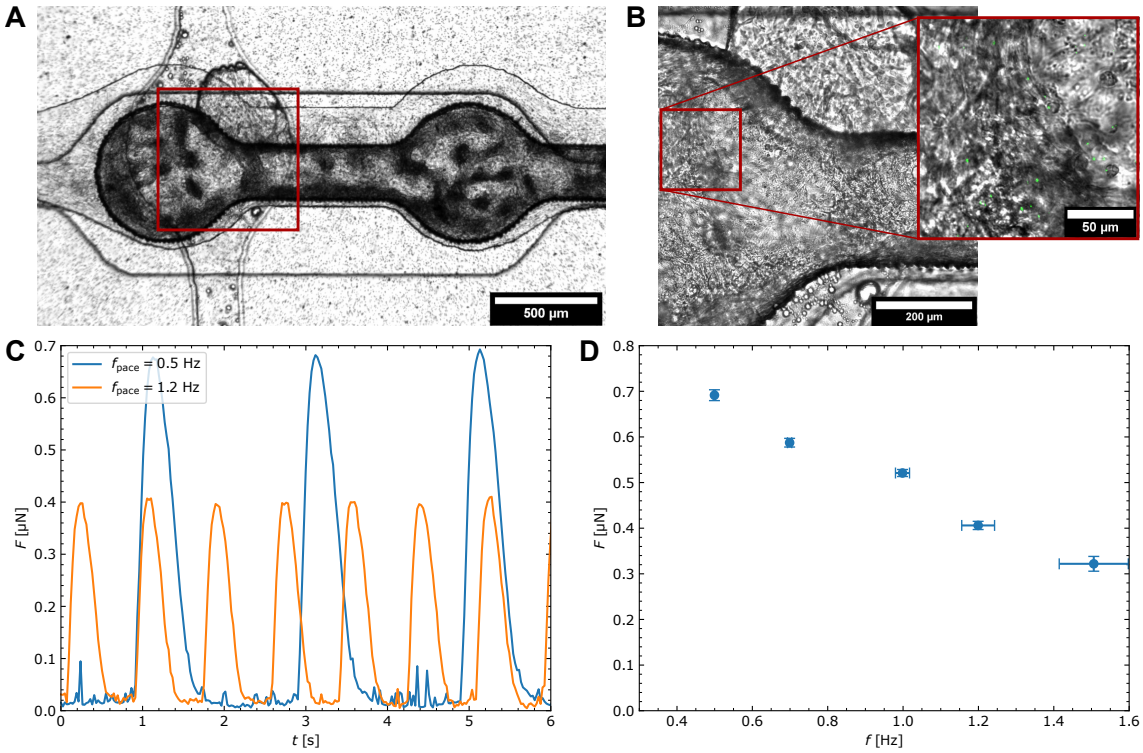

Figure 5.6 Investigation of traction forces coupled to electrical stimulation in the Spheroflow-HoC. **(A)** Formed tissue in a fibronectin-coated Spheroflow-HoC with integrated force sensors on day 3 after loading. **(B)** Magnified view of region marked in (A) with overlay of tracked beads used for the determination of traction forces. **(C)** Integrated traction forces extracted from bead movement in (B) for pacing at $f = 0.5\,\mathrm{Hz}$ and $f = 1.2\,\mathrm{Hz}$. **(D)** Force-frequency relation determined by TFM in a paced HoC. Mean peak forces are extracted from integrated traction forces for pacing with frequencies ranging from $f = (0.5\text{–}1.5)\,\mathrm{Hz}$.

5.1.5 Discussion

Electrical stimulation is one of the key elements in cardiac tissue engineering, enabling tissue maturation, probing of excitability, and synchronization to a defined baseline beating frequency for drug testing. Thus, a facile integration into existing HoCs is desired. By stimulating tissues via electrical fields in the media compartment, a simple integration approach, with minimal changes in chip fabrication, is achieved. We electrically stimulated cardiac µ-tissues in both HoCs and combined stimulation with readouts of Ca propagation, O_2 levels and contractile forces, demonstrating several future applications.

Integration of pacing We presented two approaches for integrating pacing capabilities into HoCs: Pacing via inserted wire electrodes and pacing via fluidic media connectors. Both implementations integrate electrodes within the media compartment and successfully stimulate tissues in the tissue chamber, leading to precise con-

trol and an adaption of observed tissue beating rate within a tissue-specific range. Each integration was investigated for a distinct HoC, however, both concepts can be utilized with any chip geometry.

Both approaches offer a facile electrode integration with minimal necessary adaptions in chip fabrication. Pacing via inserted wire electrodes solely requires the punching of two additional access ports compared to the default chip fabrication. The integration strategy allows a flexible choice of employed electrode material, which can even be arbitrarily exchanged. However, the integration of pacing wires via additional inlets creates an additional leakage source, especially crucial for the centrifugal HoC which is heavily loaded during centrifugation. Due to the manual punching procedure, perfect electrode placement can not be granted, most likely yielding small deviations in electrical field distribution between the four upper and four lower tissue chambers succeeding the branching. More crucial, wrong placement of the electrode could even clog the media supply. Contrary, pacing via fluidic media connectors evades any changes in chip fabrication, representing the most facile integration. However, stimulation via fluidic connectors constrains the electrode material to the connector material (stainless steel), which might not be necessarily optimized for electrophysiology and could lead to the generation of toxic byproducts. We did not observe adverse effects in pacing for short time periods (up to 10 min). However, compared to pacing in a static system, existing media flow could help in removing toxic byproducts, such that pacing can be also carried out for longer time periods [226].

As both approaches utilize media as conductor, they are prone to air bubbles in the media channel, preventing electrical signal transduction. So far, all tissues formed in one system were paced with the same parameters. By splitting the media supply in the centrifugal HoC to two individual supplies perfusing four tissues each, chips could be paced under two conditions within the same chip, enabling the direct comparison of both pacing conditions. In general, contacting the electrodes required attachment of crocodile clamps for each individual chip, mechanically stressing the media compartment during attachment. In future electrode integration strategies, a simplified standardized connection is desired, achievable by, e.g., fixing the whole chip and contacting electrode pads on the microscope slide via pogo pins.

Our simulations predict a homogeneous electrical field in the shaft region for both investigated HoCs. Compared to electrical fields in the order of $E \approx 5\,\mathrm{V/cm}$, conventionally applied for pacing cardiac tissues, the predicted field strengths (centrifugal HoC: $E = 0.3\,\mathrm{V/cm}$, Spheroflow-HoC: $E = 0.8\,\mathrm{V/cm}$) are reduced with chosen pacing parameters [214]. The utilized parameters however still induced robust pacing which is most probably balanced by an increased pulse width of 50 ms compared to commonly used 5 ms. If higher fields are desired, tissue channel sealing plugs could be used as electrodes (leading to a reduced electrode distance in the Spheroflow-HoC) or the positioning of external electrodes adjusted.

Our findings reveal a negligible influence of the porous membrane onto electrical field distribution. Contrary to hydrodynamic considerations, the electrical resistance of a single pore can be neglected compared to the resistance in the media channel,

yielding considerable charge flow into the tissue layer. Presented simulations modeled the tissue chamber in a simplified way as empty compartment filled with media, similar to a previous approach [62]. However, subsequent studies should also explicitly include distinct electrical properties of the tissue to further elucidate occurring field strengths. So far, we investigated the application of a static voltage. However upon pacing, the voltage is applied in short pulses of pulse width $\leq 50\,\mathrm{ms}$. Thus, compared to a static simulation, electrical fields are probably initially increased and further decrease below estimated field strengths, induced by capacitance effects.

We developed the low-cost pulse generator EASYPACE as a valuable open source hardware tool for the scientific community offering easy fabrication and scriptable pacing capabilities. Provided automation capabilities are of special interest for running low-cost and efficient overnight experiments involving various pacing parameters or frequency sweeps. Compared to previously presented do it yourself pulse generators, EASYPACE does not rely on potentially code-blocking calls to the `delay()` function, granting accurate pulse timings and maintaining continuous response to user input [218]. Furthermore, the ability to control the pulse generator via serial commands is a unique feature, enabling arbitrary remote control of pacing cycles. In contrast, the pulse generator presented by Tamargo *et al.* requires the flashing of a modified firmware upon changing of individual pulse parameters for frequency sweeps [100].

Analysis of Ca signaling We demonstrated the applicability of the Spheroflow-HoC for a fluorescence-based readout of Ca propagation velocities. Due to the chamber-guided tissue shape of an aligned fiber, a linear propagation along the fiber main axis occurs. The direction of signal propagation can be adjusted by the pulse polarity. Determined Ca propagation velocity of $\bar{v}_{\mathrm{sig}} = 55\,\mathrm{mm/s}$, averaged over both pacing directions, coincides with velocities measured in comparable systems of $v_{\mathrm{sig}} = 46\,\mathrm{mm/s}$ and $v_{\mathrm{sig}} = 95\,\mathrm{mm/s}$ [25, 276]. Thus, developed system allows in future studies the investigation of external effects, e.g., tissue maturation via electrical stimulation or drug administration, onto Ca handling properties. Determined propagation velocity is a rough assessment, restricted in resolution by the temporal acquisition resolution. Increasing the acquisition frame rate in future studies would lead to a more precise determination of propagation velocity. The accompanying increase in signal noise could be circumvented by an increase in dye concentration.

Combination with O_2 monitoring We provided a biological proof-of-concept of combined stimulation and O_2 probing inside a HoC, assessing metabolic tissue activity under the influence of external pacing. As a sensor calibration obtained from uncovered substrates was applied, measured absolute O_2 levels slightly deviate from actually occurring levels (cf. subsection 4.2.2) but provide a valid qualitative evaluation of observed pacing influence.

Our findings revealed increased O_2 consumption of cardiac tissues upon electrical stimulation within a microphysiological system, in line with a similar study con-

ducted on O_2 consumption in myobundles undergoing electrical stimulation [277]. We rule out oxygen scavenging as cause of observed drops in p_{O_2}. The comparison with long-term measurements in empty chambers perfused with media indicated that employed resin does not scavenge O_2 contrary to chips fabricated from OSTEMER, a thiol-ene based resin similar to employed resin NOA 81 [176]. Observed drops in p_{O_2} are synchronized with phases of pacing, strongly hinting to an influence of pacing. As pacing of empty chambers under identical culture conditions did not reveal any influence on p_{O_2}, we rule out electrically induced changes in p_{O_2}. It is plausible that electrical stimulation increased the tissue beating frequency, yielding increased O_2 consumption. With increasing pacing frequency, tissue metabolism and thus oxygen consumption is increased, explaining observed correlation between O_2 consumption and pacing frequency.

So far, we only investigated relative jumps in O_2 consumption. As the sensor is directly integrated below the tissue, further theory-assisted considerations are needed to quantify the tissue consumption rate from measured localized partial pressure. Developed chip design distinguished by O_2 impermeable side walls should allow simplified modeling by an O_2 sink and defined O_2 influx, enabling the exact quantification of stimulation-dependent O_2 consumption rates in future studies.

Combination with force sensing We presented proof-of-concept for integrated force measurements coupled to electrical stimulation in the Spheroflow-HoC. We observed clear influence of externally applied electrical stimulation, yielding to an adaption of beating rate as well as decreased force amplitude. We highlight that magnitudes of determined forces are accompanied by great uncertainty due to low bead densities and the acquisition from a minimal, not necessarily representative, subset of the complete chamber. Hence, we focus in our discussion on relative force changes.

Observed force-frequency relationship supports the findings of Ronaldson-Bouchard *et al.*, who determined a negative force-frequency relationship in non-stimulated tissues composed of hiPSC-derived CMs, suspended between elastic pillars [81]. According to the authors, a negative force-frequency relation is an indication of the immature state of the cells. As introduced spheroids were investigated on day 3 after injection and did not undergo extended electrical stimulation, we also assume an immature state of investigated tissues, leading to observed force decrease with increasing stimulation frequency. Ronaldson-Bouchard *et al.* described the transition to a positive force-frequency relation upon tissue maturation achieved with pacing.

Developed platform thus allows in future studies the investigation of force development upon tissue maturation via electrical stimulation. As fundamental improvement, the deposited bead density has to be optimized, allowing a more accurate determination of the displacement field within the whole pad region. We observed tissue adhesion throughout the whole channel, including side walls. For a reliable quantification of twitch forces, constrained attachment to the soft pad with lifting

of the tissue fiber in the shaft region is necessary, mapping all fiber contractions to measurable tractions.

5.2 Cyclic stretching of endothelial cells

We developed and investigated a novel microphysiological system allowing the application of defined strain onto monolayers of cells adhered to a flexible membrane. Although several stretching platforms already exist, the major goal is the implementation of a novel membrane material which promises improvements for a scaled up fabrication and chip integration, compared to conveniently employed PDMS membranes.

Conducted studies investigate the applicability of a thermoplastic elastomer (TPE) membrane integration into thermoplastic-based microfluidic environments and analyze deflection and strain properties. The ultimate goal is the integration of a stretchable porous membrane into an existing Alveolous-on-Chip model (based on the MOTIF chip), which cultures endothelial cells on the liquid side of the membrane and epithelial cells on the air side [192]. For an accurate emulation of human physiology, both cell layers should be stretched, actuated by periodically varying pressures in the air compartment. To minimize stresses on cells cultured on the air side, it is therefore crucial that employed membrane deflects under pressures naturally occurring in the human breathing cycle, i.e., $\leq 10\,\mathrm{mbar}$ [278]. The initial investigation focuses on deflection and integration capabilities of a plane membrane without integrated pores to verify required actuation under low pressures. If investigated membrane can be integrated and actuated in an appropriate way, pores can be incorporated during the membrane manufacturing process in subsequent stages.

The characterization of absorption properties of TPE was part of a study investigating TPE as alternative chip material and is published in "Schneider, S. *et al.* Facile Patterning of Thermoplastic Elastomers and Robust Bonding to Glass and Thermoplastics for Microfluidic Cell Culture and Organ-on-Chip. *Micromachines* **12,** 575 (2021) [28]".

5.2.1 Small molecule absorption of TPE

Due to its superior bonding (intrinsically adhesive surface) and microstructuring (amenable for scaled up production techniques such as hot embossing and laser cutting) properties, TPE is a promising material for microfluidic systems. One of the major limitations of conveniently used PDMS-based systems is the absorption of small molecules, potentially affecting concentrations of, e.g., injected drugs in an uncontrolled manner, confounding read-outs [271, 272]. We therefore compared the absorption of small molecules into TPE systems against PDMS systems.

Three different rhodamine dye molecules with similar molecular weights ((479–491) g/mol) were used as test system providing different hydrophobicities ($2.1 < \mathrm{logP} < 7.8$) [279]. Dye solutions were injected into straight microchannels

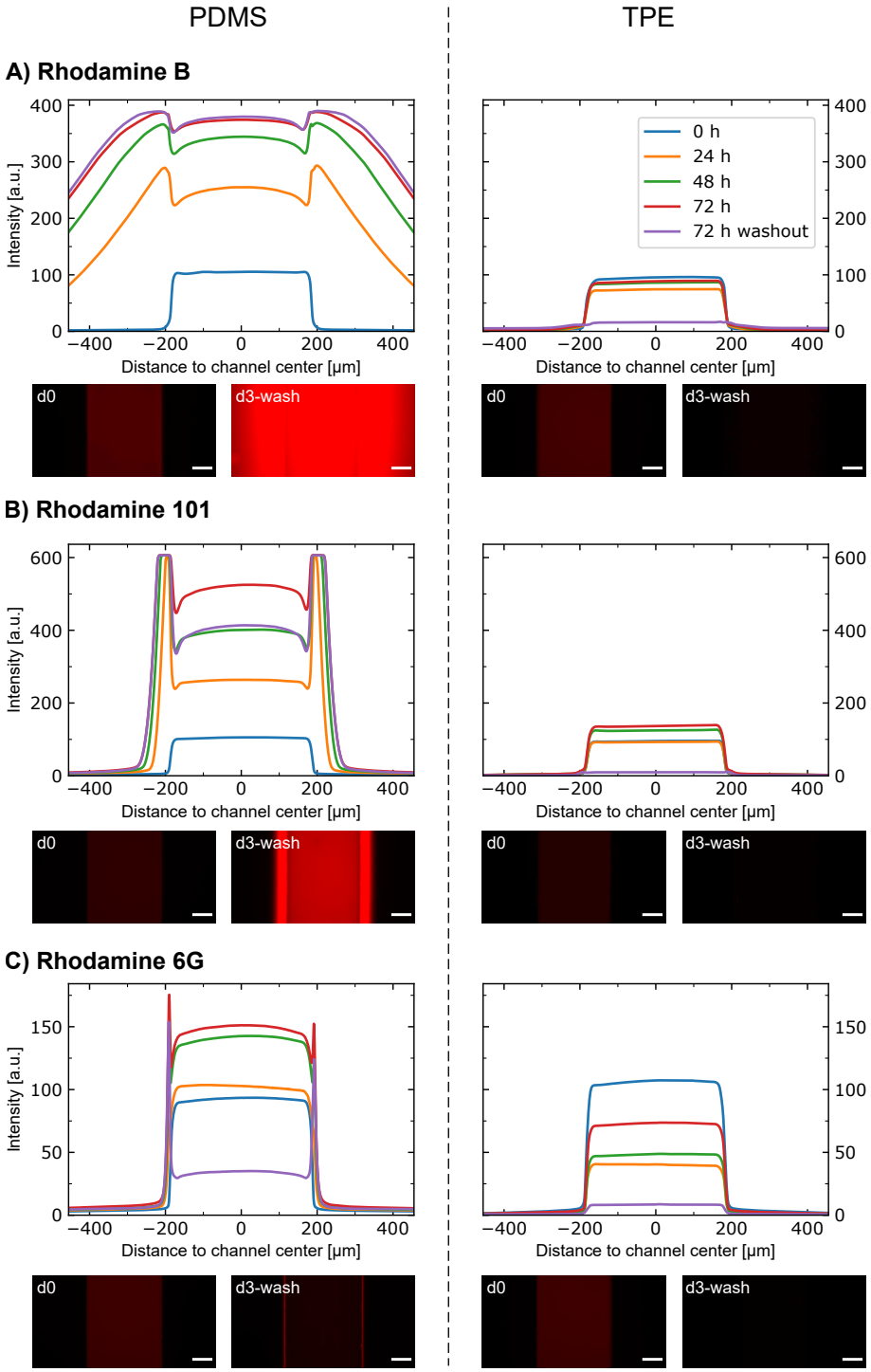

Figure 5.7 Characterization of small molecule absorption of TPE. Comparison with absorption in PDMS channels over a timespan of three days. Profiles at different incubation time points as well as images right after dye perfusion and after three days are shown. **(A)** Rhodamine B. **(B)** Rhodamine 101. **(C)** Rhodamine 6G. Figure adapted from Ref. [28] under CC BY 4.0 license.

bonded to glass, fabricated from TPE and PDMS in identical geometry. Fluorescence profiles were monitored at different time points up to 72 h after dye injection in the microchannels (Fig. 5.7). After 72 h, the channel was thoroughly rinsed with PBS and monitored again. In the TPE devices, there is no visible change in signal profile for all three tested molecules. The fluorescence signal can only be detected in the channel region (distance to channel center x, $|x| < 200\,\mu m$). Similarly, after washout, a remaining signal of diluted rhodamine can only be detected in the channel region. In the PDMS devices, rhodamine signals are detectable in the channel side wall ($|x| > 200\,\mu m$). The signal increases in the channel region with increasing incubation time. Rhodamine B displays a higher integrated signal in the side wall than rhodamine 101. For rhodamine 6G, peaks in signal intensity can be observed directly at the channel edge. After washout, the rhodamine signal profile corresponds to the profile at 72 h for rhodamine B. Rhodamine 101 and 6G display a slightly reduced signal intensity in the channel center with remaining side wall intensity.

5.2.2 Integration of TPE membranes in microfluidic systems

As TPE membranes were extruded from TPE pallets by an external service provider and not purchased as a standardized and well-characterized starting product, elastic material properties are not known *a priori*. The thickness of extruded TPE sheets was estimated by the manufacturer to $d = 40\,\mu m$.

For the investigation of membrane integration and deflection properties, we designed a simplified testing chip mimicking the blueprint of an OoC with two superposed channels (Fig. 5.8 A). Investigated TPE membrane is sandwiched between two lasercut PMMA layers. The upper compartment is sealed with PDMS, ensuring tight connections for pressurizing the chamber while the lower compartment is open for direct membrane access, providing optimal imaging conditions. The bottom chamber comprises dimensions similar to the channel geometry in envisioned successive microphysiological system adapted to the MOTIF chip geometry.

We established the integration of fragile TPE membranes into thermoplastic microfluidic environments. Membranes were structured with a laser cutter and bonded to PMMA modules following plasma-treatment and clamping at elevated temperatures. The chip was sealed by attaching the PDMS top layer with double-sided adhesive tape (Fig. 5.8 B).

Membrane integration was verified by attaching an empty syringe to the upper layer and manually applying pressures by slightly tapping the syringe plunger. By monitoring the membrane with a microscope, we verified repeated membrane deflections. We integrated the TPE membrane into the injection molded basic component of the MOTIF Lung-on-Chip model following previously developed protocol. The thermoplastic basic component encompasses a tissue and media channel, featuring an inset for membrane integration. In the standard composition, the chip is sealed with polymer foils after the integration of a PET membrane. Due to a reduced bonding surface area, a stamp covering the membrane inset was lasercut out of PMMA

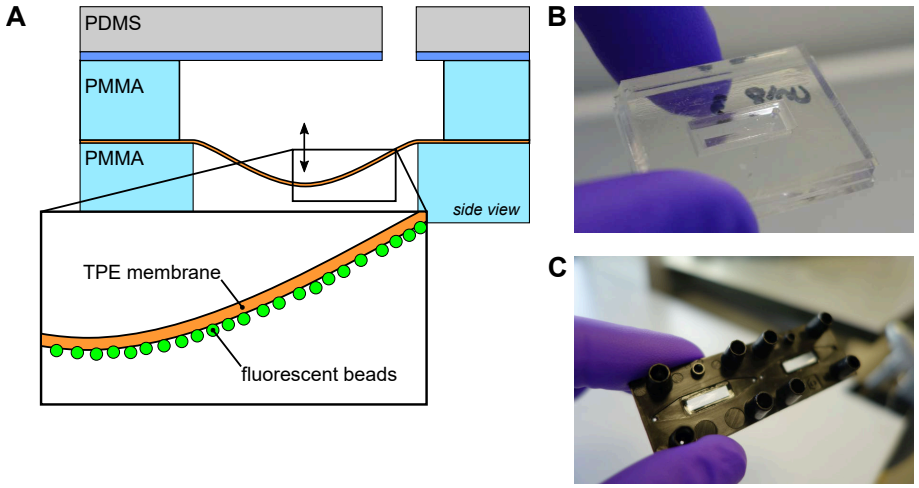

Figure 5.8 Embedding of TPE membrane in microfluidic systems. **(A)** Composition of test system for verifying membrane integration and probing of mechanical membrane properties. The membrane is sandwiched between two PMMA layers and sealed with PDMS. Membrane deflections can be recorded from attached fluorescent beads. **(B)** Picture of assembled characterization chip. The sealed top compartment allows application of pressures while the lower part is left unsealed. **(C)** Picture demonstrating the integration of a TPE membrane into an established Alveolus-on-Chip (MOTIF chip).

and placed during the bonding step onto the liner-covered TPE membrane. By carefully blowing compressed air onto the integrated membrane, we asserted membrane deflections without rupture. Visual inspection revealed a smooth integration of the membrane (Fig. 5.8 C).

5.2.3 Simulation of deflection profiles

We investigated the deflection profile and area strain of a uniformly loaded rectangular plate of geometry identical to employed membrane ($w = 2\,\text{mm}$, $l = 10\,\text{mm}$, $d = 40\,\mu\text{m}$) via FEM analysis. Compared to the theoretical description in subsection 1.3.2, the shorter membrane side runs along the y coordinate, describing deflections of the central profile at $x = 5\,\text{mm}$. An elastic material with $E = 1.3\,\text{MPa}$ and $\nu = 0.49$ is assumed, adapting Young's modulus from experimentally determined values and Poisson ratio ν from literature [240, 241].

The 2D deflection profile for $p = 20\,\text{mbar}$ reveals a deflection which is almost independent of the x-position in the central area ($2\,\text{mm} < x < 8\,\text{mm}$) with a maximum deflection of $w_0 = -270\,\mu\text{m}$ (Fig. 5.9 A). Corresponding area strain evaluated at the bottom surface indicates a homogeneous stretching of $\epsilon_\text{A} \approx 6\,\%$ in the majority of the surface ($2\,\text{mm} < x < 8\,\text{mm}$, $0.2\,\text{mm} < y < 1.8\,\text{mm}$; Fig. 5.9 B). At both sides of the long axis, two localized maxima of $\epsilon_\text{A} \approx 7\,\%$ are noticed.

Area strain profiles of the central plane ($x = 5\,\mu\text{m}$) reveal a homogeneous area

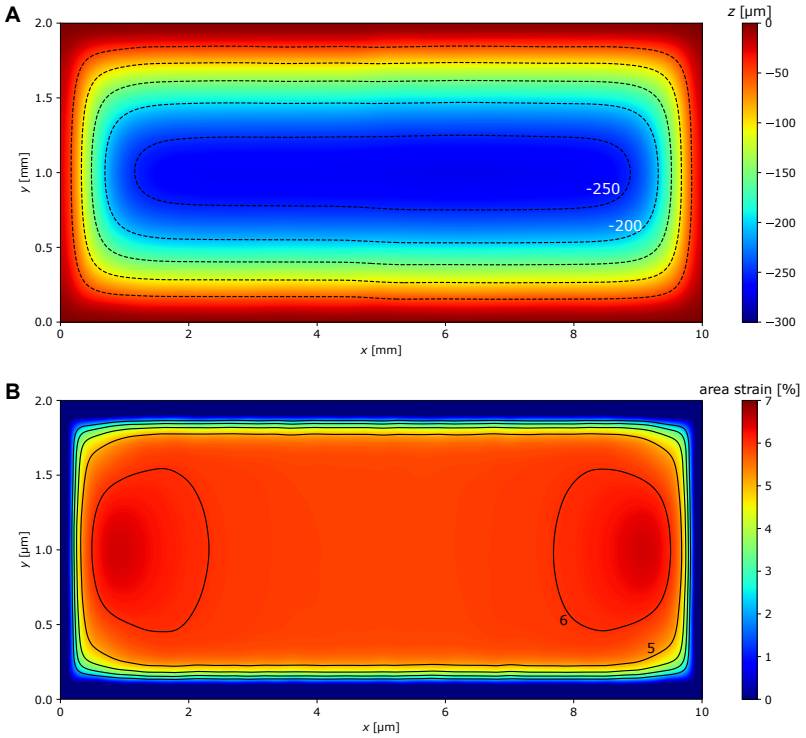

Figure 5.9 FEM analysis of membrane deflection ($l = 10\,\text{mm}$, $w = 2\,\text{mm}$) upon application of 20 mbar. **(A)** 2D deflection profile indicating deflections $z < -250\,\mu\text{m}$ in the central region. **(B)** Area strain indicating homogeneous stretching among the bulk of the membrane. Local maxima appear at both ends of the longer side.

strain in the center region ($0.2\,\text{mm} < y < 1.8\,\text{mm}$) for applied pressures of up to 40 mbar (Fig. 5.10 A). In close distance to the clamped membrane edge, negative strains are predicted. For membranes with aspect ratios approaching infinity, a condition which is according to theory already sufficiently fulfilled by employed aspect ratio of $length/width = 5$, analytical solutions can be employed to estimate the membrane deformation following eqs. 1.12 and 1.13 [197].

Comparing the central strain as a function of central deflection, good agreement with the analytical parabolic relation is found (Fig. 5.10 B). Similarly, strains obtained from FEM simulations agree well with the analytical consideration of a $\epsilon_\text{A} \propto p^{3/2}$ dependence (Fig. 5.10 C). Compared to the analytical solution, simulated values are, however, elevated: e.g., for an applied pressure of 30 mbar, the analytical solution predicts $\epsilon_\text{A} = 6.8\,\%$, whereas the FEM solution reveals $\epsilon_\text{A} = 7.5\,\%$.

5.2.4 Mechanical characterization of TPE membranes

For an experimental characterization of integrated TPE membrane, deflection profiles were recorded in the characterization platform. Increasing pressures were applied to the compression compartment with a pressure pump and z-stacks of deposited fluorescent beads recorded. Following filtering of obtained raw bead posi-

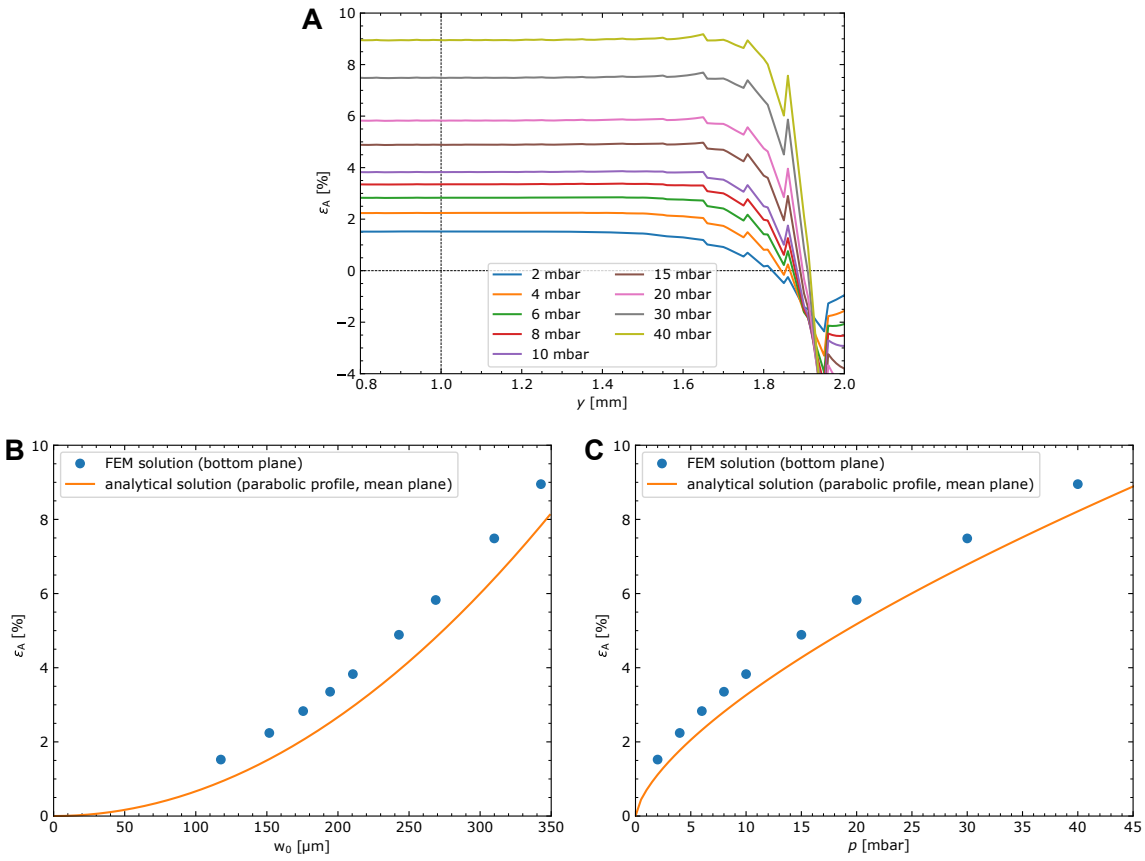

Figure 5.10 FEM analysis of central plane ($x = 5\,\text{mm}$) strain on the bottom of deflected membrane. The vertical line marks the channel center. **(A)** Strain profile along channel width y for various applied pressures. **(B)** Area strain as function of central membrane deflection w_0. The numerical solution evaluated on the bottom plane is compared with the analytical mid plane solution for a parabolic deflection profile. **(C)** Area strain as a function of applied pressure p. FEM solution is compared with analytical solution similar to (B).

tions, individual beads were linked between consecutive pressure steps to obtain a pressure-dependent displacement field. As the major membrane displacement occurred in z direction with displacements exceeding the distance between neighboring beads, particles were initially wrongly linked. Therefore, the average local z-position was subtracted for each particle, allowing accurate tracking of particles in an almost planar configuration. After adding previously subtracted z-displacements, particles were accurately linked between deformation states of applied pressures. Visual inspection reveals a plausible linking of particles, following a parabolic compression profile (Fig. 5.11 A). As z-stacks were recorded in the homogeneous central region where no variation of $z(x)$ is expected, we project all tracked particle positions on the same y-coordinate to obtain the central deflection profile $z(x, y) \rightarrow z(y)$. Similarly, we neglect deflections in x direction ($u_x \approx 0$) and map the displacement field

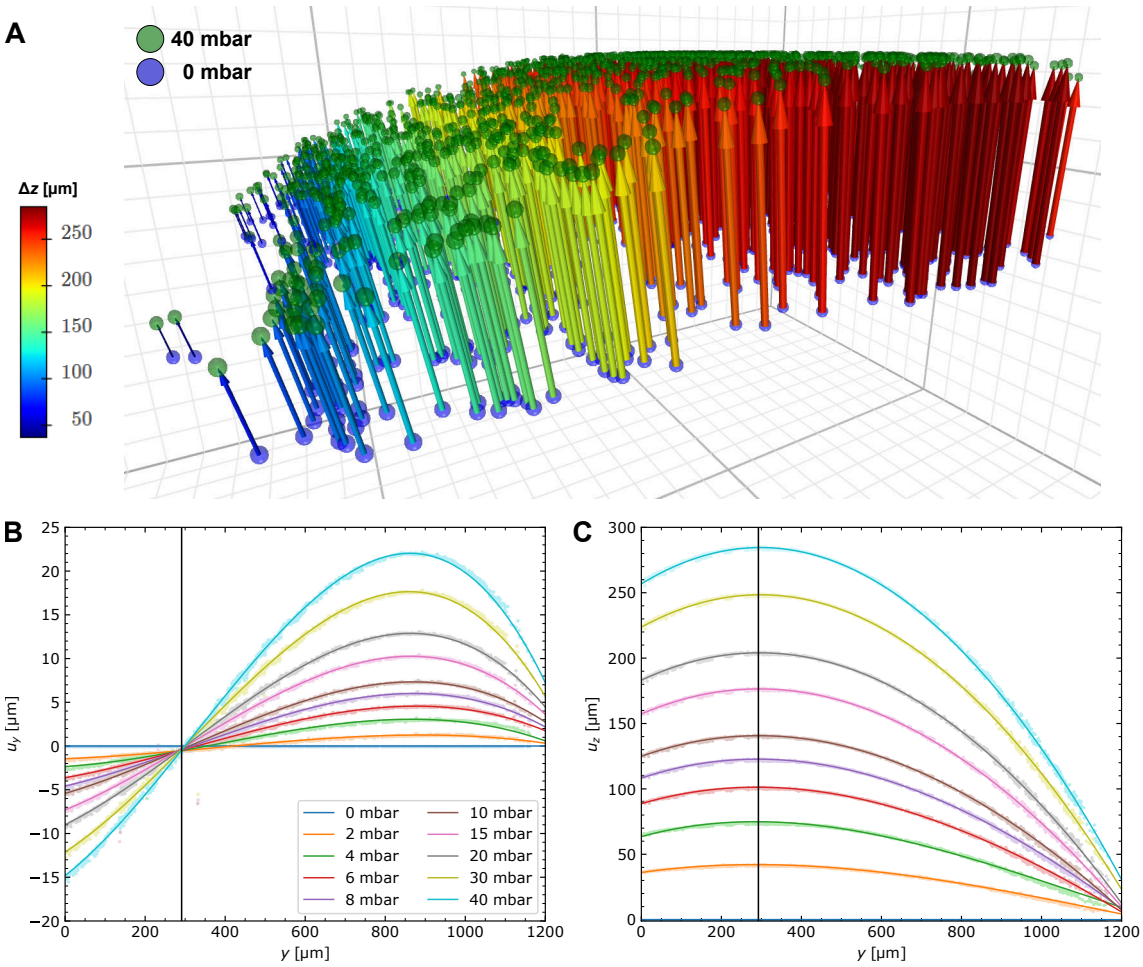

Figure 5.11 Displacement field obtained from tracking of membrane attached beads. **(A)** 3D view of particles linked between positions for two applied pressures. **(B)** Extracted center profile of displacement along the short side of the membrane (y direction) u_y. **(C)** Extracted center profile of displacement parallel to membrane normal (z direction) u_z. Vertical lines in (B) and (C) mark the channel center.

as a function of y. Individual displacement components $u_y(y)$ and $u_z(y)$ are then interpolated on a regular grid along the y-axis, yielding differentiable expressions for $u_y(y)$ and $u_z(y)$ (Fig. 5.11 B, C).

At the membrane center ($y = 300\,\mu\text{m}$), a displacement is absent in y direction; beads solely move straight upwards in z direction. For y-positions next to the membrane center, beads move in opposite directions perpendicular to the channel($u_y < 0$ for $y < 300\,\mu\text{m}$, $u_y > 0$ for $y > 300\,\mu\text{m}$) upon membrane deflection. A maximum in u_y is observed between the channel center and the edge. Displacements u_z are about one order of magnitude larger and correspond in shape to the theoretical description of a smoothed parabolic profile with a horizontal transition to the clamped membrane edge (Fig. 5.11 C).

To investigate the membrane deflection for varying pressures, membrane profiles

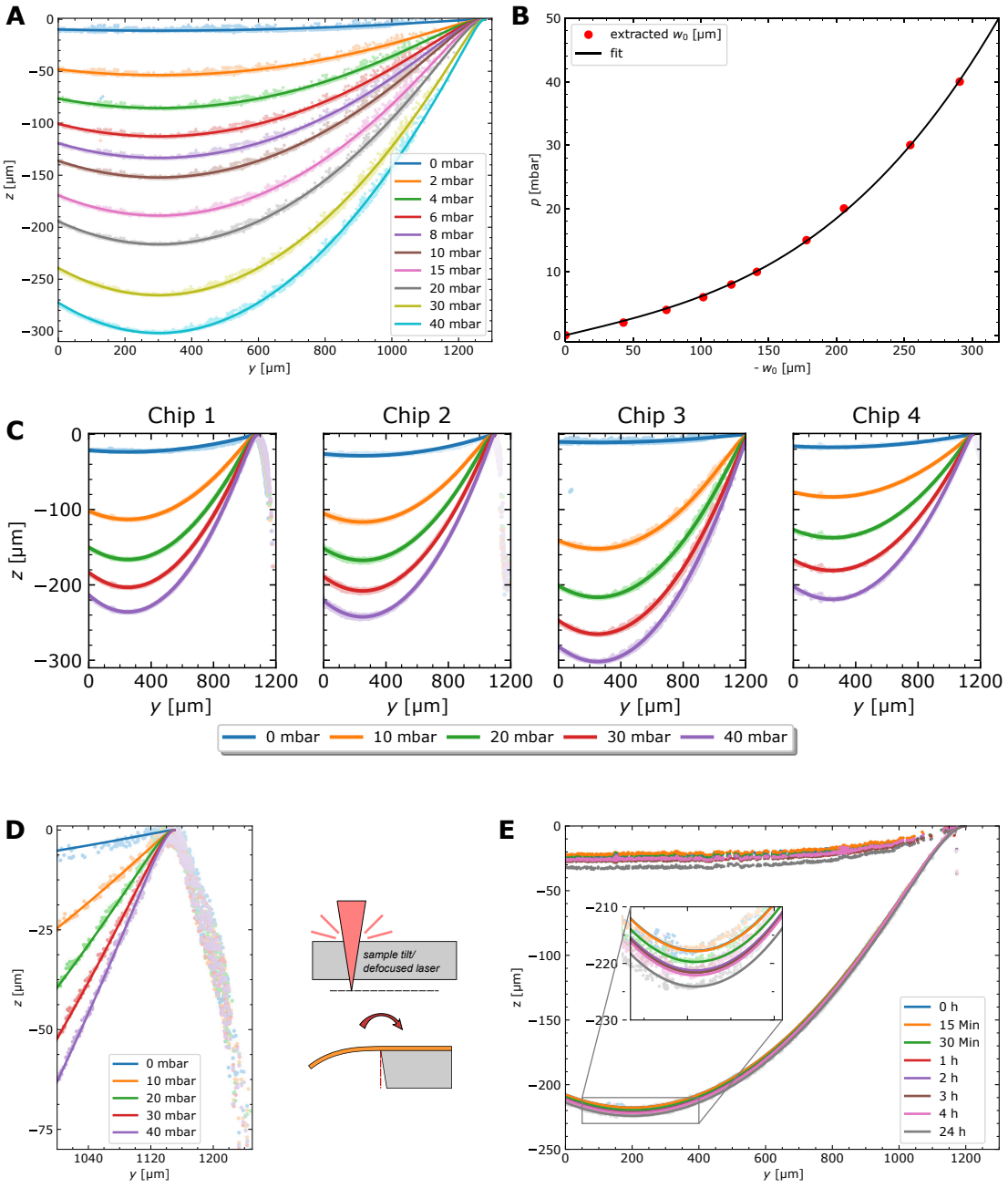

Figure 5.12 Evaluation of membrane deflection profiles. **(A)** Fits to deflection profiles acquired in fine pressure steps, enabling precise tracking of deformations. **(B)** Applied pressure p as a function of central deflection w_0 extracted from fits in (A). The elastic modulus is extracted from the fit to $p(-w_0)$. **(C)** Inter-sample comparison of deflection profiles. **(D)** Magnified deflection profile at membrane edge. Detected tilted edge is attributed to irregularities in the laser cutting process yielding a reduced chamber width and skewed side wall. **(E)** Comparison of deflection profiles measured at various time points (t = (0–24) h) under repeated stretching (cyclic pressure variation p = (0–20) mbar at f = 0.3 Hz).

were fitted with introduced fit function from eq. 1.15 corresponding to a parabolic center deflection smoothed to the clamped edge by a tanh function. Extracted central profiles could be fitted in good agreement with provided fit function yielding values for the central deflection w_0, corrected by a possible sample tilt and shift in z direction (Fig. 5.12 A). Determined central deflection $-w_0$ is further fitted to applied pressure p following 1.10. The fit agrees well with the experimentally determined $p(-w_0)$ relation and yields the product $\frac{E}{1-\nu^2}$ (Fig. 5.12 B).

Comparing deflection profiles for four stretched samples, all samples depict a similar deflection behaviour. However, inter-sample deviations can still be observed (Fig. 5.12 C). While Chip 1 and Chip 2 exhibit maximum deflections of $w_0 \approx -240\,\mu\text{m}$ at $p = 40\,\text{mbar}$, Chip 3 deflects to $w_0 \approx -300\,\mu\text{m}$ and Chip 4 to $w_0 \approx -220\,\mu\text{m}$. For all investigated samples the membrane is not perfectly flat in the unloaded state but exhibits a sagging of $w_0 \approx -20\,\mu\text{m}$. Comparing all profiles, they furthermore seem to differ in width. Examining the membrane edge of Chip 1 in detail, a steep straight increase in extracted profile is observed, which is attributed to the channel wall and not considered in the fit (Fig. 5.12 D, left panel).

For each sample, the elastic modulus is extracted from fits of $p(-w_0)$, considering the individual channel width a from the profile fit and assuming a Poisson ratio of $\nu = 0.49$ (Table 5.1). Extracted Young's moduli range from $E = (1.12\text{–}1.38)\,\text{MPa}$ with a mean of $E = (1.3 \pm 0.1)\,\text{MPa}$.

Table 5.1 Comparison of Young's moduli extracted from fits to $p(-w_0)$.

sample	width a [µm]	Young's modulus E [MPa]
C1	830	1.34
C2	846	1.27
C3	980	1.38
C4	900	1.12

As the envisioned use of the developed platform is an extended periodical stretching, we compared the long-term reproducibility of membrane deflection. Therefore the membrane was continuously loaded with a sinusoidal pressure variation of peak pressure $p = 20\,\text{mbar}$ at $f = 0.3\,\text{Hz}$. At distinct time points up to 24 h after initiation of actuation, actuation is stopped and profiles recorded in the unloaded state and at $p = 20\,\text{mbar}$ (Fig. 5.12 E). We observe minimal differences between profiles recorded after extended stretching periods. The absolute central deflection of $|w_0| = 218\,\mu\text{m}$ upon stretch initiation is increased by $\Delta|w_0| = 6\,\mu\text{m}$ to $|w_0| = 224\,\mu\text{m}$ after 24 h of continuous actuation.

We derive the spatial distribution of area strain from the interpolated central displacement field following eq. 1.14 (Fig. 5.13 A). Increasing strain is observed with increasing loading pressure, ranging up to $\epsilon_\text{A} = 5.8\%$ in the channel center. Strain is generally homogeneous in the central region with variations of less than $\Delta\epsilon_\text{A} = 0.5\%$ for applied pressures $p \leq 30\,\text{mbar}$. A decrease in strain is observable

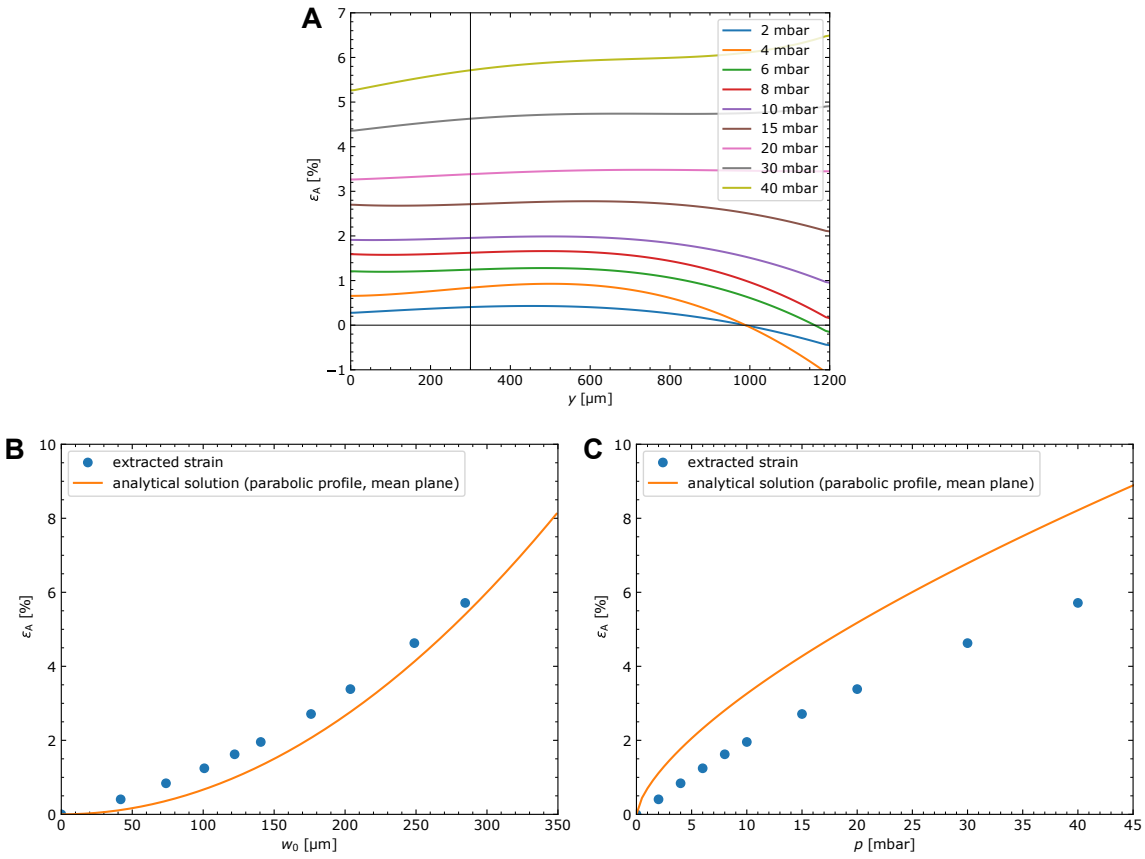

Figure 5.13 Measured strain inferred from tracking of beads on deflected membrane. **(A)** Central plane strain profile for varying applied pressures. The vertical line marks the channel center. **(B)** Area strain ϵ_A as function of central membrane deflection w_0. The measurement on the bottom plane is compared with the analytical mid plane solution for a parabolic deflection profile. **(C)** Measured area strain as a function of applied pressure p. The FEM solution is compared with the analytical solution similar to (B).

towards the edge region for $p \leq 15\,\text{mbar}$. Strain profiles for higher applied pressures deviate, showing an increase towards the edge ($p = 30, 40\,\text{mbar}$) or a horizontal trend ($p = 20\,\text{mbar}$).

Similar to the FEM analysis, we compare extracted central strain as a function of applied pressure and central deflection with the analytical solution for a parabolic deflection profile (Fig. 5.13 B, C). Extracted strains are of same order of magnitude and follow a similar parabolic and root-like trend. Considering the deflection-strain relation, extracted strains lie above the analytical approximation. A maximum deviation between measured strain of $\epsilon_a = 1.3\,\%$ and analytical strain of $\epsilon_a = 0.7\,\%$ is observed for $w_0 \approx 100\,\mu\text{m}$. However, contrary to FEM analysis, strains measured as a function of applied pressure are reduced in magnitude compared to the analytical solution. Higher deviations are detected for the strain-pressure relation, e.g., the analytical solution predicts $\epsilon_A = 6.8\,\%$ for $p = 30\,\text{mbar}$ while we measured $\epsilon_A = 4.6\,\%$.

5.2.5 Microphysiological stretching platform

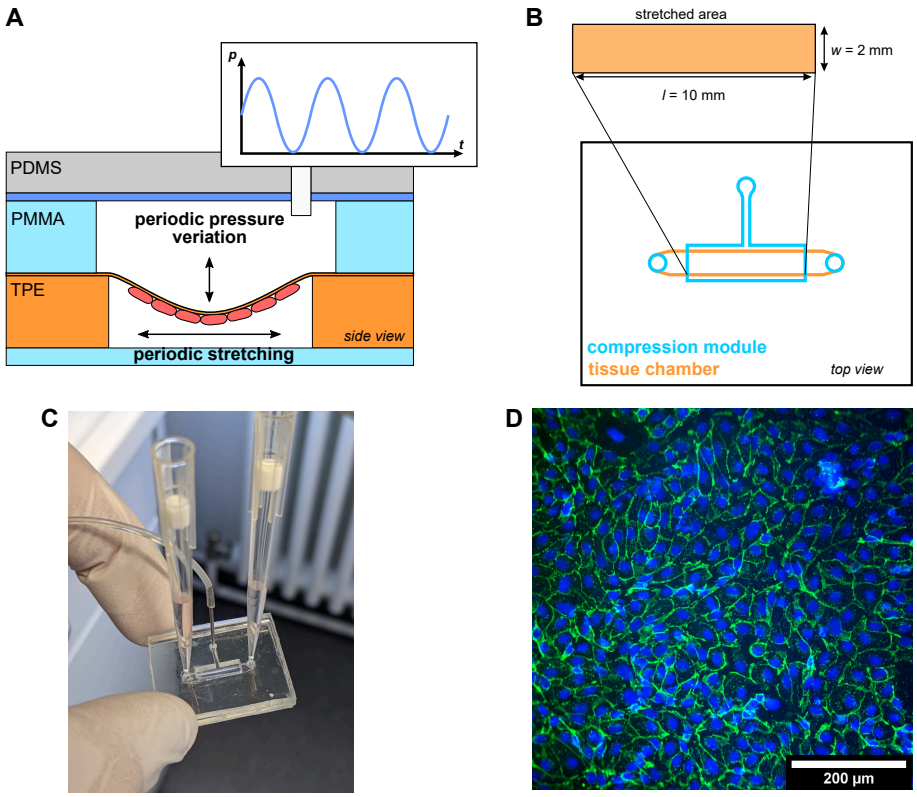

Figure 5.14 Microphysiological stretching platform integrating a TPE membrane. **(A)** Chip concept. Cells attached to the membrane in the lower compartment are stretched by applying a periodic pressure variation in the upper compartment. Compared to the characterization chip, the tissue layer is fabricated from TPE and sealed with PMMA. **(B)** Lateral chip design: The tissue chamber is comprised of a 2 mm wide channel, overlapped by the dead-end pressure module enabling membrane actuation. **(C)** Picture of assembled stretching platform for cell culture. Attached pipet tips provide a static media supply. **(D)** Immunofluorescence staining of iPSC-derived ECs cultured on the TPE membrane within developed chip (blue: DAPI, green: VE-cadherin).

Based on the introduced membrane characterization platform, a complete microphysiological system is developed. In contrast to the characterization chip, the bottom layer was fabricated out of TPE and sealed with a PMMA layer (500 µm; Fig. 5.14 A). By sealing the bottom layer, a tissue chamber is generated where cells can be injected, subsequently forming a monolayer on the flexible membrane (Fig. 5.14 A). The height of the tissue layer (750 µm) is comparable to the one of the established MOTIF chip (800 µm) such that similar culture conditions prevail. By utilizing established flow rates for media perfusion the same shear stress is applied on cultured cell layers. The overhead compression compartment allows the application

of defined pressures, leading to stretching of cultured cells. The culture chamber is designed as straight channel with two access ports. The above compression chamber overlaps the tissue chamber in a rectangular region matching the dimensions previously employed for investigations of mechanical membrane properties (Fig. 5.14 B). Hence, for initial stretching experiments, previously extracted pressure-strain relation can be assumed.

To verify the biocompatibility of the TPE membrane with employed cell type assuring cell attachment and precluding cytotoxicity, TPE membrane cutouts were bonded to PMMA and placed as insets into well plates. Subsequent seeding of hiPSC-derived ECs (differentiated by Hristina Koceva, Universitätsklinikum Jena) onto TPE-covered insets and culture following established well plate culture protocols revealed satisfactory attachment, comparable to the well plate control.

hiPSC-derived ECs were injected into developed microphysiological system and the was chip flipped upside down, leading to a sedimentation of cells onto the membrane. Cells were cultured using static media supply by pipet tips and fixed on day 2 after injection (Fig. 5.14 C). Immunofluorescence staining of VE-cadherin and DAPI reveals the formation of a confluent layer with expression of junction proteins between ECs (Fig. 5.14 D).

5.2.6 Discussion

Current stretching platforms mostly integrate PDMS membranes which are prone to small molecule absorption and rely on complex fabrication procedures. We identified TPE as suitable alternative offering facile and scalable chip integration as well as appropriate elastic properties, allowing deflections under physiological pressures. Absorption studies on TPE revealed decreased absorption compared to PDMS, which is crucial for subsequent unadulterated drug testing studies. Following chip integration and mechanical characterization, we presented successful culture of ECs in a microphysiological stretching platform integrating a TPE membrane. Our developed chip can thus be applied in future stretching studies.

Small molecule absorption of TPE The absolute fluorescence intensity on different days can be affected by absorption to the tubing and connectors, bleaching of fluorescence dye, variation in lamp intensity and evaporation. Hence, we focused on the comparison of lateral fluorescence profiles for the interpretation of the results.

We exclude critical absorption of investigated test molecules into TPE due to the restriction of monitored signal to the channel region. The channel signal is reduced after washout, indicating a residual dilution of rhodamine dye with negligible absorption to the channel ceiling. Contrary, the high signal in the channel side wall indicates absorption into the PDMS devices. The absorption of the three dyes is demonstrated not only by an increasing profile width over time but also by the remaining high intensity after washout which we attribute to absorption to the channel ceiling.

Our observation is in line with other studies using SEBS formulations for microfluidic chip fabrication: Domansky *et al.* show significantly lower absorption of rhodamine B and the drug pirfenidone in oil-free SEBS compared to PDMS [280]. In general, low absorption rates of small molecules make TPE an attractive alternative for microfluidic cell culture platforms. The ability to precisely deliver cellular stimulants while not losing cellular outputs provides TPE with an advantage over common materials used in the field, such as PDMS [281]. Regarding absorption properties we therefore consider TPE as superior membrane and chip material compared to PDMS.

TPE integration We verified successful TPE membrane integration into microfluidic systems. Observed membrane deflections indicate satisfactory sealing of the compartment by the membrane. Hence, developed membrane integration protocol provides a simple embedding of TPE membranes into thermoplastic chip components and can also be used to join individual layers. Due to its facile combination with other microfluidic modules, we expect a wide adaption. Especially the roll-to-roll production process allows a scaled up production and implementation on industrial scale. One of the remaining challenges is the optimization of – so far – tedious handling procedures of thin TPE layers as well as standardized fabrication of membranes of defined thickness.

Deflection simulation FEM simulations predict a homogeneous stretching of the bulk part of the membrane, which is crucial for intended use in cell stretching experiments, yielding precisely defined experimental conditions. Stress maxima are attributed to the close distance to the longitudinal edge, restricting membrane deflection. As verified by the simulation, it is sufficient to investigate the central plane ($x = 5\,\mathrm{mm}$) deflection offering a good description of the bulk part of the membrane.

The observed slight discrepancy between FEM simulation and analytical solution is attributed to the high, yet finite, aspect ratio, deviating from the estimation for infinite extents. Furthermore, the analytical solution is calculated for the vertical midplane ($z = 20\,\mu\mathrm{m}$), whereas the simulation is evaluated on the membrane bottom surface ($z = 0\,\mu\mathrm{m}$). As the strain varies linearly over the membrane cross section, observed increased strains at the bottom surface are plausible.

All in all, we verify the use of the analytical expression as suitable initial estimation for strains achievable with a chosen channel geometry. Thus, the membrane geometry can be tailored to achieve the desired load-strain dependence. In projected application the membrane is deflected into an enclosed channel structure. Hence, it is important to design the microfluidic device accordingly, allowing enough space for deflection. Contact of the membrane with the channel bottom might lead to membrane attachment, leading to permanent clogging. The deflection corresponding to the maximum applied strain should therefore yield a sufficient remaining channel height, preventing excessive changes in flow resistance. Otherwise, upon perfusion at constant flow rate, an increased fluidic resistance would lead to extensive pressure

buildup in the lower compartment countering the applied top pressure, resulting in a less defined adjustment of area strain.

Mechanical characterization We successfully developed a framework for an accurate determination of deflection profiles by tracking bead positions. Additional linking of bead positions at varying pressures allows an accurate determination of the central plane displacement fields $u_y(y)$ and $u_z(y)$ in addition to a bare description of the deflection shape $z(y)$. The implemented approach thus provides extended insights, allowing a direct measurement of strain and comparison with theoretical estimations. Comparable investigations of stretching platforms usually limit themselves to estimate applied stretch from the central deflection [193, 282].

We observed inter-sample variations in deflection behaviour which we mainly attribute to variations in the production process leading to varying channel widths. Observed skewed side wall could be the effect of a defocused laser or a tilt of the whole layer. A defocused laser during the cutting process would result in a cone-shaped ablation leading to a tilted channel edge as well as a reduced width (Fig. 5.12 D, right panel). Compared to a designed channel width of 2 mm, channel widths obtained from fitted profiles were all reduced, supporting this hypothesis. We successfully determined the elastic modulus to $E = (1.3 \pm 0.1)\,\mathrm{MPa}$ which lies in the range of PDMS ($E \approx 2\,\mathrm{MPa}$), making investigated material a suitable replacement for PDMS membranes. Other studies specified the elastic modulus to $E = (1.75 \pm 0.02)\,\mathrm{MPa}$ which differs by 26 % from our observation [283]. As we could only determine the combined material parameter $\frac{E}{1-\nu^2}$, an assumed reduced Poisson ratio would yield higher Young's moduli. Observed difference in material properties might also arise from variations in employed foil extrusion process parameters. Furthermore, utilized membrane was characterized by optically distinguishable spots on the surface which hints on local variations in thickness and/or material properties.

As minimal changes in deflection upon continuous loading are detected, we confirm long-term stability of integrated membrane, suitable for the application in extended cell stretching experiments. Observed changes in central deflection translate to changes in applied strains smaller than 0.5 percentage points, verifying its appliance for a defined stretching stimulation.

Our findings confirm that the spatial determination of area strain is feasible with chosen bead tracking approach. Homogeneous strain fields are verified, a crucial premise for applications requiring defined strains. Obtained strain fields reveal a homogeneous central strain for low applied pressures, decreasing towards the membrane edge, similar to the FEM solution. However, inconsistencies compared to the FEM solution are also observed, i.e, for 40 mbar the strain is not symmetrically distributed and actually increasing towards the edge. Generally, we did not verify how well beads are bonded to the membrane. An extensive membrane deflection might lead to shifting of beads on the membrane, accounting for a wrong determination of area strain profiles. Furthermore, as membranes were produced as prototypes in a non-established extrusion process, employed membranes might comprise local

inhomogeneities yielding strain fields which deviate from the FEM solution.

Central strains measured as a function of center displacement displayed sufficient agreement with the analytical solution, deviating to higher strains, similarly to the FEM solution. Thus, the strain from the actual deflection profile can be well approximated from the estimation of a parabolic deflection profile, guiding the design process of further microfluidic systems. Contrary, strains measured as a function of applied pressure were overestimated by the analytical solution. We attribute this difference to a reduced membrane deflection. As previously discussed, it is conceivable that the actual elastic modulus is higher than estimated, such that an increase of elastic modulus in the analytical approximation would yield better agreement with the experimentally determined strain. Furthermore, due to individual sagging of membranes, the actual membrane width is underestimated in the analytical approximation.

All in all, we demonstrated a thorough mechanical characterization of embedded TPE membranes, showcasing the capability for delivering defined mechanical strains. We verified the generation of strains of up to $\epsilon_A = 6\,\%$ for applied pressures of 40 mbar. Needed pressures are elevated compared to physiological pressures of $p \leq 10$ mbar. Nevertheless, Zamprogno *et al.* also applied pressures of 40 mbar to stretch lung alveolar ECs by $\epsilon_A = 10\,\%$ without reported detrimental effects [193]. In a next step, geometrical parameters can be tweaked to achieve desired pressure-stretch relation. As the membrane is extruded from the raw material, it seems promising to adjust the extrusion process, aiming at membranes of even reduced thickness, e.g., in the range of conveniently used PET-membranes (10 µm). Reduced thicknesses would automatically result in a reduction of needed deflection pressures, approaching the physiological range. Generally, a standardized membrane fabrication is essential for future integration into OoC systems.

Biological proof-of-concept Satisfactory cell attachment reveals the biocompatibility of investigated TPE membrane for used cell type. Our findings demonstrate the applicability of developed stretch chip for culturing monolayers of ECs within a controlled microfluidic environment, forming cell-cell contacts. Due to the thin bottom layer, immunofluorescence staining and subsequent optical analysis of cell morphology is feasible without the need to disassemble the chip. Developed system is thus appropriate for investigating the effect of cyclical stretching onto cultured EC layers in future experiments. A prospective integration of pores into the TPE membrane will enable the extension of currently static air-liquid culture systems to dynamic cultures incorporating mechanical stimulation.

In further applications for cell stretching experiments it is important to also consider the mechanical influence of adhered cell layer, potentially affecting the deflection behaviour. For a quick characterization without the deposition of fluorescent beads, we recommend to extract z-positions in deflected and undeflected state of the channel center by focusing on the surface in brightfield microscopy. From the central deflection, prevailing stress can be then calculated following eq. 1.12.

5.3 Homogeneous 3D compression of hydrogels

Another common mechanical stimulus in the human body is compression, occurring, e.g., in cartilage tissue during walking. In following subsections we develop and characterize a novel platform for culturing cells dispersed in hydrogel, providing capabilities for a homogeneous gel compression. The system is designed to enable the study of pathophysiology of osteoarthritic diseases, or more generally, how mechanobiological cues influence the differentiation of stem cells to chondrocytes.

5.3.1 Simulation of compression chambers

So far, compression stimuli are mostly studied in macroscopic platforms. Our aim is to provide a microfluidic stretching platform allowing for a continuous media perfusion.

OoCs are commonly designed as multilayer system, integrating several stacked 2D layers. Following mentioned approach, a simple compression platform is obtained by combining a tissue compartment for hydrogel injection with a flexible top which can be actuated and compress the hydrogel.

We simulated described model system as chamber featuring a circular footprint filled with hydrogel, compressed from top with homogeneous pressure. The flexible membrane is modeled 200 µm thick PDMS layer. Compression was simulated with FEM assuming large deflections and radial symmetry for a compression chamber of diameter $d = 1.5\,\mathrm{mm}$, filled with elastic material of $E = 1\,\mathrm{kPa}$ (Fig. 5.15 A, left simulation). The simulation of described 2D chamber geometry reveals a gradient in spatial pressure distribution. Upon application of 70 mbar, the elastic material is compressed right below the compression membrane by $\epsilon_\mathrm{V} \approx 10\,\%$ in the chamber center, whereas a compression of $\epsilon_\mathrm{V} \approx 4\,\%$ is observed at the radially outer chamber edge.

In order to circumvent the inhomogeneous compression distribution of a planar chamber design, we investigated the compression profile for a hemispherically-shaped tissue chamber (dome) under homogeneous load. The chamber was simulated using identical elastic material properties and membrane thickness for a hemispherical chamber of the same radius. The dome region is further elevated by 350 µm, accounting for injection channels, present in a real-world device (Fig. 5.15 A, right simulation). The spatial distribution of compression is more homogeneous for chosen non-planar dome geometry. For comparison of both compression chamber geometries, a uniform load of $p = 480\,\mathrm{mbar}$ was simulated, yielding a comparable maximum compression of $\epsilon_\mathrm{V} \approx 10\,\%$. The maximum compression is reached at the upper dome wall at an angle of $\approx 30°$, with respect to the central axis. The minimum compression is reached at the radially outer chamber bottom and amounts to $\epsilon_\mathrm{V} \approx 6\,\%$. We observe, that the 3D dome arrangement benefits from a reduced spatial inhomogeneity in compression. Throughout the bulk part of the dome, compressions of $\epsilon_\mathrm{V} = (7\text{–}10)\,\%$ are predicted, whereas in the planar chamber compressions occur in the range from $\epsilon_\mathrm{V} = (3\text{–}9)\,\%$.

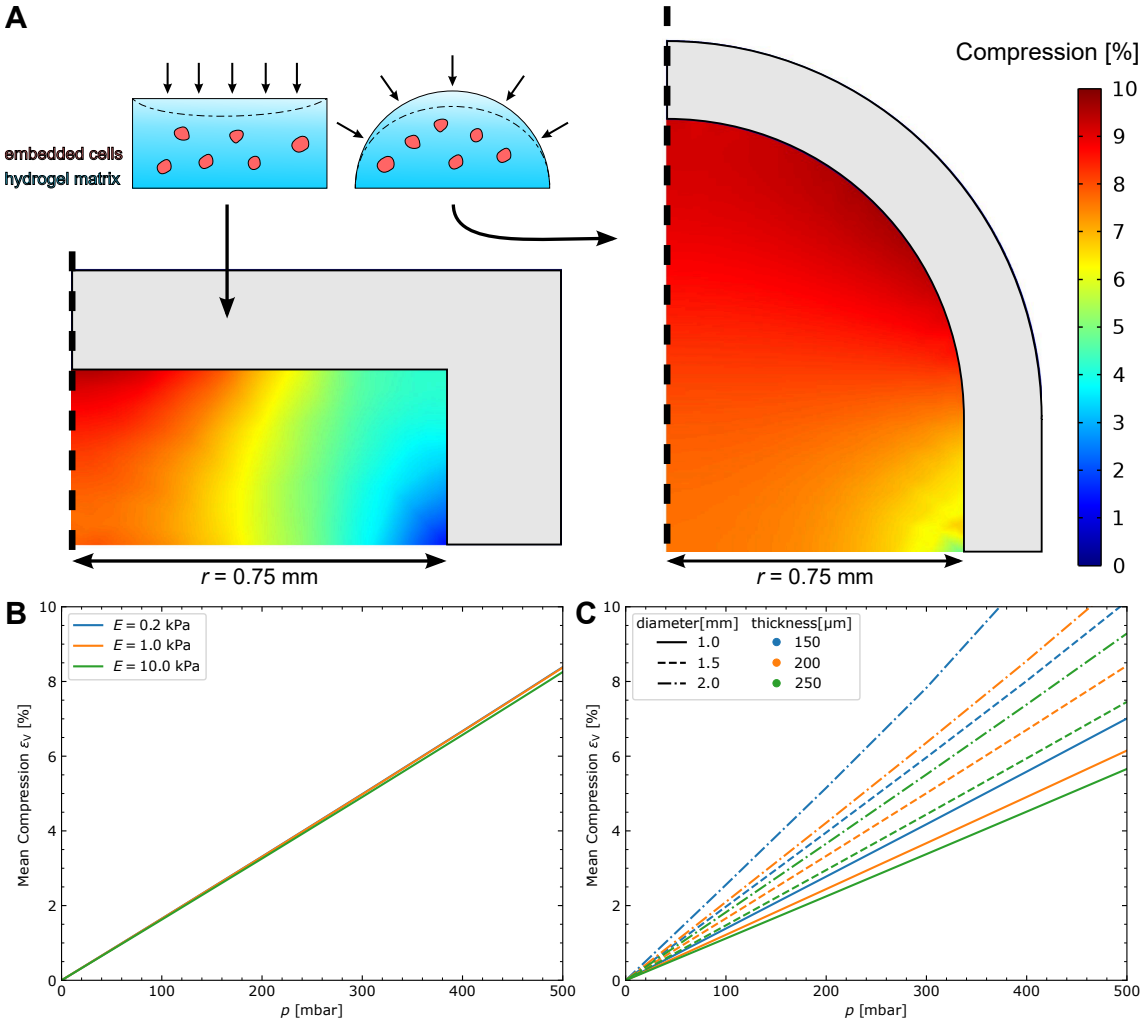

Figure 5.15 FEM analysis of hydrogel compression. **(A)** Comparison between compression platform designs filled with a material of $E = 1\,\mathrm{kPa}$ for pressures achieving a maximum compression of $\epsilon_V \approx 10\,\%$ in each design. One-sided compression from the top results in a gradient of achievable compression (left panel), whereas a compression from all sides yields a more homogeneous compression profile (right panel). **(B)** Mean compression in dome-shaped platform for a compression compartment filled with a material of varying elastic moduli. **(C)** Mean compression for $E = 1\,\mathrm{kPa}$, evaluated for varying dome diameters and thicknesses.

The simulated compression averaged over the elastic material inside the dome yields a linear dependence between applied pressure and mean compression for the application of pressures ranging up to 500 mbar (Fig. 5.15 B).

Furthermore, we investigated the compression behaviour for materials of varying Young's moduli [$E = (0.2,\ 1.0$ and $10.0)\,\mathrm{kPa}$], corresponding to stiffnesses of typically used hydrogels collagen [$E = (0.5\text{–}12)\,\mathrm{kPa}$] and HyStem®-C [$E \approx 0.2\,\mathrm{kPa}$] [284, 285]. It is observable, that even a variation in Young's modulus of two orders

of magnitude leads to a negligible change in mean compression. We simulated the compression for dome geometries varying in diameter [(1.0, 1.5 and 2.0) mm] and wall thickness [(150, 200 and 250) µm; Fig. 5.15 C]. The mean compression increases with increasing diameter and decreasing thickness. Investigated combinations of geometrical parameters allow to tune the applied compression in a range of (1–2.5) % for $p = 100\,\mathrm{mbar}$.

5.3.2 Compression chip

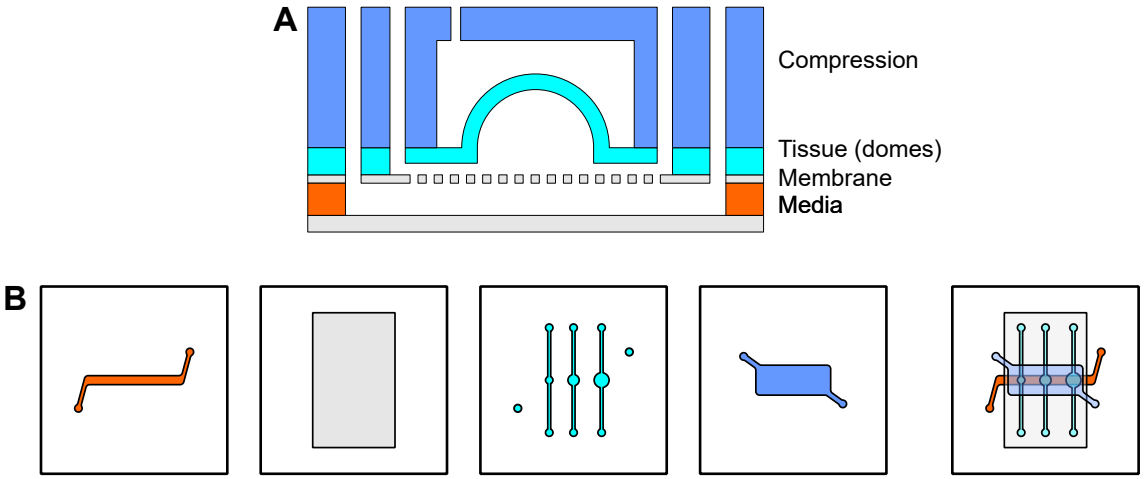

Figure 5.16 Hydrogel compression platform. **(A)** Side view of chip design. The hemispherical tissue compartment is compressed by the overlying compression module. Cultured tissues are separated by a porous membrane from a subjacent media channel, enabling continuous media perfusion. **(B)** Top view of chip design highlighting individual layers, matching in color layers from A. Three individual compression systems are located on one chip featuring diameters of $d = (1.0,\ 1.5 \text{ and } 2.0)\,\mathrm{mm}$. All tissue compartments are supplied with media from the same media channel.

We designed an OoC enabling the perfused culture and homogeneous compression of cell-laden hydrogels. The compression chamber is shaped according to foregoing considerations as hemisphere, providing homogeneous compression of embedded cells (Fig. 5.16 A, B).

The dome-shaped tissue layer out of PDMS comprises a loading channel for hydrogel injection. To prevent pressure buildup during gel injection, the tissue chamber contains an inlet and outlet channel, such that the gel can be fully pushed into the chip during loading. A media channel is located below the tissue compartment, separated by a porous membrane. Implemented design aims at constraining the injected gel to the tissue compartment while providing continuous media perfusion, supplying nutrients by diffusion through the membrane towards embedded cells.

The media module is molded from PDMS and bonded to a #1.5 coverslip. The top

part of the chip is sealed with a PDMS module providing tight fluidic connections for tissue and media inlet as well as outlet channel. Protruding dome is embedded in a pressure chamber which can be actuated by an external pressure pump. The pressure chamber is designed as channel with inlet and outlet port. Three independent domes with diameters $d = (1.0,\ 1.5$ and $2.0)$ mm are included in each chip (Fig. 5.16 B). Domes are supplied with media from a shared media channel, overlapping all domes serially. In order to allow bonding between media and tissue layer, the membrane solely covers all features of the tissue layer such that it is sandwiched during assembly and no crosstalk between both modules can occur.

5.3.3 Dome fabrication

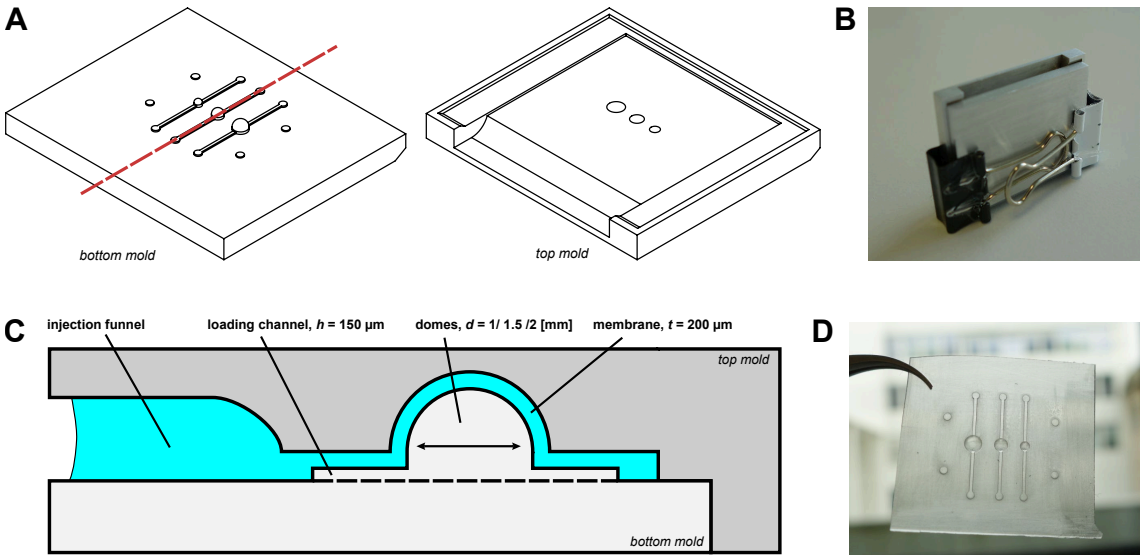

Figure 5.17 Microfabrication of dome compression layer. **(A)** Design of two-part mold for defined molding of PDMS layers featuring hemispherical domes. Red line indicates cross section displayed in (C). **(B)** Assembled CNC-milled molds prior to PDMS injection. **(C)** Cross section of clamped mold highlighting clamping alignment, injection funnel and geometrical parameters. **(D)** Picture of released molded dome layer.

We designed a two-part mold to fabricate dome-shaped PDMS membranes of defined thickness (200 µm; Fig. 5.17 A). For molding, both parts were clamped together providing an injection cavity of defined layer height and the PDMS prepolymer is injected into the injection funnel (Fig. 5.17 B, C). The bottom part comprises positive channel and dome structures, as well as features marking punching positions to create through-holes for accessing the media channel during later complete device assembly. The top mold integrates hemispherical cutouts with defined offset to positive dome structures, thus allowing the molding of out-of-plane features in these regions. Apart from that, the mold provides a flat surface, enabling

subsequent bonding steps.

As investigated molds are not transparent, an alignment of dome structure to dome cavity is not feasible by eye, as employed in the fabrication of aligning PDMS layers on top of each other, is not feasible. Therefore, both molds were designed to precisely fit to each other, providing an alignment of both layers by the general mold geometry. The top mold possesses a rim into which the bottom mold exactly fits. The rim is skewed at the injection side, enabling a levering of both molds after PDMS solidification. For a reliable alignment, the bottom mold is thus pushed to the opposite end of the injection area and tightly clamped.

In order to provide a user-friendly injection of PDMS prepolymer, the molding region is extended in the top mold from a layer height of 350 µm to 2 mm, providing an injection funnel (Fig. 5.17 C). Thus, the mixed polymer could be added with a pipet into the injection funnel and filled the void formed from both molds. After polymer solidification, the mold was opened from the injection side with help of a screw driver, the molded PDMS layer removed and the injection funnel cut away, yielding the tissue layer (Fig. 5.17 D).

In order to achieve similar compression throughout multiple fabricated devices, an accurate molding of the dome layer is crucial. We investigated two mold manufacturing methods: SLA-printing in photocurable resin and CNC-milling of aluminum.

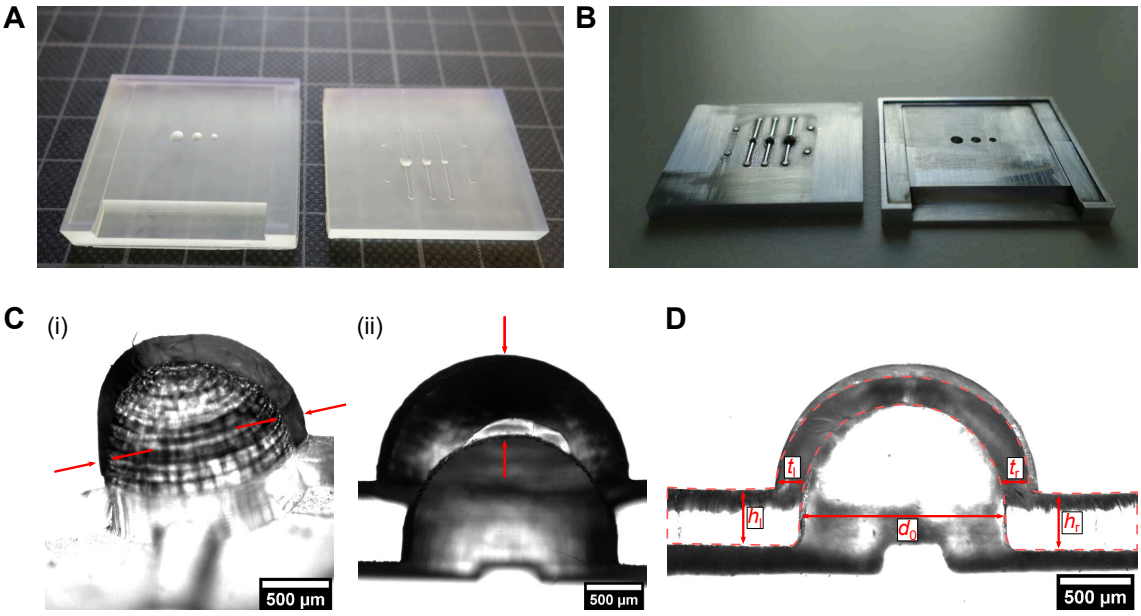

Figure 5.18 Comparison between utilized molds and PDMS replicas. **(A)** Picture of SLA-printed molds. **(B)** Picture of CNC-milled molds. **(C)** Side cuts of dome layers molded from SLA-printed molds highlighting observed variability. (i) Horizontal misalignment leads to asymmetric side walls, (ii) vertical misalignment to increased thickness. **(D)** Side cut of a dome layer molded from a CNC-milled master. Key dimensions used for mold characterization are marked in red.

SLA printed molds were printed in layer resolution of $\Delta l = 25\,\mu m$ (Fig. 5.18

A). Comparing various prints of the same mold, we observed slight variations in the fitting of both parts, indicating variations in the printing process. To allow curing of PDMS prepolymer inside the mold, prints were post-processed following established protocols for subsequent PDMS molding. Nevertheless, we observed varying molding results with molds undergoing the identical treatment. For several molds, PDMS stuck to the master, yielding to a rupture of the molded membrane during removal.

CNC-milled molds were produced by a contract manufacturer. A manual polishing step was applied by the manufacturer to smoothen the surface. As manually accessing the region between tissue channel with abrasive paper is challenging, the surface is only fined down in the bulk region, visible by streaks on the surface (Fig. 5.18 B). Generally, molds from CNC-milled masters did not exhibit any cure inhibition and could be easily removed from the mold after solidification. We performed $N > 20$ molding cycles without observable degradation. Both molds could be assembled in a snug fit without noticeable shifts of both parts.

To investigate structural accuracy of molded PDMS layers, a central piece of molded membranes was cut from the center and imaged from the side. We observed greater variations in membranes molded from SLA-printed masters. Common defects were a slight lateral misalignment of both layers leading to uneven wall thicknesses and/or a vertical misalignment (Fig. 5.18 C). Depending on the vertical misalignment, thicker membranes, or even membranes of reduced thickness with holes were obtained.

Contrary, we observed less variations in membranes molded from CNC-milled masters. PDMS residuals between both molds lead to sparsely occurring increased layer thicknesses, which, however, could be avoided by proper cleaning of both molds.

To assess the reproducibility of domes molded from CNC-milled masters, we compared key dimensions of three molded membranes for all three dome diameters (Fig. 5.18 D). We determined the layer height left and right of each dome, h_l and h_r, respectively, as well as the dome diameter d_0. Due to the manual cutting, a perfect cut in the dome center is not feasible, such that side cuts yield apparently reduced dome diameters. To nevertheless assess a potential lateral misalignment, we compare left and right membrane thicknesses, t_l & t_r respectively, and calculate the parameter λ, describing the asymmetry between left and right thickness, defined as

$$\lambda = \frac{|t_\mathrm{l} - t_\mathrm{r}|}{t_\mathrm{l} + t_\mathrm{r}}. \tag{5.1}$$

As the central cut is guided by all three domes and the parallel mold edge, we estimate the deviation in cut tilt from an ideal parallel cut as negligible, such that a comparison of t_l & t_r can be used to determine a potential asymmetry of central alignment.

Measured layer heights yield for all investigated samples mean heights of $\bar{h} \approx 400\,\mu\mathrm{m}$ (Table 5.2). Determined thickness is larger than the designed layer height of 350 µm. As the variation $\Delta\bar{h}$ lies for each sample below 10 µm, the elevated membrane thickness is maintained throughout the sample.

Table 5.2 Characterization of mean layer heights and standard deviations (3 domes, height measured to the left and right of each dome, $N = 3 \cdot 2 = 6$) of domes molded from a CNC-milled master.

sample	$\bar{h}$ [µm]	$\Delta\bar{h}$ [µm]
M1	407	8
M2	394	9
M3	400	6

Table 5.3 Characterization of width and asymmetry of domes molded from CNC-milled master.

dome diameter	d_0 [µm]	Δd_0 [µm]	λ [%]	$\Delta\lambda$ [%]
1 mm	978	8	3.5	2.9
1.5 mm	1459	16	2.6	1.8
2 mm	1976	20	2.5	0.3

Comparing measured dome diameters between three replicas for each dome, we observe reduced diameters compared to the specified dimensions, most likely originating from variations in the side cut position (Table 5.3). The asymmetry parameter Λ is below 4 % for all dome diameters with absolute variations of less than 3 %. For a pursued dome thickness of $t = 200\,\mu\text{m}$, this variation would result in a maximum deviation in membrane thickness of $\Delta t = 14\,\mu\text{m}$.

5.3.4 Analysis of hydrogel compression

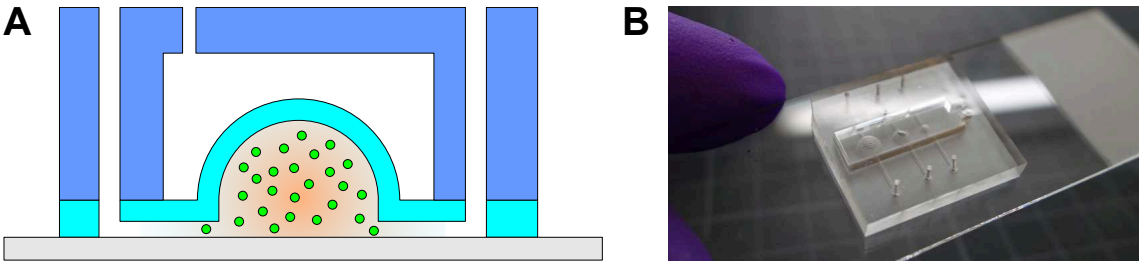

Figure 5.19 Compression chip for dome compression characterization. **(A)** Chip design. Membrane and media layer are omitted. Pressure-dependent compressions can be extracted from fluorescent beads embedded into injected hydrogel. **(B)** Picture of assembled characterization chip (early stage design comprising four domes shown).

For characterizing the compression behaviour of the dome-shaped compression compartment, media and tissue layer were omitted and the dome layer was bonded to

glass (Fig. 5.19 A). Similar to the culture chip, the dome is sealed with a compression module out of PDMS, enabling defined dome actuation (Fig. 5.19 B). We verified successful assembly by manually applying pressure with a syringe connected to the compression compartment and observing dome deflections under the microscope. To visualize the compression within an elastic material in the compression chamber, fluorescent beads were mixed with investigated hydrogel and injected into the dome chamber, following a previously published approach [286].

As the dome chamber branches from the loading channel, air bubbles can be easily trapped during injection. We established the following procedure to prevent trapping of bubbles inside the dome structure. The chip is initially plasma treated yielding to a hydrophilization of channel walls. An empty tip is added to the channel outlet. To inject hydrogel, a pipet tip with gel prepolymer is inserted without pressure application into the channel inlet of the dome chamber and the pipet removed. We observed hydrostatically-driven flow filling the channel and chamber without trapping of bubbles. If ceasing of filling flow was observed, slight pressure was applied to the injection pipet by barely re-attaching the pipet. After complete bubble-free filling of the chamber, gel is equilibrated in both pipet tips by applying pressure to the inlet tip.

Compression of collagen in unsealed domes. We investigated the compression behaviour of developed dome-shaped compression system for a $d = 1.5\,\mathrm{mm}$ dome molded from a SLA-printed master, filled with collagen hydrogel.

Collagen was injected into the compression chamber and injection tips with remaining gel left attached to the chip. After gel solidification, the pressure chamber was attached to a pressure pump. We acquired z-stacks of the whole dome region to detect the position of fluorescent beads, making sure to include several planes below the lowest and above the highest plane with detectable beads. By applying defined pressures of $p = (0,\ 100,\ 200 \text{ and } 300)\,\mathrm{mbar}$, deformations and shifts in bead positions within the gel were observed. For each applied pressure, a z-stack with identical settings was acquired. Bead positions were extracted from recorded z-stacks and wrongly detected particles rejected based on a minimum particle intensity. Subsequently, bead positions, detected from z-stacks recorded at increasingly applied pressures, were linked to obtain particle trajectories (Fig. 5.20 A).

Visual inspection of extracted displacement field indicates correct tracking of beads, as trajectories display rotational symmetry and point to the dome center. The extracted displacement field is a sparse field with beads located at randomly distributed positions. For a detailed investigation of obtained displacement field, in-plane components of beads located around discrete cut planes, e.g. $z = (600 \pm 25)\,\mu\mathrm{m}$, are evaluated (Fig. 5.20 B). Trajectories pointing in opposite directions with respect to the local displacement field can be distinguished. They are attributed to wrongly linked tracks. We reject these trajectories by comparing the displacement of each bead with the average displacements of neighboring particles at distance r. If any of the displacement components u_x, u_y, u_z deviates by more

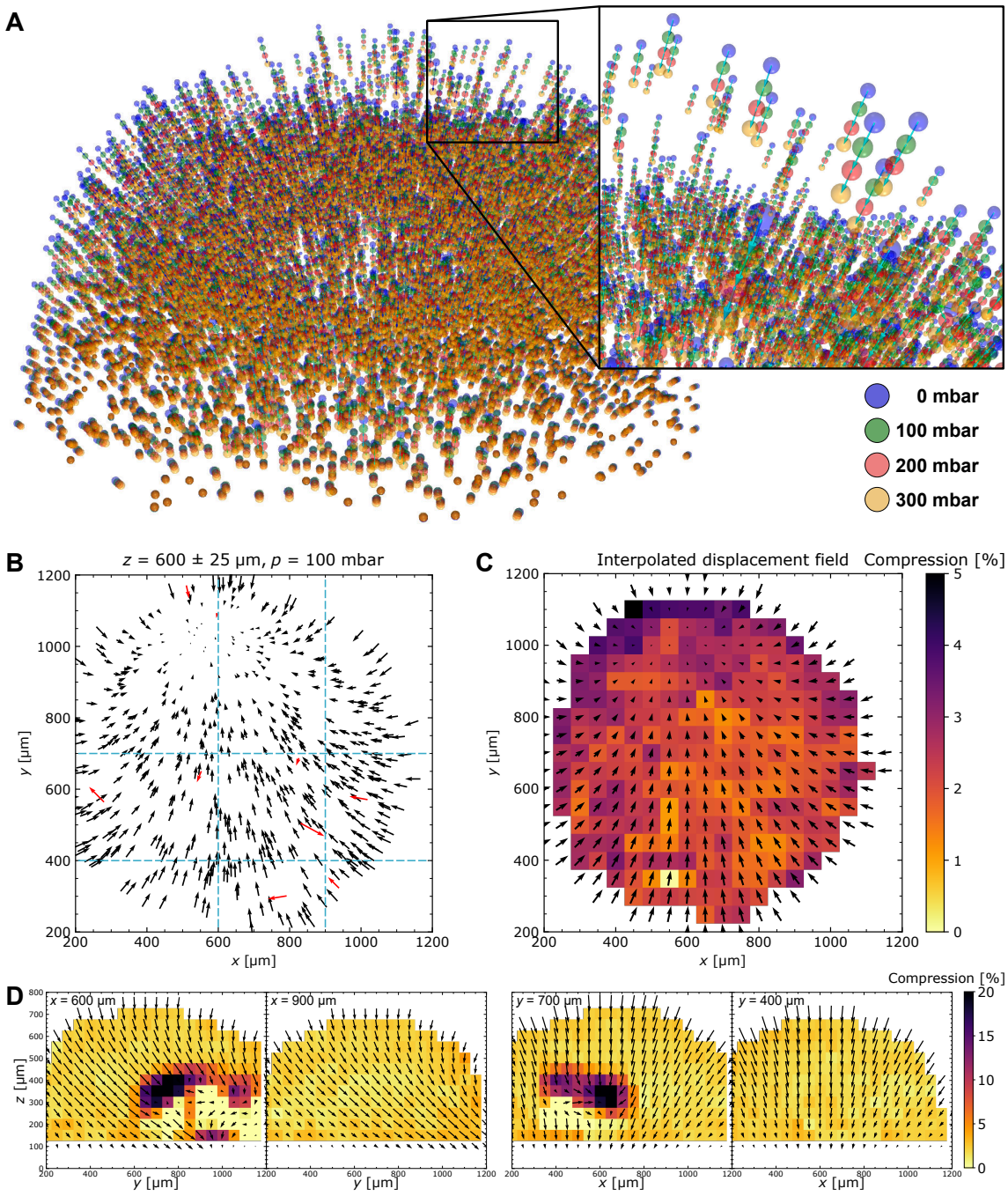

Figure 5.20 Extraction of displacement fields within a collagen-filled dome (SLA mold, $d = 1.5\,\mathrm{mm}$). **(A)** Overview of tracked and linked fluorescent beads for various actuation pressures. Particles could be tracked within the hydrogel yielding pressure-dependent 3D displacement fields. **(B)** z cut plane of displacement field illustrating particle trajectories within $z = (600 \pm 25)\,\mu\mathrm{m}$ upon application of 100 mbar. Filtered local outliers are marked in red. Blue lines mark positions of cut planes evaluated in (D). **(C)** Interpolated displacement field and extracted compression obtained from (B). **(D)** x and y cut planes of interpolated displacement fields and compressions for slices marked in B. While particles are displaced towards the dome center in x direction, a clear displacement towards the upper dome edge (corresponding to the channel inlet) is observable in y direction.

than one standard deviation from the mean displacement of each component, the tracked bead is rejected. Visual comparison of rejected beads confirms an accurate removal of outliers with utilized filtering algorithm (Fig. 5.20 B, red arrows).

In the following, we interpolated the filtered displacement field on a regular grid. The grid spacing is chosen to yield roughly the same amount of particle positions as number of tracked particles (Fig. 5.20 C). We estimated the spatial compression ϵ_V from the divergence of obtained interpolated displacement field (Fig. 5.20 C). For an investigated applied pressure of 100 mbar, we observe a spatially varying compression within the whole cut plane in the range of $\epsilon_V = (2\text{–}5)\,\%$. The interpolated displacement field exposes a continuous displacement towards a sink in the upper central region ($x = 600\,\mu m$, $y = 1000\,\mu m$).

The y cut plane of the interpolated field at at $x = 400\,\mu m$ reveals a homogeneous compression coupled to a displacement towards the dome center. The displacement field at the left and right edge predominantly points downwards to the center (Fig. 5.20 D, left panel). Investigating another y cut plane ($x = 700\,\mu m$), we similarly observe a homogeneous compression within a majority of the cross section with a displacement pointing inwards. However, a region with clearly elevated compression is distinguishable. Contrary to y cut planes, x cut planes reveal a non-symmetrical displacement field with a vertically downwards pointing displacement and a horizontally predominant displacement towards the lower right edge (Fig. 5.20 D, right panel). Just as extracted y cut planes, x cut planes also indicate anomalies of high compression for other x-positions.

Comparing z cut planes at $z = (200,\ 400 \text{ and } 600)\,\mu m$ for the applied pressures of $p = (100,\ 200 \text{ and } 300)$ mbar, an increase in compression is distinguishable in the bulk region (Fig. 5.21 A). Cut planes for $z = (200 \text{ and } 400)\,\mu m$ reveal, similarly to previous observations, inhomogeneities of compression in the upper central region. Averaging the compression over the whole dome region, a linear dependence of compression from applied compressing pressure p is observed (Fig. 5.21 B). Mean compressions increase to $\epsilon_V = 9\,\%$ at $p = 300$ mbar. A linear fit agrees well with extracted mean compression. The spatial variation in compression is of order $\Delta\epsilon_V \approx 5\,\%$.

Compression of HyStem®-C in plugged domes Following the establishment of a bead-based compression characterization, we compared the compression behaviour for domes of varying diameter. Domes were molded from CNC-milled masters, yielding higher reproducibility than SLA-printed masters. We employed the commercial, chemically-defined, hydrogel HyStem®-C and added fluorescent beads into the mixture of individual gel components. After gel injection into all domes, inlet and outlet ports were sealed with stainless steel plugs to prevent any potential gel movement out of the loading chamber during compression. Succeeding gel solidification, z-stacks were recorded for domes compressed with $p = (100,\ 200,\ 300 \text{ and } 345)$ mbar, beads tracked, linked and the displacement field calculated as previously described. Comparing the displacement field overlain with

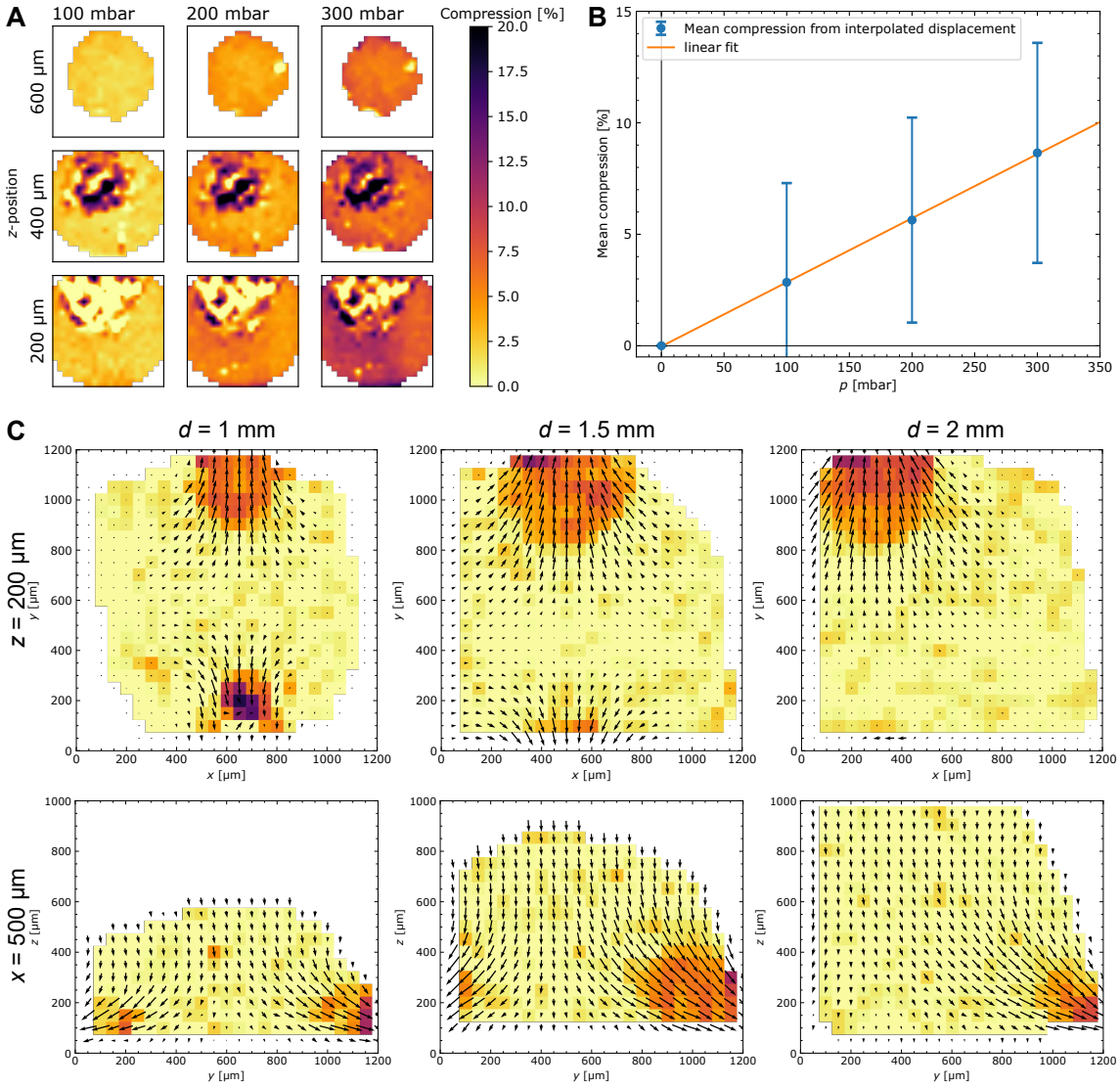

Figure 5.21 Hydrogel compression analysis in domes with varying sealing procedures and diameters. **(A)** Extracted compression in unsealed domes loaded with collagen. Compression is compared for three applied pressures with xy slices shown for three z cut planes. With increasing pressure, the local compression is larger. Inhomogeneous regions are observable in the lower cut planes. **(B)** Analysis of mean compression, averaged over the whole dome investigated in (A). A linear dependence of mean compression on applied pressure is observed. **(C)** Comparison of z and x cut planes of displacement fields for three dome diameters at $p = 100\,\mathrm{mbar}$ ($d = (1,\ 1.5$ and $2)\,\mathrm{mm}$, molded from CNC-milled master). Domes are filled with HyStem®-C and injection inlets are sealed. For all dome diameters, a predominant displacement towards the chamber inlet is observed. Same scale bar applied as in (A).

local compression for $p = 100\,\text{mbar}$, a predominant bead movement towards both inlet channels is observable from x and z slices (Fig. 5.21 C). The behaviour is the same for all investigated dome diameters. The bulk part of the dome remains in an uncompressed state, whereas compression occurs localized in vicinity of the filling channels with observed compressions of $\epsilon_V \approx 5\,\%$. For all applied pressures, no bulk compression can be determined.

5.3.5 Biological proof-of-concept

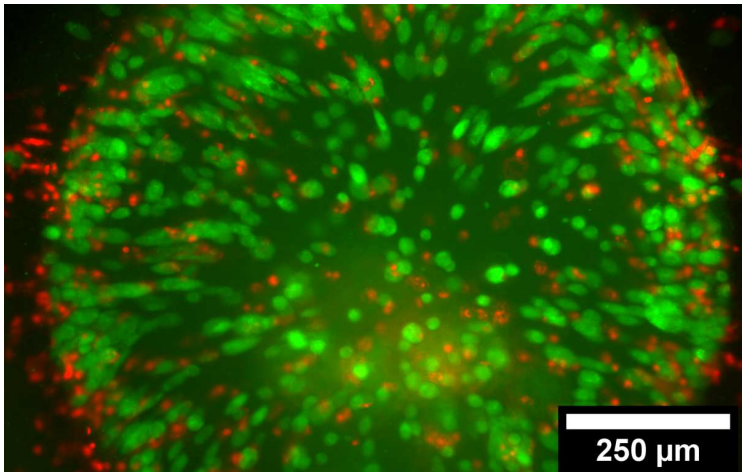

Figure 5.22 Integration of FBs into a $d = 1\,\text{mm}$ dome. Live/dead staining recorded on day 3 after injection and static culture of cells embedded in HyStem®-C hydrogel (green: FDA, red: PI).

To verify the culture of cells embedded in developed compression platform, we injected FBs in a HyStem®-C gel into the dome compartment. The culture chip was equipped with a media channel separated by a porous membrane from the dome compartment (Fig. 5.16 A). Pipet tips filled with media, connected to the media channel, provided static supply of nutrients. On day 3 after cell injection, live/dead staining was performed via the media channel (Fig. 5.22, culture and staining carried out by Ning Zhang, University of Tübingen). A distribution of cells within the whole gel compartment is observable. Despite an apparently large amount of viable (green) cells, approximately half of imaged cells are marked as dead (red).

5.3.6 Discussion

We introduced a microphysiological compression platform featuring a novel hemispherical chamber geometry. Simulations revealed a more homogeneous compression distribution compared to a conventional planar geometry, enabling the delivery of precisely defined mechanical stimuli. Designed domes could be successfully fabricated by injection molding of PDMS in two-part molds, allowing subsequent integration into microfluidic environments. We could successfully extract displacement

fields and compression distributions within actuated domes, revealing a predominant hydrogel displacement towards the injection inlets, hampering the application of a defined compression in current device design. Successful dome-integrated culture of cell-laden hydrogels verifies the applicability of introduced platform for further compression experiments.

Simulation of compression chambers Comparing a planar chamber with a hemispherical chamber, improved homogeneity could be asserted for the 3D shape. Hence, the 3D dome geometry is preferred for a compression platform providing defined compressions for the investigation of cell-laden hydrogels. Generally, other 3D chamber designs might be advantageous for further improving homogeneity, however, we focus on the fabrication and characterization of compressible domes as initial enhancement of a planar chamber, furthermore mimicking hip joint shape with chosen design [287]. The predicted linear dependence of applied pressure and mean compression in the dome shape is beneficial, offering precise control of compression by applied pressure.

As negligible influence of inserted gel's Young's modulus could be detected, we attribute the major influence on compression behaviour to the PDMS membrane, encompassing a Young's modulus of at least one order of magnitude larger than that of inserted compressed gel. By tailoring the chamber design (thickness and diameter), it is possible to engineer platforms offering precisely defined pressure-compression relations which are similar for inserted gels, providing a valuable scientific apparatus for studying compression effects.

Dome-shaped compression chip We presented the concept of a novel microphysiological system, enabling the perfused culture of cell-laden hydrogels inside compressible domes of varying diameters. In current design, a shared media channel perfuses all tissue chambers. To eliminate extended gradients in nutrient supply, triggered by domes acting as consecutive sinks along the media perfusion path, the media channel could also be arranged in a branching geometry. For the study of different conditions between domes, it is also conceivable to perfuse each dome with an individual media channel, however, raising complexity in needed chip connections.

As PDMS is gas-permeable, elevated pressures and/or the application of pressure over an extended time, might lead to diffusion of gas throughout the membrane into the dome compartment for an actuation with compressed air. Introduced gas would then form unwanted bubbles inside the dome. By designing the pressure chamber as channel, the compartment can be filled with a compression liquid (e.g. oil/water), preventing the introduction of bubbles. In case of air compression or after filling of the chamber with liquid, the outlet can be sealed with a stainless steel plug, ensuring hydrostatic pressure transmission inside the compression compartment, compressing the dome structure homogeneously.

Dome fabrication We investigated the microfabrication of dome-shaped PDMS layers via injection molding in molds fabricated by SLA printing or CNC milling. Contrary to previously reported approaches, our developed two-part master molds could be successfully replicated without enclosure of air bubbles potentially hindering proper device functionality by bypassing both layers [288].

Molding of dome layers from SLA-printed masters yielded reduced mold reproducibility compared to CNC-milled masters. We attribute the lateral alignment issues in SLA-printed masters to variations between individual prints as well as material abrasion occurring in the assembly process of both layers. Repeated clamping of both molds can lead to abrasion, increasing the alignment play. Increased dome and layer thicknesses can be explained by print deformations or remaining PDMS in the edge rail, resulting in an elevated distance between both molds. We observed bending of printed molds upon removal from the printing plate. Even with utmost care, the print had to be leveraged from the build platform. As the material is not fully cured at that moment, it is still flexible and can undergo permanent deformations, yielding individual variations for each mold. After UV curing, masters could not be bent manually, however depending on the clamping position, sagging of the central part was observed, indicating remaining flexibility of the master. Reduced dome thicknesses were observed for a clamp placement too far in the center, resulting in a wrong pressure distribution, bending the central region. Although too thin membranes were subsequently avoided by a correct clamp placement, molding of dome membranes from SLA-printed masters yielded reduced mold reproducibility compared to CNC-milled masters.

To further improve the reproducibility of molds from SLA-printed masters, one could enhance mold transparency. This would allow manual alignment of both molds, leading to decreased variations in wall thickness. The master transparency could be further improved by polishing, an additional coating, or the coverage with IPA in the alignment process, compensating master roughness [289]. The issue of master bending during clamping could be alleviated by sandwiching top and bottom mold between a rigid clamping plate. In addition, adding a support below the print on the printing platform, bending of printed parts upon removal could be prevented. However, adding a support layer could also lead to a deterioration of surface roughness. To prevent cured polymer from sticking to the mold and furthermore improve surface roughness, it is conceivable to coat both 3D-printed molds with Parylene, as previously demonstrated [290].

Generally, domes could be molded from CNC-milled masters in satisfactory reproducibility, enabling the generation of 3D compression layers. We did not observe any abrasion of the CNC-milled mold leading to a comparable fitting for subsequent moldings. Measured thickness of molded layers is elevated compared to the designed thickness, which we attribute to the manufacturing process of utilized mold. However, as the thickness is comparable for various samples, adequate reproducibility is achieved. We consider the determined alignment asymmetry of $\Lambda \leq 4\,\%$, resulting in a maximum deviation in membrane thickness of $\Delta t = 14\,\mu\text{m}$, as sufficiently accurate, considering a manufacturing tolerance of $\pm 20\,\mu\text{m}$ of utilized mold.

As remaining disadvantage of CNC-milled masters we identify increased mold roughness compared to SLA- or wafer-molded layers. The roughness is replicated by the PDMS molds, hindering thorough bonding of the layer to glass. Insufficient bonding could lead in compression experiments to spilling of hydrogel in regions next to the channel between glass and dome layer. Polishing or electroplating steps could help in decreasing surface roughness in further iterations.

Analysis of hydrogel compression We successfully established a framework for the spatial determination of compression in elastic materials within developed dome chip. With our developed injection strategy, domes could be filled without introducing air bubbles, a prerequisite for reproducible cell injection. Individual bead positions could be determined and displacement fields extracted as a function of applied pressure. By filtering and interpolating obtained displacement fields we could calculate spatial compression distributions. A fraction of apparently correctly linked particles is rejected during the filtering process, which we do not consider problematic, as the removal of wrong links is advantageous over a minimal reduction of tracked particles.

We observed regions of elevated compression in extracted compression fields. We attribute observed anomalies to reduced bead densities in corresponding region, leading to a artifacts in the interpolated displacement field.

Collagen gel was investigated in initial compression experiments and pipet tips left inserted in the chip, without additional chip sealing. The observed predominant displacement towards the chamber edge, observed only in y direction, hints at a displacement of hydrogel towards the loading channel, which is arranged parallel to the y-axis. As the channel was not completely sealed, a displacement of injected hydrogel towards the injection tip at lower liquid level (yielding reduced hydrostatic pressure) seems plausible. Nevertheless, we asserted a linearly increasing mean compression, confirming the trend of the theoretical preconsideration. However, the magnitude of measured compressions is roughly twice of the results obtained by FEM simulations. As the layer was molded from a SLA-printed master mold which is prone to deformations, we attribute measured increased compression to a reduced dome membrane thickness.

Experiments on HyStem®-C gel with sealed channel inlets also revealed a predominant displacement towards the chamber inlet. As observed displacement is recorded for all investigated dome diameters, the observation most likely points to a systematic issue in the compression platform. If inserted sealing plugs do not close the channel inlets properly, water can be pushed out of the loading channel resulting in a movement towards the chamber inlets. Furthermore, the rough bottom surface of PDMS layers molded from CNC-milled molds provides not optimal sealing to the glass substrate, such that a hydrogel displacement into this region is also conceivable. A displacement of elastic material between glass and PDMS layer would however also result in a visible displacement towards every edge of the dome, which is not observed.

Employed hydrogel HyStem®-C is approximately one order of magnitude less stiff than collagen, for which an increasing bulk compression was observed. Therefore, contrary to initial theoretical considerations, the reduced stiffness might play a bigger role than expected. Especially a real-world device comprising additional loading channels for gel injection might behave differently than the simulated geometry which neglected channels. Enclosed air bubbles introduced during plugging of the system could compress, leading to observed predominant displacement into the loading channel. It is also conceivable that added fluorescent beads are not physically linked with the hydrogel and travel upon compression with the liquid phase.

To address observed challenges, the dome design could be adjusted, decreasing the length of the loading channel, or, sealing the channel in closer distance to the dome. Generally, a stiffer hydrogel could help in preventing a predominant hydrogel displacement. Further optimization of mold roughness seems necessary, providing better layer sealing.

All in all, we presented proof-of-concept for spatially determining deformations in the newly developed dome-shaped platform. Further studies should employ CNC-milled molds for improved device reproducibility and adjust the bead density for a more accurate determination of the displacement field.

Biological proof-of-concept As proof-of-concept of designed platform, cells were cultured under static media supply without the application of compression. The live/dead staining revealed a successful culture of cells embedded in hydrogel inside developed OoC. Culture conditions should be further optimized by, e.g., utilizing dynamic perfusion or precisely tailoring the integrated biomaterial providing suitable mechanical properties and biocompatibility [291]. Thus, in a next step, the effect of dynamic compression on cell-laden hydrogels can be investigated.

Generally, it is unclear how embedded porous membrane will influence the compression behaviour, as gel might be squeezed through the pores, leading to a predominant gel displacement instead of a compression. Thus, the complete culture chip with added media channel should be mechanically characterized following established framework.

For further cell culture experiments the exact dome diameter is expected to play a crucial role. Larger diameters simplify dome fabrication by reducing demands for fabrication accuracy, however, issues with supply of nutrients might arise. Due to an increased distance, a sufficient supply with nutrients in remote regions is not granted *a priori*. However, cyclic compression might actually be beneficial, leading to forced convection by actively squeezing liquid out of the dome region, which is enriched with nutrients and again aspirated into the dome region upon removal of applied pressure.

Summary & outlook

To date, the full potential of OoCs has only been partially unveiled, as the introduced systems mostly focused on tissue generation. Many prototypes and proof-of-concept studies have been presented so far, however, chip developers are in most cases the only users of developed systems. To fully unfold its tremendous potential, it is important to not only generate more advanced model systems (physiological tissue structure, perfusion, cell-media ratios), it is just as important to include readout and stimulation capabilities for gaining advanced insights from cultured tissues. Only if investigators are provided with tools to investigate key biological questions, a true adaptation from development stage to real applications will occur.

The studies presented in this thesis designed, implemented, and investigated novel tools and integration approaches for biophysical probing and stimulation in microphysiological systems. We established three novel OoCs which enabled the integrated study of biomechanics.

First, we presented a novel cell stretching platform, delivering defined strain to ECs cultured on a flexible membrane within a perfusable microfluidic environment. In particular, we characterized the deflection properties of a TPE membrane, advantageous over commonly used PDMS membranes. Due to its large-scale fabrication potential, inherent bonding properties, and reduced absorption of small molecules, we believe in a broad adaption in OoCs requiring stretchable membranes. For instance, Schneider S. *et al.* recently presented an OoC featuring an integrated micropump based on a flexible TPE layer [292]. With developed stretching platform, the effect of cyclical stretching onto cultured EC cell layers can be investigated in future experiments, comparing the alignment of stretched and unstretched samples. An integration of pores into the membrane will enable a co-culture of ECs and alveolar cells in future studies, which can be mechanically actuated via the air interface using low pressures in the physiological range. So far, we employed a complex approach for characterizing membrane deflections by tracking membrane-deposited fluorescent beads in recorded z-stacks. In future studies, surface profiles might be recorded in a more user-friendly way via white light interferometry.

Second, we developed a hemispherically-shaped microphysiological system facilitating the homogeneous compression of cell-laden hydrogels, enhancing currently used planar compression geometries. We investigated two microfabrication techniques and successfully fabricated hemispherical PDMS layers. Within our developed platform, we established a framework for the spatial determination of com-

pression by tracking of embedded beads and characterized displacement fields in initial dome prototypes. Ultimately, we provided a biological proof-of-concept of successful cell culture inside a chip integrating a media channel below the compression compartment. In summary, all building blocks are provided for a thorough analysis of compression behaviour of cell-laden hydrogels in following studies. Our developed platform can thus be employed for, e.g., studying the effects of periodical mechanical loading on chondrocyte differentiation.

Third, we studied approaches for integrating soft pads into microphysiological systems to determine twitch forces of cardiac µ-tissues via TFM. We successfully demonstrated integration, calibration, and initial proof-of-concept measurements on cultured tissues. However, the developed concepts are characterized by complex integration protocols, fragile chip handling, and constraints on subsequent bonding approaches. We envision the application of established chip concept in assays investigating the precise space-resolved distribution of contractile forces. For applications which investigate total contractile forces of cardiac tissues as key metric among other parameters, alternative approaches, which can be read out in a more scalable manner, seem preferable.

In this thesis, we mainly focused on microphysiological models of the human heart. Due to intricate coupling of vital functioning to chemical, electrical, and mechanical hallmarks, it is an ideal testbed for studying biophysical aspects in OoCs. For an accurate recapitulation of the myocardium, the generation of an aligned contracting cardiac muscle fiber is essential. We developed two innovative platforms enabling the generation, perfused culture, as well as subsequent probing and stimulation of aligned cardiac tissues.

As currently employed manual cell injection protocols result in uncontrolled loading pressures and high variations in formed tissues, we realized a novel approach for loading OoCs. In our developed centrifugal HoC, hiPSC-derived CMs are introduced into eight dog bone-shaped tissue chambers via centrifugation. Centrifugation provides precise control of injection pressures, automatized metering, and dense compaction of introduced cells. Following subsequent dynamic culture, introduced cells fuse and form aligned muscle fibers.

Although the introduced concept allows for a parallelized tissue generation of eight tissues per chip, it still involves manual handling of single chip units, impeding an adaption on industrial scale. Therefore, we expanded the concept in a follow-up study to the Organ-on-a-Disc [293]. It leverages developed centrifugal loading of OoCs, permitting the automated culture of more than 100 tissues in one integrated unit. Standardized disk design allows automated handling procedures, and an implementation into established workflows. So far, successful culture of dog bone-shaped tissues composed of FBs was presented, which will be extended to cardiac tissues in the next steps.

In addition to manual cell injection, cell sourcing and hiPSC-differentiation presents another bottleneck for envisioned industrial large-scale applications of OoCs. One emerging technology enabling the upscaling and automation of cell culture is spheroid culture, allowing the generation of 3D tissue constructs within bioreactors in large

quantities. Our second developed HoC merges spheroid and OoC technology, pointing the way for potential upscaling approaches. 3D cardiac spheroids are introduced into dog bone-shaped chambers, further fusing to aligned muscle fibers.

Both systems were able to generate aligned cardiac muscle fibers, recapitulating a fundamental physiological key feature and thus composing an ideal testbed for subsequent biophysical investigations. The centrifugal HoC benefits from dense tissue compaction and parallelization, whereas the Spheroflow-HoC combines OoC technology with scalable spheroid formation. It thus stands to reason to combine both approaches and introduce spheroids via centrifugation in future studies.

Our developed open source software OpenHeartWare allowed the optical analysis of beating kinetics of cultured cardiac tissues. Adapting this non-invasive readout as a key metric, established HoCs can already be employed as drug screening platform without the need for further modification. We successfully demonstrated the applicability of the centrifugal HoC for parallelized drug testing studies.

We further extended both HoCs and presented a facile electrode integration approach, enabling electrical stimulation of cultured tissues. Moreover, we provided the blueprint of the Arduino-based low-cost pulse generator Easypace, granting research groups easy access to specialized experimental hardware, allowing a scripted control of pacing experiments. In follow-up studies, integrated pacing capability can be utilized to investigate effects of electric stimulation on tissue maturation, similar to LaBarge *et al.* [215].

Besides the integration of force sensing pads, we explored concepts for integrating oxygen sensing capabilities into the Spheroflow-HoC. The approach of embedding sensor particles directly into injected spheroids represents a user-friendly procedure which does not require further modifications in chip fabrication. We demonstrated sensor integration into tissues composed of FBs, further studies should evaluate possible influence of embedded particles on rather fragile iPSC-derived CMs. As integrated beads can also be magnetic, the concept is adoptable for mechanical actuation, similar to previous approaches [123, 294].

In addition, we demonstrated a novel resin-based fabrication concept for integrating luminescent sensor spots into the tissue channel. As the chip is directly fabricated on top of a sensor substrate, there is no need to ship pre-assembled chip components to external facilities for sensor deposition. The integration concept is universal and can be directly transferred to other chip types or analytes such as pH or Glucose. As proof-of-concept, we could verify changes in O_2 levels linked to electrical stimulation of cardiac tissues. Developed chip is thus a valuable tool for assessing changes in metabolism, which can also be triggered by biochemical or mechanical stimuli in future studies.

In summary, we established a comprehensive framework of various tools to probe and actuate tissues within microphysiological systems. Developed tools can now be applied in drug testing or disease modeling. Especially a combination of individual capabilities is also feasible, e.g., integrating a force pad in one end and an O_2 sensor in the other end of the aligned cardiac fiber. The developed concepts thus leverage OoCs from bare tissue generation tools to advanced experimental platforms, enabling the collection of valuable biological data in a standardized and parallelized manner.

Appendix: Videos of cardiac µ-tissues

The following section provides an overview of electronically available supplementary videos appended to the thesis with specified file names. Videos have been previously published under CC BY 4.0 license in "Schneider, O. *et al.* User-Friendly and Parallelized Generation of Human Induced Pluripotent Stem Cell-Derived Microtissues in a Centrifugal Heart-on-a-Chip. *Tissue Eng. Part A* **25,** 786–798 (2019) [29]" and can also be directly accessed from the publisher by clicking on respective image snapshot in the digital version of presented thesis.

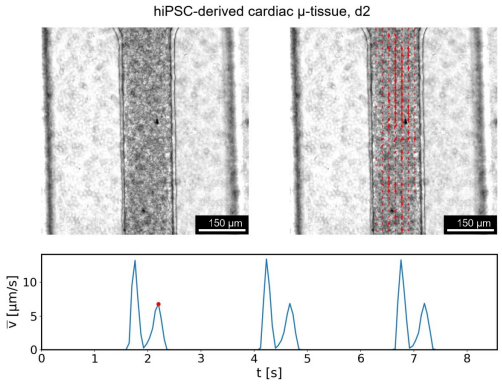

Video 1 Beating in cardiac µ-tissue formed from hiPSC-derived CMs in centrifugal HoC, d2 after cell injection.

file name	`SuppVid1.mp4`
metadata	8 s, 1828 px × 1386 px

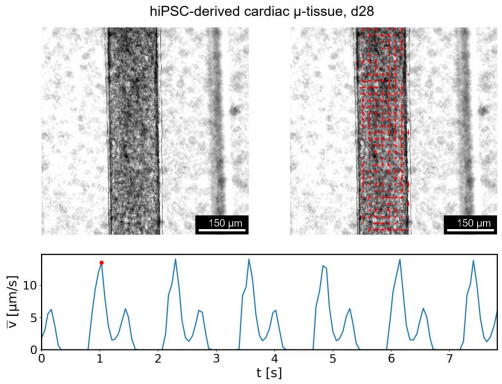

Video 2 Beating in cardiac µ-tissue formed from hiPSC-derived CMs in centrifugal HoC, d28 after cell injection.

file name	`SuppVid2.mp4`
metadata	7 s, 1828 px × 1386 px

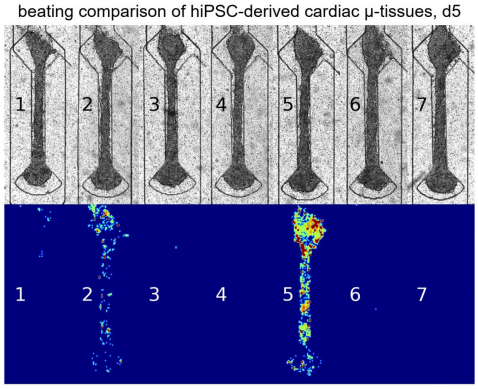

Video 3 Beating comparison of cardiac µ-tissues within one chip, d5 after cell injection. Tissues formed from hiPSC-derived CMs in centrifugal HoC.

file name	`SuppVid3.mp4`
metadata	6 s, 1508 px × 1214 px

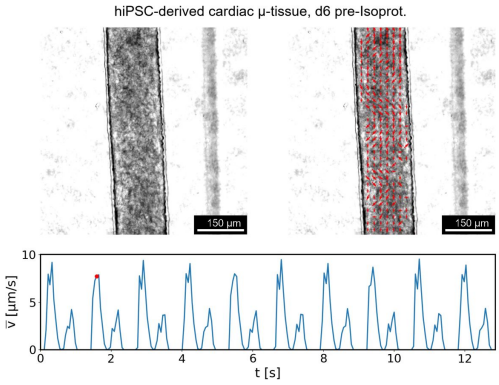

Video 4 Beating in cardiac µ-tissue formed from hiPSC-derived CMs in centrifugal HoC, d6 after cell injection prior to chemical stimulation by isoproterenol.

file name	`SuppVid4.mp4`
metadata	12 s, 1828 px × 1386 px

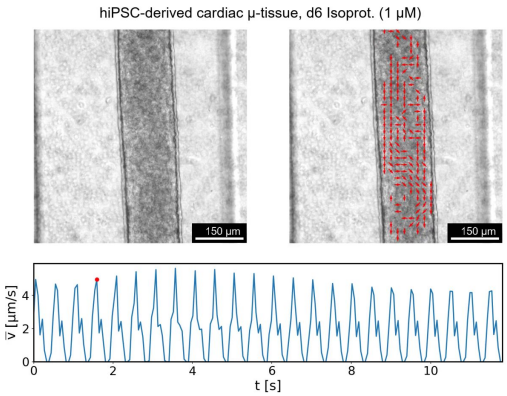

Video 5 Beating in cardiac µ-tissue formed from hiPSC-derived CMs in centrifugal HoC, d6 after cell injection during chemical stimulation by isoproterenol.

file name	`SuppVid5.mp4`
metadata	11 s, 1774 px × 1386 px

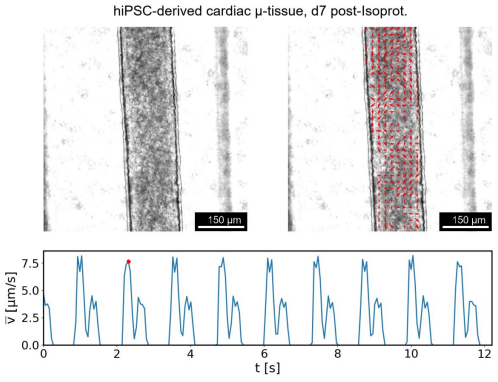

Video 6 Beating in cardiac µ-tissue formed from hiPSC-derived CMs in centrifugal HoC, d7 after cell injection following washout of stimulation reagent.

file name	`SuppVid6.mp4`
metadata	12 s, 1854 px × 1386 px

Bibliography

[1] Si, L. *et al.* Human Organ Chip-Enabled Pipeline to Rapidly Repurpose Therapeutics during Viral Pandemics. *bioRxiv,* 2020.04.13.039917 (2020).

[2] Marx, U. *et al.* Biology-Inspired Microphysiological System Approaches to Solve the Prediction Dilemma of Substance Testing. *ALTEX* **33,** 272–321 (2016).

[3] Paul, S. M. *et al.* How to Improve R&D Productivity: The Pharmaceutical Industry's Grand Challenge. *Nat. Rev. Drug Discov.* **9,** 203–214 (2010).

[4] Kessel, M. & Frank, F. A Better Prescription for Drug-Development Financing. *Nat. Biotechnol.* **25,** 859–866 (2007).

[5] DiMasi, J. A., Grabowski, H. G. & Hansen, R. W. Innovation in the Pharmaceutical Industry: New Estimates of R&D Costs. *J. Health Econ.* **47,** 20–33 (2016).

[6] Scannell, J. W. *et al.* Diagnosing the Decline in Pharmaceutical R&D Efficiency. *Nat. Rev. Drug Discov.* **11,** 191–200 (2012).

[7] Mullard, A. Parsing Clinical Success Rates. *Nat. Rev. Drug Discov.* **15,** 447–447 (2016).

[8] Ma, C. *et al.* Organ-on-a-Chip: A New Paradigm for Drug Development. *Trends Pharmacol. Sci.* **42,** 119–133 (2021).

[9] Wikswo, J. P. The Relevance and Potential Roles of Microphysiological Systems in Biology and Medicine. *Exp. Biol. Med.* **239,** 1061–1072 (2014).

[10] Ye, L. *et al.* The Application of Induced Pluripotent Stem Cells in Cardiac Disease Modeling and Drug Testing. *J. Cardiovasc. Transl. Res.* **11,** 366–374 (2018).

[11] Bruyneel, A. A. *et al.* Will iPSC-cardiomyocytes Revolutionize the Discovery of Drugs for Heart Disease? *Curr. Opin. Pharmacol.* **42,** 55–61 (2018).

[12] Moraes, C., Sun, Y. & Simmons, C. A. (Micro)Managing the Mechanical Microenvironment. *Integr. Biol.* **3,** 959 (2011).

[13] Thompson, C. L. *et al.* Mechanical Stimulation: A Crucial Element of Organ-on-Chip Models. *Front. Bioeng. Biotechnol.* **8,** 602646 (2020).

[14] Paluch, E. K. *et al.* Mechanotransduction: Use the Force(s). *BMC Biol.* **13,** 47 (2015).

[15] Huang, H., Kamm, R. D. & Lee, R. T. Cell Mechanics and Mechanotransduction: Pathways, Probes, and Physiology. *Am. J. Physiol.-Cell Physiol.* **287,** C1–C11 (2004).

[16] Mammoto, T., Mammoto, A. & Ingber, D. E. Mechanobiology and Developmental Control. *Annu. Rev. Cell Dev. Biol.* **29,** 27–61 (2013).

[17] Ahmadzadeh, H. *et al.* Modeling the Two-Way Feedback between Contractility and Matrix Realignment Reveals a Nonlinear Mode of Cancer Cell Invasion. *Proc. Natl. Acad. Sci. USA* **114,** E1617–E1626 (2017).

[18] Dobbs, L. G. & Gutierrez, J. A. Mechanical Forces Modulate Alveolar Epithelial Phenotypic Expression. *Comp. Biochem. Physiol. A. Mol. Integr. Physiol.* **129,** 261–266 (2001).

[19] Huh, D. *et al.* Reconstituting Organ-Level Lung Functions on a Chip. *Science* **328,** 1662–1668 (2010).

[20] Occhetta, P. *et al.* Hyperphysiological Compression of Articular Cartilage Induces an Osteoarthritic Phenotype in a Cartilage-on-a-Chip Model. *Nat. Biomed. Eng.* **3,** 545–557 (2019).

[21] Nikolaev, M. *et al.* Homeostatic Mini-Intestines through Scaffold-Guided Organoid Morphogenesis. *Nature* **585,** 574–578 (2020).

[22] Onakpoya, I. J., Heneghan, C. J. & Aronson, J. K. Post-Marketing Withdrawal of 462 Medicinal Products Because of Adverse Drug Reactions: A Systematic Review of the World Literature. *BMC Med.* **14,** 1–11 (2016).

[23] Mathur, A. *et al.* Human iPSC-based Cardiac Microphysiological System for Drug Screening Applications. *Sci. Rep.* **5,** 1–7 (2015).

[24] Marsano, A. *et al.* Beating Heart on a Chip: A Novel Microfluidic Platform to Generate Functional 3D Cardiac Microtissues. *Lab Chip* **16,** 599–610 (2016).

[25] Ellis, B. W. *et al.* Human iPSC-derived Myocardium-on-Chip with Capillary-like Flow for Personalized Medicine. *Biomicrofluidics* **11,** 024105 (2017).

[26] Vivas, A. *et al.* Generation and Culture of Cardiac Microtissues in a Microfluidic Chip with a Reversible Open Top Enables Electrical Pacing, Dynamic Drug Dosing and Endothelial Cell Co-Culture. *bioRxiv,* 2021.11.01.465885 (2021).

[27] Schneider, O. *et al.* Fusing Spheroids to Aligned µ-Tissues in a Heart-on-Chip Featuring Oxygen Sensing and Electrical Pacing Capabilities. *Mater. Today Bio* **15,** 100280 (2022).

[28] Schneider, S. *et al.* Facile Patterning of Thermoplastic Elastomers and Robust Bonding to Glass and Thermoplastics for Microfluidic Cell Culture and Organ-on-Chip. *Micromachines* **12,** 575 (2021).

[29] Schneider, O. *et al.* User-Friendly and Parallelized Generation of Human Induced Pluripotent Stem Cell-Derived Microtissues in a Centrifugal Heart-on-a-Chip. *Tissue Eng. Part A* **25,** 786–798 (2019).

[30] Bhatia, S. N. & Ingber, D. E. Microfluidic Organs-on-Chips. *Nat. Biotechnol.* **32,** 760–772 (2014).

[31] Ahadian, S. *et al.* Organ-On-A-Chip Platforms: A Convergence of Advanced Materials, Cells, and Microscale Technologies. *Adv. Healthcare Mater.* **7,** 1700506 (2018).

[32] Sung, J. H. *et al.* Recent Advances in Body-on-a-Chip Systems. *Anal. Chem.* **91,** 330–351 (2019).

[33] Oleaga, C. *et al.* Multi-Organ Toxicity Demonstration in a Functional Human in Vitro System Composed of Four Organs. *Sci. Rep.* **6,** 20030 (2016).

[34] Probst, C., Schneider, S. & Loskill, P. High-Throughput Organ-on-a-chip Systems: Current Status and Remaining Challenges. *Curr. Opin. Biomed. Eng.* **6,** 33–41 (2018).

[35] Jalili-Firoozinezhad, S., Miranda, C. C. & Cabral, J. M. Modeling the Human Body on Microfluidic Chips. *Trends Biotechnol.* **39,** 838–852 (2021).

[36] Reardon, S. 'Organs-on-chips' Go Mainstream. *Nature* **523,** 266 (2015).

[37] Esch, E. W., Bahinski, A. & Huh, D. Organs-on-Chips at the Frontiers of Drug Discovery. *Nat. Rev. Drug Discov.* **14,** 248–260 (2015).

[38] Keller, P. J., Pampaloni, F. & Stelzer, E. H. Life Sciences Require the Third Dimension. *Curr. Opin. Cell Biol.* **18,** 117–124 (2006).

[39] Huh, D., Hamilton, G. A. & Ingber, D. E. From 3D Cell Culture to Organs-on-Chips. *Trends Cell Biol.* **21,** 745–754 (2011).

[40] Wikswo, J. P. *et al.* Scaling and Systems Biology for Integrating Multiple Organs-on-a-Chip. *Lab Chip* **13,** 3496 (2013).

[41] Moraes, C. *et al.* On Being the Right Size: Scaling Effects in Designing a Human-on-a-Chip. *Integr. Biol.* **5,** 1149 (2013).

[42] Karimi, M. *et al.* Microfluidic Systems for Stem Cell-Based Neural Tissue Engineering. *Lab Chip* **16,** 2551–2571 (2016).

[43] McBeath, R. *et al.* Cell Shape, Cytoskeletal Tension, and RhoA Regulate Stem Cell Lineage Commitment. *Dev. Cell* **6,** 483–495 (2004).

[44] Feinberg, A. W. *et al.* Controlling the Contractile Strength of Engineered Cardiac Muscle by Hierarchal Tissue Architecture. *Biomaterials* **33,** 5732–5741 (2012).

[45] Li, J. *et al.* Extracellular Recordings of Patterned Human Pluripotent Stem Cell-Derived Cardiomyocytes on Aligned Fibers. *Stem Cells Int.* **2016,** 2634013 (2016).

[46] Franco, D. *et al.* Control of Initial Endothelial Spreading by Topographic Activation of Focal Adhesion Kinase. *Soft Matter* **7,** 7313 (2011).

[47] Malek, A. & Izumo, S. Mechanism of Endothelial Cell Shape Change and Cytoskeletal Remodeling in Response to Fluid Shear Stress. *J. Cell Sci.* **109,** 713–726 (1996).

[48] Gutierrez, E. *et al.* Microfluidic Devices for Studies of Shear-Dependent Platelet Adhesion. *Lab Chip* **8,** 1486 (2008).

[49] Estrada, R. *et al.* Microfluidic Endothelial Cell Culture Model to Replicate Disturbed Flow Conditions Seen in Atherosclerosis Susceptible Regions. *Biomicrofluidics* **5,** 032006 (2011).

[50] Huang, Q. *et al.* Fluid Shear Stress and Tumor Metastasis. *Am. J. Cancer Res.* **8,** 763–777 (2018).

[51] Naskar, S., Kumaran, V. & Basu, B. Reprogramming the Stem Cell Behavior by Shear Stress and Electric Field Stimulation: Lab-on-a-Chip Based Biomicrofluidics in Regenerative Medicine. *Regen. Eng. Transl. Med.* **5,** 99–127 (2019).

[52] Huh, D. *et al.* Acoustically Detectable Cellular-Level Lung Injury Induced by Fluid Mechanical Stresses in Microfluidic Airway Systems. *Proc. Natl. Acad. Sci. USA* **104,** 18886–18891 (2007).

[53] Schürch, D. *et al.* Modeling Nanoparticle–Alveolar Epithelial Cell Interactions under Breathing Conditions Using Captive Bubble Surfactometry. *Langmuir* **30,** 4924–4932 (2014).

[54] Shemesh, J. *et al.* Flow-Induced Stress on Adherent Cells in Microfluidic Devices. *Lab Chip* **15,** 4114–4127 (2015).

[55] Grodzinsky, A. J. *et al.* Cartilage Tissue Remodeling in Response to Mechanical Forces. *Annu. Rev. Biomed. Eng.* **2,** 691–713 (2000).

[56] De Croos, J. *et al.* Cyclic Compressive Mechanical Stimulation Induces Sequential Catabolic and Anabolic Gene Changes in Chondrocytes Resulting in Increased Extracellular Matrix Accumulation. *Matrix Biol.* **25,** 323–331 (2006).

[57] Sanchez-Adams, J. *et al.* The Mechanobiology of Articular Cartilage: Bearing the Burden of Osteoarthritis. *Curr. Rheumatol. Rep.* **16,** 451 (2014).

[58] Sinha, R. *et al.* Endothelial Cell Alignment as a Result of Anisotropic Strain and Flow Induced Shear Stress Combinations. *Sci. Rep.* **6,** 29510 (2016).

[59] Dessalles, C. A. *et al.* Integration of Substrate- and Flow-Derived Stresses in Endothelial Cell Mechanobiology. *Commun. Biol.* **4,** 764 (2021).

[60] Ahadian, S. *et al.* Electrical Stimulation as a Biomimicry Tool for Regulating Muscle Cell Behavior. *Organogenesis* **9,** 87–92 (2013).

[61] Hirt, M. N. *et al.* Functional Improvement and Maturation of Rat and Human Engineered Heart Tissue by Chronic Electrical Stimulation. *J. Mol. Cell. Cardiol.* **74,** 151–161 (2014).

[62] Visone, R. *et al.* A Microscale Biomimetic Platform for Generation and Electro-Mechanical Stimulation of 3D Cardiac Microtissues. *APL Bioeng.* **2,** 046102 (2018).

[63] Gladkov, A. *et al.* Design of Cultured Neuron Networks in Vitro with Predefined Connectivity Using Asymmetric Microfluidic Channels. *Sci. Rep.* **7,** 15625 (2017).

[64] Aung, A. *et al.* An Engineered Tumor-on-a-Chip Device with Breast Cancer–Immune Cell Interactions for Assessing T-cell Recruitment. *Cancer Res.* **80,** 263–275 (2020).

[65] Maulana, T. I. *et al.* Immunocompetent Cancer-on-Chip Models to Assess Immuno-Oncology Therapy. *Adv. Drug Deliv. Rev.* **173,** 281–305 (2021).

[66] Ahn, S. I. *et al.* Microengineered Human Blood–Brain Barrier Platform for Understanding Nanoparticle Transport Mechanisms. *Nat. Commun.* **11,** 175 (2020).

[67] Shamloo, A. *et al.* Endothelial Cell Polarization and Chemotaxis in a Microfluidic Device. *Lab Chip* **8,** 1292 (2008).

[68] Soucy, J. R. *et al.* Instrumented Microphysiological Systems for Real-Time Measurement and Manipulation of Cellular Electrochemical Processes. *iScience* **21,** 521–548 (2019).

[69] Lewandowska, M. K. *et al.* Recording Large Extracellular Spikes in Microchannels along Many Axonal Sites from Individual Neurons. *PLoS One* **10,** e0118514 (2015).

[70] Maoz, B. M. *et al.* Organs-on-Chips with Combined Multi-Electrode Array and Transepithelial Electrical Resistance Measurement Capabilities. *Lab Chip* **17,** 2294–2302 (2017).

[71] Griep, L. M. *et al.* BBB ON CHIP: Microfluidic Platform to Mechanically and Biochemically Modulate Blood-Brain Barrier Function. *Biomed. Microdevices* **15,** 145–150 (2013).

[72] Van der Helm, M. W. *et al.* Direct Quantification of Transendothelial Electrical Resistance in Organs-on-Chips. *Biosens. Bioelectron.* **85,** 924–929 (2016).

[73] Wang, Y. I., Abaci, H. E. & Shuler, M. L. Microfluidic Blood–Brain Barrier Model Provides in Vivo-like Barrier Properties for Drug Permeability Screening. *Biotechnol. Bioeng.* **114,** 184–194 (2017).

[74] Fuchs, S. *et al.* In-Line Analysis of Organ-on-Chip Systems with Sensors: Integration, Fabrication, Challenges, and Potential. *ACS Biomater. Sci. Eng.* **7,** 2926–2948 (2021).

[75] Radisic, M. *et al.* Oxygen Gradients Correlate with Cell Density and Cell Viability in Engineered Cardiac Tissue. *Biotechnol. Bioeng.* **93,** 332–343 (2006).

[76] Tanumihardja, E. *et al.* Measuring Both pH and O_2 with a Single On-Chip Sensor in Cultures of Human Pluripotent Stem Cell-Derived Cardiomyocytes to Track Induced Changes in Cellular Metabolism. *ACS Sens.* **6,** 267–274 (2021).

[77] Müller, B. *et al.* Measurement of Respiration and Acidification Rates of Mammalian Cells in Thermoplastic Microfluidic Devices. *Sens. Actuators B Chem.* **334,** 129664 (2021).

[78] McCain, M. L. *et al.* Micromolded Gelatin Hydrogels for Extended Culture of Engineered Cardiac Tissues. *Biomaterials* **35,** 5462–5471 (2014).

[79] Mannhardt, I. *et al.* Human Engineered Heart Tissue: Analysis of Contractile Force. *Stem Cell Rep.* **7,** 29–42 (2016).

[80] Zhao, Y. *et al.* A Platform for Generation of Chamber-Specific Cardiac Tissues and Disease Modeling. *Cell* **176,** 913–927.e18 (2019).

[81] Ronaldson-Bouchard, K. *et al.* Advanced Maturation of Human Cardiac Tissue Grown from Pluripotent Stem Cells. *Nature* **556,** 239–243 (2018).

[82] Huebsch, N. *et al.* Miniaturized iPS-Cell-Derived Cardiac Muscles for Physiologically Relevant Drug Response Analyses. *Sci. Rep.* **6,** 24726 (2016).

[83] LeGrice, I. J. *et al.* Laminar Structure of the Heart: Ventricular Myocyte Arrangement and Connective Tissue Architecture in the Dog. *Am. J. Physiol. - Heart Circ. Physiol.* **269,** H571–H582 (1995).

[84] Kanzaki, Y. *et al.* Three-Dimensional Architecture of Cardiomyocytes and Connective Tissue in Human Heart Revealed by Scanning Electron Microscopy. *Circulation* **122,** 1973–1974 (2010).

[85] Li, Y. *et al.* Engineering Cell Alignment in Vitro. *Biotechnol. Adv.* **32,** 347–365 (2014).

[86] Kofron, C. M. & Mende, U. *In Vitro* Models of the Cardiac Microenvironment to Study Myocyte and Non-Myocyte Crosstalk: Bioinspired Approaches beyond the Polystyrene Dish. *J. Physiol.* **595,** 3891–3905 (2017).

[87] Denning, C. *et al.* Cardiomyocytes from Human Pluripotent Stem Cells: From Laboratory Curiosity to Industrial Biomedical Platform. *Biochim. Biophys. Acta, Mol. Cell Res.* **1863,** 1728–1748 (2016).

[88] Del Álamo, J. C. *et al.* High Throughput Physiological Screening of iPSC-derived Cardiomyocytes for Drug Development. *Biochim. Biophys. Acta, Mol. Cell Res.* **1863,** 1717–1727 (2016).

[89] Sun, N. *et al.* Patient-Specific Induced Pluripotent Stem Cells as a Model for Familial Dilated Cardiomyopathy. *Sci. Transl. Med.* **4,** 130ra47 (2012).

[90] Veerman, C. C. *et al.* Immaturity of Human Stem-Cell-Derived Cardiomyocytes in Culture: Fatal Flaw or Soluble Problem? *Stem Cells Dev.* **24,** 1035–1052 (2015).

[91] Santoni, S. M. *et al.* Microsystems for Electromechanical Stimulations to Engineered Cardiac Tissues. *Microphysiol. Syst.* **2,** 11–11 (2018).

[92] Goversen, B. *et al.* The Immature Electrophysiological Phenotype of iPSC-CMs Still Hampers in Vitro Drug Screening: Special Focus on I_{K1}. *Pharmacol. Ther.* **183,** 127–136 (2018).

[93] Vunjak-Novakovic, G. *et al.* Challenges in Cardiac Tissue Engineering. *Tissue Eng. Part B Rev.* **16,** 169–187 (2010).

[94] Zhang, Y. S. *et al.* From Cardiac Tissue Engineering to Heart-on-a-Chip: Beating Challenges. *Biomed. Mater.* **10,** 34006 (2015).

[95] Kitsara, M. *et al.* Heart on a Chip: Micro-nanofabrication and Microfluidics Steering the Future of Cardiac Tissue Engineering. *Microelectron. Eng.* **203–204,** 44–62 (2019).

[96] Eschenhagen, T. *et al.* Three-dimensional Reconstitution of Embryonic Cardiomyocytes in a Collagen Matrix: A New Heart Muscle Model System. *FASEB J.* **11,** 683–694 (1997).

[97] Radisic, M. *et al.* Functional Assembly of Engineered Myocardium by Electrical Stimulation of Cardiac Myocytes Cultured on Scaffolds. *Proc. Natl. Acad. Sci. USA* **101,** 18129–18134 (2004).

[98] Hansen, A. *et al.* Development of a Drug Screening Platform Based on Engineered Heart Tissue. *Circ. Res.* **107,** 35–44 (2010).

[99] Boudou, T. *et al.* A Microfabricated Platform to Measure and Manipulate the Mechanics of Engineered Cardiac Microtissues. *Tissue Eng. Part A* **18,** 910–919 (2012).

[100] Tamargo, M. A. *et al.* milliPillar: A Platform for the Generation and Real-Time Assessment of Human Engineered Cardiac Tissues. *ACS Biomater. Sci. Eng.* **7,** 5215–5229 (2021).

[101] Nunes, S. S. *et al.* Biowire: A Platform for Maturation of Human Pluripotent Stem Cell–Derived Cardiomyocytes. *Nat. Methods* **10,** 781–787 (2013).

[102] Sidorov, V. Y. *et al.* I-Wire Heart-on-a-Chip I: Three-dimensional Cardiac Tissue Constructs for Physiology and Pharmacology. *Acta Biomater.* **48,** 68–78 (2017).

[103] Schroer, A. K. *et al.* I-Wire Heart-on-a-Chip II: Biomechanical Analysis of Contractile, Three-Dimensional Cardiomyocyte Tissue Constructs. *Acta Biomater.* **48,** 79–87 (2017).

[104] Feyen, D. A. *et al.* Metabolic Maturation Media Improve Physiological Function of Human iPSC-Derived Cardiomyocytes. *Cell Rep.* **32,** 107925 (2020).

[105] Morimoto, Y. *et al.* Human Induced Pluripotent Stem Cell-Derived Fiber-Shaped Cardiac Tissue on a Chip. *Lab Chip* **16,** 2295–2301 (2016).

[106] Grosberg, A. *et al.* Ensembles of Engineered Cardiac Tissues for Physiological and Pharmacological Study: Heart on a Chip. *Lab Chip* **11,** 4165–4173 (2011).

[107] Carrier, R. L. *et al.* Perfusion Improves Tissue Architecture of Engineered Cardiac Muscle. *Tissue Eng.* **8,** 175–188 (2002).

[108] Cruz-Moreira, D. *et al.* Assessing the Influence of Perfusion on Cardiac Microtissue Maturation: A Heart-on-chip Platform Embedding Peristaltic Pump Capabilities. *Biotechnol. Bioeng.* **118,** 3128–3137 (2021).

[109] Huebsch, N. *et al.* Metabolically-Driven Maturation of hiPSC-Cell Derived Cardiac Chip. *bioRxiv,* 10.1101/485169 (2020).

[110] Charrez, B. *et al.* Heart Muscle Microphysiological System for Cardiac Liability Prediction of Repurposed COVID-19 Therapeutics. *Front. Pharmacol.* **12,** 684252 (2021).

[111] Mainardi, A. *et al.* A Dynamic Microscale Mid-Throughput Fibrosis Model to Investigate the Effects of Different Ratios of Cardiomyocytes and Fibroblasts. *Lab Chip* **21,** 4177–4195 (2021).

[112] Lai, B. F. L. *et al.* InVADE: Integrated Vasculature for Assessing Dynamic Events. *Adv. Funct. Mater.* **27,** 1–11 (2017).

[113] Zhang, Y. S. *et al.* Bioprinting 3D Microfibrous Scaffolds for Engineering Endothelialized Myocardium and Heart-on-a-Chip. *Biomaterials* **110,** 45–59 (2016).

[114] Molino, D. *et al.* On-Chip Quantitative Measurement of Mechanical Stresses during Cell Migration with Emulsion Droplets. *Sci. Rep.* **6,** 1–11 (2016).

[115] Polacheck, W. J. & Chen, C. S. Measuring Cell-Generated Forces: A Guide to the Available Tools. *Nat. Methods* **13,** 415–423 (2016).

[116] Boghdady, C.-M. *et al.* Revisiting Tissue Tensegrity: Biomaterial-based Approaches to Measure Forces across Length Scales. *APL Bioeng.* **5,** 041501 (2021).

[117] Bell, E., Ivarsson, B. & Merrill, C. Production of a Tissue-like Structure by Contraction of Collagen Lattices by Human Fibroblasts of Different Proliferative Potential in Vitro. *Proc. Natl. Acad. Sci. USA* **76,** 1274–1278 (1979).

[118] Stopak, D. & Harris, A. K. Connective Tissue Morphogenesis by Fibroblast Traction. *Dev. Biol.* **90,** 383–398 (1982).

[119] Zimmermann, W. H. *et al.* Three-Dimensional Engineered Heart Tissue from Neonatal Rat Cardiac Myocytes. *Biotechnol. Bioeng.* **68,** 106–114 (2000).

[120] Legant, W. R. *et al.* Microfabricated Tissue Gauges to Measure and Manipulate Forces from 3D Microtissues. *Proc. Natl. Acad. Sci. USA* **106,** 10097–10102 (2009).

[121] Serrao, G. W. *et al.* Myocyte-Depleted Engineered Cardiac Tissues Support Therapeutic Potential of Mesenchymal Stem Cells. *Tissue Eng. Part A* **18,** 1322–1333 (2012).

[122] Dostanic, M. *et al.* A Miniaturized EHT Platform for Accurate Measurements of Tissue Contractile Properties. *J. Microelectromech. Syst.* **29,** 881–887 (2020).

[123] Zhao, R. *et al.* Decoupling Cell and Matrix Mechanics in Engineered Microtissues Using Magnetically Actuated Microcantilevers. *Adv. Mater.* **25,** 1699–1705 (2013).

[124] Ma, Z. *et al.* Contractile Deficits in Engineered Cardiac Microtissues as a Result of MYBPC3 Deficiency and Mechanical Overload. *Nat. Biomed. Eng.* **2,** 955–967 (2018).

[125] Agarwal, A. *et al.* Microfluidic Heart on a Chip for Higher Throughput Pharmacological Studies. *Lab Chip* **13,** 3599 (2013).

[126] Lind, J. U. *et al.* Cardiac Microphysiological Devices with Flexible Thin-Film Sensors for Higher-Throughput Drug Screening. *Lab Chip* **17,** 3692–3703 (2017).

[127] Qian, F. *et al.* Simultaneous Electrical Recording of Cardiac Electrophysiology and Contraction on Chip. *Lab Chip* **17,** 1732–1739 (2017).

[128] Ribeiro, A. J. *et al.* For Whom the Cells Pull: Hydrogel and Micropost Devices for Measuring Traction Forces. *Methods* **94,** 51–64 (2016).

[129] Hazeltine, L. B. *et al.* Effects of Substrate Mechanics on Contractility of Cardiomyocytes Generated from Human Pluripotent Stem Cells. *Int. J. Cell Biol.* **2012,** 1–13 (2012).

[130] McCain, M. L. *et al.* Matrix Elasticity Regulates the Optimal Cardiac Myocyte Shape for Contractility. *Am. J. Physiol. - Heart Circ. Physiol.* **306,** H1525–H1539 (2014).

[131] Kijlstra, J. D. *et al.* Integrated Analysis of Contractile Kinetics, Force Generation, and Electrical Activity in Single Human Stem Cell-Derived Cardiomyocytes. *Stem Cell Rep.* **5,** 1226–1238 (2015).

[132] Ribeiro, A. J. *et al.* Multi-Imaging Method to Assay the Contractile Mechanical Output of Micropatterned Human iPSC-derived Cardiac Myocytes. *Circ. Res.* **120,** 1572–1583 (2017).

[133] McCain, M. L. *et al.* Cooperative Coupling of Cell-Matrix and Cell-Cell Adhesions in Cardiac Muscle. *Proc. Natl. Acad. Sci. USA* **109,** 9881–9886 (2012).

[134] Schaefer, J. A. & Tranquillo, R. T. Tissue Contraction Force Microscopy for Optimization of Engineered Cardiac Tissue. *Tissue Eng. Part C Methods* **22,** 76–83 (2016).

[135] Pasqualini, F. S. *et al.* Traction Force Microscopy of Engineered Cardiac Tissues. *PLoS ONE* **13,** 1–14 (2018).

[136] Aratyn-Schaus, Y. *et al.* Coupling Primary and Stem Cell–Derived Cardiomyocytes in an in Vitro Model of Cardiac Cell Therapy. *J. Cell Biol.* **212,** 389–397 (2016).

[137] Das, T., Maiti, T. K. & Chakraborty, S. Traction Force Microscopy On-Chip: Shear Deformation of Fibroblast Cells. *Lab Chip* **8,** 1308 (2008).

[138] Guo, J. *et al.* Elastomer-Grafted iPSC-Derived Micro Heart Muscles to Investigate Effects of Mechanical Loading on Physiology. *ACS Biomater. Sci. Eng.* **7,** 2973–2989 (2021).

[139] Tan, J. L. *et al.* Cells Lying on a Bed of Microneedles: An Approach to Isolate Mechanical Force. *Proc. Natl. Acad. Sci. USA* **100,** 1484–1489 (2003).

[140] Fu, J. *et al.* Mechanical Regulation of Cell Function with Geometrically Modulated Elastomeric Substrates. *Nat. Methods* **7,** 733–736 (2010).

[141] Lam, R. H. *et al.* Elastomeric Microposts Integrated into Microfluidics for Flow-Mediated Endothelial Mechanotransduction Analysis. *Lab Chip* **12,** 1865–1873 (2012).

[142] Morimatsu, M. *et al.* Molecular Tension Sensors Report Forces Generated by Single Integrin Molecules in Living Cells. *Nano Lett.* **13,** 3985–3989 (2013).

[143] Lee, W. *et al.* Dispersible Hydrogel Force Sensors Reveal Patterns of Solid Mechanical Stress in Multicellular Spheroid Cultures. *Nat. Commun.* **10,** 144 (2019).

[144] Harris, A. K., Wild, P. & Stopak, D. Silicone Rubber Substrata: A New Wrinkle in the Study of Cell Locomotion. *Science* **208,** 177–179 (1980).

[145] Oliver, T., Jacobson, K. & Dembo, M. Traction Forces in Locomoting Cells. *Cell Motil. Cytoskeleton* **31,** 225–240 (1995).

[146] Dembo, M. *et al.* Imaging the Traction Stresses Exerted by Locomoting Cells with the Elastic Substratum Method. *Biophys. J.* **70,** 2008–2022 (1996).

[147] Dembo, M. & Wang, Y. L. Stresses at the Cell-to-Substrate Interface during Locomotion of Fibroblasts. *Biophys. J.* **76,** 2307–2316 (1999).

[148] Sabass, B. *et al.* High Resolution Traction Force Microscopy Based on Experimental and Computational Advances. *Biophys. J.* **94,** 207–220 (2008).

[149] Schwarz, U. S. & Soiné, J. R. Traction Force Microscopy on Soft Elastic Substrates: A Guide to Recent Computational Advances. *Biochim. Biophys. Acta - Mol. Cell Res.* **1853,** 3095–3104 (2015).

[150] Trepat, X. *et al.* Physical Forces during Collective Cell Migration. *Nat. Phys.* **5,** 426–430 (2009).

[151] Franck, C. *et al.* Three-Dimensional Traction Force Microscopy: A New Tool for Quantifying Cell-Matrix Interactions. *PLoS ONE* **6,** e17833 (2011).

[152] Xu, Y. *et al.* Imaging In-Plane and Normal Stresses near an Interface Crack Using Traction Force Microscopy. *Proc. Natl. Acad. Sci. USA* **107,** 14964–7 (2010).

[153] Style, R. W. *et al.* Traction Force Microscopy in Physics and Biology. *Soft Matter* **10,** 4047–4055 (2014).

[154] Landau, L. & Lifshitz, E. *Theory of Elasticity* 3rd edition (Pergamon Press, 1986).

[155] Butler, J. P. *et al.* Traction Fields, Moments, and Strain Energy That Cells Exert on Their Surroundings. *Am. J. Physiol. Cell Physiol.* **282,** C595–C605 (2002).

[156] Moraes, C. *et al.* Supersoft Lithography: Candy-Based Fabrication of Soft Silicone Microstructures. *Lab Chip* **15,** 3760–3765 (2015).

[157] MacNearney, D. *et al.* Nanocontact Printing of Proteins on Physiologically Soft Substrates to Study Cell Haptotaxis. *Langmuir* **32,** 13525–13533 (2016).

[158] Gutierrez, E. & Groisman, A. Measurements of Elastic Moduli of Silicone Gel Substrates with a Microfluidic Device. *PLoS ONE* **6,** e25534 (2011).

[159] Teo, J. L. *et al.* A Biologist's Guide to Traction Force Microscopy Using Polydimethylsiloxane Substrate for Two-Dimensional Cell Cultures. *STAR Protocols* **1,** 100098 (2020).

[160] Young, E. W. K. & Simmons, C. A. Macro- and Microscale Fluid Flow Systems for Endothelial Cell Biology. *Lab Chip* **10,** 143–160 (2010).

[161] Semenza, G. L. Life with Oxygen. *Science* **318,** 62–64 (2007).

[162] Zirath, H. *et al.* Bridging the Academic–Industrial Gap: Application of an Oxygen and pH Sensor-Integrated Lab-on-a-Chip in Nanotoxicology. *Lab Chip* **21,** 4237–4248 (2021).

[163] Pfeiffer, S. A. & Nagl, S. Microfluidic Platforms Employing Integrated Fluorescent or Luminescent Chemical Sensors: A Review of Methods, Scope and Applications. *Methods Appl. Fluoresc.* **3,** 034003 (2015).

[164] Thete, A. *et al.* Microfluidic Arrangement with an Integrated Micro-Spot Array for the Characterization of pH and Solvent Polarity. *Chem. Eng. J.* **135,** S327–S332 (2008).

[165] Shaegh, S. A. M. *et al.* A Microfluidic Optical Platform for Real-Time Monitoring of pH and Oxygen in Microfluidic Bioreactors and Organ-on-Chip Devices. *Biomicrofluidics* **10,** 1–14 (2016).

[166] Lladó Maldonado, S. *et al.* A Fully Online Sensor-Equipped, Disposable Multiphase Microbioreactor as a Screening Platform for Biotechnological Applications. *Biotechnol. Bioeng.* **116,** 65–75 (2019).

[167] Borisov, S. M., Nuss, G. & Klimant, I. Red Light-Excitable Oxygen Sensing Materials Based on Platinum(II) and Palladium(II) Benzoporphyrins. *Anal. Chem.* **80,** 9435–9442 (2008).

[168] Grist, S. M., Chrostowski, L. & Cheung, K. C. Optical Oxygen Sensors for Applications in Microfluidic Cell Culture. *Sensors* **10,** 9286–9316 (2010).

[169] Bambot, S. B. *et al.* Phase Fluorometric Sterilizable Optical Oxygen Sensor. *Biotechnol. Bioeng.* **43,** 1139–1145 (1994).

[170] Morgan, C. G. & Mitchell, A. C. Fluorescence Lifetime Imaging: An Emerging Technique in Fluorescence Microscopy. *Chromosome Res.* **4,** 261–263 (1996).

[171] Quaranta, M., Borisov, S. M. & Klimant, I. Indicators for Optical Oxygen Sensors. *Bioanal. Rev.* **4,** 115–157 (2012).

[172] Gruber, P. *et al.* Integration and Application of Optical Chemical Sensors in Microbioreactors. *Lab Chip* **17,** 2693–2712 (2017).

[173] Sin, A. *et al.* The Design and Fabrication of Three-Chamber Microscale Cell Culture Analog Devices with Integrated Dissolved Oxygen Sensors. *Biotechnol. Prog.* **20,** 338–345 (2008).

[174] Ehgartner, J. *et al.* Online Analysis of Oxygen inside Silicon-Glass Microreactors with Integrated Optical Sensors. *Sens. Actuators B Chem.* **228,** 748–757 (2016).

[175] Zirath, H. *et al.* Every Breath You Take: Non-invasive Real-Time Oxygen Biosensing in Two- and Three-Dimensional Microfluidic Cell Models. *Front. Physiol.* **9,** 815 (2018).

[176] Sticker, D. *et al.* Oxygen Management at the Microscale: A Functional Biochip Material with Long-Lasting and Tunable Oxygen Scavenging Properties for Cell Culture Applications. *ACS Appl. Mater. Interfaces* **11,** 9730–9739 (2019).

[177] Knudsen, L. & Ochs, M. The Micromechanics of Lung Alveoli: Structure and Function of Surfactant and Tissue Components. *Histochem. Cell Biol.* **150,** 661–676 (2018).

[178] Mead, J. & Collier, C. Relation of Volume History of Lungs to Respiratory Mechanics in Anesthetized Dogs. *J. Appl. Physiol.* **14,** 669–678 (1959).

[179] Wirtz, H. R. & Dobbs, L. G. The Effects of Mechanical Forces on Lung Functions. *Respir. Physiol.* **119,** 1–17 (2000).

[180] Wirtz, H. R. W. & Dobbs, L. G. Calcium Mobilization and Exocytosis After One Mechanical Stretch of Lung Epithelial Cells. *Science* **250,** 1266–1269 (1990).

[181] Gutierrez, J. A., Gonzalez, R. F. & Dobbs, L. G. Mechanical Distension Modulates Pulmonary Alveolar Epithelial Phenotypic Expression in Vitro. *Am. J. Physiol. - Lung Cell. Mol. Physiol.* **274,** L196–L202 (1998).

[182] Tan, W. *et al.* Development and Evaluation of Microdevices for Studying Anisotropic Biaxial Cyclic Stretch on Cells. *Biomed. Microdevices* **10,** 869–882 (2008).

[183] Anderson, J. E. *et al.* Measurement of Strain in Cultured Bone and Fetal Muscle and Lung Cells. *In Vitro Cell. Dev. Biol.* **29A,** 183–186 (1993).

[184] Moraes, C. *et al.* Microfabricated Arrays for High-Throughput Screening of Cellular Response to Cyclic Substrate Deformation. *Lab Chip* **10,** 227–234 (2010).

[185] Kamotani, Y. *et al.* Individually Programmable Cell Stretching Microwell Arrays Actuated by a Braille Display. *Biomaterials* **29,** 2646–2655 (2008).

[186] Tremblay, D. *et al.* A Microscale Anisotropic Biaxial Cell Stretching Device for Applications in Mechanobiology. *Biotechnol. Lett.* **36,** 657–665 (2014).

[187] Walker, M., Godin, M. & Pelling, A. E. A Vacuum-Actuated Microtissue Stretcher for Long-Term Exposure to Oscillatory Strain within a 3D Matrix. *Biomed. Microdevices* **20,** 43 (2018).

[188] Stucki, A. O. *et al.* A Lung-on-a-Chip Array with an Integrated Bio-Inspired Respiration Mechanism. *Lab Chip* **15,** 1302–1310 (2015).

[189] Stucki, J. D. *et al.* Medium Throughput Breathing Human Primary Cell Alveolus-on-Chip Model. *Sci. Rep.* **8,** 14359 (2018).

[190] Raasch, M. *et al.* Microfluidically Supported Biochip Design for Culture of Endothelial Cell Layers with Improved Perfusion Conditions. *Biofabrication* **7,** 015013 (2015).

[191] Jain, A. *et al.* Primary Human Lung Alveolus-on-a-chip Model of Intravascular Thrombosis for Assessment of Therapeutics. *Clin. Pharmacol. Ther.* **103,** 332–340 (2018).

[192] Deinhardt-Emmer, S. *et al.* Co-Infection with *Staphylococcus Aureus* after Primary Influenza Virus Infection Leads to Damage of the Endothelium in a Human Alveolus-on-a-Chip Model. *Biofabrication* **12,** 025012 (2020).

[193] Zamprogno, P. *et al.* Second-Generation Lung-on-a-Chip with an Array of Stretchable Alveoli Made with a Biological Membrane. *Commun. Biol.* **4,** 168 (2021).

[194] Pasman, T. *et al.* Development of Porous and Flexible PTMC Membranes for In Vitro Organ Models Fabricated by Evaporation-Induced Phase Separation. *Membranes* **10,** 330 (2020).

[195] Timoshenko, S. & Woinowsky-Krieger, S. *Theory of Plates and Shells* 2nd edition (McGraw-Hill Book Company, 1959).

[196] Van Rijn, C. *et al.* Deflection and Maximum Load of Microfiltration Membrane Sieves Made with Silicon Micromachining. *J. Microelectromech. Syst.* **6,** 48–54 (1997).

[197] Ziebart, V. *et al.* Mechanical Properties of Thin Films from the Load Deflection of Long Clamped Plates. *J. Microelectromech. Syst.* **7,** 320–328 (1998).

[198] Kraft, O. & Volkert, C. A. Mechanical Testing of Thin Films and Small Structures. *Adv. Eng. Mater.* **3,** 99–110 (2001).

[199] Lee, D. *et al.* Mechanical Stimulation of Growth Plate Chondrocytes: Previous Approaches and Future Directions. *Exp. Mech.* **59,** 1261–1274 (2019).

[200] Lee, D. A. & Bader, D. L. Compressive Strains at Physiological Frequencies Influence the Metabolism of Chondrocytes Seeded in Agarose. *J. Orthop. Res.* **15,** 181–188 (1997).

[201] Amini, S., Veilleux, D. & Villemure, I. Tissue and Cellular Morphological Changes in Growth Plate Explants under Compression. *J. Biomech.* **43,** 2582–2588 (2010).

[202] Sergerie, K. *et al.* Growth Plate Explants Respond Differently to in Vitro Static and Dynamic Loadings. *J. Orthop. Res.* **29,** 473–480 (2011).

[203] Bougault, C. *et al.* Molecular Analysis of Chondrocytes Cultured in Agarose in Response to Dynamic Compression. *BMC Biotechnol.* **8,** 71 (2008).

[204] Moraes, C. *et al.* A Microfabricated Platform for High-Throughput Unconfined Compression of Micropatterned Biomaterial Arrays. *Biomaterials* **31,** 577–584 (2010).

[205] Lee, D. *et al.* Pneumatic Microfluidic Cell Compression Device for High-Throughput Study of Chondrocyte Mechanobiology. *Lab Chip* **18,** 2077–2086 (2018).

[206] Hsieh, H.-Y. *et al.* Gradient Static-Strain Stimulation in a Microfluidic Chip for 3D Cellular Alignment. *Lab Chip* **14,** 482–493 (2014).

[207] Paggi, C. A. *et al.* Monolithic Microfluidic Platform for Exerting Gradients of Compression on Cell-Laden Hydrogels, and Application to a Model of the Articular Cartilage. *Sens. Actuators B Chem.* **315,** 127917 (2020).

[208] Stoppel, W. L., Kaplan, D. L. & Black, L. D. Electrical and Mechanical Stimulation of Cardiac Cells and Tissue Constructs. *Adv. Drug Deliv. Rev.* **96,** 135–155 (2016).

[209] Zhao, Y. *et al.* Towards Chamber Specific Heart-on-a-Chip for Drug Testing Applications. *Adv. Drug Deliv. Rev.* **165–166,** 60–76 (2020).

[210] Volz, A. Longevity of Adult Ventricular Rat Heart Muscle Cells in Serum-Free Primary Culture. *J. Mol. Cell. Cardiol.* **23,** 161–173 (1991).

[211] Ellingsen, O. *et al.* Adult Rat Ventricular Myocytes Cultured in Defined Medium: Phenotype and Electromechanical Function. *Am. J. Physiol. - Heart Circ. Physiol.* **265,** H747–H754 (1993).

[212] Berger, H. J. *et al.* Continual Electric Field Stimulation Preserves Contractile Function of Adult Ventricular Myocytes in Primary Culture. *Am. J. Physiol. - Heart Circ. Physiol.* **266,** H341–H349 (1994).

[213] Nuccitelli, R. Endogenous Ionic Currents and DC Electric Fields in Multicellular Animal Tissues. *Bioelectromagnetics* **13,** 147–157 (1992).

[214] Tandon, N. *et al.* Electrical Stimulation Systems for Cardiac Tissue Engineering. *Nat. Protoc.* **4,** 155–173 (2009).

[215] LaBarge, W. *et al.* Maturation of Three-Dimensional, hiPSC-derived Cardiomyocyte Spheroids Utilizing Cyclic, Uniaxial Stretch and Electrical Stimulation. *PLoS ONE* **14,** e0219442 (2019).

[216] Barash, Y. *et al.* Electric Field Stimulation Integrated into Perfusion Bioreactor for Cardiac Tissue Engineering. *Tissue Eng. Part C Methods* **16,** 1417–1426 (2010).

[217] Chan, Y.-C. *et al.* Electrical Stimulation Promotes Maturation of Cardiomyocytes Derived from Human Embryonic Stem Cells. *J. Cardiovasc. Transl. Res.* **6,** 989–999 (2013).

[218] Ronaldson-Bouchard, K. *et al.* Engineering of Human Cardiac Muscle Electromechanically Matured to an Adult-like Phenotype. *Nat. Protoc.* **14,** 2781–2817 (2019).

[219] Pavesi, A. *et al.* How to Embed Three-Dimensional Flexible Electrodes in Microfluidic Devices for Cell Culture Applications. *Lab Chip* **11,** 1593–1595 (2011).

[220] Zhang, N. *et al.* Multifunctional 3D Electrode Platform for Real-Time in Situ Monitoring and Stimulation of Cardiac Tissues. *Biosens. Bioelectron.* **112,** 149–155 (2018).

[221] Zhao, Y. *et al.* A Multimaterial Microphysiological Platform Enabled by Rapid Casting of Elastic Microwires. *Adv. Healthcare Mater.* **8,** 1801187 (2019).

[222] Yip, J. K. *et al.* Contact Photolithography-Free Integration of Patterned and Semi-Transparent Indium Tin Oxide Stimulation Electrodes into Polydimethylsiloxane-Based Heart-on-a-Chip Devices for Streamlining Physiological Recordings. *Lab Chip* **21,** 674–687 (2021).

[223] Merrill, D. R., Bikson, M. & Jefferys, J. G. Electrical Stimulation of Excitable Tissue: Design of Efficacious and Safe Protocols. *J. Neurosci. Methods* **141,** 171–198 (2005).

[224] Serena, E. *et al.* Electrical Stimulation of Human Embryonic Stem Cells: Cardiac Differentiation and the Generation of Reactive Oxygen Species. *Exp. Cell Res.* **315,** 3611–3619 (2009).

[225] Tandon, N. *et al.* Characterization of Electrical Stimulation Electrodes for Cardiac Tissue Engineering. *2006 International Conference of the IEEE Engineering in Medicine and Biology Society* **1,** 845–848 (2006).

[226] Tandon, N. *et al.* Optimization of Electrical Stimulation Parameters for Cardiac Tissue Engineering. *J. Tissue Eng. Regen. Med.* **5,** e115–e125 (2011).

[227] Dvir, T. *et al.* Nanowired Three-Dimensional Cardiac Patches. *Nat. Nanotechnol.* **6,** 720–725 (2011).

[228] Ryan, A. J. *et al.* Electroconductive Biohybrid Collagen/Pristine Graphene Composite Biomaterials with Enhanced Biological Activity. *Adv. Mater.* **30,** 1–8 (2018).

[229] Rogal, J. *et al.* WAT-on-a-chip Integrating Human Mature White Adipocytes for Mechanistic Research and Pharmaceutical Applications. *Sci. Rep.* **10,** 6666 (2020).

[230] Xia, Y. & Whitesides, G. M. Soft Lithography. *Annu. Rev. Mater. Sci.* **28,** 153–84 (1998).

[231] Jo, B.-H. *et al.* Three-Dimensional Micro-Channel Fabrication in Polydimethylsiloxane (PDMS) Elastomer. *J. Microelectromech. Syst.* **9,** 76–81 (2000).

[232] Goral, V. N. *et al.* Hot Embossing of Plastic Microfluidic Devices Using Poly(Dimethylsiloxane) Molds. *J. Micromech. Microeng.* **21,** 017002 (2011).

[233] Sonney, S., Shek, N. & Moran-Mirabal, J. M. Rapid Bench-Top Fabrication of Poly(Dimethylsiloxane)/Polystyrene Microfluidic Devices Incorporating High-Surface-Area Sensing Electrodes. *Biomicrofluidics* **9** (2015).

[234] Lian, X. *et al.* Directed Cardiomyocyte Differentiation from Human Pluripotent Stem Cells by Modulating Wnt/ -Catenin Signaling under Fully Defined Conditions. *Nat. Protoc.* **8,** 162–175 (2013).

[235] Guo, L. *et al.* Use of Human Induced Pluripotent Stem Cell-Derived Cardiomyocytes (hiPSC-CMs) to Monitor Compound Effects on Cardiac Myocyte Signaling Pathways: hiPSC-CMs to Study Myocyte Signaling Pathways. *Curr. Protoc. Chem. Biol.* **7,** 141–185 (2015).

[236] Hookway, T. A. *et al.* Aggregate Formation and Suspension Culture of Human Pluripotent Stem Cells and Differentiated Progeny. *Methods* **101,** 11–20 (2016).

[237] Dahlmann, J. *et al.* The Use of Agarose Microwells for Scalable Embryoid Body Formation and Cardiac Differentiation of Human and Murine Pluripotent Stem Cells. *Biomaterials* **34,** 2463–2471 (2013).

[238] Guatimosim, S., Guatimosim, C. & Song, L.-S. Imaging Calcium Sparks in Cardiac Myocytes. *Methods Mol. Biol.* **689,** 205–214 (2011).

[239] Loskill, P. *et al.* WAT-on-a-chip: A Physiologically Relevant Microfluidic System Incorporating White Adipose Tissue. *Lab Chip* **17,** 1645–1654 (2017).

[240] Wilkinson, A., Clemens, M. & Harding, V. The Effects of SEBS-g-maleic Anhydride Reaction on the Morphology and Properties of Polypropylene/PA6/SEBS Ternary Blends. *Polymer* **45,** 5239–5249 (2004).

[241] Motomatsu, M., Mizutani, W. & Tokumoto, H. Microphase Domains of Poly(Styrene-Block-Ethylene/Butylene-Block-Styrene) Triblock Copolymers Studied by Atomic Force Microscopy. *Polymer* **38,** 1779–1785 (1997).

[242] Allan, D. B. *et al.* Trackpy. *Zenodo,* 10.5281/zenodo.1213240 (2021).

[243] Crocker, J. C. & Grier, D. G. Methods of Digital Video Microscopy for Colloidal Studies. *J. Colloid Interface Sci.* **179,** 298–310 (1996).

[244] Musy, M. *et al.* Vedo, a Python Module for Scientific Analysis and Visualization of 3D Objects and Point Clouds. *Zenodo,* 10.5281/zenodo.5655358 (2021).

[245] Strohmeier, O. *et al.* Centrifugal Microfluidic Platforms: Advanced Unit Operations and Applications. *Chem. Soc. Rev.* **44,** 6187–6229 (2015).

[246] Bartolo, D. *et al.* Microfluidic Stickers. *Lab Chip* **8,** 274–279 (2008).

[247] Morel, M. *et al.* Microfluidic Stickers for Cell- and Tissue-Based Assays in Microchannels. *Lab Chip* **9,** 1011–1013 (2009).

[248] Sollier, E. *et al.* Rapid Prototyping Polymers for Microfluidic Devices and High Pressure Injections. *Lab Chip* **11,** 3752 (2011).

[249] Li, R. *et al.* A Rapidly Fabricated Microfluidic Chip for Cell Culture. *J. Chromatogr. Sci.* **54,** 523–530 (2016).

[250] Gao, Y., Stybayeva, G. & Revzin, A. Fabrication of Composite Microfluidic Devices for Local Control of Oxygen Tension in Cell Cultures. *Lab Chip* **19,** 306–315 (2019).

[251] Agostini, M., Greco, G. & Cecchini, M. Polydimethylsiloxane (PDMS) Irreversible Bonding to Untreated Plastics and Metals for Microfluidics Applications. *APL Mater.* **7,** 081108 (2019).

[252] Nguyen, D. C. *et al.* Microscale Generation of Cardiospheres Promotes Robust Enrichment of Cardiomyocytes Derived from Human Pluripotent Stem Cells. *Stem Cell Rep.* **3,** 260–268 (2014).

[253] Daly, A. C., Davidson, M. D. & Burdick, J. A. 3D Bioprinting of High Cell-Density Heterogeneous Tissue Models through Spheroid Fusion within Self-Healing Hydrogels. *Nat. Commun.* **12,** 753 (2021).

[254] Burger, R. *et al.* Centrifugal Microfluidics for Cell Analysis. *Curr. Opin. Chem. Biol.* **16,** 409–414 (2012).

[255] Glynn, M. *et al.* Cluster Size Distribution of Cancer Cells in Blood Using Stopped-Flow Centrifugation along Scale-Matched Gaps of a Radially Inclined Rail. *Microsyst. Nanoeng.* **1,** 15018 (2015).

[256] Espulgar, W. *et al.* Centrifugal Microfluidic Platform for Single-Cell Level Cardiomyocyte-Based Drug Profiling and Screening. *Lab Chip* **15,** 3572–3580 (2015).

[257] Park, J. *et al.* Hypergravity-Induced Multicellular Spheroid Generation with Different Morphological Patterns Precisely Controlled on a Centrifugal Microfluidic Platform. *Biofabrication* **9,** 45006 (2017).

[258] Bruzewicz, D. A., McGuigan, A. P. & Whitesides, G. M. Fabrication of a Modular Tissue Construct in a Microfluidic Chip. *Lab Chip* **8,** 663 (2008).

[259] Bergström, G. *et al.* Stem Cell Derived in Vivo-like Human Cardiac Bodies in a Microfluidic Device for Toxicity Testing by Beating Frequency Imaging. *Lab Chip* **15,** 3242–3249 (2015).

[260] Kuddannaya, S. *et al.* Surface Chemical Modification of Poly(Dimethylsiloxane) for the Enhanced Adhesion and Proliferation of Mesenchymal Stem Cells. *ACS Appl. Mater. Interfaces* **5,** 9777–9784 (2013).

[261] Huebsch, N. *et al.* Automated Video-Based Analysis of Contractility and Calcium Flux in Human-Induced Pluripotent Stem Cell-Derived Cardiomyocytes Cultured over Different Spatial Scales. *Tissue Eng. Part C Methods* **21,** 467–479 (2015).

[262] Maddah, M. *et al.* A Non-Invasive Platform for Functional Characterization of Stem-Cell-Derived Cardiomyocytes with Applications in Cardiotoxicity Testing. *Stem Cell Rep.* **4,** 621–631 (2015).

[263] Czirok, A. *et al.* Optical-Flow Based Non-Invasive Analysis of Cardiomyocyte Contractility. *Sci. Rep.* **7,** 1–11 (2017).

[264] Nitsch, S. *et al.* Functional Video-Based Analysis of 3D Cardiac Structures Generated from Human Embryonic Stem Cells. *Stem Cell Res.* **29,** 115–124 (2018).

[265] Nikolov, N. *et al.* A New Algorithm to Analyze the Video Data of Cell Contractions in Microfluidic Platforms. *Innov. Biosyst. Bioeng.* **2,** 74–83 (2018).

[266] Sala, L. *et al.* MUSCLEMOTION. *Circ. Res.* **122,** e5–e16 (2018).

[267] Gray, D. S., Tien, J. & Chen, C. S. Repositioning of Cells by Mechanotaxis on Surfaces with Micropatterned Young's Modulus. *J. Biomed. Mater. Res.* **66A,** 605–614 (2003).

[268] Ohm, C. & Ober, C. K. From Surface Coatings to Polymer Nanofilms: Lifting off Polymer Brushes. *RSC Adv.* **3,** 18482 (2013).

[269] Teng, L. *et al.* Robust, Multiscale Liquid-Metal Patterning Enabled by a Sacrificial Sealing Layer for Flexible and Wearable Wireless Powering. *J. Mater. Chem. C* **7,** 15243–15251 (2019).

[270] Vertelov, G. *et al.* Rigidity of Silicone Substrates Controls Cell Spreading and Stem Cell Differentiation. *Sci. Rep.* **6,** 33411 (2016).

[271] Van Meer, B. *et al.* Small Molecule Absorption by PDMS in the Context of Drug Response Bioassays. *Biochem. Biophys. Res. Commun.* **482,** 323–328 (2017).

[272] Toepke, M. W. & Beebe, D. J. PDMS Absorption of Small Molecules and Consequences in Microfluidic Applications. *Lab Chip* **6,** 1484 (2006).

[273] Madsen, E. L. *et al.* Instrument for Determining the Complex Shear Modulus of Soft-Tissue-like Materials from 10 to 300 Hz. *Phys. Med. Biol.* **53,** 5313–5342 (2008).

[274] Lesher-Pérez, S. C. *et al.* Dispersible Oxygen Microsensors Map Oxygen Gradients in Three-Dimensional Cell Cultures. *Biomater. Sci.* **5,** 2106–2113 (2017).

[275] Gabay, T. *et al.* Electro-Chemical and Biological Properties of Carbon Nanotube Based Multi-Electrode Arrays. *Nanotechnology* **18,** 035201 (2007).

[276] Petersen, A. P. *et al.* Microenvironmental Modulation of Calcium Wave Propagation Velocity in Engineered Cardiac Tissues. *Cel. Mol. Bioeng.* **11,** 337–352 (2018).

[277] Davis, B. N. *et al.* Oxygen Consumption in Human, Tissue-Engineered Myobundles during Basal and Electrical Stimulation Conditions. *APL Bioeng.* **3,** 11 (2019).

[278] Otis, A. B. & Proctor, D. F. MEASUREMENT OF ALVEOLAR PRESSURE IN HUMAN SUBJECTS. *Am. J. Physiol. - Legacy Content* **152,** 106–112 (1947).

[279] Reese, W. M. *et al.* Facile Macrocyclic Polyphenol Barrier Coatings for PDMS Microfluidic Devices. *Adv. Funct. Mater.* **30,** 2001274 (2020).

[280] Domansky, K. *et al.* SEBS Elastomers for Fabrication of Microfluidic Devices with Reduced Drug Absorption by Injection Molding and Extrusion. *Microfluid. Nanofluid.* **21,** 107 (2017).

[281] Moore, T. A., Brodersen, P. & Young, E. W. K. Multiple Myeloma Cell Drug Responses Differ in Thermoplastic vs PDMS Microfluidic Devices. *Anal. Chem.* **89,** 11391–11398 (2017).

[282] Zamprogno, P. *et al.* Mechanical Properties of Soft Biological Membranes for Organ-on-a-Chip Assessed by Bulge Test and AFM. *ACS Biomater. Sci. Eng.* **7,** 2990–2997 (2021).

[283] Malic, L. *et al.* Epigenetic Subtyping of White Blood Cells Using a Thermoplastic Elastomer-Based Microfluidic Emulsification Device for Multiplexed, Methylation-Specific Digital Droplet PCR. *Analyst* **144,** 6541–6553 (2019).

[284] Raub, C. *et al.* Predicting Bulk Mechanical Properties of Cellularized Collagen Gels Using Multiphoton Microscopy. *Acta Biomater.* **6,** 4657–4665 (2010).

[285] Prestwich, G. D. Hyaluronic Acid-Based Clinical Biomaterials Derived for Cell and Molecule Delivery in Regenerative Medicine. *J. Control. Release* **155,** 193–199 (2011).

[286] Hall, M. S. *et al.* Mapping Three-Dimensional Stress and Strain Fields within a Soft Hydrogel Using a Fluorescence Microscope. *Biophys. J.* **102,** 2241–2250 (2012).

[287] Moutos, F. T. *et al.* Anatomically Shaped Tissue-Engineered Cartilage with Tunable and Inducible Anticytokine Delivery for Biological Joint Resurfacing. *Proc. Natl. Acad. Sci. USA* **113,** E4513–E4522 (2016).

[288] Mat Nawi, M. N. *et al.* Fabrication Techniques for PDMS Dome-Shaped Membrane Using Soft Lithography Process. *Appl. Mech. Mater.* **660,** 899–903 (2014).

[289] Musgrove, H. B., Catterton, M. A. & Pompano, R. R. Best Practices for Design and Fabrication of Biomicrofluidic Devices by Resin 3D Printing. *bioRxiv,* 2021.11.23.468853 (2021).

[290] O'Grady, B. J. *et al.* Rapid Prototyping of Cell Culture Microdevices Using Parylene-Coated 3D Prints. *bioRxiv,* 2021.08.02.454773 (2021).

[291] Cambria, E. *et al.* Cell-Laden Agarose-Collagen Composite Hydrogels for Mechanotransduction Studies. *Front. Bioeng. Biotechnol.* **8,** 346 (2020).

[292] Schneider, S. *et al.* Peristaltic On-Chip Pump for Tunable Media Circulation and Whole Blood Perfusion in PDMS-free Organ-on-Chip and Organ-Disc Systems. *Lab Chip* **21,** 3963–3978 (2021).

[293] Schneider, S. *et al.* Organ-on-a-Disc: A Platform Technology for the Centrifugal Generation and Culture of Microphysiological 3D Cell Constructs Amenable for Automation and Parallelization. *APL Bioeng.* **4,** 046101 (2020).

[294] Sniadecki, N. J. *et al.* Magnetic Microposts as an Approach to Apply Forces to Living Cells. *Proc. Natl. Acad. Sci. USA* **104,** 14553–14558 (2007).

Acknowledgments

As science is a team sport, presented work would not have been possible without the contribution of several people to whom I am greatly indebted. First of all, I would like to express my deepest gratitude to Prof. Dr. Peter Loskill for the unique opportunity to perform my PhD thesis in his laboratory. It was an exciting time witnessing and contributing to the cutting-edge field of OoC technology full of sparking new ideas and artistic sketches. Second, I would like to thank Prof. Oliver Röhrle, PhD and Prof. Dr. Torsten Mayr for supervising and examining this thesis.

I would like to thank the institute heads Prof. Dr. Katja Schenke-Layland and Dr. Markus Wolperdinger as well as the Fraunhofer Gesellschaft for the opportunity to pursue my research at the Fraunhofer Institute for Interfacial Engineering and Biotechnology IGB in Stuttgart. In general, I want to thank the whole institute for its support and infrastructure with special thanks to Dr. Anke Burger-Kentischer who adopted me in times of lab turmoil into her group, allowing me to finish all experiments at the institute.

I want to thank all members of the Broffice™ where we created a wonderful balance between productivity and fun. Special thanks to Stefan Schneider; we did not only share the last name but also the same boat. It was amazing seeing members maturing like Ibrahim Maulana advancing from mixing PDMS 1:100 in his novice days to winning the young presentation award at EUROoCS Conference 2021 or Cristhian A. E. Rojas advancing from master's student to a full time project manager, managing an army of student assistants for chip fabrication. Moreover I would like to thank my fellow starting PhD students Julia Rogal & Johanna Chuchuy, remembering great trips and parties, in the early days even with Christopher Probst.

Thanks to all other µOrganoLab members (Kirstin, Madalena, Tanvi, Kathi, Eduardo, Julia, Elena) for their motivation and support. An exceptional thanks goes to Alessia Moruzzi as wizard of cells who handled most biological aspects of the cardiac projects, without which the successful realization of all presented concepts would not have been possible. Further thanks to Silvia Kolbus-Hernandez for assistance with cell culture and differentiations.

It is no secret that the monetary payment for pursuing a PhD is a drop in the bucket, however, the real payment and encouragement is the opportunity to work with highly motivated students, developing unprecedented solutions. I would like to thank my supervised students Stefanie Fuchs, Lisa Zeifang, Carla Sailer, Isaac Stamper, Alina Grobel, Marina Albaladejo Siguan, and Henrike Schulze for all their

work and dedication. Thanks to all other students (Kaori, Scott, Raylin, Huub, Lejla, Annika, Thomas, Florian, Dominic, Dominick, Jillian, Roua, Kimberly, and many more) for the great atmosphere and special thanks to Elena for inviting the whole group to Sardinia. Thanks to Joost for sharing his passion for lifelong learning.

As I was privileged to visit and perform experiments in cutting-edge iPSC and OoC laboratories, I would like to thank for the cooperation and all the things I learnt. Thanks to Ana Silva, Sarah Rockwood, Oriane Matthys, and Ron Manlapaz at the McDevitt Lab at Gladstone Institutes in San Francisco and the DAAD for funding this academic exchange. Thanks to Berend van Meer and Ruben van Helden from the Mummery Lab at Leiden University Medical Center. Thanks to Hristina Koceva from the Mosig Lab at Uniklinikum Jena. Thanks to Dominik Rabl and Stefanie Fuchs from Torsten Mayr's lab in Graz for the fruitful cooperation and the supply of O_2 sensor substrates. Further thanks to Elena Cambria and Ning Zhang for the great time and collaboration on the compression chip project.

Furthermore, I was fortunate to attend an amazing summer school in Coimbra learning a lot on computational biology, working on a group project and enjoying great food. Thanks to the organizers Rui Travasso and Armindo Salvador for putting together such an exceptional event.

I want to thank all my friends for all the great times and fun we had and will have together, shaping who I am. Furthermore, I want to thank my whole family for always being there for me.

Dear Katrin, I remember a plethora of amazing trips we have done during our time in Stuttgart and look forward to many more adventures involving coffee, bikes and trains!

Curriculum Vitæ

Oliver Schneider

Education

2017–2022	PhD candidate University of Stuttgart, Germany
2014–2016	M.Sc. Nanotechnology Julius Maximilians University Würzburg, Germany
2010–2013	B.Sc. Nanotechnology (solid state physics program) Julius Maximilians University Würzburg, Germany

Research experience

2017–2021	PhD student with Prof. Dr. P. Loskill Fraunhofer IGB Stuttgart, Germany
2015–2016	Master's thesis with Prof. Dr. J. Pflaum Julius Maximilians University Würzburg, Germany
2013–2014	Visiting researcher with Prof. Dr. F. Hellman University of California, Berkeley, USA

Awards

2020	Young investigator award (best presentation) at the EUROoCS Annual Meeting
2019	DAAD scholarship for a monthly research stay at the Gladstone Institutes, San Francisco, USA
2019	Travel award & selected talk at the EUROoCs Annual Meeting
2017	Award for best poster at the DGMB Annual Meeting
2013	DAAD scholarship for a 9 month research stay at the University of California, Berkeley, USA

Publications

- Schneider, O., Moruzzi, A., Fuchs, S., Grobel, A., Schulze, H. S., Mayr, T. & Loskill, P. Fusing Spheroids to Aligned µ-Tissues in a Heart-on-Chip Featuring Oxygen Sensing and Electrical Pacing Capabilities. *Mater. Today Bio* **15**, 100280 (2022)
- Schneider, S., Brás, E. J. S., Schneider, O., Schlünder, K. & Loskill, P. Facile Patterning of Thermoplastic Elastomers and Robust Bonding to Glass and Thermoplastics for Microfluidic Cell Culture and Organ-on-Chip. *Micromachines* **12**, 575 (2021)
- Schneider, S., Erdemann, F., Schneider, O., Hutschalik, T. & Loskill, P. Organ-on-a-Disc: A Platform Technology for the Centrifugal Generation and Culture of Microphysiological 3D Cell Constructs Amenable for Automation and Parallelization. *APL Bioeng.* **4**, 046101 (2020)
- Schneider, O., Zeifang, L., Fuchs, S., Sailer, C. & Loskill, P. User-Friendly and Parallelized Generation of Human Induced Pluripotent Stem Cell-Derived Microtissues in a Centrifugal Heart-on-a-Chip. *Tissue Eng. Part A* **25**, 786–798 (2019)
- Ceballos, A., Chen, Z., Schneider, O., Bordel, C., Wang, L., & Hellman, F. Effect of strain and thickness on the transition temperature of epitaxial FeRh thin-films. *Appl. Phys. Lett.* **111**, 172401 (2017)

Patents

- Loskill, P., Schneider, O., Schneider S., Device and method for cultivating cells. US20200199509A1 (2018)
- Loskill, P., Schneider, O., Method for cultivating cells. US20200109361A1 (2018)
- Borowski, P., Schneider, O. Solar module with an electrically insulated module support and method for production thereof. US20160155874A1 (2014)

Conference contributions

- Electrical pacing of hiPSC-derived cardiac µ-tissues in a centrifugal Heart-on-Chip platform, talk (online presentation due to COVID-19 pandemic), *EUROoCs (European Organ-on-Chip Society) Annual Meeting*, Uppsala, SE (2020)
- Centrifugal Heart-on-a-Chip: User-friendly and parallelized generation of hiPSC-derived µ-tissues, **selected talk**, *EUROoCs (European Organ-on-Chip Society) Annual Meeting*, Graz, AT (2019)
- Integrating Traction Force Microscopy into Organ-on-a-Chip platforms: In situ characterization of contractile forces in 3D cardiac µ-tissues, poster, *TERMIS (Tissue Engineering and Regenerative Medicine International Society) World Congress*, Kyoto, JP (2018)
- Integrated Heart-on-a-Chip systems: In situ characterization of contractile forces in 3D cardiac µ-tissues, **invited institute seminar talk**, *Institute of Applied Physics, University of Tübingen*, Tübingen, DE (2018)
- Integrated Heart-on-a-Chip systems: In situ characterization of contractile forces in 3D cardiac µ-tissues, talk, *DPG (German Physical Society) Spring Meeting*, Berlin, DE (2018)
- Heart-on-a-Chip: In situ characterization of contractile forces in 3D cardiac µ-tissues, talk & poster, *DGMB (German Society for Matrix Biology) Annual Meeting*, Stuttgart, DE (2018)
- Single Molecule Spectroscopy in a tunable cavity system, poster, *DPG (German Physical Society) Spring Meeting*, Regensburg, DE (2016)